Susana Isabel Conde Jesus Palma

Mestre em Engenharia Biomédica

Engineered MRI nanoprobes based on superparamagnetic iron oxide nanoparticles

Dissertação para obtenção do Grau de Doutor em Bioengenharia (MIT-Portugal)

Orientador: Prof. Doutora Ana Cecília Roque, FCT-UNL

FACULDADE DE CIÊNCIAS E TECNOLOGIA
UNIVERSIDADE NOVA DE LISBOA

Setembro 2015

Engineered MRI nanoprobes based on superparamagnetic iron oxide nanoparticles

In memory of my dear Tia Germina, Avó Laura e Avô João

Acknowledgements

During the four years of the PhD Adventure, I had the chance to work in a multidisciplinary environment, building bridges between different areas of expertise in bioengineering research. It has been a very interesting challenge, which was only possible with the contribution and support of several people.

I deeply thank my supervisor Prof. Ana Cecília Roque for having given me the opportunity to be part of her research group and work with her in this challenging project. I am very grateful for the rigor, exigence, brainstorming and advice but also for the patience and confidence that you had in me, Cecília. Without your support, the achievements of this "nano-adventure" were not possible.

When I met Dr. M. Puerto Morales in a conference, in Lubeck, I could not imagine the importance she would have in my PhD. I thank Puerto for my stay in her Lab at ICCM (Madrid), for giving me the opportunity to meet and/or work with Marzia Marciello, Sabino Vientemillas, Gorka Salas, Amalia Ruiz, Yurena Luengo, Fernando Herranz and Jesús Ruiz-Cabello. I am very grateful to Puerto for her availability to make VSM measurements of my nanoparticles and to discuss the results of the work, giving an important input to my PhD project. It was such a fruitful partnership.

I thank Prof. Alexandra R. Fernandes for receiving me in her Lab at UCIBIO, DCV (FCT-UNL) for the *in vitro* assays with HC116 cell line, and for her availability to discuss the results. I leave here also a very sincere "thank you" to Joana Silva and Pedro Martins, from Prof. Alexandra's Lab, for having introduced me to the human cell culture techniques and for the technical support during my experiments in the cell culture lab. I express also my gratitude to Prof. Pedro Baptista and his team for sharing the Lab equipment with me.

This work would be more difficult without the collaboration of Alexandra Carvalho at CENIMAT (FCT-UNL), who I acknowledge for the support regarding the MRI experiments and availability to discuss results and share ideas. It was a nice and fruitful collaboration.

I thank Prof. Joaquim Sampaio Cabral for the opportunity to work with the cell line ReNcell VM in his Lab (SCBL at iBB (IST-UL)) and for providing the resources and facilities for the experiments.

I would also like to thank all my colleagues in the Biomolecular Engineering Group. I am very happy for being part of this team! I really enjoyed working in the good mood of Lab 523,

always with a friendly and fun environment, but also very well organized and tidy. Dear colleagues Abid Hussain, Ricardo Branco, Ana Pina, Íris Batalha, Telma Barroso, Margarida Dias, Vijaykumar Dahdge, Cláudia Fernandes, Henrique Carvalho, Carina Rodrigues and, more recently, José Almeida, Aline Viecinski, Luís Silva and Arménio Barbosa: thank you for the nice environment in the Lab, and for the discussions in the group meetings and during the lab daily routine. A special acknowledgement goes to Abid, who was the first to introduce me to the Lab bench and nanoparticle synthesis. Íris Batalha, Margarida Dias and Ana Pina, the self-named "orsinhas": thanks for the healthy discussions, for all the laughing and for being there also in the frustrating and unhappy moments of life during the PhD. A big and smiley "thank you" to all the members that passed by the Biomolecular Engineering Group during my PhD, not forgetting my "aluninhas" Rosarinho Nazaré and Patrícia Traguedo, who introduced me to the teaching side of academic research life.

I acknowledge the technical support of Dr. Carla Rodrigues, from Laboratório de Análises of REQUIMTE and also Prof. César Laia (for the collaboration with using the DLS at DQ), Prof. Luísa Ferreira (for the help with FTIR analyses), Dr. Paulo Lemos and Dr. Christophe Roca (for the help with the fluorescence microscope). I would like to acknowledge also D. Maria José Carapinha and Isabel Rodrigues for their help with bureaucratic paper work, and D. Maria da Palma Afonso and Mafalda Manita for the assistance in keeping the labware clean for the daily laboratory activities.

None of the achievements of this thesis would have been possible without the support and love of my friends and family. They helped me to relax and patiently listened to my concerns and doubts in the most stressful days. But, at the same time, they were also the ones who celebrated with me the enthusiasm of positive results and published papers!

Agradeço aos meus colegas da Banda da Sociedade Musical Sesimbrense e da Bota Big Band pela Música, pelos momentos de companheirismo e de paródia. Aos meus amigos Cristina, Ângelo (e Bia, claro), Sara, Maria da Luz, Carla, Tânia, e Ana Dionísio obrigada por me terem ouvido nos dias mais depressivos do doutoramento e por terem partilhado comigo momentos de descontracção e festa para sair da rotina do Lab!

Ao meu pai, à minha mãe e ao meu irmão, agradeço o interesse e o esforço que sempre demonstraram em perceber e acompanhar o meu trabalho, apesar ser pouco convencional e complexo de explicar… Obrigada pela enooorrrrme paciência e todo o apoio e carinho.

Deixo um agradecimento muito grande e muito especial ao Carlos por ter estado sempre ao meu lado, tanto cientificamente como emocionalmente. Obrigada pela participação e grande ajuda nos ensaios celulares no SCBL, pela tua paciência, carinho, amizade e compreensão, mesmo quando tudo parecia correr mal.

Abstract

This project aimed to engineer new T_2 MRI contrast agents for cell labeling based on formulations containing monodisperse iron oxide magnetic nanoparticles (MNP) coated with natural and synthetic polymers. Monodisperse MNP capped with hydrophobic ligands were synthesized by a thermal decomposition method, and further stabilized in aqueous media with citric acid or *meso*-2,3-dimercaptosuccinic acid (DMSA) through a ligand exchange reaction. Hydrophilic MNP-DMSA, with optimal hydrodynamic size distribution, colloidal stability and magnetic properties, were used for further functionalization with different coating materials. A covalent coupling strategy was devised to bind the biopolymer gum Arabic (GA) onto MNP-DMSA and produce an efficient contrast agent, which enhanced cellular uptake in human colorectal carcinoma cells (HCT116 cell line) compared to uncoated MNP-DMSA. A similar protocol was employed to coat MNP-DMSA with a novel biopolymer produced by a biotechnological process, the exopolysaccharide (EPS) Fucopol. Similar to MNP-DMSA-GA, MNP-DMSA-EPS improved cellular uptake in HCT116 cells compared to MNP-DMSA. However, MNP-DMSA-EPS were particularly efficient towards the neural stem/progenitor cell line ReNcell VM, for which a better iron dose-dependent MRI contrast enhancement was obtained at low iron concentrations and short incubation times. A combination of synthetic and biological coating materials was also explored in this project, to design a dynamic tumor-targeting nanoprobe activated by the acidic pH of tumors. The pH-dependent affinity pair neutravidin/iminobiotin, was combined in a multilayer architecture with the synthetic polymers poy-L-lysine and poly(ethylene glycol) and yielded an efficient MRI nanoprobe with ability to distinguish cells cultured in acidic pH conditions form cells cultured in physiological pH conditions.

Keywords: iron oxide magnetic nanoparticles (MNP), magnetic resonance imaging (MRI), gum Arabic, biopolymer, pH-dependent affinity, tumor-targeting

x

Resumo

O objectivo desta tese consiste na engenharia de novos agentes de contraste T_2 para marcação celular através de imagiologia por ressonância magnética (MRI), usando formulações com nanopartículas magnéticas de óxido de ferro (MNP) revestidas com polímeros naturais e com polímeros sintéticos. O método da decomposição térmica foi usado para sintetizar MNP monodispersas revestidas com ligandos hidrofóbicos. Para as estabilizar em meio aquoso, os ligandos hidrofóbicos foram substituídos por moléculas hidrofílicas, como o ácido cítrico ou o ácido *meso*-2,3,-dimercaptosuccínico (DMSA), através de uma reacção de intercâmbio de ligandos. As MNP-DMSA, hidrofílicas, com estabilidade coloidal e propriedades magnéticas optimizadas, foram revestidas com diferentes materiais. Para acoplar o biopolímero goma arábica às MNP-DMSA, foi usada uma ligação covalente que permitiu obter um agente de contraste eficiente e com um nível de captação celular melhorado face às MNP-DMSA em células humanas de carcinoma colorectal (linha celular HCT116). Um protocolo experimental semelhante foi usado para revestir as MNP-DMSA com um biopolímero novo produzido por via biotecnológica, o exopolisacarídeo (EPS) Fucopol. Tal como as MNP-DMSA-GA, as MNP-DMSA-EPS melhoraram o nível de captação celular nas células HCT116 face às MNP-DMSA. No entanto, foram particularmente eficientes numa linha de células estaminais/progenitoras neurais (ReNcell VM), nas quais se obteve um melhoramento mais intenso do contraste em função da dose de ferro nas imagens por MRI, para doses baixas de ferro e tempos de incubação curtos. Neste projecto foi também explorada uma combinação de materiais de revestimento sintéticos e biológicos para desenvolver uma nano-sonda dinâmica para marcação de tumores, activada pelo pH ácido tumoral. O par de afinidade dependente do pH neutravidina/iminobiotina foi combinado com poli-L-lisina e poli(etilenoglicol) através de uma arquitectura multi-camada, resultando numa nano-sonda para MRI eficiente e capaz de distinguir células cultivadas em condições ácidas de células cultivadas em condições fisiológicas.

Palavras-chave: nanopartículas magnéticas de óxido de ferro (MNP), imagiologia por ressonância magnética, goma arábica, afinidade dependente de pH, marcação de tumores

Table of Contents

Index of Figures

Index of Tables

Abbreviations

bPEG	Biotin-modified PEG
CA	Citric acid
Cyst	Cysteamine hydrochloride
DAPI	(4',6-diamidino-2-phenylindole)
DLS	Dynamic Light Scattering
DMEM	Dulbecco's modified Eagle's medium
DMSA	*Meso*-2,3-dimercaptosuccinic acid
DMSO	Dimethylsulfoxide
DTA	Differential thermal analysis
DTDP	2,2'-dithiodipyridine
EDC	N-(3-dimethylaminopropyl)-N'-ethyl-carbodiimide
EPS	Exopolysaccharide
FBS	Fetal bovine serum
FC	Field cooling
FTIR	Fourier transform infrared spectroscopy
GA	Gum Arabic
ib	Iminobiotin
IC_{50}	Relative half-maximal inhibitory concentration
ICP-AES	Inductively coupled plasma atomic emission spectroscopy
LbL	Layer-by-Layer
MNP	Iron oxide Magnetic Nanoparticles
MNP-CA	Iron oxide magnetic nanoparticles coated with citric acid
MNP-DMSA	Iron oxide magnetic nanoparticles coated with *meso*-2,3-dimercaptosuccinic acid
MNP-DMSA-Cyst-GA	MNP-DMSA coated with Cyst and GA
MNP-DMSA-EPS	MNP-DMSA coated with the exopolysaccharide Fucopol
MNP-DMSA-GA	MNP-DMSA coated with gum Arabic
MNP-DMSA-PLLib-Nav-bPEG	MNP-DMSA coated with iminobiotin-modified Poly-L-lysine, neutravidin and biotin-modified poly(ethyleneglycol)
MNP-OA	Iron oxide magnetic nanoparticles coated with oleic acid and oleylamine
MR	Magnetic resonance
MRI	Magnetic Resonance Imaging
M_S	Saturation Magnetization
MTT	3-(4,5-dimethylthiazol-2-yl)-2,5-diphenyl tetrazolium bromide
Nav	Neutravidin
NHS	N-hydroxysuccinimide
NMR	Nuclear magnetic resonance
PBS	Phosphate buffered saline
PdI	Polydispersity index
PEG	Poly(ethyleneglycol)
PLL	Poly-L-Lysine
PLLib	Ib-modified PLL

SPION	Superparamagnetic Iron Oxide Nanoparticles
TE	Echo time
TR	Repetition time
TEM	Transmission Electron Microscopy
TGA	Thermogravimetric analysis
TR	Repetition time
VSM	Vibrating sample magnetometry
ZFC	Zero-field cooling

Background

Magnetic Resonance Imaging (MRI) is a noninvasive medical imaging technique with a wide range of applications in diagnostics which has been used in the clinic for more than 30 years. Among the currently available clinical imaging techniques, MRI offers important advantages, mainly because it does not use harmful radiation and, besides being noninvasive, provides excellent spatial resolution (sub-millimeter, the best among X-ray CT, PET, SPECT and ultrasound), and anatomical information of deep tissue structures. The major challenge with MRI is its relatively low sensitivity (10^{-3} M to 10^{-5} M) compared to other imaging methods, but it can be improved with the administration of better contrast agents, which augment the visibility of specific body structures by enhancing the contrast of the images. Traditionally, gadolinium-based paramagnetic compounds are used for this purpose (as T_1 contrast agents) and, currently, these are the only products approved by health regulatory agencies being used in the clinic as MRI contrast agents.[1–3]

Superparamagnetic iron oxide nanoparticles (MNP) are a different class of MRI contrast agents (T_2 contrast agents) and potential alternatives to gadolinium-based agents. They possess a superior magnetic moment than gadolinium and therefore lower doses of MNP are required to provide adequate image contrast.[4] In addition, iron oxides are biocompatible and biodegradable at the doses needed for contrast enhancement.[5] Since iron is a naturally occurring metal in the human body, there are specialized metabolic pathways and clearance mechanisms for regulation of iron homeostasis, unlike for gadolinium. The potential for long-term cytotoxicity of MNP is thus reduced. Some MNP-based MRI contrast agents have been approved for clinical use in the past, but were withdrawn from the market due to economical rather than safety reasons.[6,7] Therefore, research continues dedicating large efforts to the development of new nanoprobes based on iron oxide nanoparticle formulations with MRI applications.

Due to their nanosize, MNP possess a large and highly reactive surface area, to which other chemical compounds or biomolecules can be conjugated. MNPs surface functionalization is versatile, which facilitates particle engineering to render MNPs with additional properties besides the inherent MRI contrast enhancement ability. Several materials, functionalization strategies and nanoprobe architectures have been explored to produce MRI nanoplatforms, and in the last years, the enormous interest in these systems has expanded the use of MRI beyond disease diagnosis. Currently, several applications of MRI are enabled due to the possibility of conjugating MNP with targeting agents, therapeutic agents or even reporter molecules for other

imaging modalities. Detecting cancer and metastases, monitoring cancer treatment response, detecting inflammation or tracking the fate of transplanted stem cells are some of the current applications of MNP-based MRI nanoprobes under research.[1,8]

Natural and synthetic polymers are popular classes of materials used as the basis for MNP coating and engineering, with polysaccharides (e.g. dextran) and poly(ethyleneglycol) (PEG) among the most employed materials. While polymeric coatings aim primarily at stabilizing the MNP in biological fluids, they can also modulate the particles magnetic properties and be modified with biologically active molecules or responsive chemical groups towards the design of multifunctional nanoprobes, namely tissue or cell-targeted and stimuli-responsive nanoprobes.[9]

Continuous advances in polysaccharide production by biotechnological means are leading to greener and more sustainable processes which isolate new biocompatible and biodegradable materials. However, the exploitation of new polysaccharides for the design of MNP-based MRI nanoprobes is limited and the commercially available polymers are still preferred.[10–12] On the other hand, a number of polymer-coated nanoprobes have been developed based on engineered synthetic polymers bearing environment-sensitive bonds or chemical groups that make them change properties as a response to changes in environmental characteristics.[13] Yet, some biological interactions found in Nature could be used instead to provide the same type of responsiveness.

The project presented in this thesis aimed to engineer new T_2 MRI contrast agents based on formulations containing monodisperse iron oxide MNP coated with natural and synthetic polymers. The novelty of the work relies on:

- **The development of a new strategy to couple natural polymers onto monodisperse superparamagnetic iron oxide nanoparticles;**
- **The demonstration of the feasibility of a new exopolysaccharide, produced through a biotechnological process, as a coating material in a MNP-based MRI nanoprobe;**
- **The development of an affinity triggered magnetic nanoprobe for selective targeting of acidic tumor environments using a biologically-derived affinity pair.**

References

(1) Sharifi, S.; Seyednejad, H.; Laurent, S.; Atyabi, F.; Saei, A. A.; Mahmoudi, M. Superparamagnetic Iron Oxide Nanoparticles for *in Vivo* Molecular and Cellular Imaging. *Contrast Media Mol. Imaging* **2015**, DOI:10.1002/cmmi.1638.

(2) Sim, N.; Parker, D. Critical Design Issues in the Targeted Molecular Imaging of Cell Surface Receptors. *Chem. Soc. Rev.* **2015**, *44*, 2122–2134, DOI:10.1039/c4cs00364k.

(3) Srivastava, A. K.; Kadayakkara, D. K.; Bar-Shir, A.; Gilad, A. A.; McMahon, M. T.; Bulte, J. W. M. Advances in Using MRI Probes and Sensors for *in Vivo* Cell Tracking as Applied to Regenerative Medicine. *Dis. Model. Mech.* **2015**, *8*, 323–336, DOI:10.1242/dmm.018499.

(4) Wang, Y.-X. J. Superparamagnetic Iron Oxide Based MRI Contrast Agents: Current Status of Clinical Application. *Quant. Imaging Med. Surg.* **2011**, *1*, 35–40, DOI:10.3978/j.issn.2223-4292.2011.08.03.

(5) Weissleder, R.; Stark, D. D.; Engelstad, B. L.; Bacon, B. R.; Compton, C. C.; White, D. L.; Jacobs, P.; Lewis, J. Superparamagnetic Iron Oxide: Pharmacokinetics and Toxicity. *AJR. Am. J. Roentgenol.* **1989**, *152*, 167–173, DOI:10.2214/ajr.152.1.167.

(6) Corot, C.; Warlin, D. Superparamagnetic Iron Oxide Nanoparticles for MRI: Contrast Media Pharmaceutical Company R&D Perspective. *Wiley Interdiscip. Rev. Nanomed. Nanobiotechnol.* **2013**, DOI:10.1002/wnan.1225.

(7) Modo, M.; Kolosnjaj-Tabi, J.; Nicholls, F.; Ling, W.; Wilhelm, C.; Debarge, O.; Gazeau, F.; Clement, O. Considerations for the Clinical Use of Contrast Agents for Cellular MRI in Regenerative Medicine. *Contrast Media Mol. Imaging* **2013**, *8*, 439–455, DOI:10.1002/cmmi.1547.

(8) Rosen, J. E.; Chan, L.; Shieh, D.-B.; Gu, F. X. Iron Oxide Nanoparticles for Targeted Cancer Imaging and Diagnostics. *Nanomedicine* **2012**, *8*, 275–290, DOI:10.1016/j.nano.2011.08.017.

(9) Boyer, C.; Whittaker, M. R.; Bulmus, V.; Liu, J.; Davis, T. P. The Design and Utility of Polymer-Stabilized Iron-Oxide Nanoparticles for Nanomedicine Applications. *NPG Asia Mater.* **2010**, *2*, 23–30, DOI:10.1038/asiamat.2010.6.

(10) Chang, P. R.; Yu, J.; Ma, X.; Anderson, D. P. Polysaccharides as Stabilizers for the Synthesis of Magnetic Nanoparticles. *Carbohydr. Polym.* **2011**, *83*, 640–644, DOI:10.1016/j.carbpol.2010.08.027.

(11) Sivakumar, B.; Aswathy, R. G.; Sreejith, R.; Nagaoka, Y.; Iwai, S.; Suzuki, M.; Fukuda, T.; Hasumura, T.; Yoshida, Y.; Maekawa, T.; *et al.* Bacterial Exopolysaccharide Based Magnetic Nanoparticles: A Versatile Nanotool for Cancer Cell Imaging, Targeted Drug Delivery and Synergistic Effect of Drug and Hyperthermia Mediated Cancer Therapy. *J. Biomed. Nanotechnol.* **2014**, *10*, 885–899.

(12) Uthaman, S.; Lee, S. J.; Cherukula, K.; Cho, C.-S.; Park, I.-K. Polysaccharide-Coated Magnetic Nanoparticles for Imaging and Gene Therapy. *Biomed Res. Int.* **2014**, Article ID 959175.

(13) Medeiros, S. F.; Santos, A. M.; Fessi, H.; Elaissari, A. Stimuli-Responsive Magnetic Particles for Biomedical Applications. *Int. J. Pharm.* **2011**, *403*, 139–161, DOI:10.1016/j.ijpharm.2010.10.011.

Chapter 1

Hybrid magnetic-polymeric iron oxide nanoprobes for MRI: from preparation to application

In the last decades, the advent of nanotechnology has driven the study and application of nanoscale (~ 1 - 200 nm) versions of magnetic materials. The enormous interest in nanomaterials is understood as on the nanoscale magnetic materials display properties different from the respective bulk materials. Among the various nanoparticles under research, iron oxide magnetic nanoparticles (MNP), mostly the iron oxides magnetite (Fe_3O_4) and maghemite (γ-Fe_2O_3), have attracted particular interest due to their superparamagnetism, biocompatibility and biodegradability. MNP are thus ideal platforms to work on a cellular and molecular level in several biomedical applications. Favored by their unique magnetic properties, iron oxide nanoparticles have been widely used in the development of engineered nanoplatforms for imaging through magnetic resonance imaging (MRI). Polymers are among the most explored materials to coat MNPs towards versatile MRI nanoprobes This chapter introduces the properties and applications of MNP and reviews the recent applications of MRI nanoprobes with polymeric coatings.

1.1. Physical properties of MNP

At the macroscale, bulk magnetite (Fe_3O_4) and maghemite (γ-Fe_2O_3) are ferrimagnetic, meaning that they exhibit permanent magnetic moment at room temperature even in the absence of an external magnetic field. Ferrimagnetic behavior arises from the combination of atomic composition and crystal structure of these materials. Bulk iron oxides consist of Fe^{2+} and Fe^{3+}, which possess unpaired electrons. As a consequence, the sum of the magnetic moments generated by the unpaired electrons creates a net magnetic moment for each atom. Due to strong magnetic coupling interactions and to the organization of the atoms in the metal crystalline structure, net magnetic moments of adjacent atoms align with each other (either in parallel or antiparallel direction), thus creating a permanent magnetization within the solid, even in the absence of an external magnetic field. Due to energetic requirements, a ferrimagnetic solid is organized in regions called magnetic domains, where there is a mutual alignment of all atomic magnetic moments in the same direction. Between domains, magnetic moments are oriented in random directions. In a macroscopic piece of iron oxide there are a large number of domains, and all may have different magnetization orientations (Figure 1.1 A).

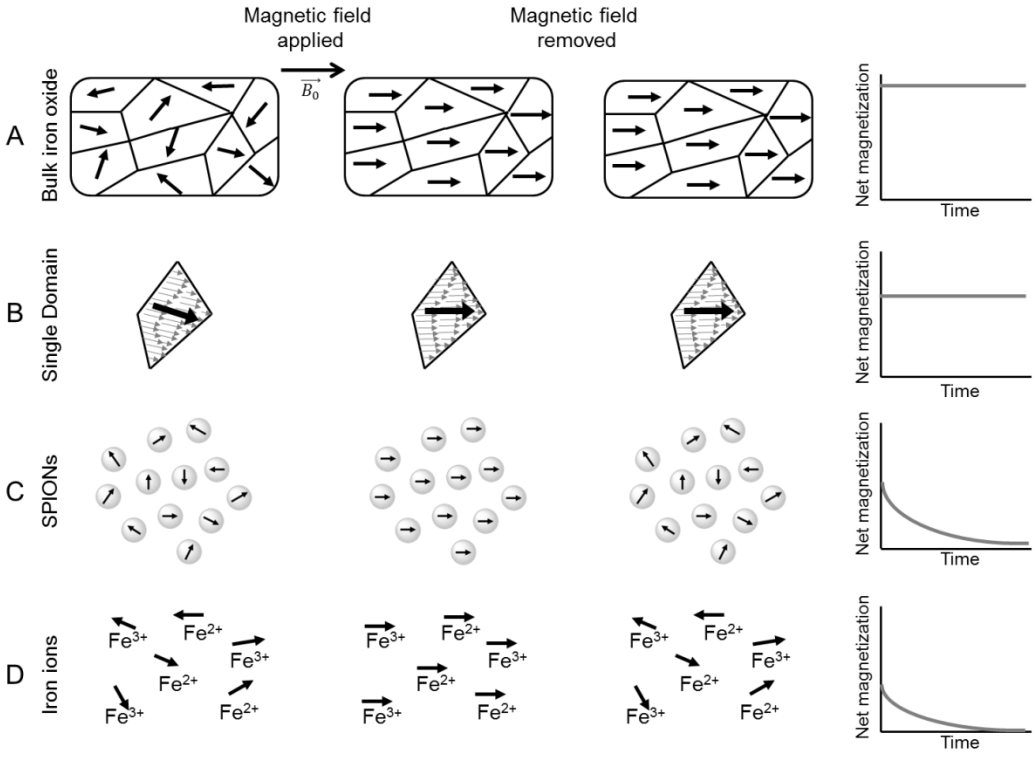

Figure 1.1. Schematic representation of the effect of applying an external magnetic field on magnetite at different size scales. (A) bulk magnetite; (B) single domain magnetite nanoparticles; (C) superparamagnetic iron oxide nanoparticles (SPIONs); (D) iron ions. Adapted from Stephen *et al.*[1]

When the volume of the solid iron oxides is reduced until a critical diameter, as in the case of MNP, each particle will consist of a single magnetic domain with ferromagnetic behavior (Figure 1.1 B). The critical diameter corresponds to the size at which domain boundaries are no longer energetically favorable and varies for differing materials.[2] In the case of spherical magnetite (Fe_3O_4) the critical diameter is between 70 – 100 nm.[2,3] If the size of spherical magnetite nanoparticles is further reduced to below approximately 20 nm,[2] the nanoparticles become superparamagnetic (Figure 1.1 C): in the absence of an external magnetic field, the thermal energy available at room temperature is sufficient to make the magnetization of the particle as a whole to change, despite the individual atomic moments maintaining their ordered state relative to each other (Figure 1.2 A). Therefore, in a system containing superparamagnetic nanoparticles, due to the random fluctuations of the magnetic moment of each particle, the net magnetization of the system will be zero. However, when a magnetic field is applied, there will be a net statistical alignment of particles' magnetic moments. This behavior is similar to what happens with paramagnetic materials except that the magnetic moment is not that of a single atom but of the MNP containing various atoms (can be up to 10^4 times larger than for a paramagnetic material);[1,3] this being the reason for the designation of superparamagnetism. (Figure 1.1)

At a high enough magnetic field all the MNP magnetic moments in the system will be aligned and a maximum magnetization will be reached (the saturation magnetization), which can be very close to the bulk M_s. The evolution of the magnetization with the intensity of the externally applied magnetic field in superparamagnetic nanoparticles is described by a non-hysteretic sigmoidal M-H curve (Figure 1.2 B) proportional to the Langevin function, which takes into account a Boltzman distribution of the energy levels corresponding to all of the possible orientations of the particle magnetization moment:[4]

$$m(B_0) = m(\infty)L(x) \tag{1.1}$$

where $m(B_0)$ is the magnetization of the suspension at a field B_0, $m(\infty)$ is the magnetization at saturation and L(x) is the Langevin function:

$$L(\mathrm{x}) = \coth(x) - 1/x \tag{1.2}$$

with

$$x = \frac{M_S(T)VB_0}{k_BT} \tag{1.3}$$

where $M_S(T)$ is the saturation magnetization of the bulk at temperature T, V is the volume of the MNP core, B_0 is the applied magnetic field and k_B is the Boltzman constant.

In order to flip the magnetic moment of a nanoparticle there is an energy barrier that needs to be overcome, the magnetic anisotropy energy (E_a). E_a is proportional to the product of the magnetic anisotropy constant (K) and the volume of the magnet (V). When the nanoparticle

volume is small enough at a given temperature, E_a is equal or inferior to the thermal energy available (k_BT, where k_B is the Boltzman constant and T is the temperature) and therefore, the magnetic moment is able to fluctuate just by thermal effect. This relation shows that superparamagnetism itself depends on the size of the MNP. In general, the smaller the MNP, the lower the transition temperature from ferrimagnetic to superparamagnetic behavior.[2,3] Another effect of size reduction is the enhancement of the relative contribution of surface effects to the saturation magnetization of the particles, due to surface disorder.[3] Besides size, shape also affects the magnetic properties of superparamagnetic MNP since it is known to strongly affect the magnetic anisotropy constant K and consequently the anisotropy energy barrier.

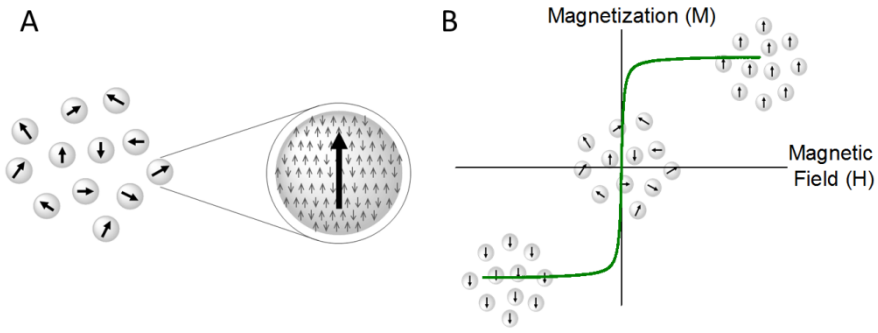

Figure 1.2. Superparamagnetism features. (A) Schematic representation of a superparamagnetic nanoparticle in the absence of an external magnetic field. (B) Magnetization curve of a superparamagnetic fluid.

1.2. MNP synthesis methods

In general, biological applications require magnetic particle cores with a number of well-defined and reproducible structural, physio-chemical and toxicity properties. While some intrinsic properties, such as MNP core size, shape, surface chemistry and core magnetic properties can be tuned through the choice of appropriate synthesis procedures, the application of appropriate surface coatings tailors other features like colloidal stability, functionality and biocompatibility.

There are several methods available to synthesize iron oxide magnetic nanoparticles, ranging between physical, chemical and biological procedures.[2,4] Chemical synthesis methods are the most popular and can be divided in hydrolytic and non-hydrolytic methods. While hydrolytic methods produce MNP with surface chemistries that make them dispersible in aqueous media, non-hydrolytic methods involve the use of organic solvents and the resultant MNP are hydrophobic. Both categories of syntheses have advantages and drawbacks depending on the intended application of the resultant nanoparticles. The most commonly employed hydrolytic method is the co-precipitation method, also known as Massart method,

firstly described in 1981.[5] It consists in the co-precipitation of a stoichiometric mixture (2:1) of ferrous (Fe^{2+}) and ferric ions (Fe^{3+}) salts (usually chlorides) in alkaline conditions. Although the co-precipitation method produces large amounts of MNP and permits *in situ* functionalization of the particles using additives (e.g. polymers), it usually yields a mixture of magnetite and maghemite, due to uncontrolled oxidation, which minimizes the magnetic properties of the ferrofluid. Tight control over synthesis parameters such as pH, ionic strength, concentration of the growth solution and nature of the base is needed in order to control MNP core size and shape, ensure the formation of mostly magnetite, and make the method reproducible.[3,6] Other hydrolytic methods include hydrothermal routes,[7] developed in order to improve the magnetic properties of co-precipitation MNP, or microemulsion techniques, which intend to overcome the drawback of limited control over MNP size distribution in co-precipitation by confining the space for MNP growth inside emulsions or reverse micelles.[8]

However, none of these methods offers such control over crystallinity, core size and monodispersity as the thermal decomposition method, which is the most popular non-hydrolytic MNP synthesis method. Organic precursors of iron like $Fe(Cup)_3$, $Fe(CO)_5$ and $Fe(acac)_3$ or iron oleate complexes decomposed at elevated temperatures using organic solvents (including polyols) and surfactants result in highly monodisperse and crystalline nanoparticles of magnetite coated with hydrophobic ligands.[9–13] Therefore a phase transfer step is needed in order to solubilize the MNP for biological applications. The success of this synthetic strategy relies in the separate occurrence of crystal nucleation and crystal growth. Control over particle size and shape is provided by adjusting the reaction times and the temperature but also the concentration and ratios of the reactants, nature of the solvent, precursors or addition of seeds.[3,4]

Details about these and other synthesis methods are addressed extensively in the literature[2,4] and reveal the efforts made in the last years towards the development of methods to produce biocompatible MNP with controllable physiochemical characteristics.

1.3. Biomedical applications of MNP

Iron oxide MNP are appealing platforms for biological applications as they are biocompatible and biodegradable and possess sizes in the range of macromolecules. Their superparamagnetic character is advantageous since, after introduction of MNP in living systems, it enables MNP magnetization to be activated only in the presence of an external magnetic field while at zero field the dispersions of MNP behave like colloids (ferrofluids), avoiding magnetic aggregation. Superparamagnetism can be exploited in a range of biomedical applications, summarized in Table 1.1.

Through the application of a magnetic field gradient in the proximity of the ferrofluid, a magnetic force is generated and MNP can be manipulated to exert control over their biodistribution in order to deliver therapeutic agents to specific organs or tissues;[14–16] to transfect cells with genes; or to induce mechanical actuation towards tissue engineering scaffolds.[17–19]

Another interesting property is the capability of MNP to generate heat when subjected to an alternating magnetic field (AMF). Under an appropriate AMF, the magnetic moments of the MNP reorient themselves and then release energy in the form of heat during the demagnetization process. This effect is explored as a therapeutic approach for cancer cells through hyperthermia. [20,21]

Table 1.1. Applications of superparamagnetic iron oxide nanoparticles in the biomedical field.

Application	***Function***	***Ref.***
Magnetic focusing	Cell/Drug delivery	14–16
Contrast Agents for MRI	Disease diagnosis / treatment monitoring	22–29
	In vivo cell tracking	30–32
	Gene/drug delivery	29,33–35
	Multimodal imaging/multifunctional	32,36–38
Contrast agents for MPI	Disease diagnosis/treatment monitoring	39–41
Hyperthermia	Treatment	20,21
Magnetic-Mechano actuation	Stem cell differentiation; tissue engineering	17–19
Magnetofection	Transfection of DNA associated with MNP into cells	42,43

The most remarkable and explored property of MNP ferrofluids is, however, their ability to generate small local magnetic fields that shorten the relaxation times T_1 and T_2 of the surrounding water protons. The shorter relaxation times lead to a change in the nuclear magnetic resonance signal intensity in that region and MRI contrast is improved due to the presence of MNP acting as contrast agents.[22–29] The local magnetic field generated by MNP can be a source for imaging itself if it can to be detected by external devices. This is the concept of using MNP as agents for magnetic particle imaging (MPI), a new medical imaging technique under research.[39–41]

1.4. MNP as MRI contrast agents

Magnetic Resonance Imaging (MRI) was first reported back in 1973,[44] with the first contrast agent for *in vivo* MRI (based in manganese) being demonstrated in 1978.[45] In the same year, through nuclear magnetic resonance (NMR) studies, Ohgushi *et al.*[46] discovered the ability of iron oxide nanoparticles (crosslinked with dextran) to shorten the T_2 relaxation time of water and showed that they were more efficient (by one or more orders of magnitude) than the paramagnetic ions or free radical contrast agents in relaxing neighboring nuclei.[46] During the 1980's iron oxide MNP were then demonstrated to produce contrast in *in vivo* MRI.[47,48,49] From then on, iron oxides have been extensively used as MRI contrast agents and, in 1995, the first iron oxide MNP-based MRI contrast agent (Ferumoxides, from Guerbet, Advanced Magnetics) was approved by the American Food and Drug Administration (FDA) for human use in liver imaging.[50] While many other iron oxide MNP commercial agents have appeared in the last years, some have been withdrawn from market. By now, the only approved iron oxide MNP for pharmaceutical use is Ferumoxytol,[51] for the treatment of anemia, although this MNP also has properties as MRI contrast agent. In the meanwhile numerous research studies continue being reported in the literature seeking for improved MNP towards MRI applications.

MRI makes use of a strong permanent magnetic field, B_0, which causes the magnetic moments of water protons in a tissue to align in its direction, precessing around B_0 (at the Larmor frequency) and producing an equilibrium magnetization along the z-axis, M_z (with amplitude M_0). By applying a radiofrequency (RF) magnetic field at the same frequency of the hydrogen protons precession and perpendicular to B_0 (in the xy plane), the protons resonate (absorb energy form the RF pulse) and their magnetic moments start precessing coherently, such that the net magnetic moment is rotated to the transverse plate (M_{xy}) and precesses at the Larmor frequency. In practice, the RF transverse field is applied in a pulsed sequence. From the instant that the RF pulse is turned off, the magnetic moments of the protons relax back to equilibrium and this response is measured via induced currents in pick-up coils in the MRI scanner.[1,52,53] The time required for the magnetic moments to relax to the equilibrium state (relaxation time), and therefore, MRI contrast, is tissue dependent.

MRI contrast is due to differences in proton density, spin-lattice relaxation time (T_1, longitudinal relaxation time) and spin-spin relaxation time (T_2, transversal relaxation time) of protons.

T_1 is the time constant of the exponential recovery process of longitudinal magnetization M_0 along the z-axis after a RF pulse. T_1 reflects an exchange of energy, as heat, from the system to its surrounding, which is related to the dipolar coupling of the proton moments to their surrounding; therefore isolated protons show negligible rates of T_1 relaxation.[1,3]

T_2 is time constant of the exponential decay of transverse magnetization M_{xy} after a RF pulse, which corresponds to the amount of time for precessing magnetic moments to become randomly aligned (dephased) in the xy-plane after a RF pulse, eventually resulting in a net magnetic moment of zero in the xy plane. Dephasing of the magnetization of the precessing protons is due to magnetic interactions with each other and with other fluctuating moments in their surroundings.[1,3]

Since the natural variations of T_1 and T_2 in tissues are small, sometimes exogenous materials are used to enhance the contrast between tissues – contrast agents. Most contrast agents influence both T_1 and T_2 but usually their effect is more pronounced in either T_1 or T_2.

T_1 contrast agents increase the MRI signal intensity, providing positive contrast enhancement in T_1-weighted MR images (lighter image regions), while T_2 contrast agents decrease signal intensity resulting in negative contrast in T_2-weighted images (darker image regions). The current clinical contrast agents are based on paramagnetic chelates of lanthanide metals such as gadolinium, which is a T_1 agent.[51] The presence of paramagnetic ions near water protons shortens their T_1 relaxation time through coordination with water molecules providing increased contrast. The short blood circulation times, poor detection sensitivity and toxicity concerns of gadolinium chelates had led to the continued development of superparamagnetic iron oxide-based T_2 MRI contrast agents.[54] Due to their larger magnetic moments, MNP-based MRI contrast agents produce higher relaxation rates at lower doses than paramagnetic ions like Gd^{3+}.[1] The low toxicity of iron, which is normally processed through various metabolic pathways, makes these agents very attractive.[55]

Iron oxide MNP are mainly T_2 contrast agents, enhancing contrast by inducing a pronounced decrease in T_2 along with a less pronounced decrease in T_1. When MNP are present in the tissues and are subjected to an external magnetic field, their large magnetic moments align with it, consequently creating gradients of magnetic fields in the tissues, i.e., local inhomogeneities in the net magnetic field, through which the water protons diffuse. The dipolar coupling between magnetic moments of water protons and the magnetic moments of MNP causes dephasing of the protons magnetic moments, thereby shortening their T_2 relaxation time. Due to localized differences in the uptake of the MNP by tissues, there will be regions of different MRI signal intensity, with less intensity (darkening) in the vicinity of MNP.

The addition of a MNP contrast agent causes an increase in the longitudinal ($1/T_1$) and transversal ($1/T_2$) relaxation rates of the water protons. The relaxation rate in the presence of MNP depends linearly on the concentration of the MNP and is given by

$$(1/T_i)_{obs} = (1/T_i)_{dia} + r_i[\mathrm{MNP}] \qquad i = 1,2 \tag{1.4}$$

where $(1/T_i)_{obs}$ is the observed relaxation rate in the presence of the MNP contrast agent, $(1/T_i)_{dia}$ is the diamagnetic of the solvent (water) alone and r_i (in $Mol^{-1}s^{-1}$) is the relaxivity.

Relaxivity is defined as the slope of the above linear relation and is a measure of the efficacy of the MNP as MRI contrast agent since it defines the ability of a fixed concentration of MNP to increase the relaxation rate of the protons.

Although MNP have been used mainly as T_2 contrast agents, it is possible to model their characteristics so that they have an effect on T_1. For example, reduction of MNP core size to diameters of less than 10 nm, are capable of producing positive contrast in T_1-weighted images. However, under these conditions their T_2 effects are reduced.[56,57] Nonetheless, MNP-based T_1-contrast agents could be an alternative to gadolinium chelates to produce contrast enhancement in tissue regions where MR signal is naturally low.

1.4.1. Structure of MNP-based nanoprobes for MRI

The quality of a MNP MRI contrast agent *in vivo* depends on the physiochemical properties of magnetic core but also on the MNP ability to be stealth and escape from the reticuloendothelial system so that they can circulate in blood for sufficient time to reach the target tissues and be taken up by target cells. The stability of the MNP in biological fluids (like blood) is therefore of uttermost importance.

Bare iron oxide nanoparticles do not present colloidal stability at physiological pH due to the proximity of their isoelectric point (pH 6.8),[58] tending to agglomerate and flocculate rapidly. Besides having neutral pH, biological fluids are complex and contain various macromolecules that readily interact with iron oxide surface and can cause colloidal instability of the nanoparticles. Also, the high surface–to-volume ratio of nanoparticles yields high surface energies which make the surface prone to oxidation, with consequences on the magnetic and relaxometric properties.[1] To overcome these limitations, MNP-based MRI contrast agents are usually composed of magnetic core(s) involved in biocompatible and hydrophilic coating materials (Figure 1.3) that prevent MNP agglomeration through electrostatic and/or steric interparticle repulsions and enhance biocompatibility of the system in biological media.

MNP coatings also play significant roles in tuning MNP physiochemical properties like hydrodynamic size, magnetic core aggregation, surface charge and surface chemistry and, in particular, the magnetic[59,60] and relaxometric properties[61–65] of the nanoprobes. Importantly, free functional groups on the MNP wrapping molecules can be used to bind other compounds to the MNPs, such as reporter molecules for different imaging modalities,[32] therapeutic agents (such as drugs, peptides, proteins, DNA/RNA),[34] photoactive moieties[37,66,67] and targeting moieties specific for certain cell types[23] (Figure 1.3 and Table 1.1).

Taking advantage of the myriad of available biocompatible hydrophilic materials, nanoparticle coatings can be manipulated to engineer improved MRI contrast agents.[68,69]

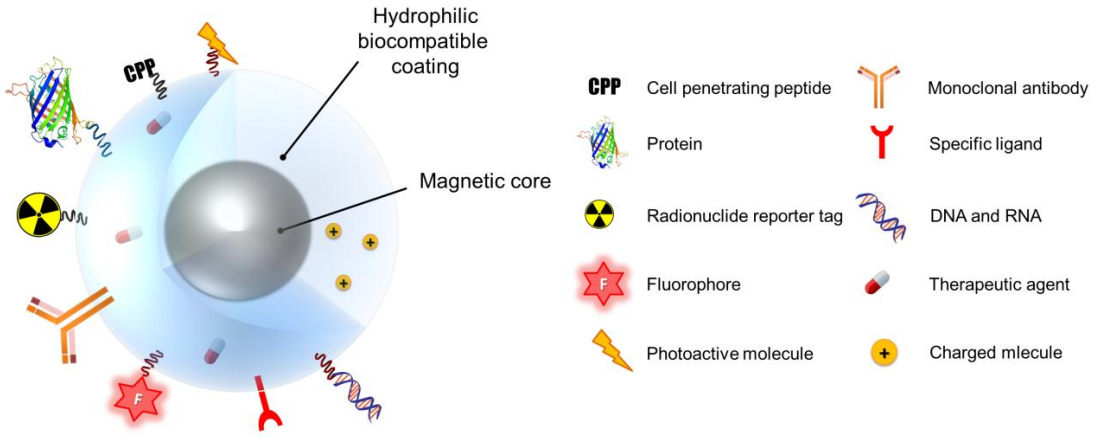

Figure 1.3. Schematic representation of MNP surface modification with biocompatible coating and functional moieties.

1.4.2. MNP coating materials towards stabilization and functionalization of MRI nanoprobes

Depending on the chemistry of the ligand molecules present at the surface of particles after synthesis and on the purpose intended for the final particles, different coating materials and methods can be chosen. For example, it may be necessary to add new coating layers, to exchange the ligand, crosslink it or modify it with functional groups to provide particles' stabilization and/or functionality. The most common for MNP include small organic molecules (e.g. citric acid, phosphonic acid), inorganic materials (e.g. silica) and natural/synthetic polymers natural and synthetic (e.g. dextran, poly(ethylene glycol)).

1.4.2.1. Small organic molecules

Small organic molecules bearing functionalities with affinity for iron oxide Fe-OH surface groups adsorb onto the MNPs by coordination processes, similar to covalent bonds with the Fe ions at the surface of the iron oxide crystals.[70] These functionalities can be carboxylic acid, phosphonic acid, amines or cathecol groups.[3,4,6] The chemical structure of the coating molecules usually contains multiple functional groups (of the same type or not), so that (at least) one of them coordinates with the nanoparticles surface while the other(s) are left exposed to the solvent, being responsible by stabilizing the particles at physiological pH, for example by electrostatic interactions. This coating method was employed to stabilize MNPs with citric acid, either *in situ* (during the synthesis), such as the case of the commercial VSOP C148 iron oxide MRI contrast agent,[71–73] or post-synthesis, as it was employed recently to produce MNPs for stem cell labeling and tracking by MRI.[74] Other coating molecules such as 2,3-

dimercaptosuccinic acid (DMSA),[75] or methylene diphosphonic acid,[76] were also used to provide increased stability to MNP synthesized in aqueous medium. Another example of the utilization of organic small molecules is the phase transfer of MNP synthesized in organic solvents. The carboxylic acid group functionality (in oleic acid) is first employed for MNP synthesis and stabilization in hydrophobic medium. Then, to render the resulting particles hydrophilic, the oleic moieties are replaced by hydrophilic small molecules with higher affinity towards iron oxide due to the presence of a larger number of iron oxide reactive groups or of groups with higher reactivity. Citric acid[10,77] and DMSA[78–80] are commonly employed for this purpose, leaving free carboxylic acid (and thiol groups, in the case of DMSA) at the surface of the particles to provide stability in aqueous media. The free functional groups are also useful as reactive groups for conjugation with other molecules such as targeting ligands,[78] fluorophores[81] or more complex polymeric constructs to engineer hybrid efficient MRI nanoprobes.[82] Finally, these small organic molecules with affinity for iron oxide surfaces can be conjugated first with other molecules (e.g. PEG) to serve as anchoring moieties onto MNP. This strategy was employed to PEGylate initially hydrophobic MNPs using catechol (dopamine), dihydroxybenzamide, phosphonic or carboxylic acid moieties.[61,83]

1.4.2.2. Silica

One of the most commonly used inorganic coating materials is silica. Organosilane compounds attach onto MNP surfaces through stable covalent Fe-O-Si bonds between the surface Fe-OH and the $Si\text{-}OCH_3$ moieties, similar to the coordination mechanism of carboxylates or phosphates.[6] The silica shell introduces negative charges on the particles surface, thereby stabilizing them through electrostatic interactions. MNP coating with organofunctional silane shells is interesting because of these properties, but also because silica-based coatings improve particles biocompatibility,[84] protect the iron oxide cores from chemical degradation,[84–86] and are optically transparent, which allows to conjugate molecules with optical properties in the silica matrix and build multimodal nanoprobes.[87,88] Different routes can be followed to obtain MNPs with silica shells. Among them are the *in situ* formation of silica around iron oxide seeds through hydrolysis and condensation of a sol-gel precursor such as tetraethyl orthosilicate (TEOS)[89,90] (known as Stöber process), the microemulsion method,[84] the water-in-oil microemulsion (or inverse microemulsion),[85,91] the post-synthesis deposition[88,92] and aerosol pyrolysis.[93] The functionalization of MNP using silane chemistry is versatile, as functional chemical groups can be introduced in the structure or organosilanes (e.g. amine,[86,92] carboxylic acid,[88,94] thiol[95]) and pre-functionalized organosilanes are also available commercially, ready to couple with biofunctional molecules. In addition, engineering of alternative synthesis and coating assembly methods allows producing alternative

nanoparticulate structures, such as mesopourous silica-coated MNP[96,97] useful to combine imaging and drug delivery; and ultrasmall core-shell MNP with T_1-weighted MRI contrast agent properties.[56] Also, exploitation of the photoacoustic properties of core-shell silica-coated MNP demonstrated their potential for imaging through photoacoustic Radar imaging.[98]

1.4.2.3. Polymers

Along with silica-based coatings, hydrophilic polymeric coatings are preferred over small organic molecules for MNP functionalization. The main reasons for this preference are their colloidal and chemical stabilization properties and higher versatility for chemical modifications. Polymers provide colloidal stability through steric interactions established between the polymeric chains or through a combination of steric and electrostatic interactions, when charged moieties are present in the polymer. Importantly, polymeric shells also offer protection to iron oxide magnetic cores at physiological pH, which contributes for the chemical stability of the constructs. In biological terms, the polymer coating mediates the interface between the iron oxide surface and the biological medium. Therefore it dictates the way the cells "see" the nanoprobes (overall size, surface chemistry) and contributes to biodistribution and pharmacokinetics of MNP upon administration. Polymers provide MNPs with surface functionality, making possible to tailor their biological and physio-chemical properties, namely to design hybrid nanoprobes with ability to provide multimodal imaging, specific targeting, delivery and stimulated release of therapeutic agents. The MRI properties of the hybrid nanoparticles are intrinsically dependent on the interactions between the magnetic dipole created by the iron oxide core and the water protons in the vicinity. In particular, the magnitude of MRI relaxivity depends on the number of water molecules disturbed by the magnetic field generated by the MNPs. The presence of a hydrophilic polymer is of uttermost importance as it mediates the access of water molecules to the magnetic core. Manipulation of parameters such as the hydrophilicity[65] and the thickness[99] of the coating and the aggregation degree of magnetic cores surrounded by the polymer[100] can affect the MRI properties of a hybrid MNP.

Due to the high reactivity of MNP surface, there is a range of strategies for the coating of MNP with polymers, which can be carried out either *in situ* during the MNP synthesis, or post-synthesis. Basically, polymers can be directly conjugated to the "naked" MNP through chemical groups in their native structure which are able to coordinate with iron oxide surface or indirectly, through interaction with small ligands previously coupled onto the MNP. Electrostatic interactions, hydrophobic interactions and hydrogen bonding are involved in the adsorption mechanism of polymers onto MNP but the establishment of covalent bonds is also an important alternative because it is more permanent. Most *in situ* coating strategies rely on coordination of the polymer onto iron oxide surface while post-synthesis coating strategies generally involve (a)

using a linker ligand between the MNP surface and the polymer or (b) replacement of the ligands initially at the MNP surface by a polymer bearing iron oxide anchoring ligands. The later strategy can be employed when the MNP as-synthesized are hydrophobic and solubilization into aqueous medium is performed by ligand-exchange reaction.[65]

1.4.3. Types of polymers used to coat MNP-based MRI nanoprobes

From the large number of polymeric materials described in the literature to produce hybrid MRI nanoprobes, two main groups can be identified: polymers with biological origin (biopolymers, in particular polysaccharides) and synthetic polymers. Table 1.2, Table 1.3 and Table 1.4 present examples of the utilization of polysaccharides and synthetic polymers to produce MNP-based MRI nanoprobes.

Polysaccharides are one of the three types of biopolymers found in Nature (polynucleotides, polypeptides and polysaccharides). The abundance of polysaccharides in Nature allied with the advances towards low cost and greener extraction/production processes have increased the interest in exploitation of polysaccharide materials for a range of applications, including nanotechnology. These biopolymers present favorable characteristics and biological properties that make them versatile materials to employ as coating materials for MNP to be used in biomedical applications. Polysaccharides are water soluble, biocompatible and biodegradable, which is crucial for clinical application in humans because health regulatory agencies demand that, besides being biocompatible, materials shall be biodegradable upon administration.[50] In addition to these advantages, polysaccharides generally have biological activity, as most of them are present in structural tissues of living organisms, and can be involved in molecular recognition mechanisms.[101–104] Also, they naturally present a large number of functional groups in their chains, which can serve as anchoring points onto MNP and as reactive groups for modification.

However, polysaccharides can have high degradation rates and sometimes need to be combined with other polymers or crosslinked to reduce degradation rates and enhance stability in biological environment.[105] That is the case of CLIOs (cross-linked iron oxide particles), for which carboxymethyl groups were added to the dextran coating and cross-linked to epichlorohydrin to increase stability of the MNP.[106] Optimal performance of polysaccharides is a challenge because synthesis of natural polymers is carried out in living organisms and thus is not strictly controlled. The alteration in structural properties of the polymers during production is difficult as well as the strict reproducibility of the polymer structure from batch to batch.

Synthetic polymers, on the other hand, can be tailored to meet specific properties (e.g. degradation rates, responsiveness to certain stimuli[67,107]). This class of materials is attractive to engineer biocompatible materials to stabilize and functionalize MNP because of its controllable

synthesis and modifiable properties, which potentially facilitates reproducibility and production scale-up. Indeed, polymer synthesis methodologies are well studied and are controllable, making possible to systematically add chemical modifications and functionalities on the polymer during its synthesis or to combine different polymers to obtain new materials (e.g. block copolymers) with tailor-made properties.[108–113] Synthetic methods such as living radical polymerization (atom-transfer radical-polymerization (ATRP) and reversible addition–fragmentation chain-transfer polymerization (RAFT)),[110] ring opening polymerization (ROP)[111] and polymerization induced self-assembled approach (PISA)[114] can be used to produce a virtually infinite number of tailor-made polymers with specific properties, including well defined molecular weights, polydispersity, and engineered modes of attachment to the MNPs[115] that may facilitate the control of iron oxide cores aggregation to form single or multi-core MNPs. With these strategies, innovative hybrid multifunctional nanoprobes are emerging but there is still lack of *in vitro* and *in vivo* studies compared to polysaccharide-coated MNPs.

To get the best of both worlds, there is also the possibility to employ mixed coatings that combine natural and synthetic polymers, for example by covalent coupling[116] or by formation of copolymers.[35]

1.4.3.1. MNP-polysaccharide hybrid MRI nanoprobes

Polysaccharides consist of repeating units of mono or disaccharides linked by glycosidic bonds to form linear or branched chain structures. Due to the high variability of building block composition, type of branching, molecular weight of the polymer and eventual combination with proteins (peptidoglycans) or lipids (glycolypids), polysaccharides have diverse biological and physico-chemical properties that are interesting from a biomedical perspective.

The polysaccharides most commonly used to coat MNP for use as MRI contrast agents include dextran and modified versions of dextran (e.g. carboxymethyl dextran, diethylamino ethyl dextran), hyaluronan, chitosan, pullulan, heparin, gum arabic, starch, fucoidan, cellulose, alginate and mannan. They can be obtained either by extraction from natural sources (e.g., plants, algae, animal tissues, shells) or by microbial production via biotechnological processes (e.g., bacterial exopolysaccharydes), as summarized in Table 1.2 and Table 1.3, where some examples of polysaccharide-coated MNP for MRI are presented. Polysaccharides usually contain multiple hydroxyl groups and part of them are neutral (dextran, pullulan, starch, cellulose and mannan), but in in some cases, also contain charged groups such as amine (in chitosan), carboxylate (in alginate, hyaluronan and gum arabic) and sulfate (in heparin and fucoidan).[117] Therefore they can establish strong bonding interactions with the surface of iron oxide MNP. Co-precipitation method is the most commonly used for preparation of polysaccharide-coated MNP. The coating may be performed *in situ*, during the synthesis of the

magnetic iron oxide nanoparticles, or after the particles are synthesized, through addition of the polymer and conjugation to the MNP by adsorption or chemical bonding.

Dextran is undoubtedly the most popular natural polymer used as MNP coating for MRI application. It is synthesized from sucrose by several lactic acid bacteria and is a branched polysaccharide that can be found with varying molecular weights and branching degrees. It is composed of glucose molecules with a linear backbone of repeating units of an α-linked D-glucopyranosyl.[117,118] Dextran has anti-coagulant properties and is FDA-approved for clinical application as blood-thinning agent.[115] The iron oxide MNP-based MRI T_2 contrast agent Ferumoxides (Endorem/Feridex), with a hydrodynamic diameter of 50 – 150 nm, possesses a dextran coating. In addition, charged versions of dextran were employed to produce other commercial iron oxide MNP based MRI T_2 contrast agents with smaller hydrodynamic diameters. Carboxydextran was used to produce Resovist (20 nm, blood pool agent) and Ferocarbotran (60 nm, liver imaging) while Ferumoxytol (30 nm, blood pool agent and macrophage imaging) has a carboxylmethyl-dextran coating.[4] Transfection agents can be administered in combination with the MNP to increase cellular uptake. For example, a nanomaterial consisting of a mixture of ferumoxytol, heparin sulfate and protamine sulfate is presently undergoing a clinical trial for neural stem cell-mediated enzyme/prodrug therapy for glioma.[119,120] The literature reports other approaches for cell-targeted MRI labeling using dextran-coated MNPs where targeting moieties are bond to the dextran coating to enhance specific cellular MNP uptake. In the recent work of Jafari *et al.*[121], SPIONs coated with dextran (DSPIONs) were conjugated with bombesin (BBN) to produce a targeted contrast agent for detection of breast cancer using MRI. Through binding studies, DSPIONs-BBN were shown to bind to T47D breast cancer cells overexpressing gastrin-releasing peptide (GRP) receptors. *In vivo* MRI T_2^*-weighted of mice bearing breast tumors after administration of the particles showed increased contrast. Dai *et al.*[28] functionalized glucose-dextran-MNP with folic acid by covalent conjugation onto the polysaccharide coating to produce a MRI nanoprobe to detect inflammation sites of arthritis. In addition to specific detection of inflammation in mice, treatment efficacy was able to be monitored because there was a lack of contrast enhancement in the injured site after treatment compared to the images of non-treated mice. Optimization of core and particle size and magnetic properties of these MNPs was carried out by adding glucose to the synthesis reactor besides dextran. Glucose served as a chelating agent that controlled the iron oxide core size and could reduce the thickness of dextran coating. A different study [122] focused on the utilization of dextran-coated MNP for mesenchymal stem cell labeling and tracking by tailoring the surface charge of the particles to promote cellular uptake. *In vitro* MRI of cells labeled with the produced nanoparticles confirmed the increased cellular uptake through increased contrast for cells incubated with the more positively charged MNPs.

Table 1.2. Utilization of biopolymers extracted from natural sources in the development of MNP-based MRI contrast agents.

Biopolymer	***Biological source***	***MNP synthesis method***	***MNP-biopolymer assembly strategy***	***Biopolymer or MNP modification / functionalization***	***Intended purpose***	***Ref.***
Gum Arabic	*Acacia senegal* and *seyal* trees	Co-precipitation	Post-synthesis adsorption	Citrate-modified cyclodextrin	Magnetic drug targeting for hydrophobic drugs	123
			Post-synthesis adsorption (ultrasounds and vortex)	Rhodamine B	Simultaneous magnetic targeting and *in vivo* imaging of brain tumor cells	124
			Post synthesis covalent conjugation	-	MNP stabilization for biomedical and biotechnological purposes	125,126
Fucoidan	Brown seaweed	Co-precipitation	Adsorption onto carboxymethyldextran-coated MNP	Fucoidan amination with diaminopropane	*In vivo* imaging of activated platelets for detection of intraluminal thrombus and aneurisms	102,127
Chitosan	Crustaceans shell	Co-precipitation	Post-synthesis adsorption (ultrasounds and vortex)	Carboxymethylation of chitosan; rhodamine isothiocyanate (RITC); folic acid	Cancer-specific targeting, detection and imaging (fluorescence and MRI)	128
		Sonochemical	Post-synthesis adsorption (ultrasounds)	MNPs mixed with Poly-L-Lysine solution prior to administration.	*In vivo* tracking of human mesenchymal stem cells	129
Heparin	Animal tissues (extracellular matrix)	Co-precipitation	Post-synthesis adsorption (stirring, ultrasounds)	Fluorescein isothiocyanate (FITC)	*In vivo* imaging of human mesenchymal stem cells	103
		Co-precipitation	Post-synthesis adsorption onto APTES-coated MNP	Photosensitizer pheophorbide-A (PheoA) covalently conjugated to heparin	Simultaneous *in vitro* photodynamic therapy and dual-mode fluorescence/MRI imaging of cancer cells	66
Starch	Green plants	Co-precipitation under high pressure homogenization conditions	Post-synthesis adsorption	Red fluorescent dye DY-555–N-hydroxysuccinimide ester covalently attached to the MNP's starch coating followed by poly-D-lysine adsorption	MRI tracking of adipose tissue-derived progenitor cells	130
		Co-precipitation	*In situ* coating	Human hepatocellular carcinoma cell line homing peptide (A54) labeled with 5-carboxyl-fluorescein	Biomolecular-targeted diagnostics and therapeutics of human tumor	131

Table 1.2. Utilization of biopolymers extracted from natural sources in the development of MNP-based MRI contrast agents. (continued)

Biopolymer	***Biological source***	***MNP synthesis method***	***MNP-biopolymer assembly strategy***	***Biopolymer or MNP modification / functionalization***	***Intended purpose***	***Ref.***
Cellulose	Green plants	Thermal decomposition of iron oleate in organic solvent	Encapsulation of several oleic acid stabilized Fe_3O_4 nanocrystals within the polymer matrix; oil-in-water single emulsion technique	-	Long-term, noninvasive cell tracking *in vivo*	107
		Co-precipitation	Post-synthesis encapsulation in folate-conjugated, drug-loaded carboxymethyl cellulose nanoparticles	Carboxymethyl cellulose (CMC); folic acid and 5-FU anticancer drug conjugated to CMC; fluorescein isothyocyanate (FITC) adsorbed onto the final CMC-MNP.	Folate receptor targeted drug delivery, cellular imaging and magnetic hyperthermia	132

Table 1.3. Utilization of biopolymers obtained by biotechnological processes in the development of MNP-based MRI contrast agents.

Biopolymer	***Biological source***	***MNP synthesis method***	***MNP-biopolymer assembly strategy***	***Biopolymer or MNP modification / functionalization***	***Intended purpose***	***Ref.***
Dextran	Lactic acid bacteria, such as *L. mesenteroides*, *L. brevis* and *S. mutants*	Co-precipitation	*In situ* coating	Carboxylmethylation of dextran on MNP; bombesin peptide covalently conjugated onto carboxymethyl dextran-coated MNP	Targeting and imaging of breast cancer cells	121
		Co-precipitation in presence of glucose		Folic acid covalently bond to glu-dex-MNP	Diagnosis and monitoring of treatment response of rheumatoid arthritis	28
		Co-precipitation		Diethylamino ethyl-modified dextran was employed to tune MNPs charge; FITC	Stem cell tracking	122
Alginate	*Pseudomonas* and *Azotobacter*[(a)]	Two step co-precipitation	Post-synthesis	-	Detection of liver cancer	133,134

Table 1.3. Utilization of biopolymers obtained by biotechnological processes in the development of MNP-based MRI contrast agents. (continued)

Biopolymer	***Biological source***	***MNP synthesis method***	***MNP-biopolymer assembly strategy***	***Biopolymer or MNP modification / functionalization***	***Intended purpose***	***Ref.***
		Co-precipitation	*In situ* coating; alginate was cross-linked with ferrous ions, precipitated with sodium hydroxide and oxidized to iron oxide	-	Tracking of implanted alginate microcapsules with encapsulated rat myoblast recombinant cells.	135
Pullulan	*Aureobasidium pullulans* (fungus)	Co-precipitation	*In situ* coating	Ethylenediamine and succinic anhydride.	*In vitro* magnetic labeling of bone marrow-derived rat mesenchymal stem cells.	136
		Co-precipitation	Post synthesis coating by adsorption	Cross-linked pullulan chains, with glutaraldehyde	*In vitro* labeling of human fibroblasts	105
Hyaluronan (or hyaluronic acid)[137]	*Streptococci* group A and C;[138] *Bacilus subtilis*	Co-precipitation in presence of dextran	Post-synthesis covalent coupling onto aminated MNP	Dextran coating was cross-linked and aminated with NH_4OH; Doxorubicin bound to hyaluronan-coated MNP through hydrazone linkage	Targeted drug delivery and bimodal imaging (MRI and fluorescence) of ovarian cancer cells expressing CD44 cell surface marker.	101
		Commercial oleic-acid stabilized hydrophobic MNP (Sigma-Aldrich)	Post-synthesis; encapsulation in hyaluronan micelles by probe-type ultrasonication method	Acylation (oleil-modification) of hyaluronan	Selective *in-vitro* cytotoxicity towards cancer cells and imaging of tumor tissues	139
		One pot hydrothermal synthesis in the presence of PEI	Post-synthesis covalent conjugation onto PEI-stabilized MNP	PEI stabilized-MNP previously labeled with FITC.	Imaging of surgically induced endometriosis model in rats	140,141
		Thermal decomposition in of iron precursor in organic solvent	Post-synthesis electrostatic interactions with the ligand a t the surface of the MNP and coordination with MNP surface	Hyaluronan conjugated with dopamine; MNP solubilized with cetyltrimethylammonium bromide (CTAB)	Imaging of CD44 overexpressing in cancer-associated angiogenesis	142

Table 1.3. Utilization of biopolymers obtained by biotechnological processes in the development of MNP-based MRI contrast agents. (continued)

Biopolymer	***Biological source***	***MNP synthesis method***	***MNP-biopolymer assembly strategy***	***Biopolymer or MNP modification / functionalization***	***Intended purpose***	***Ref.***
Mannan	*Saccharomyces cerevisae*	Co-precipitation	Post-synthesis adsorption	-	*In vitro* and *in vivo* mannose-mediated targeted imaging of macrophages	143
			Post-synthesis adsorption	Carboxylation of mannan	Imaging of lymph node through MNP targeting to immune cells.	144,145
			In situ coating	-	Imaging of rabbit atherosclerotic aortic wall	146

[(a)]can also be extracted from brown algae

1.4.3.2. MNP-based MRI nanoprobes assembled with synthetic polymers

Hydrophilic, biodegradable, nontoxic synthetic polymers have been widely explored and well developed by biomaterials and nanotechnology research fields in the last decades. Some popular synthetic polymers that have been described to produce MRI contrast agents include poly(ethylene glycol) (PEG), poly(lactic acid) (PLA) and poly(lactic-*co*-glycolic acid) (PLGA), which present the advantage of being FDA approved materials for clinical use, but polyacrylic acid (PAA), polyethyleneimine (PEI), poly-L-lysine (PLL), poly(styrene sulfonate) (PSS), polyvinyl alcohol (PVA) and polyvinylpyrrolidone (PVP) are also frequently reported as part of MNP-polymer assemblies, as summarized in Table 1.4.

Methods for iron oxide MNP assembly with synthetic polymers are generically divided in two groups: (a) coating, when the polymer chains wrap around the magnetic core(s) to form a network of MNP and polymer; and (b) encapsulation, when many magnetic cores are within a polymer matrix in a core-shell fashion. Coating MNP cores with polymeric materials is usually performed during the synthesis of hydrophilic particles, or post-synthesis by adsorption onto the naked hydrophilic MNP or in ligand-exchange process when the initial MNP are hydrophobic. Encapsulation is a popular strategy to assemble hydrophobic MNP by making use of amphiphilic tailor-made synthetic block co-polymers. Two preparation methods can be employed: single emulsion method (oil-in-water emulsion – w/o) or double emulsion method (water-in-oil-in-water emulsion - w/o/w),[50] depending on the desired particle structure and intended purpose. Polymeric micelles with encapsulated MNP have been studied widely as nanoplatforms for drug delivery and imaging applications. The micelles are intended to prolong the drug blood circulation time and prevent direct contact between the drug and healthy tissues or organs. At the same time, aggregation of MNP inside the micelle core results in high T_2 relaxivity MRI contrast agents.[50,147]

Poly(ethylene glycol) (PEG) is a synthetic polymer recognized for its biocompatibility and “stealth” properties, forming anti-fouling surfaces that prevent adsorption of proteins and recognition of the pegylated materials by the macrophage – monocytic system, thereby increasing materials blood circulation time. Several pharmaceuticals currently in the market have FDA-approved PEG coatings in order to enhance their blood circulation times.[148] Due to these properties, PEG has been also widely used as coating agent for magnetic nanoparticles. Inclusively there was a commercial MRI contrast agent (which commercialization is currently abandoned) – Clariscan – that had a pegylated starch coating to avoid recognition by the monocytic system.[4] Various strategies for coating were developed to attach PEG to MNPs, either by *in situ*[110] or post-synthesis methods.[80,109,116] They rely on the use of PEG polymers

functionalized with iron oxide grafting groups or tailor made PEG-based co-polymers where one of the blocks can have multiple grafting groups.

Other synthetic polymers are charged due to the presence of many amine or carboxylic acid groups on their structure. Positively charged polymers are widely used to deliver material into cells, namely genetic material, because they can establish electrostatic interactions with the negatively charged cell membrane that facilitate the internalization. Poly-L-lysine (PLL) and polyetileneimine (PEI) are positively charged at physiological pH and are commonly used as non-viral transfection agents for gene delivery. Some authors report the utilization of PLL as transfection agent also for MNP[129,149,150] but is common to use it as MNPs' coatings for stabilization and enhancing cellular uptake in view of MRI cell labeling.[151–154] PEI-coated MNPs are commonly employed for DNA and RNA delivery by magnetofection[42,43] but also for gene delivery and simultaneous cell tracking.[155–157] However, utilization of MNP coated with PLL or PEI *in vivo* is controversial because these polymers (specially PEI) interact strongly with proteins and cell membranes due to their high density of positive charges and have cytotoxic effects.[7,158,159] Nonetheless, exploitation of the cytotoxic effect may be beneficial to create theranostic agents.[160]

The charged nature of polyelectrolytes can also be exploited to assemble them into multilayers for MNP surface modification via layer-by-layer (LbL) technique. LbL consists in the alternate adsorption of polyanions and polycations around the MNP core(s), allowing the engineering of surface attributes like charge, particle size and shell chemistry. It is also a means of engrafting biologically active macromolecules for further functionalization. For example, poly(sodium styrene sulfonate) (PSS) was reported as part of LbL magnetic nanosystems for biomedical applications, including dendritic cell labeling, in combination with poly(diallyl-dimethylammonium) chloride (PDADMAC).[161,162]

Table 1.4. Utilization of synthetic polymers in the development of MNP-based MRI contrast agents.

Synthetic Polymer	***Property***	***MNP synthesis method***	***MNP-polymer assembly strategy***	***Polymer or MNP modification / functionalization***	***Intended purpose***	***Ref.***
PAA Poly(acrylic acid)	Polyanion	Thermal decomposition of $Fe(acac)_3$ in benzyl alcohol	Post-synthesis; ligand exchange through coordination of PAA carboxylic groups onto the MNP surface	Block copolymer with PEO (PEO-b-PAA); controlled clustering of MNP-PEO-b-PAA through reaction with PEO diacrylate oligomer; loaded with cationic drug	Maximization of r_2 for sensitive MRI and cationic drug delivery	108
		High-temperature co-precipitation method	*In situ* coating	-	Preparation of hydrophilic ultra-small Fe_3O_4 MNP as contrast agents for T_1 and T_2 MRI	163
PEG Poly(ethylene glycol)	Stealth properties; FDA-approved for clinical application	Co-precipitation	*In situ* coating	Diblock copolymers of poly(oligoethylene glycol acrylate) with incorporated phosphonic acid, carboxylic acid or glycerol groups	Tailoring of crystallinity and colloidal stability of MNP in aqueous medium for potential use as MRI contrast agents	110
		Thermal decomposition of iron oleate in organic solvent	Post-synthesis; ligand exchange	Commercial PEG derivatives with OH, SH, COOH and NH_2 groups; hyaluronan covalently conjugated to MNP-PEG-NH_2	*In vitro* and *in vivo* mesenchymal stem cell-targeted MRI imaging	116
		Solvent-free thermal decomposition of iron complex	Post-synthesis; dual solvent exchange	DSPE-mPEG copolymers (amphiphilic); DSPE-mPEG-MNP conjugated with antibodies against mouse VEGF receptor-1	Optimization of MRI contrast enhancement properties of MNP, stabilization in aqueous medium and cell-targeted *in vivo* MRI imaging	109
		Thermal decomposition of iron oleate in organic solvent	Post-synthesis; covalent conjugation onto DMSA functionalized MNP	Aminated PEG derivatives; ligand-exchange between OA and DMSA for MNP phase transfer	Stabilization and increase blood circulation time of MNP-based MRI contrast agent	55,80
		Thermal decomposition of iron	Post-synthesis self-assembly through	PEG-derived amphiphilic ligands with imidazole,	Tumor pH-targeted fluorescence and MR	67

Table 1.4. Utilization of synthetic polymers in the development of MNP-based MRI contrast agents. (continued)

Synthetic Polymer	***Property***	***MNP synthesis method***	***MNP-polymer assembly strategy***	***Polymer or MNP modification / functionalization***	***Intended purpose***	***Ref.***
		oleate in the presence of oleyl alcohol	hydrophobic interactions	cathecol and phenyl groups, and conjugated with a photosensitizer (chlorin 6)	imaging and photodynamic therapy	
PEI Poly(ethyleneimine)	Polycation	Thermal decomposition of $Fe(acac)_3$ in organic solvent followed by seed mediated growth	Post-synthesis assembly through hydrophobic interactions into controlled size micelles	siRNA conjugation onto PEI-coated MNP through electrostatic interactions	Gene delivery and noninvasive monitoring *in vivo*	155,156
		Hydrothermal	*In situ* coating	PEI-MNP functionalized with PEG, acetic anhydride or succinic anhydride	One pot synthesis of PEI-stabilized MNP for biomedical applications	7
		Thermal decomposition of $Fe(acac)_3$ in organic solvent	Post-synthesis, through ligand exchange.	PEG was grafted to PEI to form PEG-g-PEI; siRNA was coupled to PEG-g-PEI coated MNP through electrostatic interactions	Simultaneous siRNA delivery and MRI cell tracking *in vitro* and *in vivo* in gastric cancer	157
PLA Polylactic acid	Hydrophobic	Thermal decomposition of $Fe(acac)_3$ in organic solvent followed by seed-mediated growth	Post-synthesis self-assembly through single emulsion method	MAL-PEG-PLA and mPEG-PLA copolymers mixture ;cRGD and DOX were loaded in the micelles	Tumor-targeted controlled drug delivery and MRI contrast agent	111
		Thermal decomposition of $Fe(acac)_3$ in organic solvent	Post-synthesis; single emulsion method and solvent evaporation	Co-polymer of PLA and mPEG (PLA-mPEG-OH); magnetic micelles coated with PEI and chitosan; Chitosan-PEI-magnetic micelle conjugation with DNA by electrostatic interactions	Theranostic system for gene delivery and MRI monitoring	112
		Thermal decomposition of $Fe(acac)_3$ in organic solvent	Single emulsion method and solvent evaporation; nanoprecipitation	Co-polymer of PLA and TPGS	*In vivo* MRI imaging of tumor tissue by passive targeting (EPR)	113

Table 1.4. Utilization of synthetic polymers in the development of MNP-based MRI contrast agents. (continued)

Synthetic Polymer	*Property*	*MNP synthesis method*	*MNP-polymer assembly strategy*	*Polymer or MNP modification / functionalization*	*Intended purpose*	*Ref.*
			method			
PLGA Poly(lactic-co-glycolic) acid	FDA-approved for use in humans	Thermal decomposition of iron oleate in organic solvent	Encapsulation of multiple oleic acid stabilized nanocrystals within the polymer matrix; oil-in-water single emulsion method	Fluorescein isothiocyanate (FITC)	Long-term, noninvasive cell tracking *in vivo* via MRI	107
		Co-precipitation	Post-synthesis; oil-in-water emulsion/solvent evaporationextraction method	PGLA functionalized with antibodies for the dendritic cell receptor DC-SIGN; MNP functionalized with a FITC-labelled peptide antigen	Targeted delivery of nanovaccine and multimodal imaging of nanocarrier-dendritic cells interaction by MRI and fluorescence	164
		Hydrophobic commercial MNP (10 nm, Ocean nanotech, San Diego, CA)	Double emulsion/solvent evaporation method	-	Dual-imaging (US/MRI); enhancement of the effects of high-intensity focused ultrasound ablation on liver tissue	165
		Commercial ferrofluid (EMG 304, Ferrotec, Santa Clara, CA)).	Double emulsion/solvent evaporation method	Microspheres loaded with hydrophobic drug sorafenib in the PLGA oil phase	MRI-monitored local delivery of sorafenib to limit proangiogenic responses in liver tumors following transcatheter embolotherapies.	166
		Thermal decomposition of $Fe(acac)_3$ in organic solvent	Double emulsion/solvent evaporation method	-	Brain-penetrating particles for MR imaging of glioblastoma treatment	167
PLL Poly-L-lysine	polycation	Co-precipitation	Post-synthesis, through electrostatic interactions	Magnetite MNP oxidized to maghemite and coated with citrate	Stem cell labeling and tracking by MRI post-transplantation in a rat model	151,154
		Precipitation from	Post-synthesis,	Magnetite MNP were	Investigation of the effect	168

Table 1.4. Utilization of synthetic polymers in the development of MNP-based MRI contrast agents. (continued)

Synthetic Polymer	***Property***	***MNP synthesis method***	***MNP-polymer assembly strategy***	***Polymer or MNP modification / functionalization***	***Intended purpose***	***Ref.***
		partially reduced ferric chloride aqueous solutions	through adsorption	oxidized to maghemite	of MNP labeling on the biological properties of cancer stem cells *in vitro*	
		Co-precipitation	Post-synthesis, through electrostatic interactions	Magnetite MNP oxidized to maghemite and coated with citrate	*In vivo* stem cell tracking post transplantation to monitor spinal cord injury treatment	152
		Co-precipitation	Post-synthesis, by adsorption	Magnetite MNP were oxidized to maghemite	*In vitro* labeling of human umbilical cord mesenchymal stem cells	153
PSS Poly(styrene sulfonate)	polyanion	Adapted co-precipitation	Post-synthesis, through electrostatic interactions (Layer by Layer)	-	MRI labeling of dendritic cells	162
PVA Polyvinyl alcohol	biocompatible	Co-precipitation	Post-synthesis, by adsorption	Native PVA, Amine-PVA; carboxyl-PVA and thiol-PVA	*In vitro* study of interactions of the MNP with brain-derived endothelial cells, microglial cells, and differentiating three-dimensional aggregates.	169
		Co-precipitation	Post-synthesis, through adsorption	Hydroxyl-PVA and amine-PVA	*In vivo* MRI contrast enhancement in bone marrow	170
PVP polyvinylpyrrolidone	biocompatible	One-pot pyrolysis method	*In situ* coating	-	Investigation of the effect of nanoparticle size on MRI of normal liver and hepatic lesions *in vivo*	171
		High-temperature hydrolysis of chelate metal alkoxide complexes in liquid polyol	*In situ* coating	PLL was administered together with the MNP-PVP	Labeling of mice β-cells for *in vivo* visualization of islet grafts by MRI in a mice islet transplantation model.	150

1.5. Concluding Remarks

Colloidal iron oxide MNPs possess unique properties that make them useful for biomedical applications. They have received particular attention as T_2 contrast agents for MRI due to their superparamagnetism, biocompatibility and biodegradability. Polymeric coatings, popularized by dextran and PEG, had initially the main goal of stabilizing the nanoprobes in biological fluids and enhancing their blood circulation times for use as diagnostic devices. As a result of the excellent chemical reactivity of MNP surface, availability of innumerous natural and synthetic polymers and functionalization chemistries, research in the last decades has extensively explored the combination of these materials to engineer more complex nanosystems: hybrid polymeric/MNP MRI nanoprobes with additional properties such as targeted drug and gene delivery, stimuli-responsiveness and/or multimodality imaging capabilities. Biopolymers, in particular polysaccharides, are appealing materials due to their biocompatibility, biodegradability and biological function but also from the point of view of availability, as nowadays production by means of biotechnological processes using genetically modified microorganisms is more and more common, less expensive and greener. However they lack the synthetic control and the possibility of introducing chemical modifications during synthesis, characteristic of synthetic polymers. These offer practically infinite possibilities of design making use of the available chemistry synthesis methods to conjugate different monomers, oligomers and adding chemical and biological functionalities. Given the potentialities of polymers, their combination with MNP is promising. There is a large number of studies published regarding this combination but general the studies involving nanosystems with polysaccharide coatings have been more extensive with the characterization of biological interactions of MNP both *in vitro* and *in vivo* than the ones employing complex synthetic polymer assemblies, which focus more on the physiochemical characterization of the nanoprobes themselves.

Some challenges remain, however, in the full development of such hybrid polymeric/MNP MRI nanoprobes. While problems with strict control of particle size distribution, stability of colloidal ferrofluids and respective magnetic properties are being researched, there is still lack of knowledge regarding large scale production, long-term stability in storage and production cost. Importantly, studies regarding the clinical effectiveness of the developed nanosystems of are still scarce and *in vivo* long term biodistribution and toxicity of MNP unknown. Besides nanoprobe development, research is needed in order to understand the fate of MNP and their coatings after administration into the human body in order to enable the transference from the bench to bedside and effective use in medicine.

Overall, the hybrid polymeric/MNP nanoprobes currently available in the form of research platforms and presented in this review show the potential of superparamagnetic iron

oxide nanoparticles in molecular imaging and therapeutics, enlightening their importance in nanomedicine as a form of levering the future of Medicine.

1.6. References

(1) Stephen, Z. R.; Kievit, F. M.; Zhang, M. Magnetite Nanoparticles for Medical MR Imaging. *Mater. Today (Kidlington).* **2011**, *14*, 330–338, DOI:10.1016/S1369-7021(11)70163-8.

(2) Krishnan, K. M. Biomedical Nanomagnetics: A Spin Through Possibilities in Imaging, Diagnostics, and Therapy. *IEEE Trans. Magn.* **2010**, *46*, 2523–2558, DOI:10.1109/TMAG.2010.2046907.

(3) Colombo, M.; Carregal-Romero, S.; Casula, M. F.; Gutiérrez, L.; Morales, M. P.; Böhm, I. B.; Heverhagen, J. T.; Prosperi, D.; Parak, W. J. Biological Applications of Magnetic Nanoparticles. *Chem. Soc. Rev.* **2012**, *41*, 4306–4334, DOI:10.1039/c2cs15337h.

(4) Laurent, S.; Forge, D.; Port, M.; Roch, A.; Robic, C.; Vander Elst, L.; Muller, R. N. Magnetic Iron Oxide Nanoparticles: Synthesis, Stabilization, Vectorization, Physicochemical Characterizations, and Biological Applications. *Chem. Rev.* **2008**, *108*, 2064–2110, DOI:10.1021/cr068445e.

(5) Massart, R. Preparation of Aqueous Magnetic Liquids in Alkaline and Acidic Media. *IEEE Trans. Magn.* **1981**, *17*, 1247–1248, DOI:10.1109/TMAG.1981.1061188.

(6) Boyer, C.; Whittaker, M. R.; Bulmus, V.; Liu, J.; Davis, T. P. The Design and Utility of Polymer-Stabilized Iron-Oxide Nanoparticles for Nanomedicine Applications. *NPG Asia Mater.* **2010**, *2*, 23–30, DOI:10.1038/asiamat.2010.6.

(7) Cai, H.; An, X.; Cui, J.; Li, J.; Wen, S.; Li, K.; Shen, M.; Zheng, L.; Zhang, G.; Shi, X. Facile Hydrothermal Synthesis and Surface Functionalization of Polyethyleneimine-Coated Iron Oxide Nanoparticles for Biomedical Applications. *ACS Appl. Mater. Interfaces* **2013**, *5*, 1722–1731, DOI:10.1021/am302883m.

(8) Gupta, A. K.; Wells, S. Surface-Modified Superparamagnetic Nanoparticles for Drug Delivery: Preparation, Characterization, and Cytotoxicity Studies. *IEEE Trans. Nanobioscience* **2004**, *3*, 66–73.

(9) Sun, S.; Zeng, H.; Robinson, D. B.; Raoux, S.; Rice, P. M.; Wang, S. X.; Li, G. Monodisperse MFe2O4 (M = Fe, Co, Mn) Nanoparticles. *J. Am. Chem. Soc.* **2004**, *126*, 273–279, DOI:10.1021/ja0380852.

(10) Lattuada, M.; Hatton, T. A. Functionalization of Monodisperse Magnetic Nanoparticles. *Langmuir* **2007**, *23*, 2158–2168, DOI:10.1021/la062092x.

(11) Salas, G.; Casado, C.; Teran, F. J.; Miranda, R.; Serna, C. J.; Morales, M. P. Controlled Synthesis of Uniform Magnetite Nanocrystals with High-Quality Properties for Biomedical Applications. *J. Mater. Chem.* **2012**, *22*, 21065, DOI:10.1039/c2jm34402e.

(12) Cai, W.; Wan, J. Facile Synthesis of Superparamagnetic Magnetite Nanoparticles in Liquid Polyols. *J. Colloid Interface Sci.* **2007**, *305*, 366–370, DOI:10.1016/j.jcis.2006.10.023.

(13) Park, J.; An, K.; Hwang, Y.; Park, J.-G.; Noh, H.-J.; Kim, J.-Y.; Park, J.-H.; Hwang, N.-M.; Hyeon, T. Ultra-Large-Scale Syntheses of Monodisperse Nanocrystals. *Nat. Mater.* **2004**, *3*, 891–895, DOI:10.1038/nmat1251.

(14) Kong, S. D.; Lee, J.; Ramachandran, S.; Eliceiri, B. P.; Shubayev, V. I.; Lal, R.; Jin, S. Magnetic Targeting of Nanoparticles across the Intact Blood-Brain Barrier. *J. Control. Release* **2012**, *164*, 49–57, DOI:10.1016/j.jconrel.2012.09.021.

(15) Landázuri, N.; Tong, S.; Suo, J.; Joseph, G.; Weiss, D.; Sutcliffe, D. J.; Giddens, D. P.; Bao, G.; Taylor, W. R. Magnetic Targeting of Human Mesenchymal Stem Cells with Internalized Superparamagnetic Iron Oxide Nanoparticles. *Small* **2013**, *9*, 4017–4026, DOI:10.1002/smll.201300570.

(16) Cheng, K.; Shen, D.; Hensley, M. T.; Middleton, R.; Sun, B.; Liu, W.; De Couto, G.; Marbán, E. Magnetic Antibody-Linked Nanomatchmakers for Therapeutic Cell Targeting. *Nat. Commun.* **2014**, *5*, 4880, DOI:10.1038/ncomms5880.

(17) Santos, L. J.; Reis, R. L.; Gomes, M. E. Harnessing Magnetic-Mechano Actuation in Regenerative Medicine and Tissue Engineering. *Trends Biotechnol.* **2015**, *33*, 471–479, DOI:10.1016/j.tibtech.2015.06.006.

(18) Shen, H.; Tong, S.; Bao, G.; Wang, B. Structural Responses of Cells to Intracellular Magnetic Force Induced by Superparamagnetic Iron Oxide Nanoparticles. *Phys. Chem. Chem. Phys.* **2014**, *16*, 1914–1920, DOI:10.1039/c3cp51435h.

(19) Henstock, J. R.; Rotherham, M.; Rashidi, H.; Shakesheff, K. M.; El Haj, A. J. Remotely Activated Mechanotransduction via Magnetic Nanoparticles Promotes Mineralization Synergistically With Bone Morphogenetic Protein 2: Applications for Injectable Cell Therapy. *Stem Cells Transl. Med.* **2014**, *3*, 1363–1374, DOI:10.5966/sctm.2014-0017.

(20) Tabatabaei, S. N.; Girouard, H.; Carret, A.-S.; Martel, S. Remote Control of the Permeability of the Blood-Brain Barrier by Magnetic Heating of Nanoparticles: A Proof of Concept for Brain Drug Delivery. *J. Control. Release* **2015**, *206*, 49–57, DOI:10.1016/j.jconrel.2015.02.027.

(21) Quinto, C. A.; Mohindra, P.; Tong, S.; Bao, G. Multifunctional Superparamagnetic Iron Oxide Nanoparticles for Combined Chemotherapy and Hyperthermia Cancer Treatment. *Nanoscale* **2015**, *7*, 12728–12736, DOI:10.1039/c5nr02718g.

(22) Ruehm, S. G.; Corot, C.; Vogt, P.; Kolb, S.; Debatin, J. F. Magnetic Resonance Imaging of Atherosclerotic Plaque With Ultrasmall Superparamagnetic Particles of Iron Oxide in Hyperlipidemic Rabbits. *Circulation* **2001**, *103*, 415–422, DOI:10.1161/01.CIR.103.3.415.

(23) Yang, L.; Peng, X.-H.; Wang, Y. A.; Wang, X.; Cao, Z.; Ni, C.; Karna, P.; Zhang, X.; Wood, W. C.; Gao, X.; *et al.* Receptor-Targeted Nanoparticles for *in Vivo* Imaging of Breast Cancer. *Clin. Cancer Res.* **2009**, *15*, 4722–4732, DOI:10.1158/1078-0432.CCR-08-3289.

(24) Hasan, D.; Chalouhi, N.; Jabbour, P.; Dumont, A. S.; Kung, D. K.; Magnotta, V. A.; Young, W. L.; Hashimoto, T.; Winn, H. R.; Heistad, D. Early Change in Ferumoxytol-Enhanced Magnetic Resonance Imaging Signal Suggests Unstable Human Cerebral Aneurysm: A Pilot Study. *Stroke.* **2012**, *43*, 3258–3265, DOI:10.1161/STROKEAHA.112.673400.

(25) Wei, Y.; Liao, R.; Liu, H.; Li, H.; Xu, H.; Zhou, Q. Biocompatible Low-Retention Superparamagnetic Iron Oxide Nanoclusters as Contrast Agents for Magnetic Resonance Imaging of Liver Tumor. *J. Biomed. Nanotechnol.* **2015**, *11*, 854–864, DOI:10.1166/jbn.2015.2042.

(26) Watada, Y.; Yamashita, D.; Toyoda, M.; Tsuchiya, K.; Hida, N.; Tanimoto, A.; Ogawa, K.; Kanzaki, S.; Umezawa, A. Magnetic Resonance Monitoring of Superparamagnetic Iron Oxide (SPIO)-Labeled Stem Cells Transplanted into the Inner Ear. *Neurosci. Res.* **2015**, *95*, 21–26, DOI:10.1016/j.neures.2015.01.010.

(27) Cheng, K. K.; Chan, P. S.; Fan, S.; Kwan, S. M.; Yeung, K. L.; Wáng, Y.-X. J.; Chow, A. H. L.; Wu, E. X.; Baum, L. Curcumin-Conjugated Magnetic Nanoparticles for Detecting Amyloid Plaques in

Alzheimer's Disease Mice Using Magnetic Resonance Imaging (MRI). *Biomaterials* **2015**, *44*, 155–172, DOI:10.1016/j.biomaterials.2014.12.005.

(28) Dai, F.; Du, M.; Liu, Y.; Liu, G.; Liu, Q.; Zhang, X. Folic Acid-Conjugated Glucose and Dextran Coated Iron Oxide Nanoparticles as MRI Contrast Agents for Diagnosis and Treatment Response of Rheumatoid Arthritis. *J. Mater. Chem. B* **2014**, *2*, 2240, DOI:10.1039/c3tb21732a.

(29) Hamilton, A. M.; Aidoudi-Ahmed, S.; Sharma, S.; Kotamraju, V. R.; Foster, P. J.; Sugahara, K. N.; Ruoslahti, E.; Rutt, B. K. Nanoparticles Coated with the Tumor-Penetrating Peptide iRGD Reduce Experimental Breast Cancer Metastasis in the Brain. *J. Mol. Med. (Berl).* **2015**, DOI:10.1007/s00109-015-1279-x.

(30) Jozwiak, S.; Habich, A.; Kotulska, K.; Sarnowska, A.; Kropiwnicki, T.; Janowski, M.; Jurkiewicz, E.; Lukomska, B.; Kmiec, T.; Walecki, J.; *et al.* Intracerebroventricular Transplantation of Cord Blood-Derived Neural Progenitors in a Child With Severe Global Brain Ischemic Injury. *Cell Med.* **2010**, *1*, 71–80, DOI:10.3727/215517910X536618.

(31) Wu, C.; Xu, Y.; Yang, L.; Wu, J.; Zhu, W.; Li, D.; Cheng, Z.; Xia, C.; Guo, Y.; Gong, Q.; *et al.* Negatively Charged Magnetite Nanoparticle Clusters as Efficient MRI Probes for Dendritic Cell Labeling and *In Vivo* Tracking. *Adv. Funct. Mater.* **2015**, *25*, 3581–3591, DOI:10.1002/adfm.201501031.

(32) Kang, S.; Lee, H. W.; Jeon, Y. H.; Singh, T. D.; Choi, Y. J.; Park, J. Y.; Kim, J. S.; Lee, H.; Hong, K. S.; Lee, I.; *et al.* Combined Fluorescence and Magnetic Resonance Imaging of Primary Macrophage Migration to Sites of Acute Inflammation Using Near-Infrared Fluorescent Magnetic Nanoparticles. *Mol. Imaging Biol.* **2015**, DOI:10.1007/s11307-015-0830-z.

(33) Adams, C. F.; Pickard, M. R.; Chari, D. M. Magnetic Nanoparticle Mediated Transfection of Neural Stem Cell Suspension Cultures Is Enhanced by Applied Oscillating Magnetic Fields. *Nanomedicine* **2013**, *9*, 737–741, DOI:10.1016/j.nano.2013.05.014.

(34) Lee, G. Y.; Qian, W. P.; Wang, L.; Wang, Y. A.; Staley, C. A.; Satpathy, M.; Nie, S.; Mao, H.; Yang, L. Theranostic Nanoparticles with Controlled Release of Gemcitabine for Targeted Therapy and MRI of Pancreatic Cancer. *ACS Nano* **2013**, *7*, 2078–2089, DOI:10.1021/nn3043463.

(35) Hsiao, M.-H.; Mu, Q.; Stephen, Z. R.; Fang, C.; Zhang, M. Hexanoyl-Chitosan-PEG Copolymer Coated Iron Oxide Nanoparticles for Hydrophobic Drug Delivery. *ACS Macro Lett.* **2015**, *4*, 403–407, DOI:10.1021/acsmacrolett.5b00091.

(36) Chen, O.; Riedemann, L.; Etoc, F.; Herrmann, H.; Coppey, M.; Barch, M.; Farrar, C. T.; Zhao, J.; Bruns, O. T.; Wei, H.; *et al.* Magneto-Fluorescent Core-Shell Supernanoparticles. *Nat. Commun.* **2014**, *5*, 5093, DOI:10.1038/ncomms6093.

(37) Wu, M.; Zhang, D.; Zeng, Y.; Wu, L.; Liu, X.; Liu, J. Nanocluster of Superparamagnetic Iron Oxide Nanoparticles Coated with Poly (dopamine) for Magnetic Field-Targeting, Highly Sensitive MRI and Photothermal Cancer Therapy. *Nanotechnology* **2015**, *26*, 115102, DOI:10.1088/0957-4484/26/11/115102.

(38) Lin, J.; Li, Y.; Li, Y.; Wu, H.; Yu, F.; Zhou, S.; Xie, L.; Luo, F.; Lin, C.; Hou, Z. Drug/Dye-Loaded, Multifunctional PEG-Chitosan-Iron Oxide Nanocomposites for Methotraxate Synergistically Self-Targeted Cancer Therapy and Dual Model Imaging. *ACS Appl. Mater. Interfaces* **2015**, *7*, 11908–11920, DOI:10.1021/acsami.5b01685.

(39) Gleich, B.; Weizenecker, J. Tomographic Imaging Using the Nonlinear Response of Magnetic Particles. *Nature* **2005**, *435*, 1214–1217, DOI:10.1038/nature03808.

(40) Ferguson, R. M.; Khandhar, A. P.; Kemp, S. J.; Arami, H.; Saritas, E. U.; Croft, L. R.; Konkle, J.; Goodwill, P. W.; Halkola, A.; Rahmer, J.; *et al.* Magnetic Particle Imaging with Tailored Iron Oxide Nanoparticle Tracers. *IEEE Trans. Med. Imaging* **2015**, *34*, 1077–1084, DOI:10.1109/TMI.2014.2375065.

(41) Panagiotopoulos, N.; Duschka, R. L.; Ahlborg, M.; Bringout, G.; Debbeler, C.; Graeser, M.; Kaethner, C.; Lüdtke-Buzug, K.; Medimagh, H.; Stelzner, J.; *et al.* Magnetic Particle Imaging: Current Developments and Future Directions. *Int. J. Nanomedicine* **2015**, *10*, 3097–3114, DOI:10.2147/IJN.S70488.

(42) Zhou, Y.; Tang, Z.; Shi, C.; Shi, S.; Qian, Z.; Zhou, S. Polyethylenimine Functionalized Magnetic Nanoparticles as a Potential Non-Viral Vector for Gene Delivery. *J. Mater. Sci. Mater. Med.* **2012**, *23*, 2697–2708, DOI:10.1007/s10856-012-4720-5.

(43) Namgung, R.; Singha, K.; Yu, M. K.; Jon, S.; Kim, Y. S.; Ahn, Y.; Park, I.-K.; Kim, W. J. Hybrid Superparamagnetic Iron Oxide Nanoparticle-Branched Polyethylenimine Magnetoplexes for Gene Transfection of Vascular Endothelial Cells. *Biomaterials* **2010**, *31*, 4204–4213, DOI:10.1016/j.biomaterials.2010.01.123.

(44) Lauterbur, P. C. Image Formation by Induced Local Interactions: Examples Employing Nuclear Magnetic Resonance. *Nature* **1973**, *242*, 190–191, DOI:10.1038/242190a0.

(45) Lauterbur, P. C. Progress in N.m.r. Zeugmatography Imaging. *Philos. Trans. R. Soc. Lond. B. Biol. Sci.* **1980**, *289*, 483–487.

(46) Ohgushi, M.; Nagayama, K.; Wada, A. Dextran-Magnetite: A New Relaxation Reagent and Its Application to T2 Measurements in Gel Systems. *J. Magn. Reson.* **1978**, *29*, 599–601, DOI:10.1016/0022-2364(78)90018-5.

(47) Renshaw, P. F.; Owen, C. S.; Evans, A. E.; Leigh, J. S. Immunospecific NMR Contrast Agents. *Magn. Reson. Imaging* **1986**, *4*, 351–357.

(48) Saini, S.; Stark, D. D.; Hahn, P. F.; Wittenberg, J.; Brady, T. J.; Ferrucci, J. T. Ferrite Particles: A Superparamagnetic MR Contrast Agent for the Reticuloendothelial System. *Radiology* **1987**, *162*, 211–216, DOI:10.1148/radiology.162.1.3786765.

(49) Renshaw, P. F.; Owen, C. S.; McLaughlin, A. C.; Frey, T. G.; Leigh, J. S. Ferromagnetic Contrast Agents: A New Approach. *Magn. Reson. Med.* **1986**, *3*, 217–225.

(50) Shapiro, E. M. Biodegradable, Polymer Encapsulated, Metal Oxide Particles for MRI-Based Cell Tracking. *Magn. Reson. Med.* **2015**, *73*, 376–389, DOI:10.1002/mrm.25263.

(51) Corot, C.; Warlin, D. Superparamagnetic Iron Oxide Nanoparticles for MRI: Contrast Media Pharmaceutical Company R&D Perspective. *Wiley Interdiscip. Rev. Nanomed. Nanobiotechnol.* **2013**, DOI:10.1002/wnan.1225.

(52) Westbrook, C. *MRI at a Glance*; 1st ed.; Blackwell Science Ltd: Oxford, UK, 2002.

(53) Pankhurst, Q. a; Connolly, J.; Jones, S. K.; Dobson, J. Applications of Magnetic Nanoparticles in Biomedicine. *J. Phys. D. Appl. Phys.* **2003**, *36*, R167–R181, DOI:10.1088/0022-3727/36/13/201.

(54) Terreno, E.; Castelli, D. D.; Viale, A.; Aime, S. Challenges for Molecular Magnetic Resonance Imaging. *Chem. Rev.* **2010**, *110*, 3019–3042, DOI:10.1021/cr100025t.

(55) Ruiz, A.; Hernández, Y.; Cabal, C.; González, E.; Veintemillas-Verdaguer, S.; Martínez, E.; Morales, M. P. Biodistribution and Pharmacokinetics of Uniform Magnetite Nanoparticles Chemically Modified with Polyethylene Glycol. *Nanoscale* **2013**, *5*, 11400–11408, DOI:10.1039/c3nr01412f.

(56) Iqbal, M. Z.; Ma, X.; Chen, T.; Zhang, L.; Ren, W.; Xiang, L.; Wu, A. Silica-Coated Super-Paramagnetic Iron Oxide Nanoparticles (SPIONPs): A New Type Contrast Agent of T 1 Magnetic Resonance Imaging (MRI). *J. Mater. Chem. B* **2015**, *3*, 5172–5181, DOI:10.1039/C5TB00300H.

(57) Macher, T.; Totenhagen, J.; Sherwood, J.; Qin, Y.; Gurler, D.; Bolding, M. S.; Bao, Y. Ultrathin Iron Oxide Nanowhiskers as Positive Contrast Agents for Magnetic Resonance Imaging. *Adv. Funct. Mater.* **2015**, *25*, 490–494, DOI:10.1002/adfm.201403436.

(58) Bacri, J.-C.; Perzynski, R.; Salin, D.; Cabuil, V.; Massart, R. Ionic Ferrofluids: A Crossing of Chemistry and Physics. *J. Magn. Magn. Mater.* **1990**, *85*, 27–32, DOI:10.1016/0304-8853(90)90010-N.

(59) Daou, T. J.; Grenèche, J. M.; Pourroy, G.; Buathong, S.; Derory, A.; Ulhaq-Bouillet, C.; Donnio, B.; Guillon, D.; Begin-Colin, S. Coupling Agent Effect on Magnetic Properties of Functionalized Magnetite-Based Nanoparticles. *Chem. Mater.* **2008**, *20*, 5869–5875, DOI:10.1021/cm801405n.

(60) Jain, N.; Wang, Y.; Jones, S. K.; Hawkett, B. S.; Warr, G. G. Optimized Steric Stabilization of Aqueous Ferrofluids and Magnetic Nanoparticles. *Langmuir* **2010**, *26*, 4465–4472, DOI:10.1021/la903513v.

(61) Smolensky, E. D.; Park, H.-Y. E.; Berquó, T. S.; Pierre, V. C. Surface Functionalization of Magnetic Iron Oxide Nanoparticles for MRI Applications - Effect of Anchoring Group and Ligand Exchange Protocol. *Contrast Media Mol. Imaging* **2011**, *6*, 189–199, DOI:10.1002/cmmi.417.

(62) Roca, A. G.; Veintemillas-Verdaguer, S.; Port, M.; Robic, C.; Serna, C. J.; Morales, M. P. Effect of Nanoparticle and Aggregate Size on the Relaxometric Properties of MR Contrast Agents Based on High Quality Magnetite Nanoparticles. *J. Phys. Chem. B* **2009**, *113*, 7033–7039, DOI:10.1021/jp807820s.

(63) Berret, J.-F.; Schonbeck, N.; Gazeau, F.; El Kharrat, D.; Sandre, O.; Vacher, A.; Airiau, M. Controlled Clustering of Superparamagnetic Nanoparticles Using Block Copolymers: Design of New Contrast Agents for Magnetic Resonance Imaging. *J. Am. Chem. Soc.* **2006**, *128*, 1755–1761, DOI:10.1021/ja0562999.

(64) Ai, H.; Flask, C.; Weinberg, B.; Shuai, X.-T.; Pagel, M. D.; Farrell, D.; Duerk, J.; Gao, J. Magnetite-Loaded Polymeric Micelles as Ultrasensitive Magnetic-Resonance Probes. *Adv. Mater.* **2005**, *17*, 1949–1952, DOI:10.1002/adma.200401904.

(65) Duan, H.; Kuang, M.; Wang, X.; Wang, Y. A.; Mao, H.; Nie, S. Reexamining the Effects of Particle Size and Surface Chemistry on the Magnetic Properties of Iron Oxide Nanocrystals: New Insights into Spin Disorder and Proton Relaxivity. *J. Phys. Chem. C* **2008**, *112*, 8127–8131, DOI:10.1021/jp8029083.

(66) Nafiujjaman, M.; Revuri, V.; Nurunnabi, M.; Cho, K. J.; Lee, Y.-K. Photosensitizer Conjugated Iron Oxide Nanoparticles for Simultaneous *in Vitro* Magneto-Fluorescent Imaging Guided Photodynamic Therapy. *Chem. Commun. (Camb).* **2015**, *51*, 5687–5690, DOI:10.1039/c4cc10444g.

(67) Ling, D.; Park, W.; Park, S.-J.; Lu, Y.; Kim, K. S.; Hackett, M. J.; Kim, B. H.; Yim, H.; Jeon, Y. S.; Na, K.; *et al.* Multifunctional Tumor pH-Sensitive Self-Assembled Nanoparticles for Bimodal Imaging and Treatment of Resistant Heterogeneous Tumors. *J. Am. Chem. Soc.* **2014**, *136*, 5647–5655, DOI:10.1021/ja4108287.

(68) Huang, J.; Zhong, X.; Wang, L.; Yang, L.; Mao, H. Improving the Magnetic Resonance Imaging Contrast and Detection Methods with Engineered Magnetic Nanoparticles. *Theranostics* **2012**, *2*, 86–102, DOI:10.7150/thno.4006.

(69) Vuong, Q. L.; Berret, J.-F.; Fresnais, J.; Gossuin, Y.; Sandre, O. A Universal Scaling Law to Predict the Efficiency of Magnetic Nanoparticles as MRI T(2)-Contrast Agents. *Adv. Healthc. Mater.* **2012**, *1*, 502–512, DOI:10.1002/adhm.201200078.

(70) Cornell, R. M.; Schwertmann, U. *The Iron Oxides: Structure, Properties, Reactions, Occurrences and Uses*; 2nd ed.; Wiley-VCH GmbH & Co. KGaA: Weinheim, 2003.

(71) Wagner, S.; Schnorr, J.; Pilgrimm, H.; Hamm, B.; Taupitz, M. Monomer-Coated Very Small Superparamagnetic Iron Oxide Particles as Contrast Medium for Magnetic Resonance Imaging: Preclinical *in Vivo* Characterization. *Invest. Radiol.* **2002**, *37*, 167–177.

(72) Pilgrimm, H. Super-Paramagnetic Particles with Increased R1 Relaxivity, Process for Producing Said Particles and Use Thereof. US6638494 B1, October 28, 2003.

(73) Taupitz, M.; Wagner, S.; Schnorr, J.; Kravec, I.; Pilgrimm, H.; Bergmann-Fritsch, H.; Hamm, B. Phase I Clinical Evaluation of Citrate-Coated Monocrystalline Very Small Superparamagnetic Iron Oxide Particles as a New Contrast Medium for Magnetic Resonance Imaging. *Invest. Radiol.* **2004**, *39*, 394–405.

(74) Andreas, K.; Georgieva, R.; Ladwig, M.; Mueller, S.; Notter, M.; Sittinger, M.; Ringe, J. Highly Efficient Magnetic Stem Cell Labeling with Citrate-Coated Superparamagnetic Iron Oxide Nanoparticles for MRI Tracking. *Biomaterials* **2012**, *33*, 4515–4525, DOI:10.1016/j.biomaterials.2012.02.064.

(75) Fauconnier, N.; Pons, J. N.; Roger, J.; Bee, A. Thiolation of Maghemite Nanoparticles by Dimercaptosuccinic Acid. *J. Colloid Interface Sci.* **1997**, *194*, 427–433, DOI:10.1006/jcis.1997.5125.

(76) Portet, D.; Denizot, B.; Rump, E.; Lejeune, J.-J.; Jallet, P. Nonpolymeric Coatings of Iron Oxide Colloids for Biological Use as Magnetic Resonance Imaging Contrast Agents. *J. Colloid Interface Sci.* **2001**, *238*, 37–42, DOI:10.1006/jcis.2001.7500.

(77) Hatakeyama, M.; Kishi, H.; Kita, Y.; Imai, K.; Nishio, K.; Karasawa, S.; Masaike, Y.; Sakamoto, S.; Sandhu, A.; Tanimoto, A.; *et al.* A Two-Step Ligand Exchange Reaction Generates Highly Water-Dispersed Magnetic Nanoparticles for Biomedical Applications. *J. Mater. Chem.* **2011**, *21*, 5959, DOI:10.1039/c0jm04381h.

(78) Jun, Y.-W.; Huh, Y.-M.; Choi, J.-S.; Lee, J.-H.; Song, H.-T.; Kim, S.; Yoon, S.; Kim, K.-S.; Shin, J.-S.; Suh, J.-S.; *et al*. Nanoscale Size Effect of Magnetic Nanocrystals and Their Utilization for Cancer Diagnosis via Magnetic Resonance Imaging. *J. Am. Chem. Soc.* **2005**, *127*, 5732–5733, DOI:10.1021/ja0422155.

(79) Chen, Z. P.; Zhang, Y.; Zhang, S.; Xia, J. G.; Liu, J. W.; Xu, K.; Gu, N. Preparation and Characterization of Water-Soluble Monodisperse Magnetic Iron Oxide Nanoparticles via Surface Double-Exchange with DMSA. *Colloids Surfaces A Physicochem. Eng. Asp.* **2008**, *316*, 210–216, DOI:10.1016/j.colsurfa.2007.09.017.

(80) Ruiz, A.; Salas, G.; Calero, M.; Hernández, Y.; Villanueva, A.; Herranz, F.; Veintemillas-Verdaguer, S.; Martínez, E.; Barber, D. F.; Morales, M. P. Short-Chain PEG Molecules Strongly Bound to Magnetic Nanoparticle for MRI Long Circulating Agents. *Acta Biomater.* **2013**, *9*, 6421–6430, DOI:10.1016/j.actbio.2012.12.032.

(81) Bertorelle, F.; Wilhelm, C.; Roger, J.; Gazeau, F.; Ménager, C.; Cabuil, V. Fluorescence-Modified Superparamagnetic Nanoparticles: Intracellular Uptake and Use in Cellular Imaging. *Langmuir* **2006**, *22*, 5385–5391, DOI:10.1021/la052710u.

(82) Palma, S. I. C. J.; Carvalho, A.; Silva, J.; Martins, P.; Marciello, M.; Fernandes, A. R.; Del Puerto Morales, M.; Roque, A. C. A. Covalent Coupling of Gum Arabic onto Superparamagnetic Iron Oxide Nanoparticles for MRI Cell Labeling: Physicochemical and *in Vitro* Characterization. *Contrast Media Mol. Imaging* **2015**, *10*, 320–328, DOI:10.1002/cmmi.1635.

(83) Xie, J.; Xu, C.; Kohler, N.; Hou, Y.; Sun, S. Controlled PEGylation of Monodisperse Fe3O4 Nanoparticles for Reduced Non-Specific Uptake by Macrophage Cells. *Adv. Mater.* **2007**, *19*, 3163–3166, DOI:10.1002/adma.200701975.

(84) Malvindi, M. A.; De Matteis, V.; Galeone, A.; Brunetti, V.; Anyfantis, G. C.; Athanassiou, A.; Cingolani, R.; Pompa, P. P. Toxicity Assessment of Silica Coated Iron Oxide Nanoparticles and

Biocompatibility Improvement by Surface Engineering. *PLoS One* **2014**, *9*, e85835, DOI:10.1371/journal.pone.0085835.

(85) Santra, S.; Tapec, R.; Theodoropoulou, N.; Dobson, J.; Hebard, A.; Tan, W. Synthesis and Characterization of Silica-Coated Iron Oxide Nanoparticles in Microemulsion: The Effect of Nonionic Surfactants. *Langmuir* **2001**, *17*, 2900–2906, DOI:10.1021/la0008636.

(86) De Palma, R.; Peeters, S.; Van Bael, M. J.; Van den Rul, H.; Bonroy, K.; Laureyn, W.; Mullens, J.; Borghs, G.; Maes, G. Silane Ligand Exchange to Make Hydrophobic Superparamagnetic Nanoparticles Water-Dispersible. *Chem. Mater.* **2007**, *19*, 1821–1831, DOI:10.1021/cm0628000.

(87) Peng, Y.-K.; Lui, C. N. P.; Lin, T.-H.; Chang, C.; Chou, P.-T.; Yung, K. K. L.; Tsang, S. C. E. Multifunctional Silica-Coated Iron Oxide Nanoparticles: A Facile Four-in-One System for in Situ Study of Neural Stem Cell Harvesting. *Faraday Discuss.* **2014**, *175*, 13–26, DOI:10.1039/c4fd00132j.

(88) Stanicki, D.; Boutry, S.; Laurent, S.; Wacheul, L.; Nicolas, E.; Crombez, D.; Vander Elst, L.; Lafontaine, D. L. J.; Muller, R. N. Carboxy-Silane Coated Iron Oxide Nanoparticles: A Convenient Platform for Cellular and Small Animal Imaging. *J. Mater. Chem. B* **2014**, *2*, 387–397, DOI:10.1039/C3TB21480J.

(89) Im, S. H.; Herricks, T.; Lee, Y. T.; Xia, Y. Synthesis and Characterization of Monodisperse Silica Colloids Loaded with Superparamagnetic Iron Oxide Nanoparticles. *Chem. Phys. Lett.* **2005**, *401*, 19–23, DOI:10.1016/j.cplett.2004.11.028.

(90) Deng, Y.-H.; Wang, C.-C.; Hu, J.-H.; Yang, W.-L.; Fu, S.-K. Investigation of Formation of Silica-Coated Magnetite Nanoparticles via Sol–gel Approach. *Colloids Surfaces A Physicochem. Eng. Asp.* **2005**, *262*, 87–93, DOI:10.1016/j.colsurfa.2005.04.009.

(91) Kunzmann, A.; Andersson, B.; Vogt, C.; Feliu, N.; Ye, F.; Gabrielsson, S.; Toprak, M. S.; Buerki-Thurnherr, T.; Laurent, S.; Vahter, M.; *et al.* Efficient Internalization of Silica-Coated Iron Oxide Nanoparticles of Different Sizes by Primary Human Macrophages and Dendritic Cells. *Toxicol. Appl. Pharmacol.* **2011**, *253*, 81–93, DOI:10.1016/j.taap.2011.03.011.

(92) Yathindranath, V.; Sun, Z.; Worden, M.; Donald, L. J.; Thliveris, J. A.; Miller, D. W.; Hegmann, T. One-Pot Synthesis of Iron Oxide Nanoparticles with Functional Silane Shells: A Versatile General Precursor for Conjugations and Biomedical Applications. *Langmuir* **2013**, *29*, 10850–10858, DOI:10.1021/la402007d.

(93) Tartaj, P.; González-Carreño, T.; Serna, C. J. Single-Step Nanoengineering of Silica Coated Maghemite Hollow Spheres with Tunable Magnetic Properties. *Adv. Mater.* **2001**, *13*, 1620–1624, DOI:10.1002/1521-4095(200111)13:21<1620::AID-ADMA1620>3.0.CO;2-Z.

(94) Bridot, J.-L.; Stanicki, D.; Laurent, S.; Boutry, S.; Gossuin, Y.; Leclère, P.; Lazzaroni, R.; Vander Elst, L.; Muller, R. N. New Carboxysilane-Coated Iron Oxide Nanoparticles for Nonspecific Cell Labelling. *Contrast Media Mol. Imaging 8*, 466–474, DOI:10.1002/cmmi.1552.

(95) Bloemen, M.; Brullot, W.; Luong, T. T.; Geukens, N.; Gils, A.; Verbiest, T. Improved Functionalization of Oleic Acid-Coated Iron Oxide Nanoparticles for Biomedical Applications. *J. Nanopart. Res.* **2012**, *14*, 1100, DOI:10.1007/s11051-012-1100-5.

(96) Ye, F.; Laurent, S.; Fornara, A.; Astolfi, L.; Qin, J.; Roch, A.; Martini, A.; Toprak, M. S.; Muller, R. N.; Muhammed, M. Uniform Mesoporous Silica Coated Iron Oxide Nanoparticles as a Highly Efficient, Nontoxic MRI T(2) Contrast Agent with Tunable Proton Relaxivities. *Contrast Media Mol. Imaging* **2012**, *7*, 460–468, DOI:10.1002/cmmi.1473.

(97) Kim, J.; Kim, H. S.; Lee, N.; Kim, T.; Kim, H.; Yu, T.; Song, I. C.; Moon, W. K.; Hyeon, T. Multifunctional Uniform Nanoparticles Composed of a Magnetite Nanocrystal Core and a Mesoporous Silica Shell for Magnetic Resonance and Fluorescence Imaging and for Drug Delivery. *Angew. Chem. Int. Ed. Engl.* **2008**, *47*, 8438–8441, DOI:10.1002/anie.200802469.

(98) Alwi, R.; Telenkov, S.; Mandelis, A.; Leshuk, T.; Gu, F.; Oladepo, S.; Michaelian, K. Silica-Coated Super Paramagnetic Iron Oxide Nanoparticles (SPION) as Biocompatible Contrast Agent in Biomedical Photoacoustics. *Biomed. Opt. Express* **2012**, *3*, 2500–2509, DOI:10.1364/BOE.3.002500.

(99) LaConte, L. E. W.; Nitin, N.; Zurkiya, O.; Caruntu, D.; O'Connor, C. J.; Hu, X.; Bao, G. Coating Thickness of Magnetic Iron Oxide Nanoparticles Affects R2 Relaxivity. *J. Magn. Reson. Imaging* **2007**, *26*, 1634–1641, DOI:10.1002/jmri.21194.

(100) Tromsdorf, U. I.; Bigall, N. C.; Kaul, M. G.; Bruns, O. T.; Nikolic, M. S.; Mollwitz, B.; Sperling, R. A.; Reimer, R.; Hohenberg, H.; Parak, W. J.; *et al.* Size and Surface Effects on the MRI Relaxivity of Manganese Ferrite Nanoparticle Contrast Agents. *Nano Lett.* **2007**, *7*, 2422–2427, DOI:10.1021/nl071099b.

(101) El-Dakdouki, M. H.; Zhu, D. C.; El-Boubbou, K.; Kamat, M.; Chen, J.; Li, W.; Huang, X. Development of Multifunctional Hyaluronan-Coated Nanoparticles for Imaging and Drug Delivery to Cancer Cells. *Biomacromolecules* **2012**, *13*, 1144–1151, DOI:10.1021/bm300046h.

(102) Suzuki, M.; Bachelet-Violette, L.; Rouzet, F.; Beilvert, A.; Autret, G.; Maire, M.; Menager, C.; Louedec, L.; Choqueux, C.; Sabourel, P.; *et al.* Ultrasmall Superparamagnetic Iron Oxide Nanoparticles Coated with Fucoidan for Molecular MRI of Intraluminal Thrombus. *Nanomedicine (Lond).* **2014**, *10*, 73–87, DOI:10.2217/nnm.14.51.

(103) Lee, J.; Jung, M. J.; Hwang, Y. H.; Lee, Y. J.; Lee, S.; Lee, D. Y.; Shin, H. Heparin-Coated Superparamagnetic Iron Oxide for *in Vivo* MR Imaging of Human MSCs. *Biomaterials* **2012**, *33*, 4861–4871, DOI:10.1016/j.biomaterials.2012.03.035.

(104) Silva, A. K. A.; Letourneur, D.; Chauvierre, C. Polysaccharide Nanosystems for Future Progress in Cardiovascular Pathologies. *Theranostics* **2014**, *4*, 579–591, DOI:10.7150/thno.7688.

(105) Gupta, A. K.; Gupta, M. Cytotoxicity Suppression and Cellular Uptake Enhancement of Surface Modified Magnetic Nanoparticles. *Biomaterials* **2005**, *26*, 1565–1573, DOI:10.1016/j.biomaterials.2004.05.022.

(106) Chen, T.-J.; Cheng, T.-H.; Chen, C.-Y.; Hsu, S. C. N.; Cheng, T.-L.; Liu, G.-C.; Wang, Y.-M. Targeted Herceptin-Dextran Iron Oxide Nanoparticles for Noninvasive Imaging of HER2/neu Receptors Using MRI. *J. Biol. Inorg. Chem.* **2009**, *14*, 253–260, DOI:10.1007/s00775-008-0445-9.

(107) Nkansah, M. K.; Thakral, D.; Shapiro, E. M. Magnetic Poly(lactide-Co-Glycolide) and Cellulose Particles for MRI-Based Cell Tracking. *Magn. Reson. Med.* **2011**, *65*, 1776–1785, DOI:10.1002/mrm.22765.

(108) Pothayee, N.; Balasubramaniam, S.; Pothayee, N.; Jain, N.; Hu, N.; Lin, Y.; Davis, R. M.; Sriranganathan, N.; Koretsky, A. P.; Riffle, J. S. Magnetic Nanoclusters with Hydrophilic Spacing for Dual Drug Delivery and Sensitive Magnetic Resonance Imaging. *J. Mater. Chem. B. Mater. Biol. Med.* **2013**, *1*, 1142–1149, DOI:10.1039/C2TB00275B.

(109) Tong, S.; Hou, S.; Zheng, Z.; Zhou, J.; Bao, G. Coating Optimization of Superparamagnetic Iron Oxide Nanoparticles for High T2 Relaxivity. *Nano Lett.* **2010**, *10*, 4607–4613, DOI:10.1021/nl102623x.

(110) Basuki, J. S.; Jacquemin, A.; Esser, L.; Li, Y.; Boyer, C.; Davis, T. P. A Block Copolymer-Stabilized Co-Precipitation Approach to Magnetic Iron Oxide Nanoparticles for Potential Use as MRI Contrast Agents. *Polym. Chem.* **2014**, *5*, 2611, DOI:10.1039/c3py01778h.

(111) Nasongkla, N.; Bey, E.; Ren, J.; Ai, H.; Khemtong, C.; Guthi, J. S.; Chin, S.-F.; Sherry, A. D.; Boothman, D. A.; Gao, J. Multifunctional Polymeric Micelles as Cancer-Targeted, MRI-Ultrasensitive Drug Delivery Systems. *Nano Lett.* **2006**, *6*, 2427–2430, DOI:10.1021/nl061412u.

(112) Wang, C.; Ravi, S.; Martinez, G. V; Chinnasamy, V.; Raulji, P.; Howell, M.; Davis, Y.; Mallela, J.; Seehra, M. S.; Mohapatra, S. Dual-Purpose Magnetic Micelles for MRI and Gene Delivery. *J. Control. Release* **2012**, *163*, 82–92, DOI:10.1016/j.jconrel.2012.04.030.

(113) Prashant, C.; Dipak, M.; Yang, C.-T.; Chuang, K.-H.; Jun, D.; Feng, S.-S. Superparamagnetic Iron Oxide--Loaded Poly(lactic Acid)-D-Alpha-Tocopherol Polyethylene Glycol 1000 Succinate Copolymer Nanoparticles as MRI Contrast Agent. *Biomaterials* **2010**, *31*, 5588–5597, DOI:10.1016/j.biomaterials.2010.03.070.

(114) Karagoz, B.; Yeow, J.; Esser, L.; Prakash, S. M.; Kuchel, R. P.; Davis, T. P.; Boyer, C. An Efficient and Highly Versatile Synthetic Route to Prepare Iron Oxide Nanoparticles/nanocomposites with Tunable Morphologies. *Langmuir* **2014**, *30*, 10493–10502, DOI:10.1021/la502656u.

(115) Barrow, M.; Taylor, A.; Murray, P.; Rosseinsky, M. J.; Adams, D. J. Design Considerations for the Synthesis of Polymer Coated Iron Oxide Nanoparticles for Stem Cell Labelling and Tracking Using MRI. *Chem. Soc. Rev.* **2015**, DOI:10.1039/c5cs00331h.

(116) Chung, H. J.; Lee, H.; Bae, K. H.; Lee, Y.; Park, J.; Cho, S.-W.; Hwang, J. Y.; Park, H.; Langer, R.; Anderson, D.; *et al.* Facile Synthetic Route for Surface-Functionalized Magnetic Nanoparticles: Cell Labeling and Magnetic Resonance Imaging Studies. *ACS Nano* **2011**, *5*, 4329–4336, DOI:10.1021/nn201198f.

(117) Dias, A. M. G. C.; Hussain, A.; Marcos, A. S.; Roque, A. C. A. A Biotechnological Perspective on the Application of Iron Oxide Magnetic Colloids Modified with Polysaccharides. *Biotechnol. Adv.* **2011**, *29*, 142–155, DOI:10.1016/j.biotechadv.2010.10.003.

(118) Uthaman, S.; Lee, S. J.; Cherukula, K.; Cho, C.-S.; Park, I.-K. Polysaccharide-Coated Magnetic Nanoparticles for Imaging and Gene Therapy. *Biomed Res. Int.* **2014**, Article ID 959175.

(119) Thu, M. S.; Bryant, L. H.; Coppola, T.; Jordan, E. K.; Budde, M. D.; Lewis, B. K.; Chaudhry, A.; Ren, J.; Varma, N. R. S.; Arbab, A. S.; *et al.* Self-Assembling Nanocomplexes by Combining Ferumoxytol, Heparin and Protamine for Cell Tracking by Magnetic Resonance Imaging. *Nat. Med.* **2012**, *18*, 463–467, DOI:10.1038/nm.2666.

(120) Gutova, M.; Frank, J. A.; D'Apuzzo, M.; Khankaldyyan, V.; Gilchrist, M. M.; Annala, A. J.; Metz, M. Z.; Abramyants, Y.; Herrmann, K. A.; Ghoda, L. Y.; *et al.* Magnetic Resonance Imaging Tracking of Ferumoxytol-Labeled Human Neural Stem Cells: Studies Leading to Clinical Use. *Stem Cells Transl. Med.* **2013**, *2*, 766–775, DOI:10.5966/sctm.2013-0049.

(121) Jafari, A.; Salouti, M.; Shayesteh, S. F.; Heidari, Z.; Rajabi, A. B.; Boustani, K.; Nahardani, A. Synthesis and Characterization of Bombesin-Superparamagnetic Iron Oxide Nanoparticles as a Targeted Contrast Agent for Imaging of Breast Cancer Using MRI. *Nanotechnology* **2015**, *26*, 075101, DOI:10.1088/0957-4484/26/7/075101.

(122) Barrow, M.; Taylor, A.; Nieves, D. J.; Bogart, L. K.; Mandal, P.; Collins, C. M.; Moore, L. R.; Chalmers, J. J.; Lévy, R.; Williams, S. R.; *et al.* Tailoring the Surface Charge of Dextran-Based Polymer Coated SPIONs for Modulated Stem Cell Uptake and MRI Contrast. *Biomater. Sci.* **2015**, *3*, 608–616, DOI:10.1039/C5BM00011D.

(123) Banerjee, S. S.; Chen, D.-H. Magnetic Nanoparticles Grafted with Cyclodextrin for Hydrophobic Drug Delivery. *Chem. Mater.* **2007**, *19*, 6345–6349, DOI:10.1021/cm702278u.

(124) Zhang, L.; Yu, F.; Cole, A. J.; Chertok, B.; David, A. E.; Wang, J.; Yang, V. C. Gum Arabic-Coated Magnetic Nanoparticles for Potential Application in Simultaneous Magnetic Targeting and Tumor Imaging. *AAPS J.* **2009**, *11*, 693–699, DOI:10.1208/s12248-009-9151-y.

(125) Roque, A. C. A.; Bicho, A.; Batalha, I. L.; Cardoso, A. S.; Hussain, A. Biocompatible and Bioactive Gum Arabic Coated Iron Oxide Magnetic Nanoparticles. *J. Biotechnol.* **2009**, *144*, 313–320, DOI:10.1016/j.jbiotec.2009.08.020.

(126) Bicho, A.; Roque, A. C. A.; Cardoso, A. S.; Domingos, P.; Batalha, Í. L. *In Vitro* Studies with Mammalian Cell Lines and Gum Arabic-coated Magnetic Nanoparticles. *J. Mol. Recognit.* **2010**, *23*, 536–542, DOI:10.1002/jmr.1066.

(127) Suzuki, M.; Serfaty, J.-M.; Bachelet, L.; Beilvert, A.; Louedec, L.; Chaubet, F.; Michel, J.-B.; Letourneur, D. *In Vivo* Targeted Molecular Imaging for Activated Platelets by Mri Using USPIO-Fucoidan in Rat Abdominal Aortic Aneuryms Model. *J. Cardiovasc. Magn. Reson.* **2011**, *13*, P372, DOI:10.1186/1532-429X-13-S1-P372.

(128) Bhattacharya, D.; Das, M.; Mishra, D.; Banerjee, I.; Sahu, S. K.; Maiti, T. K.; Pramanik, P. Folate Receptor Targeted, Carboxymethyl Chitosan Functionalized Iron Oxide Nanoparticles: A Novel Ultradispersed Nanoconjugates for Bimodal Imaging. *Nanoscale* **2011**, *3*, 1653–1662, DOI:10.1039/c0nr00821d.

(129) Reddy, A. M.; Kwak, B. K.; Shim, H. J.; Ahn, C.; Lee, H. S.; Suh, Y. J.; Park, E. S. *In Vivo* Tracking of Mesenchymal Stem Cells Labeled with a Novel Chitosan-Coated Superparamagnetic Iron Oxide Nanoparticles Using 3.0T MRI. *J. Korean Med. Sci.* **2010**, *25*, 211–219, DOI:10.3346/jkms.2010.25.2.211.

(130) Kasten, A.; Grüttner, C.; Kühn, J.-P.; Bader, R.; Pasold, J.; Frerich, B. Comparative *in Vitro* Study on Magnetic Iron Oxide Nanoparticles for MRI Tracking of Adipose Tissue-Derived Progenitor Cells. *PLoS One* **2014**, *9*, e108055, DOI:10.1371/journal.pone.0108055.

(131) Jiang, J.-S.; Gan, Z.-F.; Yang, Y.; Du, B.; Qian, M.; Zhang, P. A Novel Magnetic Fluid Based on Starch-Coated Magnetite Nanoparticles Functionalized with Homing Peptide. *J. Nanoparticle Res.* **2009**, *11*, 1321–1330, DOI:10.1007/s11051-008-9534-5.

(132) Sivakumar, B.; Aswathy, R. G.; Nagaoka, Y.; Suzuki, M.; Fukuda, T.; Yoshida, Y.; Maekawa, T.; Sakthikumar, D. N. Multifunctional Carboxymethyl Cellulose-Based Magnetic Nanovector as a Theragnostic System for Folate Receptor Targeted Chemotherapy, Imaging, and Hyperthermia against Cancer. *Langmuir* **2013**, *29*, 3453–3466, DOI:10.1021/la305048m.

(133) Ma, H.; Qi, X.; Maitani, Y.; Nagai, T. Preparation and Characterization of Superparamagnetic Iron Oxide Nanoparticles Stabilized by Alginate. *Int. J. Pharm.* **2007**, *333*, 177–186, DOI:10.1016/j.ijpharm.2006.10.006.

(134) Ma, H. L.; Xu, Y. F.; Qi, X. R.; Maitani, Y.; Nagai, T. Superparamagnetic Iron Oxide Nanoparticles Stabilized by Alginate: Pharmacokinetics, Tissue Distribution, and Applications in Detecting Liver Cancers. *Int. J. Pharm.* **2008**, *354*, 217–226, DOI:10.1016/j.ijpharm.2007.11.036.

(135) Shen, F.; Li, A. A.; Gong, Y.-K.; Somers, S.; Potter, M. A.; Winnik, F. M.; Chang, P. L. Encapsulation of Recombinant Cells with a Novel Magnetized Alginate for Magnetic Resonance Imaging. *Hum. Gene Ther.* **2005**, *16*, 971–984, DOI:10.1089/hum.2005.16.971.

(136) Jo, J.; Aoki, I.; Tabata, Y. Design of Iron Oxide Nanoparticles with Different Sizes and Surface Charges for Simple and Efficient Labeling of Mesenchymal Stem Cells. *J. Control. Release* **2010**, *142*, 465–473, DOI:10.1016/j.jconrel.2009.11.014.

(137) Boeriu, C. G.; Springer, J.; Kooy, F. K.; Broek, L. A. M. van den; Eggink, G. Production Methods for Hyaluronan. *Int. J. Carbohydr. Chem.* **2013**, *2013*, DOI:10.1155/2013/624967.

(138) Bergman, K.; Elvingson, C.; Hilborn, J.; Svensk, G.; Bowden, T. Hyaluronic Acid Derivatives Prepared in Aqueous Media by Triazine-Activated Amidation. *Biomacromolecules* **2007**, *8*, 2190–2195, DOI:10.1021/bm0701604.

(139) Smejkalová, D.; Nešporová, K.; Huerta-Angeles, G.; Syrovátka, J.; Jirák, D.; Gálisová, A.; Velebný, V. Selective *in Vitro* Anticancer Effect of Superparamagnetic Iron Oxide Nanoparticles Loaded in Hyaluronan Polymeric Micelles. *Biomacromolecules* **2014**, *15*, 4012–4020, DOI:10.1021/bm501065q.

(140) Li, J.; He, Y.; Sun, W.; Luo, Y.; Cai, H.; Pan, Y.; Shen, M.; Xia, J.; Shi, X. Hyaluronic Acid-Modified Hydrothermally Synthesized Iron Oxide Nanoparticles for Targeted Tumor MR Imaging. *Biomaterials* **2014**, *35*, 3666–3677, DOI:10.1016/j.biomaterials.2014.01.011.

(141) Zhang, H.; Li, J.; Sun, W.; Hu, Y.; Zhang, G.; Shen, M.; Shi, X. Hyaluronic Acid-Modified Magnetic Iron Oxide Nanoparticles for MR Imaging of Surgically Induced Endometriosis Model in Rats. *PLoS One* **2014**, *9*, e94718, DOI:10.1371/journal.pone.0094718.

(142) Lee, Y.; Lee, H.; Kim, Y. B.; Kim, J.; Hyeon, T.; Park, H.; Messersmith, P. B.; Park, T. G. Bioinspired Surface Immobilization of Hyaluronic Acid on Monodisperse Magnetite Nanocrystals for Targeted Cancer Imaging. *Adv. Mater.* **2008**, *20*, 4154–4157, DOI:10.1002/adma.200800756.

(143) Yoo, M. K.; Park, I. Y.; Kim, I. Y.; Park, I. K.; Kwon, J.-S.; Jeong, H.-J.; Jeong, Y. Y.; Cho, C. S. Superparamagnetic Iron Oxide Nanoparticles Coated with Mannan for Macrophage Targeting. *J. Nanosci. Nanotechnol.* **2008**, *8*, 5196–5202, DOI:10.1166/jnn.2008.1118.

(144) Vu-Quang, H.; Muthiah, M.; Kim, Y.-K.; Cho, C.-S.; Namgung, R.; Kim, W. J.; Rhee, J. H.; Kang, S. H.; Jun, S. Y.; Choi, Y.-J.; *et al.* Carboxylic Mannan-Coated Iron Oxide Nanoparticles Targeted to Immune Cells for Lymph Node-Specific MRI *in Vivo*. *Carbohydr. Polym.* **2012**, *88*, 780–788, DOI:10.1016/j.carbpol.2012.01.067.

(145) Yoon, S. J.; Jun, S. Y.; Kwon, A. S.; Kang, S. H.; Jeong, Y. Y.; Park, I. K.; Cho, C. S.; Kim, Y. K.; Kim, W. J.; Namgung, R. MRI Contrast Agent Coated with Carboxylated Mannan and Method for Producing the Same. US 8961935 B2, February 24, 2015.

(146) Tsuchiya, K.; Nitta, N.; Sonoda, A.; Otani, H.; Takahashi, M.; Murata, K.; Shiomi, M.; Tabata, Y.; Nohara, S. Atherosclerotic Imaging Using 4 Types of Superparamagnetic Iron Oxides: New Possibilities for Mannan-Coated Particles. *Eur. J. Radiol.* **2013**, *82*, 1919–1925, DOI:10.1016/j.ejrad.2013.07.017.

(147) Guthi, J. S.; Yang, S.-G.; Huang, G.; Li, S.; Khemtong, C.; Kessinger, C. W.; Peyton, M.; Minna, J. D.; Brown, K. C.; Gao, J. MRI-Visible Micellar Nanomedicine for Targeted Drug Delivery to Lung Cancer Cells. *Mol. Pharm.* **2010**, *7*, 32–40, DOI:10.1021/mp9001393.

(148) Harris, J. M.; Chess, R. B. Effect of Pegylation on Pharmaceuticals. *Nat. Rev. Drug Discov.* **2003**, *2*, 214–221, DOI:10.1038/nrd1033.

(149) Liu, G.; Yang, H.; Zhang, X. M.; Shao, Y.; Jiang, H. MR Imaging for the Longevity of Mesenchymal Stem Cells Labeled with Poly-L-Lysine-Resovist Complexes. *Contrast Media Mol. Imaging* *5*, 53–58, DOI:10.1002/cmmi.362.

(150) Huang, H.; Xie, Q.; Kang, M.; Zhang, B.; Zhang, H.; Chen, J.; Zhai, C.; Yang, D.; Jiang, B.; Wu, Y. Labeling Transplanted Mice Islet with Polyvinylpyrrolidone Coated Superparamagnetic Iron Oxide Nanoparticles for *in Vivo* Detection by Magnetic Resonance Imaging. *Nanotechnology* **2009**, *20*, 365101, DOI:10.1088/0957-4484/20/36/365101.

(151) Babič, M.; Horák, D.; Trchová, M.; Jendelová, P.; Glogarová, K.; Lesný, P.; Herynek, V.; Hájek, M.; Syková, E. Poly(l-Lysine)-Modified Iron Oxide Nanoparticles for Stem Cell Labeling. *Bioconjug. Chem.* **2008**, *19*, 740–750, DOI:10.1021/bc700410z.

(152) Amemori, T.; Romanyuk, N.; Jendelova, P.; Herynek, V.; Turnovcova, K.; Prochazka, P.; Kapcalova, M.; Cocks, G.; Price, J.; Sykova, E. Human Conditionally Immortalized Neural Stem Cells Improve Locomotor Function after Spinal Cord Injury in the Rat. *Stem Cell Res. Ther.* **2013**, *4*, 68, DOI:10.1186/scrt219.

(153) Ju, S.; Teng, G.; Zhang, Y.; Ma, M.; Chen, F.; Ni, Y. *In Vitro* Labeling and MRI of Mesenchymal Stem Cells from Human Umbilical Cord Blood. *Magn. Reson. Imaging* **2006**, *24*, 611–617, DOI:10.1016/j.mri.2005.12.017.

(154) Horák, D.; Babič, M.; Jendelová, P.; Herynek, V.; Trchová, M.; Likavčanová, K.; Kapcalová, M.; Hájek, M.; Syková, E. Effect of Different Magnetic Nanoparticle Coatings on the Efficiency of Stem Cell Labeling. *J. Magn. Magn. Mater.* **2009**, *321*, 1539–1547, DOI:10.1016/j.jmmm.2009.02.082.

(155) Liu, G.; Wang, Z.; Lee, S.; Ai, H.; Chen, X. Design and Fabrication of N-Alkyl-Polyethylenimine-Stabilized Iron Oxide Nanoclusters for Gene Delivery. *Methods Enzymol.* **2012**, *509*, 263–276, DOI:10.1016/B978-0-12-391858-1.00009-5.

(156) Liu, G.; Xie, J.; Zhang, F.; Wang, Z.; Luo, K.; Zhu, L.; Quan, Q.; Niu, G.; Lee, S.; Ai, H.; *et al.* N-Alkyl-PEI-Functionalized Iron Oxide Nanoclusters for Efficient siRNA Delivery. *Small* **2011**, *7*, 2742–2749, DOI:10.1002/smll.201100825.

(157) Chen, Y.; Lian, G.; Liao, C.; Wang, W.; Zeng, L.; Qian, C.; Huang, K.; Shuai, X. Characterization of Polyethylene Glycol-Grafted Polyethylenimine and Superparamagnetic Iron Oxide Nanoparticles (PEG-G-PEI-SPION) as an MRI-Visible Vector for siRNA Delivery in Gastric Cancer *in Vitro* and *in Vivo*. *J. Gastroenterol.* **2013**, *48*, 809–821, DOI:10.1007/s00535-012-0713-x.

(158) Theumer, A.; Gräfe, C.; Bähring, F.; Bergemann, C.; Hochhaus, A.; Clement, J. H. Superparamagnetic Iron Oxide Nanoparticles Exert Different Cytotoxic Effects on Cells Grown in Monolayer Cell Culture versus as Multicellular Spheroids. *J. Magn. Magn. Mater.* **2015**, *380*, 27–33, DOI:10.1016/j.jmmm.2014.10.039.

(159) Patnaik, S.; Gupta, K. C. Novel Polyethylenimine-Derived Nanoparticles for *in Vivo* Gene Delivery. *Expert Opin. Drug Deliv.* **2013**, *10*, 215–228, DOI:10.1517/17425247.2013.744964.

(160) Mulens-Arias, V.; Rojas, J. M.; Pérez-Yagüe, S.; Morales, M. D. P.; Barber, D. F. Polyethylenimine-Coated SPION Exhibits Potential Intrinsic Anti-Metastatic Properties Inhibiting Migration and Invasion of Pancreatic Tumor Cells. *J. Control. Release* **2015**, *216*, 78–92, DOI:10.1016/j.jconrel.2015.08.009.

(161) Wong, J. E.; Gaharwar, A. K.; Müller-Schulte, D.; Bahadur, D.; Richtering, W. Magnetic Nanoparticle-Polyelectrolyte Interaction: A Layered Approach for Biomedical Applications. *J. Nanosci. Nanotechnol.* **2008**, *8*, 4033–4040.

(162) Schwarz, S.; Wong, J. E.; Bornemann, J.; Hodenius, M.; Himmelreich, U.; Richtering, W.; Hoehn, M.; Zenke, M.; Hieronymus, T. Polyelectrolyte Coating of Iron Oxide Nanoparticles for MRI-Based Cell Tracking. *Nanomedicine* **2012**, *8*, 682–691, DOI:10.1016/j.nano.2011.08.010.

(163) Wang, G.; Zhang, X.; Skallberg, A.; Liu, Y.; Hu, Z.; Mei, X.; Uvdal, K. One-Step Synthesis of Water-Dispersible Ultra-Small Fe3O4 Nanoparticles as Contrast Agents for T1 and T2 Magnetic Resonance Imaging. *Nanoscale* **2014**, *6*, 2953–2963, DOI:10.1039/c3nr05550g.

(164) Cruz, L. J.; Tacken, P. J.; Bonetto, F.; Buschow, S. I.; Croes, H. J.; Wijers, M.; de Vries, I. J.; Figdor, C. G. Multimodal Imaging of Nanovaccine Carriers Targeted to Human Dendritic Cells. *Mol. Pharm.* **2011**, *8*, 520–531, DOI:10.1021/mp100356k.

(165) Zhou, D.; Sun, Y.; Zheng, Y.; Ran, H.; Li, P.; Wang, Z.; Wang, Z. Superparamagnetic PLGA–iron Oxide Microspheres as Contrast Agents for Dual-Imaging and the Enhancement of the Effects of High-Intensity Focused Ultrasound Ablation on Liver Tissue. *RSC Adv.* **2015**, *5*, 35693–35703, DOI:10.1039/C5RA00880H.

(166) Chen, J.; White, S. B.; Harris, K. R.; Li, W.; Yap, J. W. T.; Kim, D.-H.; Lewandowski, R. J.; Shea, L. D.; Larson, A. C. Poly(lactide-Co-Glycolide) Microspheres for MRI-Monitored Delivery of Sorafenib in a Rabbit VX2 Model. *Biomaterials* **2015**, *61*, 299–306, DOI:10.1016/j.biomaterials.2015.05.010.

(167) Strohbehn, G.; Coman, D.; Han, L.; Ragheb, R. R. T.; Fahmy, T. M.; Huttner, A. J.; Hyder, F.; Piepmeier, J. M.; Saltzman, W. M.; Zhou, J. Imaging the Delivery of Brain-Penetrating PLGA Nanoparticles in the Brain Using Magnetic Resonance. *J. Neurooncol.* **2015**, *121*, 441–449, DOI:10.1007/s11060-014-1658-0.

(168) Wang, X.; Wei, F.; Liu, A.; Wang, L.; Wang, J.-C.; Ren, L.; Liu, W.; Tu, Q.; Li, L.; Wang, J. Cancer Stem Cell Labeling Using poly(L-Lysine)-Modified Iron Oxide Nanoparticles. *Biomaterials* **2012**, *33*, 3719–3732, DOI:10.1016/j.biomaterials.2012.01.058.

(169) Cengelli, F.; Maysinger, D.; Tschudi-monnet, F.; Montet, X.; Corot, C.; Petri-fink, A.; Hofmann, H.; Juillerat-jeanneret, L. Interaction of Functionalized Superparamagnetic Iron Oxide Nanoparticles with Brain Structures. **2006**, *318*, 108–116, DOI:10.1124/jpet.106.101915.micellar.

(170) Schulze, F.; Gramoun, A.; Crowe, L. A.; Dienelt, A.; Akcan, T.; Hofmann, H.; Vallé, J.-P.; Duda, G. N.; Ode, A. Accumulation of Amino-Polyvinyl Alcohol Superparamagnetic Iron Oxide Nanoparticles in Bone Marrow: Implications for Local Stromal Cells. *Nanomedicine* **2015**, *10*, 2139–2151, DOI:10.2217/nnm.15.62.

(171) Huang, J.; Bu, L.; Xie, J.; Chen, K.; Cheng, Z.; Li, X.; Chen, X. Effects of Nanoparticle Size on Cellular Uptake and Liver MRI with Polyvinylpyrrolidone-Coated Iron Oxide Nanoparticles. *ACS Nano* **2010**, *4*, 7151–7160, DOI:10.1021/nn101643u.

Chapter 2

Effects of phase transfer ligands on monodisperse iron oxide magnetic nanoparticles

Oleic acid coated iron oxide nanoparticles synthesized by thermal decomposition in organic medium are highly monodisperse but at the same time are unsuitable for biological applications. Ligand-exchange reactions are useful to make their surface hydrophilic. However, these could alter some structural and magnetic properties of the modified particles. Here we present a comprehensive study and comparison of the effects of employing either citric acid (CA) or *meso*-2,3-dimercaptosuccinic acid (DMSA) ligand-exchange protocols for phase transfer of monodisperse hydrophobic iron oxide nanoparticles produced by thermal decomposition of $Fe(acac)_3$ in benzyl ether. We show the excellent hydrodynamic size distribution and colloidal stability of the hydrophilic particles obtained by the two protocols and confirm that there is a certain degree of oxidation caused by the ligand-exchange. CA revealed to be more aggressive towards the iron oxide surface than DMSA and greatly reduced the saturation magnetization values and initial susceptibility of the resulting particles compared to the native ones. Besides being milder and more straightforward to perform, the DMSA ligand exchange protocol produces more chemically versatile MNP for further functionalization possibilities. This versatility is shown through the covalent linkage of gum Arabic onto MNP-DMSA using carboxyl and thiol based chemical routes and yielding particles with comparable properties.

Publications

Palma, S. I. C. J.; Marciello, M.; Carvalho, A.; Veintemillas-Verdaguer, S.; Morales, M. P.; Roque, A. C. A. *J. Colloid Interface Sci.* **2015**, *437*, 147–55.

Communications in conferences

Poster

Palma S.I.C.J.; Roque A.C.A., Towards an optimized preparation of negatively-charged SPION, 9th International Conference on the Scientific and Clinical Applications of Magnetic Carriers, Minneapolis, U.S.A (2012)

2.1. Introduction

Superparamagnetic iron oxide nanoparticles (SPION) have been gaining increased attention in the last decades due to their applications in environmental sciences, memory storage and, mainly, in biomedical and pharmaceutical sciences.[1,2] Superparamagnetism, large surface to volume ratio and biocompatibility are unique physical properties of iron oxide at the nanoscale that make it one of the most studied nanomaterials nowadays. There are several forms of iron oxide but the more explored ones are magnetite (Fe_3O_4) and maghemite (γ-Fe_2O_3) due to their improved magnetic properties and biocompatibility.[3] The different crystal structure of these two iron oxides influences the net spontaneous magnetization of the particles: at 300 K, 92-98 emu/g for magnetite, and 76-84 emu/g for maghemite.[4–6]

There are several methods to synthesize SPION, ranging between physical, chemical and biological methods. The most common are chemical methods and among those, co-precipitation is widely used to obtain larger amounts of hydrophilic nanoparticles. However, SPION produced by this method have a broad size distribution and tend to easily aggregate and become colloidally unstable.[7] This behavior is not desirable for most applications, as it is associated with wide size distributions, increased average hydrodynamic diameters and decreased surface to volume ratio. For example, regarding biomedical applications, the increase in size of the aggregates reduces the area available for grafting of bioactive molecules and compromises the biocompatibility and biodistribution of the administered particles.[2] Similarly, in the case of environmental remediation applications (e.g. removal of heavy metals from water), the formation of large agglomerates reduces the adsorbing area and particle transport becomes hampered, limiting the system efficiency.[8]

Up to now, the synthesis method that allows better control of sizes and produces the narrowest size distributions is the thermal decomposition of organometallic precursors of iron in organic solvents. The magnetic properties of SPION obtained by this route are enhanced in comparison with other methods due to their more crystalline structure. However, there is a limitation: the precursors and solvents are not biocompatible, and the resulting ferrofluids are only stable in hydrophobic media. Therefore, an intermediate step of phase transfer to aqueous media is required before any biological application.[3,7] There are two approaches for the phase transfer: adding an amphiphilic molecule that binds through hydrophobic interactions to the original surfactant layer and forms a micellar structure that encapsulates the magnetic cores,[9] or replacing the native hydrophobic surfactants by hydrophilic molecules that have higher affinity for iron.[10,11] This last process is called ligand-exchange and has been widely used[10,12–17] because it is a simple and effective method. The used ligands consist of an anchoring chemical group that binds to the surface of the SPION (e.g., carboxylic acid, phosphonic acid, dopamine) and a hydrophilic region that becomes exposed to the surrounding water molecules, affording

physiological stability and conjugation capability.[18] The anchoring group of the ligand is important as it is responsible for the stability of the new coating and also because it can influence the magnetic properties of the hydrophilic MNP.[19] Due to their small size and presence of multiple carboxylic groups that readily coordinate with iron, citric acid (CA)[10,13,16] and *meso*-2,3-dimercaptosuccinic acid (DMSA)[11,15,20–22] are two frequently used molecules in ligand-exchange procedures. Good colloidal stability is generally obtained in both cases but the overall effects of the process on structural and magnetic properties of the resulting particles, to our knowledge, have never been directly compared. Some studies claim no alteration of the saturation magnetization value (M_S) compared to the precursor hydrophobic particles[23] and others show consequences on the magnetization characteristics[11,24] but this comparison is often neglected.[10,13,16,22,25] Therefore, the benefits of using one ligand instead of the other are not clear. In this work, we present a comprehensive comparison between two ligand-exchange protocols that employ either citric acid or DMSA, discussing the effects of these two ligands on the colloidal and magnetic properties of SPION intended for biological and biomedical applications. We analyze hydrophobic SPION synthesized by the thermal decomposition method and the hydrophilic SPION resulting from the ligand exchange regarding their core size, hydrodynamic diameter and colloidal stability along with surface characterization by FTIR and evaluation of the magnetic properties by VSM. DMSA-modified MNP were finally coated with gum Arabic to show their chemical versatility, taking advantage of the carboxyl and thiol groups available at the particles surface.

2.2. Experimental Section

2.2.1. Materials

All chemicals were purchased from Sigma-Aldrich and used without ulterior purification.

2.2.2. Synthesis of hydrophobic magnetic nanoparticles (MNP-OA)

Hydrophobic magnetic nanoparticles were synthesized following Sun's method[9] with slight modifications. Briefly, iron tri(acetylacetonate) (2 mmol), 1,2-tetradecanediol (10 mmol), oleic acid (6 mmol), oleylamine (6 mmol), and benzyl ether (10 ml) were mixed and stirred magnetically under a constant flow of nitrogen. The mixture was heated to 200 °C at a rate of 3ºC/min and kept at 200°C for 2 h. Then, under a blanket of nitrogen, the mixture was heated to reflux (300°C) at a rate of 4.5ºC/min and kept in reflux for 1 h. The resultant black-colored mixture was cooled to room temperature by removing the heat source. Ethanol (about 20 ml) was added to the mixture, to precipitate the particles after which they were separated via

centrifugation (9000 rcf, 15 min). The supernatant was discarded and the pellet was re-dispersed in hexane (10 ml) in the presence of oleic acid (50 µl) and oleylamine (50 µl) with the aid of vortexing and sonication. Centrifugation (7000 rcf, 10 min) was then applied to remove any undispersed material. The pellet was discarded and the supernatant was precipitated with ethanol (about 20 ml), centrifuged (9000 rcf, 10 min) to remove the solvent and redispersed into hexane.

2.2.3. Phase transfer by ligand exchange with citric acid (MNP-CA)

Ligand-exchange using citric acid was performed following the protocol described by Lattuada *et al.*[10] MNP-OA (120 mg) were previously dried, and dispersed in a 50/50 mixture of 1,2-dichlorobenzene and N,N′-dimethylformamide (15 ml of total volume), to which 0.1 g of citric acid was added. The mixture was incubated in a rotating agitator at 100ºC for approximately 18 h. MNP-CA were precipitated by the addition of diethyl ether (about 40 ml) and recovered by magnetic separation. The particles were redispersed in acetone and reprecipitated by means of a permanent magnet three times to remove all traces of free citric acid. After the final magnetic precipitation, traces of acetone were removed with a nitrogen flow and the particles were re-dispersed in milliQ water and filtered through a 0.1 µm pore membrane.

2.2.4. Phase transfer by ligand exchange with *meso*-2,3-dimercaptosuccinic acid (MNP-DMSA)

A standard ligand-exchange protocol[15] was used to replace oleic moieties by DMSA. MNP-OA (50 mg Fe_3O_4) were precipitated from the hexane suspension by adding ethanol and applying a permanent magnet several times. The supernatant was discarded. After the final precipitation, the MNP-OA were re-dispersed in toluene (20 ml), added to a solution of DMSA (90 mg) in DMSO (5 ml) and mixed with sonication. The mixture was incubated at room temperature for 48 h in a rotating agitator. After the reaction, the translucent solvent containing the oleic acid and oleylamine was discarded and the black particles (MNP-DMSA) attached to the walls of the flasks were re-dispersed in ethanol with sonication and vortexing. This mixture was centrifuged and re-dispersed in ethanol several times to clean the particles. Finally, the MNP-DMSA were re-dispersed in milliQ water, basified to pH 10 with sodium hydroxide and dialyzed against milliQ water for about 48 h. Filtration through a 0.1 µm pore membrane and adjustment of the pH to 7 was carried out as a final step.

2.2.5. Preparation of MNP-DMSA-Cyst-GA

MNP-DMSA were first aminated with cysteamine hydrochloride (Cyst) and then covalently bond to carboxylic groups of GA. For that, MNP-DMSA thiol groups were activated with 2,2'-dithiodipyridine (DTDP) as follows. MNP-DMSA (15 mg of Fe_3O_4) were precipitated from the stock solution by centrifugation and re-dispersed in a previously filtered saturated solution of DTDP (15 ml) in phosphate buffer (10 mM, pH 8). The activation reaction continued overnight in a rotating agitator at room temperature. The suspension was then centrifuged (9000 rcf, 20 min) and the unreacted DTDP in the supernatant removed. The precipitated particles were redispersed in a solution of cysteamine (15 ml, 120 mM) in phosphate buffer (10 mM, pH 8) with sonication and vortex and incubated for approximately 5 h in a rotating agitator at room temperature. To remove unreacted cysteamine, dialysis was performed (48 h). Finally, the MNP-DMSA-Cyst were precipitated by centrifugation (9000 rcf, 10 min) and redispersed in 1 ml of phosphate buffer (10 mM, pH 8). Covalent coupling of GA to MNP-DMSA-Cyst was performed using N-hydroxysuccinimide (NHS) / N-(3-dimethylaminopropyl)-N'-ethyl-carbodiimide hydrochloride (EDC) chemistry. In order to activate the carboxyl groups of GA, NHS and EDC were added to an aqueous solution of GA (45 ml, 10 mg/ml) at concentrations of 100 mM and 20 mM, respectively. The pH was adjusted to 4.5 and the mixture was left to incubate for 1.5 h under magnetic stirring. After this, MNP-DMSA-Cyst were added dropwise to the activated GA with sonication using an ultra-sound bath and the pH was adjusted to 7.5 to promote the covalent coupling. This mixture was incubated overnight in rotating agitator at room temperature and finally MNP-DMSA-Cyst-GA were washed by several centrifugations (9000 rcf, 10 min) and re-dispersed in milliQ water with sonication and vortexing.

2.2.6. Preparation of MNP-DMSA-GA

MNP-DMSA were coated with GA by covalent bond formation between GA amine groups with MNP-DMSA carboxylic groups. NHS and EDC were added to 8 ml of an aqueous solution of MNP-DMSA (~1 mg/ml Fe_3O_4, pH 4.5) at the concentration of 100 mM and 20 mM respectively to activate DMSA carboxylic acid groups. The pH was carefully monitored to be around 4.5 and the activation reaction continued for 1.5 h in a rotating agitator at room temperature. The activated MNP-DMSA were, then, added dropwise to a solution of GA (36 ml, 10 mg/ml) in phosphate buffer (5 mM, pH 8), with sonication. The pH of the mixture was adjusted to 8 and the reaction continued in a rotating agitator overnight at room temperature. MNP-DMSA-GA were recovered by applying several centrifugations (9000 rcf, 20 min) and replacing the supernatant with milliQ water.

2.2.7. Characterization of magnetic nanoparticles

Particle size and shape were characterized by Transmission Electron Microscopy (TEM) using a 100-kV JEOL JEM1010 microscope equipped with a Gatan Orius 200 SC digital camera. A drop of dilute particle suspension in hexane (MNP-OA) or in water (MNP-CA, MNP-DMSA, MNP-DMSA-Cyst-GA and MNP-DMSA-GA) was placed on a carbon-coated copper grid and dried at 50ºC before observation. The average particle core diameter was calculated by measuring about 200 particles for each sample, using ImageJ Software (National Institutes of Health, USA). Hydrodynamic size and zeta potential of the particles were characterized by Dynamic Light Scattering (DLS) using a Nanosizer ZS (Malvern) and diluted water dispersions of particles (about 0.5 mg/ml) at pH 7. The mean value of the volume-weighted size distribution was used as hydrodynamic diameter (d_h). The zeta potential (ζ-potential) variation with pH was measured in a 0.01 M KNO_3 solution, whereas HNO_3 or KOH solutions were used for pH adjustment. Inductively coupled plasma atomic emission spectroscopy (ICP-AES) (Horiba Jobin-Yvon, Ultima) was used to determine the iron and sulfur content of the MNP samples. Fourier transform infrared (FTIR) spectra were acquired using a Nicolet 20 SXC FTIR to confirm the iron oxide phase and the nature of the coating. IR spectra of the MNP were recorded between 4000 cm^{-1} and 250 cm^{-1}. Samples were prepared by diluting 2% iron oxide powder in KBr (w/w) and pressing it into a pellet.

The magnetic properties of the samples were evaluated using a vibrating sample magnetometer (VSM) (MagLab VSM, Oxford Instruments). The samples were analyzed dispersed in hexane (MNP-OA) or water (all the other samples), in frozen state. Magnetization loops were measured at 200 K (for MNP-OA) and 250 K (for the other samples) and corrected by subtracting the diamagnetic contribution of the dispersants and the sample holder. The saturation magnetization at the maximum field was normalized to the gram of iron oxide (Fe_3O_4 for MNP-OA and Fe_2O_3 for the remaining particles, as supported by FTIR analysis). The apparent particle magnetic diameter (d_{Mag}) was obtained using the magnetization loops (M(H)) and Chantrell's equation (eq. 2.1), derived for non-interacting magnetic nanoparticles and a log-normal distribution of particle sizes:[26]

$$d_{Mag} = \left[\frac{18 k_B T}{\pi M_S} \sqrt{\frac{\chi_{ini}}{3 m_S} \frac{1}{H_0}} \right] \qquad (2.1)$$

where m_S and M_S are the saturation magnetization of the nanoparticles and the bulk phase of magnetite (or maghemite), respectively, χ_{ini} is the initial susceptibility, calculated at low field, in the region where the magnetization varies linearly with the applied field, and $1/H_0$ is obtained by extrapolating M to zero at high fields, in the region where the relationship between M and 1/H is a straight line.

Temperature dependent zero-field cooling (ZFC) and field cooling (FC) magnetization measurements were performed by cooling the samples to 5 K under a zero or a 100 Oe magnetic field, respectively. Then, the magnetization was measured while the samples were heated (3 K/min) to 250 K under a 100 Oe field.

The efficiency of MNP-DMSA-Cyst-GA and MNP-DMSA-GA as MRI contrast agents was evaluated in a 7 T NMR Brucker Avance III Spectrometer at 25ºC. Samples were prepared with milliQ water at different iron concentrations (0, 0.1, 0.2, 0.4, 0.5, 0.6, 0.8 and 1 mM), placed in standard 5 mm glass tubes and sonicated for 30 min before the measurements of longitudinal and transverse relaxation rates ($R_1=1/T_1$ and $R_2=1/T_2$) T_1 was measured using an inversion recovery sequence with TR ranging from 3 to 10 s. T_2 was measured using a Call-Purcell-Meiboom-Gill sequence with TE of 1 ms and the number of echoes needed to cover a time interval of about 10 times T_2. R_1 and R_2 were plotted against iron concentration and a linear fitting of the data was performed. The slopes of lines are the longitudinal (r_1) and transverse (r_2) relaxivities.

2.3. Results and Discussion

2.3.1. Size and colloidal stability

Monodisperse magnetic nanoparticles with cores of 7.9 ± 1.1 nm were obtained through the thermal decomposition of iron acetylacetonate in benzyl ether at 300ºC in the presence of oleylamine and oleic acid. These particles (MNP-OA) are hydrophobic and therefore, very stable in non-polar organic media, such as hexane. However, for biomedical applications, dispersion in aqueous media is of uttermost importance. Ligand-exchange method was successful to stabilize the prepared MNP in water, using either citric acid (CA) or *meso*-2,3-dimercaptosuccinic acid (DMSA). TEM images (Figure 2.1 A-C) show that in both cases MNPs keep their shape and individuality after ligand exchange reaction. No evident aggregation is observed although distribution in the TEM grid changes with the solvent, from non-polar to polar, showing an increase in assembling disorder. Core diameters of 7.6 ± 1.1 nm and 7.1 ± 1.4 nm were obtained for MNP-CA, and MNP-DMSA, respectively, showing that the change of ligand at the surface causes a slight decrease on the average size of the nanoparticle cores (4% for MNP-CA and 10% for MNP-DMSA). This decrease may be explained by the release of ferrous ions from the iron oxide surface to solution which leads to partial nanoparticle dissolution during the ligand exchange reaction. Particle dissolution is a result of the chelating effect of CA and DMSA towards iron oxide and was reported previously in the literature.[21,25,27] Nevertheless, the diameters remain inside the range of sizes of the native MNP-OA. In terms of effective size, the

exchange of ligand at the surface of MNP-OA (d_h = 10.5 ± 0.8 nm) increases the hydrodynamic diameter of the particles, being the increase larger for MNP-CA (d_h = 18.5 ± 4.2) than for MNP-DMSA (d_h = 14.9 ± 3.4 nm) (Figure 2.1 D). In general, the reproducibility of the protocols is similar, since the variability of the resultant d_h around the average is comparable (26% for MNP-CA and 22% for MNP-DMSA). Polydispersity is also identical for both protocols (pdI = 0.27 ± 0.08 for MNP-CA and pdI = 0.31 ± 0.06 for MNP-DMSA) and their values fall inside the error bar of each other.

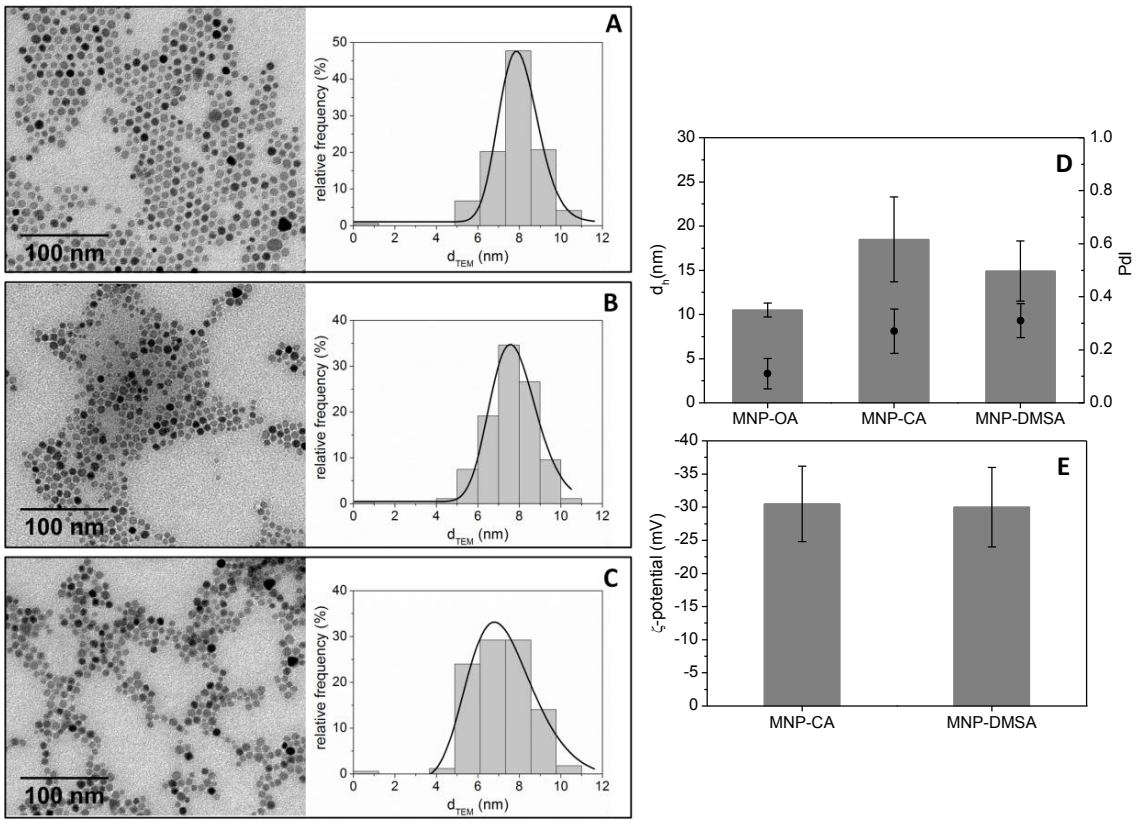

Figure 2.1. Morphology, size and zeta potential of the hydrophobic and hydrophilic nanoparticles. Representative TEM images and core size distribution for (A) MNP-OA, (B) MNP-CA and (C) MNP-DMSA (full line represents the log-normal fitting). Inter-batch variability of (D) hydrodynamic diameter (bars) and polydispersity index (dots) and (E) zeta potential. (n = 8 batches, for figures D and E)

Both citric acid and DMSA are hydrophilic small molecules with high affinity for iron oxide surfaces. The presence of multiple carboxyl groups in these molecules (three in citric acid and two in DMSA) makes them very reactive towards the MNP surface due to the strong interactions that the carboxyl groups are known to form with the iron groups at the MNP surface.[10,28] This property allows the replacement of the oleic hydrophobic moieties on MNP-OA through ligand-exchange reaction. Carboxyl (and thiol) groups not involved in the adsorption remain free at the surface of the particles and are responsible for their hydrophilic character and

colloidal stability in aqueous phase.[24] Therefore, after the ligand-exchange reaction, the average zeta potential of the particles is negative, with a value of -30 mV and around 20% variability when measured in water milliQ, at pH between 6 and 7 (Figure 2.1 E). This observation supports the presence of negatively charged groups at the surface of MNP-CA and MNP-DMSA (free carboxylic acid and thiol groups). As a visible consequence, both kinds of particles are very stable in water dispersion for months. They form a translucent colloid, for which is difficult to magnetically isolate the particles. In fact, the colloid moves as a whole when in presence of a permanent magnet. Noteworthy, when the variation of zeta potential with pH is measured under a 0.01 M ionic strength (Figure 2.2 A), MNP-DMSA proved to be more stable than MNP-CA. In fact MNP-CA zeta potential value decreased to around -20 mV, while for MNP-DMSA this value remained close to -30 mV in the pH range from 3 to 10, probably due to the net negative charge of undissociated thiols groups. Further stabilization of the ligand shells is attained through intermolecular disulfide cross-linkages between the ligands under ambient conditions.[20,21] This characteristic may be important for maintenance of the stability over a large range of pH.

2.3.2. Surface Chemistry by FTIR

To get further insight on MNP surface chemistry, samples were characterized by FTIR spectroscopy. Figure 2.2 B shows the spectra of free citric acid and DMSA together with the spectra of the prepared MNP, confirming the interchange of the MNP capping molecules. Before the ligand-exchange (MNP-OA), the IR spectrum presents a strong absorption band around 3000 cm^{-1} (C-H stretching modes) due to oleic acid and oleylamine chains.[24] It is also visible a strong and broad peak around 3400 cm^{-1} due to –OH and $–NH_2$ vibrations.[10] After the ligand-exchange, these bands (in particular the C-H band) become much weaker and new well defined bands at 1615 cm^{-1} and 1390 cm^{-1}, typical from asymmetric and symmetric stretching of carbonyl groups, respectively, appear in both MNP-CA and MNP-DMSA. In other words, the sharp carbonyl absorption bands present around 1700 cm^{-1} in DMSA and at 1700 cm^{-1} and 1750 cm^{-1} in citric acid shifted to lower frequencies because the ligands are bound to the particles and their carboxyl group is dissociated and coordinated with the iron oxide surface. Given the large splitting between the COO^- bands, the carboxylate group appears to be bound to iron through a monodentate interaction.[29] The IR bands characteristic of thiol (2250 – 2600 cm^{-1}) or disulfide groups (500-540 cm^{-1}) are not evident in the MNP-DMSA FTIR spectrum. However, by ICP it was possible to identify sulfur and quantify the S/Fe ratio in the samples of MNP-DMSA and confirm the presence of 0.2 ± 0.05 mg (DMSA) / mg (Fe) in MNP-DMSA.

The bands in the region of 400 cm^{-1} and 600 cm^{-1}, that correspond to the vibrations of Fe-O bonds in the spinel structure of magnetite,[24] present sharper peaks in the spectra of the

hydrophilic particles than in the spectra of MNP-OA. The appearance of doublets and shoulders is attributed to the higher number of modes of vibration of Fe-O bonds associated to a higher degree of oxidation of the iron oxide in MNP-CA and MNP-DMSA as compared to MNP-OA, i.e., presence of maghemite besides magnetite. The presence of a doublet in the 600 cm^{-1} region for MNP-CA is in accordance with the observed reddish color of the MNP-CA aqueous suspensions and washing supernatants, indicative of oxidation. This finding was also reported by other groups[10,16] and attributed to the strong reactivity of citric acid towards iron oxide, due to its three carboxyl groups, and to the high temperature (100ºC) at which the ligand exchange with citric acid is performed. These two factors promote the removal of iron ions from the surface of the particles when the native ligands are replaced by the citrate. The oxidation reported by FTIR is in accordance with the core size decrease observed for MNP-CA and MNP-DMSA.

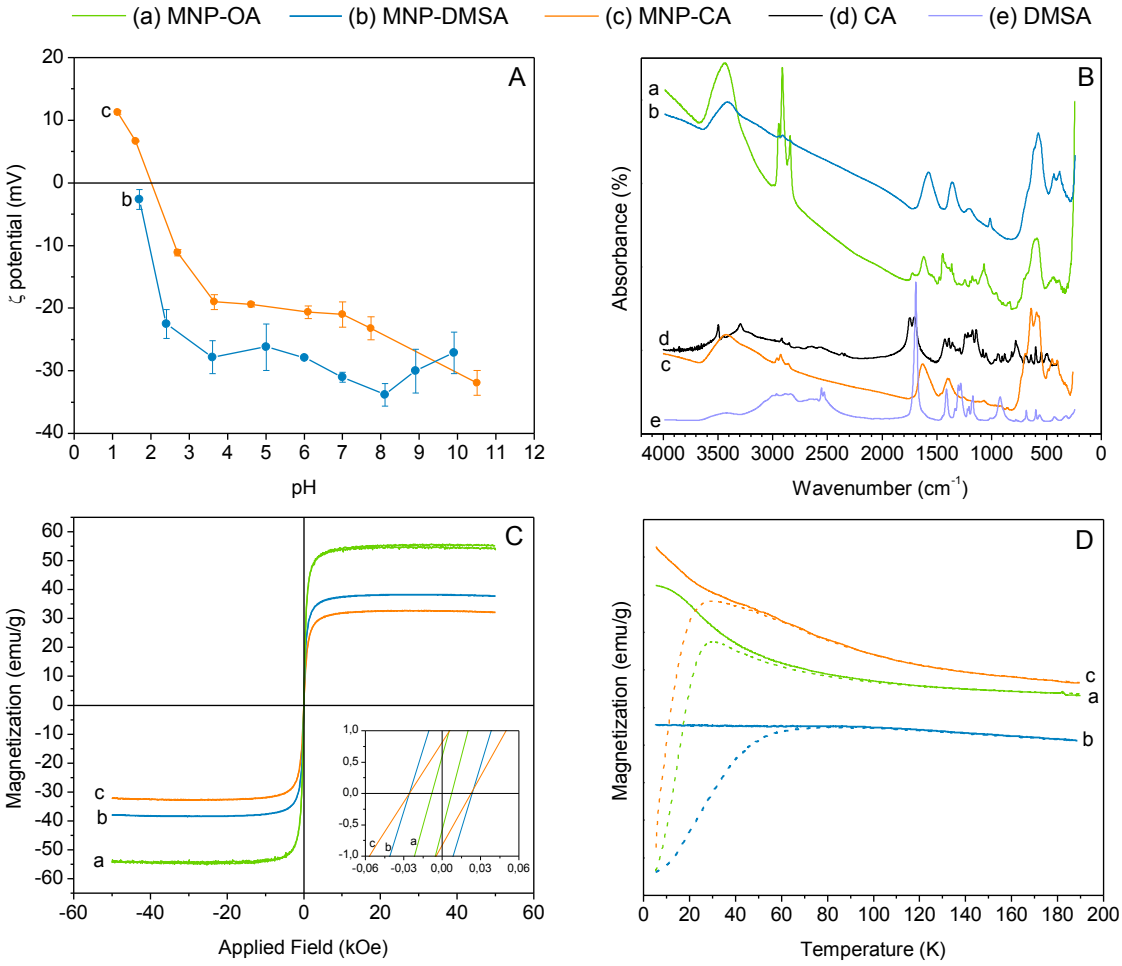

Figure 2.2. Surface and magnetic properties of the hydrophobic and hydrophilic nanoparticles. (A) variation of zeta potential with pH; (B) FTIR spectra; (C) Magnetization loops at RT (250 K for MNP-CA and MNP-DMSA and 200 K for MNP-OA); (D) ZFC/FC curves (dashed line: ZFC; solid line: FC); a: MNP-OA, b: MNP-DMSA, c: MNP-CA, d: CA, e: DMSA.

2.3.3. Magnetic properties

Figure 2.2 C and Figure 2.2 D show that the prepared nanoparticles are superparamagnetic at room temperature (RT). The magnetization curves, in Figure 2.2 C, are described by the Langevin function and do not present hysteresis for the three samples, as it is characteristic of superparamagnetic nanoparticles;[2,7] only a negligible value (less than 25 Oe) is observable, that is attributed to the remanent field of the VSM coils.

Besides this, the blocking temperature (T_B), which coincides with the maximum of the ZFC curves (Figure 2.2 D) and represents the threshold between ferromagnetic and superparamagnetic regime for particles presenting a monodisperse size distribution,[30] is far below RT for both hydrophobic and hydrophilic MNP (T_B = 29 K for MNP-OA and MNP-CA; T_B = 65 K for MNP-DMSA). Therefore, at RT, the particles are already in the superparamagnetic regime, as corroborated by the magnetization curves.

The narrow width of the ZFC curve indicates that the "magnetic volume" distribution of MNP-OA and MNP-CA is narrow,[31] in accordance to what is seen from TEM images (Figure 2.1 A and Figure 2.1 B). The rapidly increasing FC curve for temperatures below T_B in MNP-OA and MNP-CA is typical of a sample constituted by non-magnetically interacting particles, which, in the case of MNP-OA may be due to the oleic surfactant layer, that keeps particles sufficiently apart and prevents magnetic interactions between them.[31,32] In the case of MNP-CA, the particles present a larger hydrodynamic diameter associated to the formation of aggregates but citric acid seems to reduce interactions between particles within the aggregates. In contrast, the ZFC curve of MNP-DMSA presents a slightly wider peak anticipating a wider distribution of particle sizes, which is corroborated by the core size distributions obtained from TEM pictures. Also, the flat FC curve below T_B for MNP-DMSA, indicates the existence of magnetic dipole inter-particle interactions within the aggregates.[33] A possible justification may be the establishment of inter-particle disulfide bonds, which contributes to a shortening of the distance between the particles' magnetic cores and thus, increased magnetic interactions.

Magnetization loops show that there is a reduction of the saturation magnetization (M_S) values from MNP-OA (M_S = 54 emu/g) to MNP-DMSA (M_S = 38 emu/g) and MNP-CA (M_S = 33 emu/g). The lower M_S of MNP-OA compared to bulk magnetite value (M_S magnetite = 92-98 emu/g) [4–6] was expected due to the well-known nanoscale size effects: the magnetic behavior of the magnetic moments at the surface is different from those in the core, leading to an overall reduction of the net particle magnetic moment.[34] A much higher disorder of spins is present at the surface than in the core. Several factors may contribute to justify the decrease in saturation magnetization after the ligand-exchange reaction. First, core size reduction (4% for MNP-CA and 10% for MNP-DMSA) implies larger surface canting. Secondly, oxidation of magnetite to the less magnetic maghemite (M_S, maghemite = 76-84 emu/g)[4–6] also contributes negatively to the

net magnetic moment. The literature reports M_S post-oxidation decreases (at RT) of between 5% and 33%.[6,11,24] In addition, the removal of surface iron ions that takes place during ligand exchange and the formation of new bonds with the ligands may further contribute to decrease the overall magnetic moment of the particle.[35,36] In this work, we have observed a M_S reduction of 39% for MNP-CA and 30% for MNP-DMSA. To understand this change, all the previously mentioned factors have to be taken in account. Thus, it is clear that M_S reduction does not relate only with core size variation. For MNP-CA, besides particle dissolution, a larger degree of oxidation of the material (supported by FTIR and nanoparticle color) and higher surface magnetic disorder also contribute to the lower M_S value compared to the precursor particles (MNP-OA) and MNP-DMSA. As expected for SPION produced by the thermal decomposition method, the magnetic diameters estimated from Chantrell's equation (Table 2.1) approach the physical diameter measured in TEM images.[24] The slightly lower values of d_{Mag} compared to d_{core} in MNP-OA and MNP-CA suggest a core-shell structure, where the magnetic core is surrounded by a layer of less magnetic (or nonmagnetic) material, showing typical spin canting phenomenon. In contrast, for MNP-DMSA sample d_{Mag} is identical to d_{core}, in accordance with its superior M_S. DMSA coordination with iron oxide seems to prevent surface disorganization. Regarding the initial susceptibility χ_{ini}, which is the slope of the magnetization curve at low field, MNP-CA present the lowest value (Table 2.1), meaning that are more resistant to magnetization directionalization,[6] i.e. a larger field needs to be applied in order to promote magnetic moment reversal inside the particle until saturation is attained.

2.3.4. Comparison of ligand-exchange protocols

The ligand-exchange is a crucial step for the stabilization of monodisperse MNP in aqueous media. It is one of the most employed methods to obtain monodisperse MNPs for biomedical applications and its advantages are related to the ability to maintain the size distribution and the magnetic properties of the precursor hydrophobic particles, preventing aggregation through repulsive electrostatic interactions between particles.

Regarding size and colloidal stability, when compared to MNP-CA, MNP-DMSA present lower hydrodynamic size and better colloidal stability in low salt conditions (Figure 2.2 and Table 2.1). It was observed that the harsher reaction conditions (higher temperature and prolonged reaction time) needed for the CA ligand-exchange cause a larger degree of oxidation in the resultant particles, which leads to lower magnetic saturation magnetization than in MNP-DMSA. In accordance with this observation, Song *et al.*[25] showed that in a temperature driven ligand-exchange reaction, prolonging the reaction time was sufficient to decrease the M_S by 24%. CA, by itself, is a stronger iron chelating agent than DMSA due to the presence of three carboxylate

groups against the two in DMSA. On top of that, the higher temperature further enhances CA aggressivity towards iron oxide surface.

Table 2.1. Summary of size, zeta potential and magnetic characterization results for the hydrophobic (MNP-OA) and hydrophilic (MNP-CA and MNP-DMSA).

	Size and colloidal properties				***Magnetic Properties***			
Sample	**d_{core} (TEM)[a] (nm)**	**d_h (DLS)[b] (nm)**	**PdI[b]**	**ζ–potential[b] (mV)**	**d_{Mag}[c] (nm)**	**M_S[c] (emu/g)**	**χ_{ini}[c] (10^{-2} emu/g.Oe)**	**T_B[c] (K)**
MNP-OA	7.9 (1.1)	10.5 (0.8)	0.11	--	6.5	54	577	29
MNP-CA	7.6 (1.1)	18.5 (4.8)	0.27	-30.5 (6.0)	6.5	33	261	29
MNP-DMSA	7.1 (1.4)	14.9 (3.4)	0.31	-30.0 (6.0)	7.0	38	447	65

standard deviation is represented within brackets; [a] average and standard deviation of the core size distribution for one representative measurement; [b] average value of 8 batches; [c] value of one representative measurement.

Although MNP-DMSA present a higher blocking temperature and a wider magnetic size distribution compared to MNP-CA, the compromise between better saturation magnetization, lower effective size and improved colloidal stability makes the DMSA ligand-exchange method a more promising technique regarding the size and magnetic properties. Besides these, there are extra advantages of using DMSA. For surface characterization, the DMSA coating offers the possibility of being readily quantified by ICP-AES, though the determination of the S/Fe ratio in the samples. Typically TGA is used for this purpose but requires a lot more sample and is more time consuming. For example, in this work we have obtained 2 ± 0.6 μmol(S)/mg(Fe), that corresponds to 0.7 ± 0.2 μmol(DMSA)/mg(Fe_2O_3). With this data, and taking in account that the particles are spherical with 7 nm diameter (Figure 2.1 A) and the density of Fe_2O_3 is 4.89 g/cm^3, a ratio of 370 (±120) molecules of DMSA per particle was estimated. Concerning particle functionalization, the carboxyl and thiol groups remaining free at the surface of MNP-DMSA provide versatility to use different chemistries to graft molecules bearing complementary groups, while MNP-CA only has the carboxylic group available. Finally, the DMSA ligand-exchange protocol is more straightforward and ambient/economy-friendly, as it does not require heating at 100ºC. The advantages here reported for DMSA ligand-exchange protocol, are in accordance with the fact that research works based on DMSA ligand-exchange are more frequent than citric acid based ones. In addition, the protocols that employ citric acid are more complex than the one here explored, involving 2-step reactions.[13,22]

2.3.5. Exploring the chemical versatility of MNP-DMSA

To test the possibilities of chemical binding to MNP-DMSA, a proof-of-concept experiment was carried out where two chemical routes were employed to covalently bind the biopolymer gum Arabic (GA) onto the MNP-DMSA. Gum Arabic was used due to its proven properties as a coating agent for SPIONs[37,38] and also due to its composition which renders more than one chemical group for surface functionalization. One route uses cysteamine as a linker between MNP-DMSA and GA while the other directly couples GA to MNP-DMSA (Figure 2.3 A). Cysteamine has both thiol and amine groups, therefore, the strategy consisted in using DTDP to promote the formation of disulfide bonds with the thiol groups of DMSA and afterwards employing EDC/NHS chemistry to promote the formation of an amide bond between the amine groups of cysteamine and the carboxylate groups of GA. The second strategy makes use of the carboxylate groups from DMSA and the amines of GA where the formation of amide bond between these groups is promoted also using EDC and NHS.

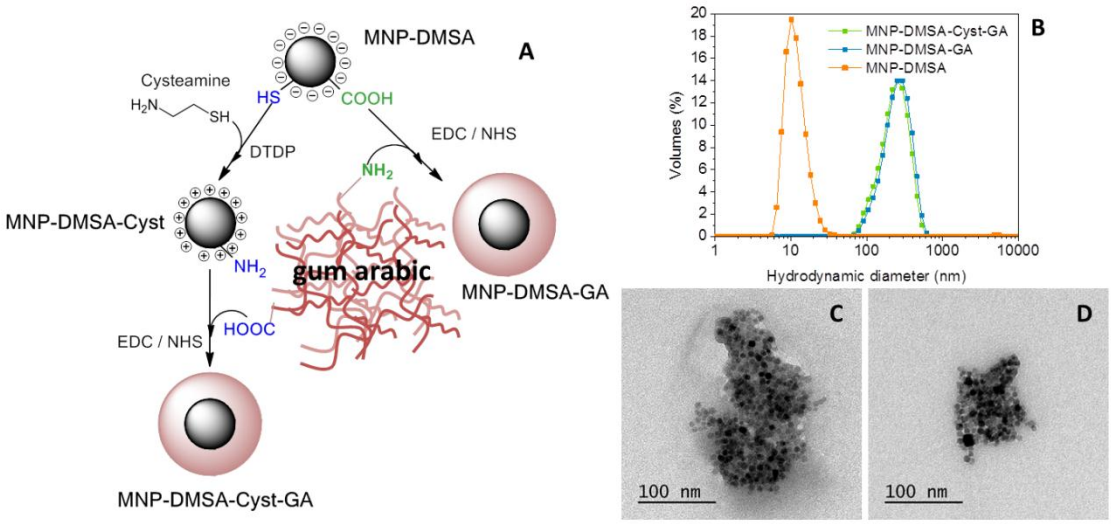

Figure 2.3. MNP-DMSA functionalization possibilities using gum Arabic as model biomolecule. (A) schematic representation of the two chemical approaches tested; (B) distribution of hydrodynamic diameters at pH 7 in water; (C) TEM image of MNP-DMSA-Cyst-GA; (D) TEM image of MNP-DMSA-GA.

Both chemical routes proved to be successful to coat MNP-DMSA with GA via covalent bonds and the resultant particle aggregates are very similar in their morphology, size, surface chemistry, colloidal and magnetic properties. The high molecular weight and highly branched character of GA promotes the formation of aggregates of around 250 nm (Figure 2.3 B and Table 2.1), composed by multiple magnetic cores of MNP-DMSA involved in a shell of GA, which is visible in the TEM images (Figure 2.3 C and Figure 2.3 D).

Figure 2.4 A shows that amination of MNP-DMSA with cysteamine was successful as the isoelectric point changes from very acid in MNP-DMSA (less than 2) to close to 6 in MNP-

DMSA-Cyst, indicating the presence of free amine groups at the surface of the particles. Afterwards, by coupling GA through EDC/NHS chemistry, it was possible to re-stabilize the particles at physiological pH. It is interesting to note that the zeta potential profile *vs* pH of MNP-DMSA-Cyst-GA is practically the same as for MNP-DMSA-GA, which means that the coating of MNP-DMSA with GA through the carboxylate moieties of the MNP-DMSA was also successful.

The success of the coupling is confirmed by FTIR analysis (Figure 2.4 B) as the characteristic band of GA, located at 1036-1071 cm^{-1} and due to C-O stretching vibrations,[39] is present in both MNP-DMSA-Cyst-GA and MNP-DMSA-GA spectra. An absorption band resembling amide I band, attributed to C=O bond stretching vibrations,[40] is present at around 1635 cm^{-1} in MNP-DMSA-Cyst-GA and MNP-DMSA-GA spectra. There is also a shoulder-like band at 1530-1540 cm^{-1} that resembles the amide II band, is associated with the N-H bond bending, C-N and C-C stretching vibrations. This suggests the presence of amide bonds resultant from the covalent bond between the ligands at the surface of the particles (Cysteamine or DMSA) and GA, although a contribution from chemical crosslinking of GA chains between themselves may also be present.

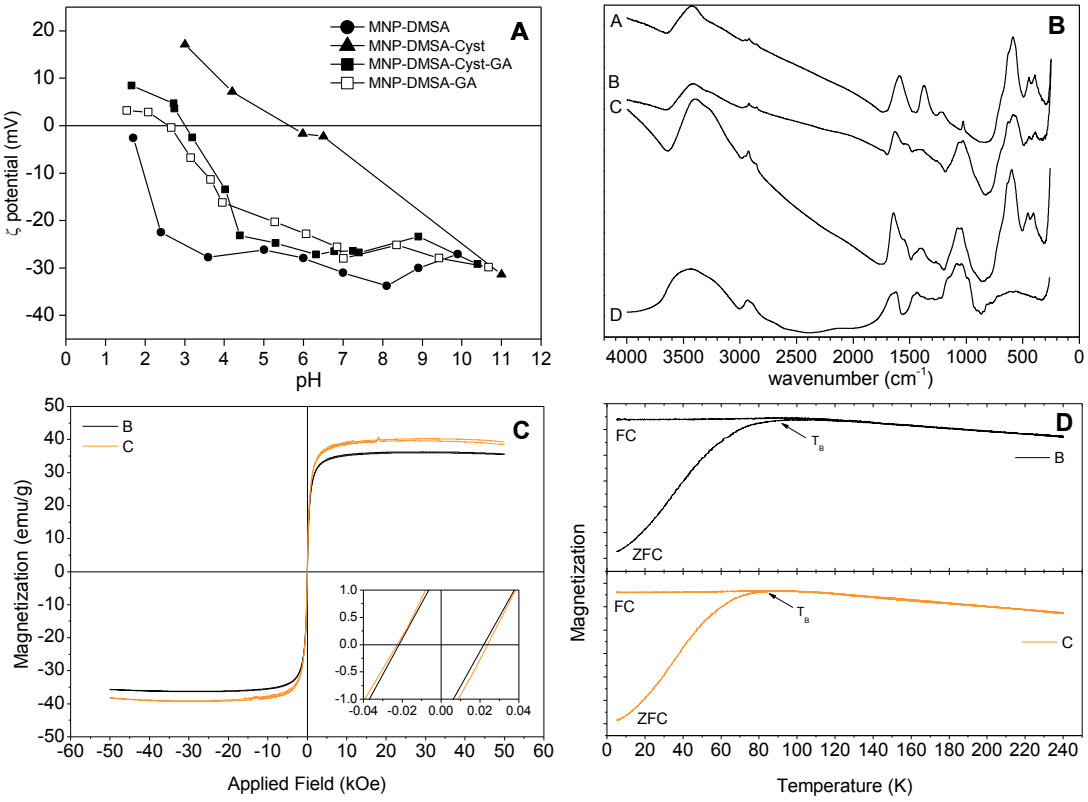

Figure 2.4. Surface and magnetic properties of the particles coated with gum Arabic. (A) Evolution of the zeta potential with pH (B) FITR spectra; (C) Magnetization loops at T=250K; (D) ZFC/FC curves. A: MNP-DMSA, B: MNP-DMSA-Cyst-GA, C: MNP-DMSA-GA, D: GA.

Regarding the magnetic properties (Figure 2.4 C and Table 2.1), the saturation magnetization values of MNP-DMSA-GA (39 emu/g) and MNP-DMSA-Cyst-GA (36 emu/g), are similar to MNP-DMSA (M_S = 38 emu/g) (Figure 2.2 C and Table 2.1). For MNP-DMSA-Cyst-GA more reaction steps were involved, which may justify the slight decrease of M_S. FTIR spectrum for these particles (Figure 2.4 B) shows extra bands in the Fe-O vibrations region, confirming a more oxidized state for MNP-DMSA-Cyst-GA. The two GA coated MNP samples have a blocking temperature (T_B) of around 85 K (Figure 2.4 D and Table 2.1), which is higher than the 65 K from MNP-DMSA (Figure 2.2 and Table 2.1), probably due to the enhanced inter-particle magnetic interactions promoted by the aggregation. Like for MNP-DMSA, the FC curve is flat below T_B, thus confirming the presence of inter-particle dipolar interactions. The width of ZFC curve is also similar to the observed for MNP-DMSA, which means that the "magnetic sizes" distribution is maintained after coupling with GA, as expected.

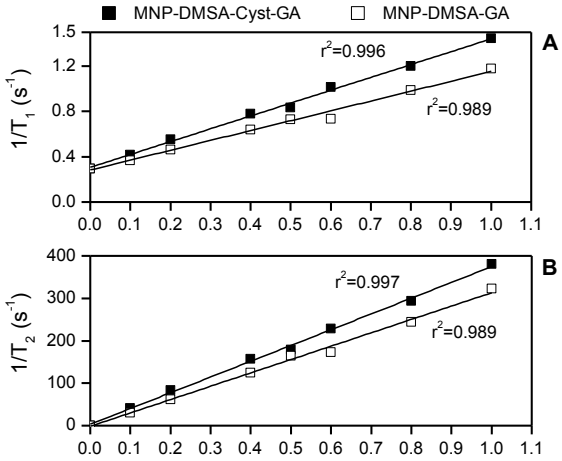

Figure 2.5. Determination of the relaxation rates of MNP-DMSA-Cyst-GA and MNP-DMSA-GA as a function of iron concentration, respective linear adjustments and r^2 values. (A) Longitudinal relaxation rates, R_1; (B) transverse relaxation rates, R_2.

The efficiency of gum Arabic coated nanoparticles as magnetic resonance imaging (MRI) contrast agents is also similar. They have low longitudinal (r_1) and high transverse (r_2) relaxivities, as is typical of superparamagnetic contrast agents. r_1 values of 1.1 and 0.9 $mM^{-1}s^{-1}$ and r_2 values of 371.4 and 314.7 $mM^{-1}s^{-1}$ were obtained for MNP-DMSA-Cyst-GA and MNP-DMSA-GA, respectively (Figure 2.5). These results are very promising for their use in MRI imaging: r_2 values are very good, higher than those of commercial MNPs (e.g. 182 $mM^{-1}s^{-1}$ Endorem/Feridex, at the same magnetic field). Though their hydrodynamic diameter (250 nm) may be large for *in vivo* applications that require long circulation times, these particles could be an alternative for passive targeting , the extravasation of particles within tumors that depends on particle size and nature of the coating. Particles interact with the innate property of the tumors in order to accumulate preferentially via an enhanced permeability and retention (EPR) effect.[41]

2.4. Conclusions

Colloidal stability in aqueous media is a key point in the production of MNP for biomedical applications. Most synthesis methods based on aqueous chemical precipitation of iron oxide yield particles that are hydrophilic but tend to aggregate and that have a polydisperse size distribution that does not suit the needs. Therefore, the generally accepted alternative to obtain monodispersity is the synthesis by thermal decomposition of organic precursors of iron in organic solvents followed by a phase transfer method that makes the nanoparticles hydrophilic while keeping the monodispersity. Ligand-exchange reaction is usually employed for this purpose and DMSA and citric acid (CA) have been used extensively as exchange ligands. In this work, the effect of CA and DMSA ligand-exchange reactions in the surface chemistry and magnetic characteristics of the particles were compared in detail. Both methods yield stable dispersions of MNP in aqueous environment. Although the core size, the hydrodynamic diameter and colloidal stability of the resulting particles are similar, the magnetic properties are altered. DMSA coated particles present superior magnetic properties. CA is more aggressive towards iron oxide surface than DMSA and, catalyzed by high temperature (100ºC), promotes a larger extent of oxidation and spin canting than DMSA, which translates in a larger decline (39%) in the magnetization saturation as compared to MNP-DMSA (30%). DMSA coated MNP present better initial susceptibility, making them more easily magnetizable. Considering that these particles are intended to be functionalized with bioactive molecules for biomedical applications, MNP-DMSA are more versatile. The thiol and carboxylic groups at the surface of MNP-DMSA serve as chemical anchors for grafting other molecules. As a proof-of-concept, the biopolymer gum Arabic, already known to be useful as a stabilizing agent for contrast agents, has proven to be successfully grafted onto the MNP-DMSA through either free thiol or carboxylic groups leading to aggregates of MNP with similar colloidal properties that maintain the magnetization saturation of MNP-DMSA and show enhanced interparticle magnetic interactions. These results contribute to the understanding of the effects of CA and DMSA in the surface and magnetic properties of MNP and show the functional versatility of MNP-DMSA.

2.5. References

(1) Teja, A. S.; Koh, P.-Y. Synthesis, Properties, and Applications of Magnetic Iron Oxide Nanoparticles. *Prog. Cryst. Growth Charact. Mater.* **2009**, *55*, 22–45, DOI:10.1016/j.pcrysgrow.2008.08.003.

(2) Krishnan, K. M. Biomedical Nanomagnetics: A Spin Through Possibilities in Imaging, Diagnostics, and Therapy. *IEEE Trans. Magn.* **2010**, *46*, 2523–2558, DOI:10.1109/TMAG.2010.2046907.

(3) Colombo, M.; Carregal-Romero, S.; Casula, M. F.; Gutiérrez, L.; Morales, M. P.; Böhm, I. B.; Heverhagen, J. T.; Prosperi, D.; Parak, W. J. Biological Applications of Magnetic Nanoparticles. *Chem. Soc. Rev.* **2012**, *41*, 4306–4334, DOI:10.1039/c2cs15337h.

(4) Cornell, R. M.; Schwertmann, U. *The Iron Oxides: Structure, Properties, Reactions, Occurrences and Uses*; 2nd ed.; Wiley-VCH GmbH & Co. KGaA: Weinheim, 2003.

(5) Cullity, B. D.; Graham, C. D. *Introduction to Magnetic Materials*; L. Habzo, R. Abari, J. Anderson, S. Basu, A. Chatterjee, T. Chen, T G. Croda, S. Farshchi, B. M. Hammerli, O. Malik, S. Nahavandi, M. S. Newman, W. R., Ed.; 2nd ed.; John Wiley & Sons: New Jersey, 2009.

(6) Rebodos, R. L.; Vikesland, P. J. Effects of Oxidation on the Magnetization of Nanoparticulate Magnetite. *Langmuir* **2010**, *26*, 16745–16753, DOI:10.1021/la102461z.

(7) Laurent, S.; Forge, D.; Port, M.; Roch, A.; Robic, C.; Vander Elst, L.; Muller, R. N. Magnetic Iron Oxide Nanoparticles: Synthesis, Stabilization, Vectorization, Physicochemical Characterizations, and Biological Applications. *Chem. Rev.* **2008**, *108*, 2064–2110, DOI:10.1021/cr068445e.

(8) Pragnesh, N. D.; Lakhan, V. C. Application of Iron Oxide Nanomaterials for the Removal of Heavy Metals. *J. Nanotechnol.* **2014**, *2014*, 14 pages, DOI:10.1155/2014/398569.

(9) Sun, S.; Zeng, H.; Robinson, D. B.; Raoux, S.; Rice, P. M.; Wang, S. X.; Li, G. Monodisperse MFe2O4 (M = Fe, Co, Mn) Nanoparticles. *J. Am. Chem. Soc.* **2004**, *126*, 273–279, DOI:10.1021/ja0380852.

(10) Lattuada, M.; Hatton, T. A. Functionalization of Monodisperse Magnetic Nanoparticles. *Langmuir* **2007**, *23*, 2158–2168, DOI:10.1021/la062092x.

(11) Chen, Z. P.; Zhang, Y.; Zhang, S.; Xia, J. G.; Liu, J. W.; Xu, K.; Gu, N. Preparation and Characterization of Water-Soluble Monodisperse Magnetic Iron Oxide Nanoparticles via Surface Double-Exchange with DMSA. *Colloids Surfaces A Physicochem. Eng. Asp.* **2008**, *316*, 210–216, DOI:10.1016/j.colsurfa.2007.09.017.

(12) Huang, G.; Zhang, C.; Li, S.; Khemtong, C.; Yang, S.-G.; Tian, R.; Minna, J. D.; Brown, K. C.; Gao, J. A Novel Strategy for Surface Modification of Superparamagnetic Iron Oxide Nanoparticles for Lung Cancer Imaging. *J. Mater. Chem.* **2009**, *19*, 6367–6372, DOI:10.1039/b902358e.

(13) Hatakeyama, M.; Kishi, H.; Kita, Y.; Imai, K.; Nishio, K.; Karasawa, S.; Masaike, Y.; Sakamoto, S.; Sandhu, A.; Tanimoto, A.; *et al.* A Two-Step Ligand Exchange Reaction Generates Highly Water-Dispersed Magnetic Nanoparticles for Biomedical Applications. *J. Mater. Chem.* **2011**, *21*, 5959, DOI:10.1039/c0jm04381h.

(14) Lartigue, L.; Innocenti, C.; Kalaivani, T.; Awwad, A.; Sanchez Duque, M. del M.; Guari, Y.; Larionova, J.; Guérin, C.; Montero, J.-L. G.; Barragan-Montero, V.; *et al.* Water-Dispersible Sugar-Coated Iron Oxide Nanoparticles. An Evaluation of Their Relaxometric and Magnetic Hyperthermia Properties. *J. Am. Chem. Soc.* **2011**, *133*, 10459–10472, DOI:10.1021/ja111448t.

(15) Ruiz, A.; Salas, G.; Calero, M.; Hernández, Y.; Villanueva, A.; Herranz, F.; Veintemillas-Verdaguer, S.; Martínez, E.; Barber, D. F.; Morales, M. P. Short-Chain PEG Molecules Strongly Bound to Magnetic Nanoparticle for MRI Long Circulating Agents. *Acta Biomater.* **2013**, *9*, 6421–6430, DOI:10.1016/j.actbio.2012.12.032.

(16) Nawara, K.; Romiszewski, J.; Kijewska, K.; Szczytko, J.; Twardowski, A.; Mazur, M.; Krysinski, P. Adsorption of Doxorubicin onto Citrate-Stabilized Magnetic Nanoparticles. *J. Phys. Chem. C* **2012**, *116*, 5598–5609, DOI:10.1021/jp2095278.

(17) Song, H.-T.; Choi, J.; Huh, Y.-M.; Kim, S.; Jun, Y.; Suh, J.-S.; Cheon, J. Surface Modulation of Magnetic Nanocrystals in the Development of Highly Efficient Magnetic Resonance Probes for Intracellular Labeling. *J. Am. Chem. Soc.* **2005**, *127*, 9992–9993, DOI:10.1021/ja051833y.

(18) Lee, N.; Hyeon, T. Designed Synthesis of Uniformly Sized Iron Oxide Nanoparticles for Efficient Magnetic Resonance Imaging Contrast Agents. *Chem. Soc. Rev.* **2012**, *41*, 2575–2589, DOI:10.1039/c1cs15248c.

(19) Smolensky, E. D.; Park, H.-Y. E.; Berquó, T. S.; Pierre, V. C. Surface Functionalization of Magnetic Iron Oxide Nanoparticles for MRI Applications - Effect of Anchoring Group and Ligand Exchange Protocol. *Contrast Media Mol. Imaging* **2011**, *6*, 189–199, DOI:10.1002/cmmi.417.

(20) Jun, Y.-W.; Huh, Y.-M.; Choi, J.-S.; Lee, J.-H.; Song, H.-T.; Kim, S.; Yoon, S.; Kim, K.-S.; Shin, J.-S.; Suh, J.-S.; *et al.* Nanoscale Size Effect of Magnetic Nanocrystals and Their Utilization for Cancer Diagnosis via Magnetic Resonance Imaging. *J. Am. Chem. Soc.* **2005**, *127*, 5732–5733, DOI:10.1021/ja0422155.

(21) Fauconnier, N.; Pons, J. N.; Roger, J.; Bee, A. Thiolation of Maghemite Nanoparticles by Dimercaptosuccinic Acid. *J. Colloid Interface Sci.* **1997**, *194*, 427–433, DOI:10.1006/jcis.1997.5125.

(22) Taboada, E.; Rodríguez, E.; Roig, A.; Oró, J.; Roch, A.; Muller, R. N. Relaxometric and Magnetic Characterization of Ultrasmall Iron Oxide Nanoparticles with High Magnetization. Evaluation as Potential T1 Magnetic Resonance Imaging Contrast Agents for Molecular Imaging. *Langmuir* **2007**, *23*, 4583–4588, DOI:10.1021/la063415s.

(23) Huh, Y.-M.; Jun, Y.; Song, H.-T.; Kim, S.; Choi, J.; Lee, J.-H.; Yoon, S.; Kim, K.; Shin, J.-S.; Suh, J.-S.; *et al. In Vivo* Magnetic Resonance Detection of Cancer by Using Multifunctional Magnetic Nanocrystals. *J. Am. Chem. Soc.* **2005**, *127*, 12387–12391, DOI:10.1021/ja052337c.

(24) Roca, A. G.; Veintemillas-Verdaguer, S.; Port, M.; Robic, C.; Serna, C. J.; Morales, M. P. Effect of Nanoparticle and Aggregate Size on the Relaxometric Properties of MR Contrast Agents Based on High Quality Magnetite Nanoparticles. *J. Phys. Chem. B* **2009**, *113*, 7033–7039, DOI:10.1021/jp807820s.

(25) Song, M.; Zhang, Y.; Hu, S.; Song, L.; Dong, J.; Chen, Z.; Gu, N. Influence of Morphology and Surface Exchange Reaction on Magnetic Properties of Monodisperse Magnetite Nanoparticles. *Colloids Surfaces A Physicochem. Eng. Asp.* **2012**, *408*, 114–121, DOI:10.1016/j.colsurfa.2012.05.039.

(26) Chantrell, R.; Popplewell, J.; Charles, S. Measurements of Particle Size Distribution Parameters in Ferrofluids. *IEEE Trans. Magn.* **1978**, *14*, 975–977, DOI:10.1109/TMAG.1978.1059918.

(27) Zhang, Y.; Kallay, N.; Matijevic, E. Interaction of Metal Hydrous Oxides with Chelating Agents. 7. Hematite-Oxalic Acid and -Citric Acid Systems. *Langmuir* **1985**, *1*, 201–206, DOI:10.1021/la00062a004.

(28) Tombácz, E.; Tóth, I. Y.; Nesztor, D.; Illés, E.; Hajdú, A.; Szekeres, M. Adsorption of Organic Acids on Magnetite Nanoparticles, pH-Dependent Colloidal Stability and Salt Tolerance. *Colloids Surf., A* **2013**, *435*, 91–96, DOI:10.1016/j.colsurfa.2013.01.023.

(29) Begin-Colin, S.; Felder-Flesch, D. *Magnetic Nanoparticles: From Fabrication to Clinical Applications*; Thanh, N. T., Ed.; CRC Press, 2012.

(30) Granitzer, P.; Rumpf, K.; Venkatesan, M.; Roca, A. G.; Cabrera, L.; Morales, M. P.; Poelt, P.; Albu, M. Magnetic Study of Fe3O4 Nanoparticles Incorporated within Mesoporous Silicon. *J. Electrochem. Soc.* **2010**, *157*, K145, DOI:10.1149/1.3425605.

(31) Guardia, P.; Batlle-Brugal, B.; Roca, A. G.; Iglesias, O.; Morales, M. P.; Serna, C. J. Surfactant Effects in Monodisperse Magnetite Nanoparticles of Controlled Size. *J. Magn. Magn. Mater.* **2007**, *316*, e756–e579, DOI:10.1016/j.jmmm.2007.03.085.

(32) Guardia, P.; Labarta, A.; Batlle, X. Tuning the Size, the Shape, and the Magnetic Properties of Iron Oxide Nanoparticles. *J. Phys. Chem. C* **2011**, *115*, 390–396, DOI:10.1021/jp1084982.

(33) Mørup, S.; Hansen, M. F.; Frandsen, C. Magnetic Interactions between Nanoparticles. *Beilstein J. Nanotechnol.* **2010**, *1*, 182–190, DOI:10.3762/bjnano.1.22.

(34) Batlle, X.; Labarta, A. Finite-Size Effects in Fine Particles: Magnetic and Transport Properties. *J. Phys. D Appl. Phys.* **2002**, *35*, R15–R42, DOI:10.1088/0022-3727/35/6/201.

(35) Daou, T. J.; Grenèche, J. M.; Pourroy, G.; Buathong, S.; Derory, A.; Ulhaq-Bouillet, C.; Donnio, B.; Guillon, D.; Begin-Colin, S. Coupling Agent Effect on Magnetic Properties of Functionalized Magnetite-Based Nanoparticles. *Chem. Mater.* **2008**, *20*, 5869–5875, DOI:10.1021/cm801405n.

(36) Morales, M. P.; Veintemillas-Verdaguer, S.; Montero, M. I.; Serna, C. J.; Roig, A.; Casas, L.; Martínez, B.; Sandiumenge, F. Surface and Internal Spin Canting in Γ-Fe 2 O 3 Nanoparticles. *Chem. Mater.* **1999**, *11*, 3058–3064, DOI:10.1021/cm991018f.

(37) Roque, A. C. A.; Bicho, A.; Batalha, I. L.; Cardoso, A. S.; Hussain, A. Biocompatible and Bioactive Gum Arabic Coated Iron Oxide Magnetic Nanoparticles. *J. Biotechnol.* **2009**, *144*, 313–320, DOI:10.1016/j.jbiotec.2009.08.020.

(38) Zhang, L.; Yu, F.; Cole, A. J.; Chertok, B.; David, A. E.; Wang, J.; Yang, V. C. Gum Arabic-Coated Magnetic Nanoparticles for Potential Application in Simultaneous Magnetic Targeting and Tumor Imaging. *AAPS J.* **2009**, *11*, 693–699, DOI:10.1208/s12248-009-9151-y.

(39) Batalha, I. L.; Hussain, A.; Roque, A. C. A. Gum Arabic Coated Magnetic Nanoparticles with Affinity Ligands Specific for Antibodies. *J. Mol. Recognit.* **2010**, *23*, 462–471, DOI:10.1002/jmr.1013.

(40) Kong, J.; Yu, S. Fourier Transform Infrared Spectroscopic Analysis of Protein Secondary Structures. *Acta Biochim. Biophys. Sin. (Shanghai).* **2007**, *39*, 549–559, DOI:10.1111/j.1745-7270.2007.00320.x.

(41) *Nanomaterials for the Life Science: Magnetic Nanomaterials*; Kumar, C. S. S. R., Ed.; 1st ed.; Wiley-VCH Verlag GmbH & Co. KGaA: Weinheim, Germany, 2009.

Chapter 3

Covalent coupling of gum Arabic onto superparamagnetic iron oxide nanoparticles for MRI cell labeling: physiochemical and *in vitro* characterization

Gum arabic (GA) is a hydrophilic composite polysaccharide derived from exudates of *Acacia senegal* and *Acacia seyal* trees. It is biocompatible, possesses emulsifying and stabilizing properties and has been explored as a coating agent on nanomaterials for biomedical applications, namely magnetic nanoparticles (MNPs). Previous studies focused on the adsorption of GA onto MNPs produced by co-precipitation methods. In this work, MNPs produced by thermal decomposition method, known to produce uniform particles with better crystalline properties, were employed for the covalent coupling of GA through its free amine groups, which increases the stability of the coating layer. MNPs were produced by thermal decomposition of $Fe(acac)_3$ in organic solvent and, after ligand-exchange with *meso*-2,3-dimercaptosuccinic acid (DMSA), GA coating was achieved by the establishment of a covalent bond between DMSA and GA moieties. Clusters of several magnetic cores entrapped in a shell of GA were obtained, with good colloidal stability and promising magnetic relaxation properties (r_2/r_1 ratio of 350). HCT116 colorectal carcinoma cell line was used for *in vitro* cytotoxicity evaluation and cell labeling efficiency studies. We show that, upon administration at the respective IC_{50}, GA coating enhances MNP cellular uptake by 19 times compared to particles only bearing DMSA moieties. Accordingly, *in vitro* MR images of cells incubated with increasing concentrations of GA-coated MNP present dose-dependent contrast enhancement. The obtained results suggest that the GA magnetic nanosystem could be used as MRI contrast agent for cell labeling applications.

Publications

Palma, S. I. C. J.; Carvalho, A.; Silva, J.; Martins, P.; Marciello, M.; Fernandes, A. R.; Morales, M. P.; Roque, A. C. A. *Contrast Media Mol. Imaging* **2015**, *10*, 320–328, DOI:10.1002/cmmi.1635.

Communications in conferences

Posters

Palma, S.I.C.J.; Marciello, M.; Carvalho A.; Veintenillas-Verdaguer S.; Morales M.P.; Roque, A.C.A.; Exploring the covalent coupling of a natural polymer on magnetic nanoparticles for Magnetic Resonance Imaging, ISN 2 A 2014 - 1st International Symposium on Nanoparticles/Nanomaterials and Applications, Caparica, Portugal (2014)

3.1. Introduction

The unique physiochemical properties of iron oxide magnetic nanoparticles (MNP), namely large surface to volume ratio, superparamagnetism and biocompatibility, make them useful for biomedical applications such as magnetic resonance imaging (MRI), magnetic particle imaging (MPI), hyperthermia, targeted drug and gene delivery, cell labeling, among others.[1] The effective size, shape and surface charge determine the successful function of a magnetic nanosystem in biological environments. Here, particle coating plays an important role because it is the interface between the magnetic core and the cellular medium. The coating mediates interactions with cells, namely by contributing to the active (via attachment of cell-specific ligands) or passive (via tumor enhanced permeation and retention effect) targeting of the particles to the tissues. Hydrophilic coatings, usually composed by polysaccharides (e.g. dextran) or synthetic polymers (e.g. polyethylene glycol (PEG)), provide colloidal stability through steric stabilization and can enhance blood circulation times upon particles administration *in vivo*.[1–3] Gum Arabic (GA) is a hydrophilic composite polysaccharide derived from exudates of *Acacia senegal* and *Acacia seyal* trees, characterized by excellent emulsifying and long-term stabilizing properties. It is also biocompatible thus having its main applications in food, pharmaceutical and cosmetic industries.[3–5] This biopolymer comprises three main components: low-protein content arabinogalactan (90%) high-protein content arabinogalactan (10%) and high-protein content glycoproteins (<1%).[4,5] MNP coated with GA were previously shown to be stable in aqueous media,[6,7] functionalized with drugs for targeted drug delivery[8–10] and used as magnetically targeted MRI contrast agents.[11] For example, *in vitro* tests showed cellular uptake of GA coated MNP in mammalian cell lines[11,12] and, by MRI, it was possible to observe their accumulation at tumor sites in mice bearing 9L glioma tumors after intravenous injection and under magnetic targeting with an external magnetic field.[11] In these studies, coating was achieved by physical adsorption but the GA charged groups (carboxyl and amine) can also be employed for covalent bonding via carbodiimide activation.[6] Unlike physical adsorption, covalent bonding provides a more permanent attachment of the polymer to the particles, avoiding its detachment and the disorganization of the MNP clusters, which may compromise temporal stability of the material.[13] Also, in the previous studies,[8–12] the MNP were synthesized by co-precipitation methods, which are known to produce less crystalline MNP with heterogeneous distribution of sizes and shapes.[14,15] The thermal decomposition method is an alternative to obtain monodisperse MNP with enhanced magnetic properties.

In this work we present a route for covalent binding of GA onto MNPs derived from the thermal decomposition of an oganometallic precursor. We show, for the first time, a comprehensive characterization of MNP coated with gum Arabic in human cells. The particles were characterized regarding their size, colloidal stability, magnetic properties and efficacy as

MRI contrast agents (longitudinal, r_1, and transverse, r_2, relaxivities). A promising r_2/r_1 ratio was found, superior to that of the commercial agent Endorem/Feridex. *In vitro* evaluation of cell-particle interactions was performed using the HCT116 human colorectal carcinoma cell line. We found that GA coating promotes a 19-fold increase in MNP uptake compared to the uncoated precursor only bearing DMSA at its surface and that *in vitro* T_2-weighted MRI of cells incubated with GA coated MNP present a dose-dependent signal decrease.

3.2. Experimental Section

3.2.1. Materials

All chemicals were purchased from Sigma-Aldrich and used without ulterior purification. Reagents for cell culture and analysis were purchased from Invitrogen.

3.2.2. Synthesis and phase transfer of magnetic nanoparticles

Hydrophobic magnetic nanoparticles were synthesized following Sun's method[16] with slight modifications. For the phase transfer to aqueous media, a ligand-exchange reaction using DMSA was performed as described previously[13] (See details in Chapter 2: Section 2.2.2 and Section 2.2.4). Following this procedure, MNP-DMSA were obtained.

3.2.3. Covalent coupling of gum Arabic to MNP-DMSA

GA was bound to the MNP-DMSA, via carbodiimide chemistry, through the formation of an amide bond between the free carboxyl groups of DMSA and the free amines of GA. (See details in Chapter 2: Section 2.2.6)

3.2.4. Characterization of magnetic nanoparticles

3.2.4.1. Size and structural characterization

Particle size and shape were characterized by Transmission Electron Microscopy (TEM) using a 100-kV JEOL JEM1010 microscope equipped with a Gatan Orius 200 SC digital camera. The average particle core diameter was calculated using ImageJ software (National Institutes of Health, USA). Hydrodynamic size (d_h) and zeta potential (ζ-potential) of the particles were determined using a Nanosizer ZS (Malvern) at pH 7. The mean value of the volume-weighted size distribution was used as d_h. ζ-potential variation with pH was measured in

a 0.01 M KNO_3 solution (HNO_3 or KOH solutions were used for pH adjustment). Colloidal stability of MNP-DMSA-GA over time was studied by evaluating the percent change in hydrodynamic diameter (Z-average) during one week for not autoclaved particles diluted in water, and for autoclaved particles diluted in water and in cell culture medium. These three conditions were chosen in order to evaluate the effect of sterilization by autoclaving and to mimic the environment found by the particles when put in contact with cells in the *in vitro* assays. To study stability, samples were placed in a DLS cuvette and hydrodynamic diameter measurements were taken in the course of one week without agitation. In the last day, samples were homogenized by pipetting up and down several times and measured again. Inductively coupled plasma (ICP) atomic emission spectroscopy (Horiba Jobin-Yvon, Ultima) was used to determine the iron content of the MNP samples. Fourier transform infrared (FTIR) spectra were acquired using a Nicolet 20 SXC FTIR. Simultaneous thermogravimetric analysis (TGA) and differential thermal analysis (DTA) of MNP-DMSA-GA powder was carried out in a Seiko TG/DTA 320 U, SSC 5200 thermobalance.

3.2.4.2. Magnetic properties and relaxivities assessment

Magnetization measurements were performed using a vibrating sample magnetometer (VSM) (MagLab VSM, Oxford Instruments). Magnetization loops were measured at 250 K and corrected by subtracting the diamagnetic contribution of the dispersants and the sample holder. The saturation magnetization at maximum field was normalized to grams of Fe_2O_3. Temperature dependent zero-field cooling (ZFC) and field cooling (FC) magnetization measurements were performed by cooling the samples to 5 K under a zero or a 100 Oe magnetic field, respectively. Then, the magnetization was measured while the samples were heated (3 K/min) to 250 K under a 100 Oe magnetic field. The relaxometric properties of MNP-DMSA-GA were evaluated in a 7 T NMR Brucker Avance III Spectrometer at 25ºC. T_1 was measured using an inversion recovery sequence (TR between 3 and 10 s). T_2 was measured using a Call-Purcell-Meiboom-Gill sequence (TE of 1 ms and the number of echoes needed to cover a time interval of about 10 times T_2). R_1 ($1/T_1$) and R_2 ($1/T_2$) were plotted against iron concentration and a linear behavior was found. The lines slopes are the longitudinal (r_1) and transverse (r_2) relaxivities, that measure the efficiency of the nanoparticles as MRI contrast agents. T_2-weighted MRI phantom images of MNP-DMSA-GA water suspensions at 0.1, 0.4, 0.8 and 1 mM (Fe) were obtained with a multi-echo image sequence (TR = 5 s; T_t = 8 ms).

3.2.5. Nanoparticle-cell interactions

3.2.5.1. Cell culture

Human colorectal carcinoma cell line (HCT116) was cultured in Dulbecco's modified Eagle's medium supplemented with 10% (v/v) fetal bovine serum and 1% (v/v) of penicillin-streptomycin at 37 ºC with 99% relative humidity and 5% CO_2. For experiments, cells were incubated with fresh medium for 24h to allow cell adhesion. Then, the culture medium was replaced by fresh medium containing the nanoparticles and cells were incubated for the required time, after which the nanoparticle-cell interaction experiments described in the following sections were carried out. Nanoparticles were sterilized prior to the addition to culture medium by filtration with a sterile membrane filter of 0.45 μm pore diameter.

3.2.5.2. Cell viability evaluation

HCT116 cells were incubated with MNP-DMSA and MNP-DMSA-GA at iron concentrations of 5, 15, 25, 40, 55, 75, 100 and 150 μg/ml and with GA at concentrations of 3, 9, 15, 24, 33, 44, 59 and 89 μg/ml. GA concentrations correspond to the GA content in MNP-DMSA-GA at the chosen iron concentrations and were calculated from TGA results (GA constitutes 21% weight of MNP-DMSA-GA).

After 48 h incubation with MNPs and GA in a 96-well plate, at 7.5×10^3 cells/well, culture media was removed and the wells were washed twice with PBS. Cell viability was evaluated using a standard 3-(4,5-dimethylthiazol-2-yl)-2,5-diphenyl tetrazolium bromide (MTT) assay and a previously defined protocol[17] with slight modifications, described in the following lines. MTT was dissolved in PBS at 5 mg/ml and diluted to 0.45 mg/ml in culture media. 110 μl of the resultant MTT solution was added to each well, followed by 2.5 h incubation at 37 ºC. After this period, the solution was removed from the wells, without disturbing the cells, and replaced by 100 μl of DMSO to dissolve the formazan crystals obtained as a result of MTT metabolization. The plate was gently shaken for 10 min at room temperature and the absorbance of the wells at 540 and 630 nm was measured in a microplate reader (Microplate Titre Infinite F200, TECAN Spectra). Cell viability was calculated using the following equation:

$$cell\ viability\ (\%) = \frac{(abs@540nm - abs@630nm)_{sample}}{(abs@540nm - abs@630nm)_{control}} \times 100 \qquad (3.1)$$

where *sample* refers to cells incubated with particles or GA and *control* refers to cells without particles or GA.

Three independent MTT assays were performed. The relative IC_{50} for each particle type was determined by fitting the viability results to a logistic dose-response curve[18] using Origin 8

software. In the following experiments, cells were incubated with the relative IC_{50} of MNP-DMSA and MNP-DMSA-GA.

3.2.5.3. Iron staining with Prussian blue

After 48 h incubation (24-well plate with 10 mm^2 coverslips on the bottom of each well; 1×10^5 cells/well) with nanoparticles at their IC_{50} values (55 μg/ml for MNP-DMSA and 43 μg/ml for MNP-DMSA-GA), cells were washed three times with 0.5 ml of PBS and fixed with 0.3 ml of cold paraformaldehyde (4% v/v in PBS) for 15 min. The paraformaldehyde was removed, cells were washed three times with PBS and, when the coverslips were dry, 0.5 ml of Prussian blue solution (equal volumes of HCl (2% v/v) and potassium ferrocyanide trihydrate 2% (m/v)) was added and incubated for 15 min at room temperature. After removal of the staining solution, cells were washed three times with PBS and counterstained for 2 min with 0.5 ml of neutral red 0.5% (m/v). Preparations were then washed three times with PBS, air-dried and mounted on the microscope slide using 1 drop of glycerol 1:3 (v/v in PBS). Slides were observed under bright-light illumination using a Olympus BX51 microscope equipped with a Olympus DP50 camera and the AnalySIS Soft Imaging software.

3.2.5.4. Nuclear staining with Hoechst 33258

After 48 h incubation (24-well plate with 10 mm^2 coverslips on the bottom of each well; 1×10^5 cells/well) with nanoparticles at their IC_{50} values (55 μg/ml for MNP-DMSA and 43 μg/ml for MNP-DMSA-GA), cells were washed three times with 0.5 ml of PBS and fixed with 0.3 ml of ice-cold paraformaldehyde (4% v/v in PBS) for 15 min in the dark, at 4ºC. The paraformaldehyde was removed, cells were washed three times with PBS and, when the coverslips were dry, 0.3 ml of Hoechst solution (containing 0.6 μl of 5mg/ml Hoechst stock solution in 0.3 ml of PBS) was added and incubated for 15 min in the dark at room temperature. After removing the Hoechst solution, preparations were then washed three times with PBS, air-dried and mounted in the microscope slide using 1 drop of glycerol 1:3 (v/v in PBS). Slides were observed by fluorescence microscopy using a Olympus BX51 microscope equipped with a Olympus DP50 camera and the AnalySIS Soft Imaging software

3.2.5.5. Cellular staining with Propidium iodide (PI) and nuclear counterstaining with DAPI

After 48 h incubation (35 mm^2 petri dish with 10 mm^2 coverslip on the bottom; 1×10^5 cells) with MNP-DMSA-GA at their IC_{50} (43 μg/ml), cells were washed three times with 1 ml of

PBS and fixed with 1 ml of ice-cold paraformaldehyde (4% v/v in PBS) for 15 min in the dark, at 4ºC. After removing the paraformaldehyde, cells were washed three times with 1 ml of PBS and incubated for 5 min with 1 ml of Triton 0.1% (v/v) for permeabilization. After this incubation, cells were washed three times with PBS to remove triton, the coverslips were dried and 1 ml of a Propidium Iodide (PI) solution (in PBS, 10 μg/ml) was added and incubated for 30 min in the dark at room temperature. PI solution was removed and the preparation was washed three times with PBS, air dried and mounted in the microscope slide using 5 μl of DAPI solution. Slides were observed by fluorescence microscopy using a Olympus BX51 microscope equipped with a Olympus DP50 camera and the Cell F View Image System Software.

3.2.5.6. GFP labeling of lysosomes and nuclear counterstaining with DAPI

Cells were incubated (35 mm^2 petri dish with 10 mm^2 coverslip on the bottom; 1×10^5 cells) for 48 h with MNP-DMSA-GA at their IC_{50} (43 μg/ml). CellLight® Lysosomes-GFP, BacMam 2.0 reagent (Life Technologies, USA) (25 particles per cell, assuming 2×10^5 cells) was added directly to the cells 20 h before the end of the incubation time and left incubating overnight according to the supplier's instructions. 25 viral particles per cell were used and 1×10^5 cells

After 48h of incubation, cells were washed three times with 1 ml of PBS and fixed with 1 ml of ice-cold paraformaldehyde (4% v/v in PBS) for 15 min in the dark, at 4ºC. The paraformaldehyde was removed, and cells were washed three times with 1 ml of PBS. At this point, the preparation was air dried and mounted in the microscope slide using 5 μl of DAPI solution. Slides were observed by fluorescence microscopy using a Olympus BX51 microscope equipped with a Olympus DP50 camera and the Cell F View Image System Software.

3.2.5.7. Iron quantification

Cells were incubated for 12 h, 24 h and 48 h in a 24-well plate (1×10^5 cells/well) with nanoparticles at their IC_{50} values (55 μg/ml for MNP-DMSA and 43 μg/ml for MNP-DMSA-GA). The iron content in three cell culture fractions was quantified by ICP.

Well supernatant (fraction 1) contains mainly culture media, dead cells and particles that remained in the extracellular space. Cells remaining in the wells were trypsinized, resuspended in medium and counted using a hemocytometer. These cell suspensions were centrifuged at 5000 rpm for 10 min to separate cell pellet (fraction 2) and cell supernatant (fraction 3). The three fractions were digested separately with 100 μl of *aqua regia* (concentrated HCl/HNO_3 3:1 (v/v)) for 30 min at 90ºC, left cool down to room temperature, diluted to a final volume of 1 ml with milliQ water and analyzed separately by ICP.

The iron in the cellular fraction (sum of fraction 2 and fraction 3) was normalized to the number of cells counted previously. To compare the interaction of each particle type with cells, the iron content in cellular fraction and well supernatant was normalized to the total amount of iron quantified (sum of cellular and supernatant iron). A control sample containing only cells was also quantified to provide a calibration for the native iron content of cells.

3.2.5.8. Quantification of apoptosis markers by real-time PCR

Cells were incubated for 3.5h, 6h, 12h and 48h (T-25 flask, 2×10^5 cells/ml) with MNP-DMSA-GA at its relative IC_{50}. Control cell cultures without MNPs were also prepared for all time points. At the end of these exposure periods, total mRNA was extracted using TRIZol Reagent kit (Life Technologies, USA) according to manufacturer's instructions. Concentration of the extracted RNA was determined using Nanodrop1000-ND. 100 ng of RNA was reverse transcribed using the NZY M-MuLV First-Strand cDNA Synthesis Kit (Nzytech, Portugal) according to the supplier's instructions. The produced first-strand cDNA was quantified using Nanodrop 1000-ND and amplified (100 ng) by real-time PCR (Corbett Rotor Gene 6000 – QUIAGEN) using the kit 5x HOT FIREPol EvaGreen qPCR Mix Plus (ROX) (Solis BioDyne, Estonia), and specific primers for *p21*, *BAX*, *BCL-2* and *rRNA18S5* (Metabion GmbH, Germany).Real-time PCR program parameters included 15 minutes at 95ºC, followed by 40 cycles involving denaturation at 95ºC for 15 seconds, annealing at $T_{melting}$ (59ºC for *p21* and *rRNA18S5*, 62ºC for *BAX* and 75ºC for *BCL-2*) for 20 seconds and elongation at 72ºC for 20 seconds. The expression level of each gene was normalized to the internal control (*rRNA18S5* gene). The fold changes of target genes expression relative to the control samples were determined by the $2^{-\Delta\Delta CT}$ method.[19,20]

3.2.5.9. *In vitro* MRI

Prior to be imaged, cells were dispersed in agarose gel. The agarose dispersions of cells were prepared as follows.[21] Cells were incubated for 48h (24-well plate, 1.25×10^5 cells/well) with MNP-DMSA and MNP-DMSA-GA at three iron concentrations: $C_1 = IC_{50} - 0.25 \times IC_{50}$; $C_2 = IC_{50;}$ and $C_3 = IC_{50} + 0.25 \times IC_{50}$. (relative IC_{50}). Two wells per condition were prepared in order to have enough cells for the assay. After incubation, cells were washed 3 times with 0.3 ml of PBS and trypsinized (0.2 ml of trypsin per well and 5 min incubation at room temperature). After neutralizing trypsin with 0.2 ml of culture medium, the content of the wells was transferred to 1.5 ml centrifuge tubes, centrifuged at 1500 rpm for 5 min and the supernatant was discarded. The pellet was re-suspended in 0.5 ml of cold paraformaldehyde (4% v/v in PBS) for 15 min at room temperature. The paraformaldehyde was then removed by

centrifugation (1500 rpm, 5 min), the pellet was re-dispersed in 0.2 ml of PBS and cells were counted. At this point, for each condition, samples with the same number of cells (3.125×10^5 cells) were prepared in 0.1 ml of PBS. These cell dispersions were added to 0.2 ml aliquots of fresh 0.75% (w/v) agarose (at around 40 ºC), mixed well and transferred to 5 mm diameter NMR tubes for imaging after solidifying. The final concentration of agarose in the dispersions was 0.5 mg/ml and the final concentration of cells was 1×10^6 cells/ml.

T2-weighted MR images were obtained under a magnetic field of 7 T, at 25 ºC, using a Bruker Avance III Spectrometer (160 G/cm imaging gradient) and a flash sequence (TR = 110 ms, TE = 1.7 ms, 20º excitation angle). MRI signal was quantified using ImageJ (National Institutes of Health, USA) to calculate the histogram, the average pixel value and the integrated density (sum of all pixel values divided by the average pixel value) over a 6 mm^2 circular region of interest placed in the center of each image.

3.3. Results and Discussion

3.3.1. Morphology, size, colloidal and structural properties of GA coated MNP

We have synthesized MNP by the thermal decomposition method and obtained monodisperse particles. After their phase transfer to aqueous media by ligand exchange with DMSA, GA was bound to particles. Chemical bonds provide stronger binding than adsorption and contribute for the structural stability of the system. Therefore, we took advantage of the presence of free amine groups in GA and free carboxyl groups at the surface of DMSA coated MNP (MNP-DMSA) to establish a covalent bond through carbodiimide chemistry. We have obtained a brownish colloid stable in aqueous media. TEM pictures and hydrodynamic diameter measurements in Figure 3.1 A and 3.1 B show the morphology and size of the particles after conjugation with GA. The high molecular weight and highly branched character of GA promotes the formation of monodisperse aggregates (d_h = 344 $\pm$ 87 nm, pdI = 0.2 $\pm$ 0.05) with multiple magnetic cores of MNP-DMSA (d_h = 14.9 $\pm$ 3.4 nm, d_{core} = 7 $\pm$ 1 nm) densely packed in a shell of GA which is visible surrounding the magnetic cores in the TEM images. Assuming that the aggregates are spherical, and taking in account the average hydrodynamic diameter of the clusters and the average core diameter of MNP-DMSA, each cluster is estimated to contain a maximum of 120 000 iron cores.

MNP-DMSA-GA show colloidal stability despite their tendency for zeta potential higher than -30 mV (Figure 3.1 C). In average, at pH~ 7, zeta potential is -21 $\pm$ 6 mV and precipitation is observed at around pH 2.5. This indicates that, as expected, the stabilization has both contributions from GA chains steric repulsions and from electrostatic interactions due to

negative charges of GA and to the presence of some free carboxyl groups from the DMSA at the surface. Autoclaved particles also showed stability when dispersed in culture medium (Figure 3.2).

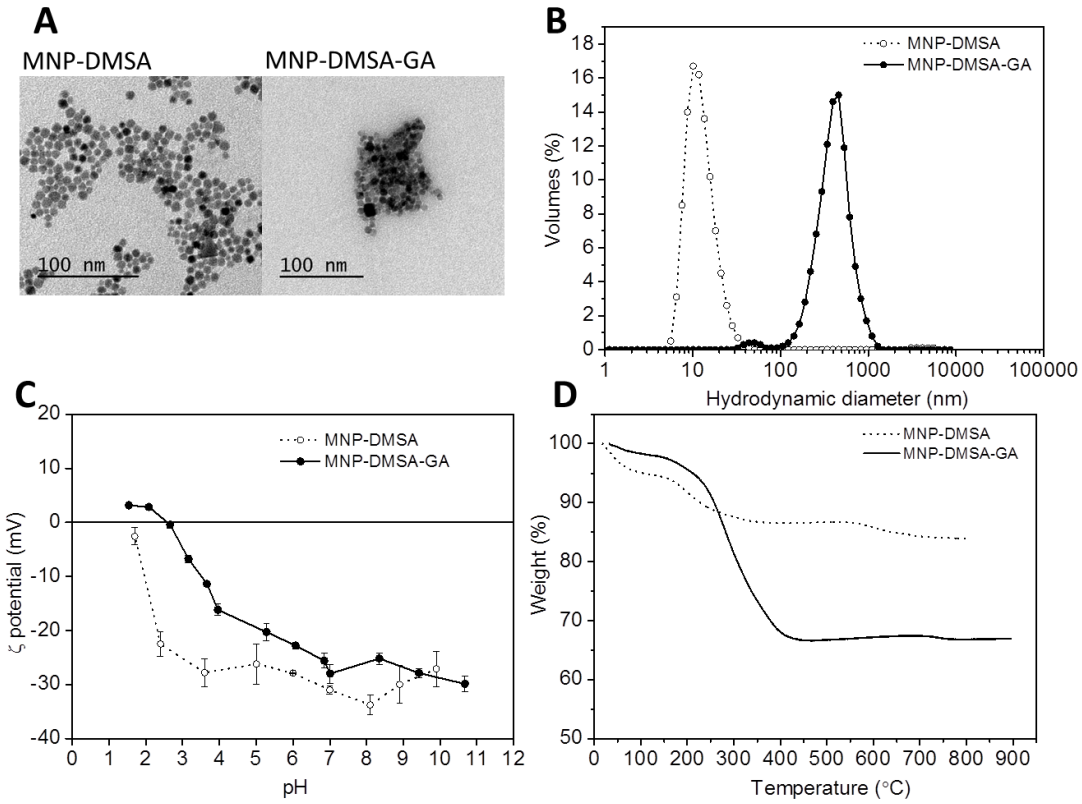

Figure 3.1. Size, colloidal stability and composition of the produced particles. Representative TEM image (A), hydrodynamic diameters distribution at pH 7 in water (B), variation of zeta potential with pH (C) and TGA data for MNP-DMSA and MNP-DMSA-GA (D).

In order to access the amount of GA attached to the particles, TGA and DTA were performed. The TGA curve of MNP-DMSA reveals a weight loss of ~ 11% due to the removal of DMSA molecules (second and third steps of weight loss, between 150ºC and 800ºC, in Figure 3.1 D), which are lost mainly at ~219ºC, corresponding to the exothermic peak in the DTA curve (Figure 3.3). On the other hand, between 145ºC and 400-450ºC, there is a ~32% loss of weight in the TGA curve of MNP-DMSA-GA (Figure 3.1 D), with maximum loss rate at 290ºC, represented by the exothermic peak of the DTA curve at this temperature (Figure 3.3). The observed weight loss can be attributed to GA decomposition (burning).[22,23] This information allows deducing that GA represents approximately 21% of the particles total weight. Taking into account that the average hydrodynamic diameter is 344 nm, the density of Fe_2O_3 is 4.89 g/cm^3, the molecular weight of GA is about 2.5 × 10^5 [22] and the iron oxide cores are spherical, with

approximately 7 nm diameter, the magnetic clusters are composed of approximately 0.7 molecules of GA per iron oxide core.

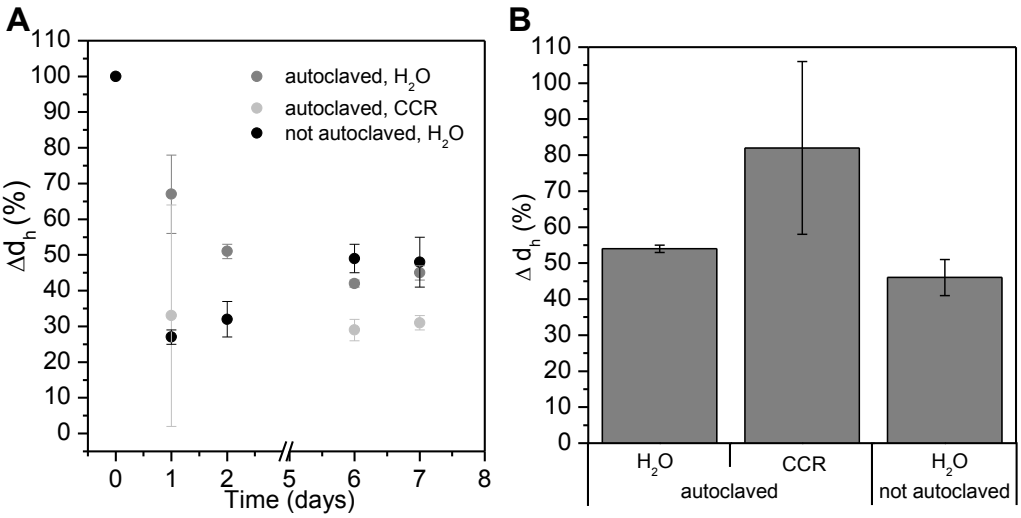

Figure 3.2. MNP-DMSA-GA colloidal stability over time, in different conditions. (A) Hydrodynamic diameter (Z-Average) variation versus settling time. (B) Hydrodynamic diameter (Z-Average) variation upon re-suspension after one week of settling.

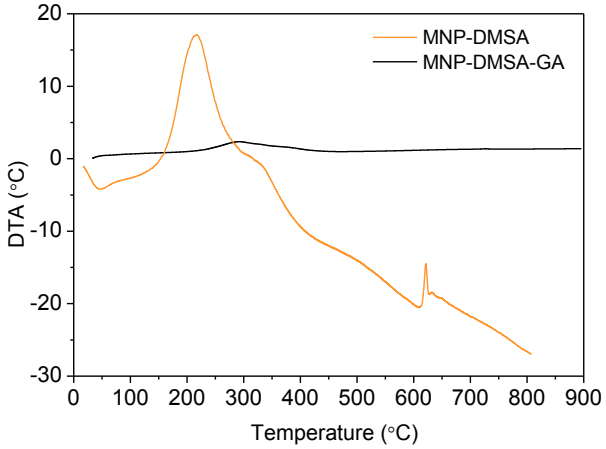

Figure 3.3. Differential Thermal Analysis (DTA) of MNP-DMSA and MNP-DMSA-GA.

The presence of the GA shell was also confirmed by FTIR spectroscopy (Figure 2 -3.4) as the GA characteristic peak, located at 1036-1071 cm^{-1} and due to C-O stretching vibrations,[24] is present in MNP-DMSA-GA spectrum. A typical amide absorption band, attributed to C=O bond stretching vibrations is present at around 1635 cm^{-1} in MNP-DMSA-GA spectrum. In addition, there is also a shoulder-like band at 1530-1540 cm^{-1} that resembles the amide II band, being associated with the N-H bond bending, C-N and C-C stretching vibrations. This suggests the presence of amide bonds resultant from the covalent bond between the DMSA at the surface of

the particles and GA, although a contribution from chemical crosslinking of GA chains between themselves may also be present.

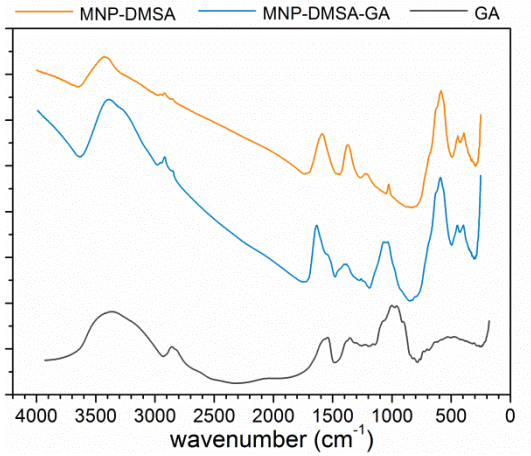

Figure 3.4. FTIR spectra of MNP-DMSA-GA in comparison with MNP-DMSA and free GA.

3.3.2. Magnetic properties and relaxivities assessment

For applications such as MRI cell labeling or magnetic drug targeting, superparamagnetic behavior and good induced relaxation properties are of paramount importance. As expected, negligible hysteresis was observed in the magnetization experiments (Figure 3.5 A), showing that the MNP-DMSA superparamagnetic behavior is maintained after the coating with GA. The saturation magnetization of the particles (M_S = 39 emu/g(Fe_2O_3)) is also maintained as seen in Figure 3.5 A and Table 3.1. This indicates that the covalent coupling protocol did not change the crystalline structure of the magnetic cores. However, the blocking temperature (T_B) increased from 65 K to 85 K (Figure 3.5 B and Table 3.1) as a result of the aggregation of several magnetic cores. The dipolar field created by a MNP is approximately proportional to its magnetic moment (and thus to its volume) and decreases with the third power of the distance.[25] Since the magnetic cores maintain their sizes compared to MNP-DMSA, the increase in T_B can be attributed to enhanced inter-particle magnetic interactions promoted by the aggregation. The GA network that surrounds the magnetic cores brings them close together in such a way that the inter-particle distance is not enough to reduce dipolar interactions and therefore, the magnetic spins couple.[26] This enhances the mean energy barrier for magnetization (T_B) because higher thermal energy is needed to promote the fluctuation of magnetic spins.[26]

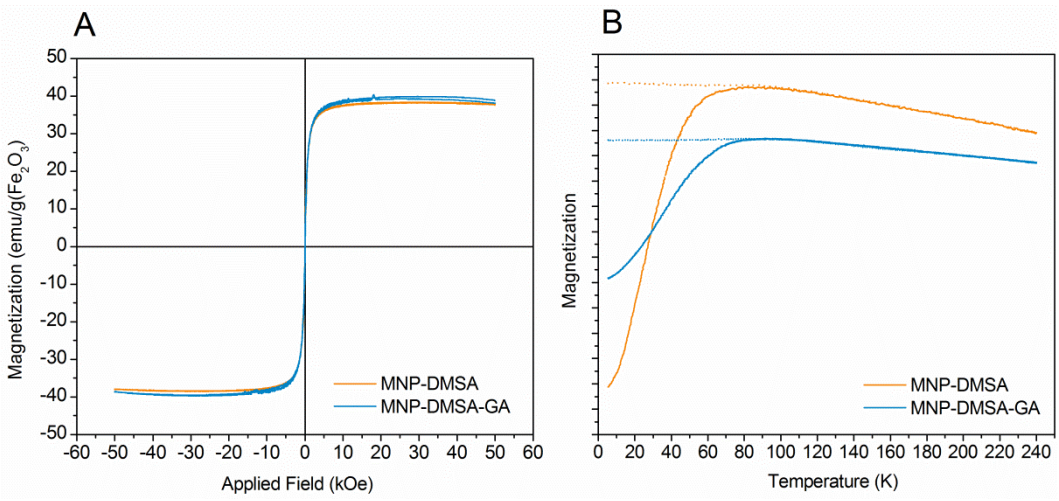

Figure 3.5. Magnetic properties of MNP-DMSA and MNP-DMSA-GA. (A) Magnetization loops at 250 K; (B) Zero Field Cooling (ZFC, dotted line) and Field Cooling (FC, solid line) curves.

Typically, superparamagnetic iron oxide nanoparticles contribute to the decrease of T_2, causing a decrease of the MRI image signal (negative contrast), which is visible as a darkening effect in the image.[14] Figure 3.6 A shows the linear relation found between the longitudinal ($1/T_1$) and transverse ($1/T_2$) relaxation rates and iron concentration for MNP-DMSA-GA. From these lines, it is concluded that, as expected, MNP-DMSA-GA have low longitudinal (0.9 mMs^{-1}) and high transverse (314.7 mMs^{-1}) relaxivities (Table 3.1). The r_2/r_1 ratio characterizes the efficiency of the particles as MRI negative contrast agents. For MNP-DMSA-GA a r_2/r_1 ratio of 350 was obtained. Besides depending on the saturation magnetization of the particles, MNP's ability to influence water protons' relaxation times depend also on the proximity of water molecules to the MNP. Here, the type of coating plays an important role.[13,27] Hydration is a relevant factor to enhance r_2 relaxivity values, especially for small core particles.[28] In the case of MNP-DMSA-GA, the large r_2 is probably aided by the hydration effect produced by the polymer chains network entrapping the small magnetic cores. Water molecules enter the network of GA surrounding the particle cores and are held there for long periods of time, increasing the water concentration closer to the high-field region, created by the magnetic cores inside the agglomerate. The obtained r_2/r_1 value is much higher than that of commercial Endorem/Feridex (r_2/r_1 of 83) at the same magnetic field strength.[29] This contrast agent also has a polysaccharide coating (dextran). We, thus, anticipate that GA-coated MNP would be expected to increase the efficacy of MRI contrast in comparison with Endorem/Feridex. High r_2/r_1 ratios imply that low concentration of particles is sufficient to obtain the darkening effect in a T_2-weighted MRI image, increasing the sensitivity of the technique. As seen in the T_2-weighted phantom MRI images of MNP-DMSA-GA water dispersions (Figure 3.6 B), MRI signal intensity lowers with the increase

of particles' concentration (image contrast increases). Even for the lowest concentration of particles, there is a signal difference between the MNP sample and water.

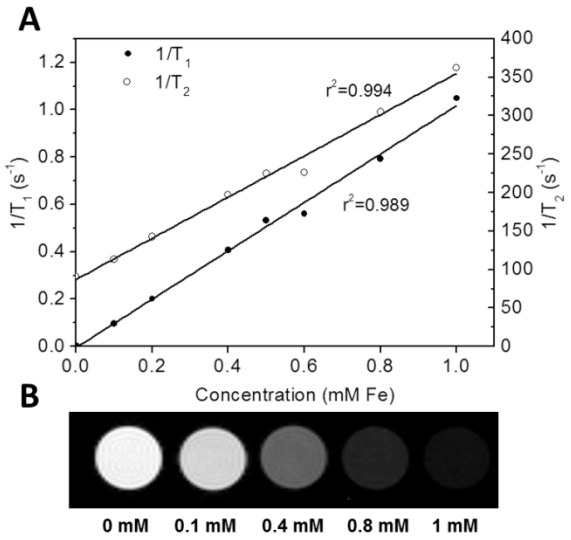

Figure 3.6. Relaxivities and T_2-MRI phantoms of MNP-DMSA-GA. (A) Linear adjustment of the plots of R_1 ($1/T_1$) and R_2 ($1/T_2$) as a function of iron concentration in MNP-DMSA-GA. (B) T_2-weighted MRI phantom images of water dispersions of MNP-DMSA-GA at different iron concentrations, obtained under a magnetic field of 7 T and using a multi-echo image sequence (TR = 5 s; T_t = 8 ms).

Table 3.1. Summary of size, magnetic and relaxometric properties of the produced MNP in comparison with a commercial MNP-based contrast agent.

Sample	*Coating (%)*	*dh (nm)*	*pdI*	*Zeta potential (mV)*	M_S *(emu/gFe_2O_3)*	T_B *(K)*	r_1 *($mM^{-1}s^{-1}$)*	r_2 *($mM^{-1}s^{-1}$)*	r_2/r_1
MNP-DMSA	11	14.9 (3.4)	0.31	-30 (6.0)	38	65	2.6	110	42.3
MNP-DMSA-GA	21	344.0 (87)	0.20	-21 (6.0)	39	85	0.9	314.7	349.7
Endorem / Feridex	-	120-180[29]	-	< 0[29]	49[11]	-	2.2[29]	182[29]	82.7[29]

Standard deviation is represented within brackets, when applicable.

3.3.3. Cell-nanoparticle interactions

The effects of GA coated particles and their precursor MNP-DMSA on the metabolic activity of HCT116 cells was evaluated using the MTT assay after 48 h of exposition (Figure 3.7 A). This epithelial cell line was chosen as model to test the particles due to its high proliferation (doubling time ~ 21.2 h).[30] At the lower iron concentrations (5 and 15 μg/ml) the average viability is still higher than 80% for both particle types, but it decreases with the increase in particles concentration in the culture medium. The decrease is more pronounced for MNP-DMSA-GA and for the same iron concentration, average viability is lower for cells treated with MNP-DMSA-GA. Interestingly, free GA (Figure 3.7 A) and MNP-DMSA are less cytotoxic than their combination

in MNP-DMSA-GA. The cytotoxicity of GA coated particles may be related with alterations in the structure of GA due to intramolecular reactions during the covalent binding process. Another possible reason is the presence of residual amount of chemicals (NHS and EDC) in the particles after the chemical linkage of GA to MNP-DMSA. A previous study[11] reported lower cytotoxicity of gum arabic coated MNP up to 20 mg(Fe)/ml. However, comparison with our results is difficult due to differences in particle mean hydrodynamic diameter, cell type and incubation times with particles. Namely, in the referred study, cells were incubated only for 4 h with particles and were allowed to recover for 24 h in fresh culture medium prior to the MTT assay. Lower incubation times would probably cause less cytotoxicity to the cells tested in our work, even incubating with a higher concentration of MNP.[11,12] The adjustment of viability data (extended up to particle concentration of 150 μg/ml) to a dose-response curve (Figure 3.7 B) provided relative IC_{50} values (particle concentration that induces a cell viability corresponding to the point halfway between 100% and the baseline)[18] of 43 μg(Fe)/ml and 55 μg(Fe)/ml for MNP-DMSA-GA and MNP-DMSA, respectively, confirming the higher toxicity of MNP-DMSA-GA.

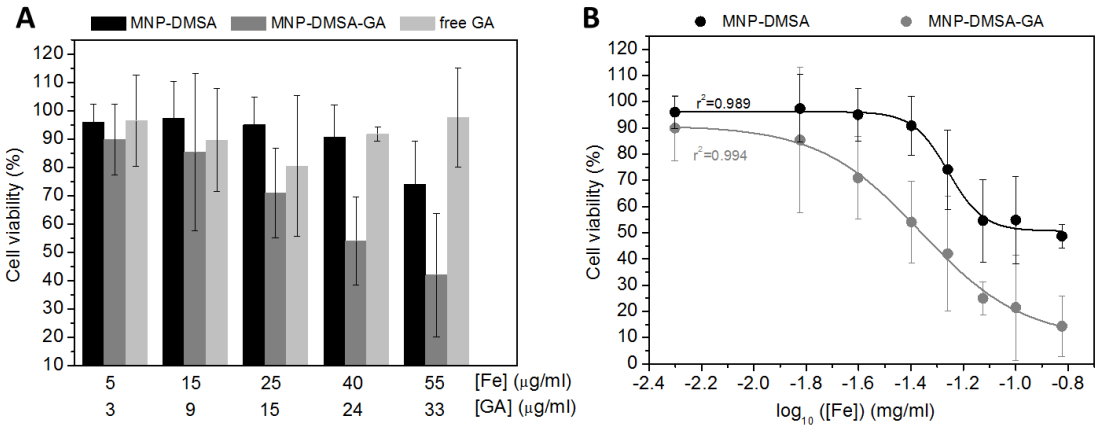

Figure 3.7. Determination of the nanoparticles and GA effects on HCT116 cell viability. (A) Cell viability evaluation by the metabolic MTT assay for HCT116 cells exposed to MNP-DMSA, MNP-DMSA-GA and free GA. (B) Determination of the IC_{50} for MNP-DMSA and MNP-DMSA-GA. Viability results are presented as the average and standard deviation of three independent assays.

Prussian blue and neutral red staining (Figure 3.8) show that after incubation with MNP-DMSA and MNP-DMSA-GA at the respective IC_{50} for 48 h (Figure 3.8 B and 3.8 C), cell morphology and size is identical to control cells, incubated without particles (Figure 3.8 A). It is also visible that, compared to MNP-DMSA, much more MNP-DMSA-GA were uptaken by cells and that particles appear to be localized in the cell cytoplasm. Quantification of the iron content found in the well supernatants and cellular fraction after 48 h incubation with MNP-DMSA-GA and MNP-DMSA shows that these particles distribute differently in the cell culture (Figure 3.8 D). In accordance with the Prussian blue images, a much larger percentage of the total iron is found in the cellular fraction (internalized and adsorbed particles) after exposure to MNP-DMSA-

GA (74%) than after exposure to MNP-DMSA (4%) (Figure 3.8 D and Table 3.2). This corresponds to 17 pg(Fe)/cell (11.4×10^{-5} % of total iron per cell) after incubation with MNP-DMSA-GA against 1 pg(Fe)/cell (0.6×10^{-5} % of total iron per cell) after incubation with MNP-DMSA. We conclude that GA coating promotes a 19-fold increase in the percent of iron internalized per cell. This tendency maintains for shorter incubation periods with particles (Figure 3.9) and the amount of iron bound per cell due to MNP-DMSA-GA is maintained approximately constant, indicating that the interaction kinetics is fast (less than 12h).

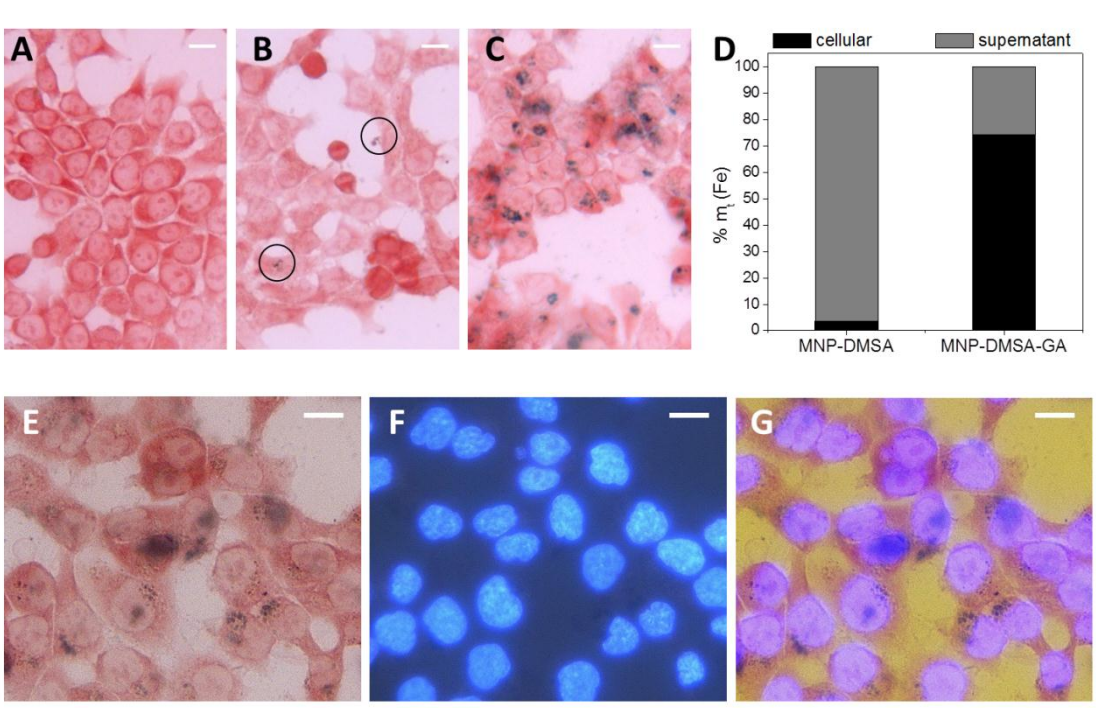

Figure 3.8. *In vitro* interactions of MNPs with HCT116 cells observed by microscopy and iron uptake quantification. Prussian blue and neutral red staining of cells incubated for 48h (A) without MNP, (B) with MNP-DMSA at the IC_{50} (55 μg/ml) and (C) with MNP-DMSA-GA at the IC_{50} (43 μg/ml). (D) Proportion of iron found in cellular and supernatant fractions, quantified by ICP. (E) Detail of the Prussian blue staining of cells incubated with MNP-DMSA-GA. (F) Same region stained with the fluorescent Hoeschst 33258 and (G) superimposition of E and F. Scale bar: 10 μm.

Several factors may contribute to justify the higher affinity of MNP-DMSA-GA to HCT116 cells than MNP-DMSA, namely the differences in hydrodynamic size and surface chemistry. It is documented that the nature of the protein corona that forms upon dispersion of the nanoparticles in complete culture medium depends on the MNPs physiochemical properties and influences the interaction with cells.[31,32] Also, uptake of MNP with more negative surface charge is lower than uptake of positively or less negatively charged particles and the increase of the agglomerate size also promotes internalization.[33] Although the expression of the gene coding for asialoglycoprotein receptor in HCT116 cell line is not documented, it is known that other colorectal carcinoma cell lines express this membrane receptor,[34,35] responsible by cell

membrane interactions with galactose residues of polysaccharides. Given the high content of galactose in gum arabic,[5] further studies to access the presence of asialoglycoprotein receptor in HCT116 cell line could help to understand the uptake mechanism of MNP-DMSA-GA.

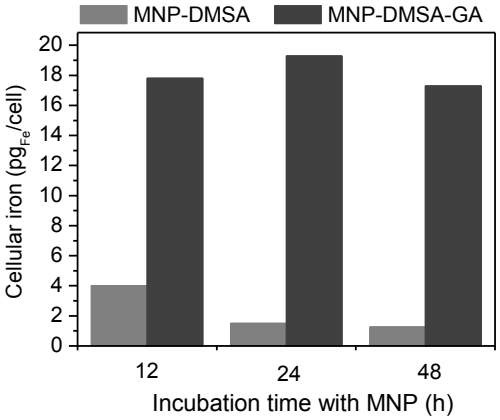

Figure 3.9. Effect of particle incubation time on the amount of iron per cell, quantified by ICP.

Table 3.2. Quantitative characterization of the cell-nanoparticles interactions.

	% m_t (Fe)						***%m_t (Fe) uptaken per cell ($\times10^{-5}$)***			***m (Fe) uptaken per cell (pg)***		
	cellular			***supernatant***								
Time point	**12h**	**24h**	**48h**	**12h**	**24h**	**48h**	**12h**	**24h**	**48h**	**12h**	**24h**	**48h**
MNP-DMSA	7.1	5.9	3.7	92.9	94.1	96.3	1.9	0.7	0.6	4.0	1.5	1.3
MNP-DMSA-GA	56.9	69.5	74.3	43.1	30.5	25.7	12	11	11.4	18.2	19.3	17.3

The comparison of neutral red and Hoechst 33258 staining images (Figure 3.8 E, F and G) confirms that the internalized MNP-DMSA-GA accumulate in the cytoplasm and do not enter the nucleus, as expected, due to their large size. Superimposition of bright field and fluorescence images of cells stained with propidium iodide and DAPI better evidences the preferential accumulation in regions surrounding the nucleus (Figure 3.10) in structures that were afterwards identified as lysosomes by labelling with a GFP-based lysosome probe (Figure 3.11).

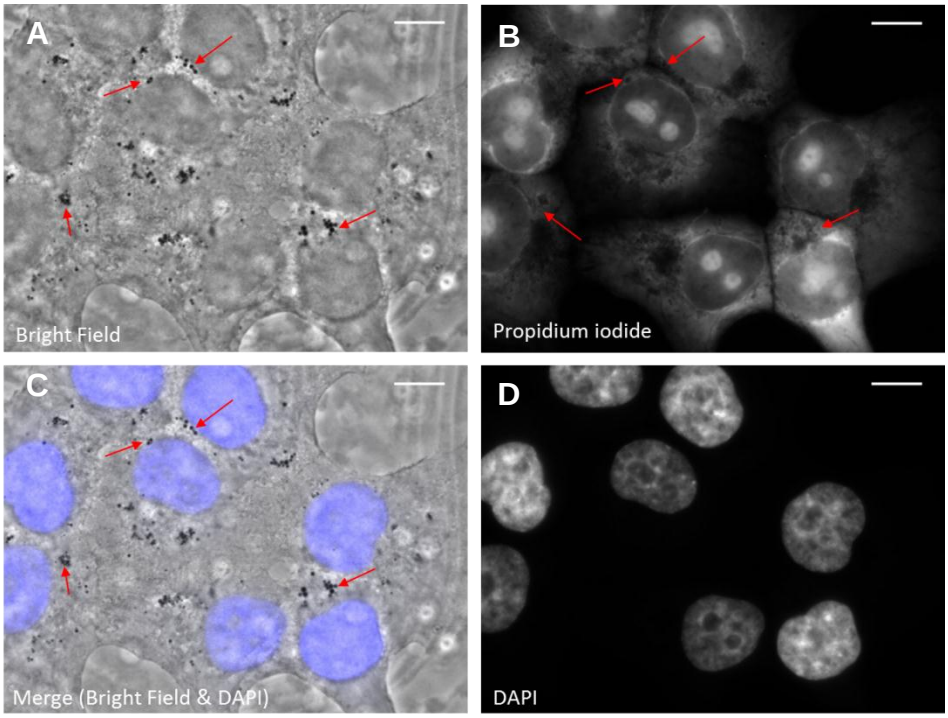

Figure 3.10. Bright field and fluorescence microscopy images of cells incubated for 48 h with MNP-DMSA-GA at IC_{50}. (A) Bright field; (B) Cellular staining with propidium iodide; (C) nuclear staining with DAPI. Agglomerates of nanoparticles are detected as black dots and are indicated by the red arrows in A, B and C. Scale bar: 10 μm.

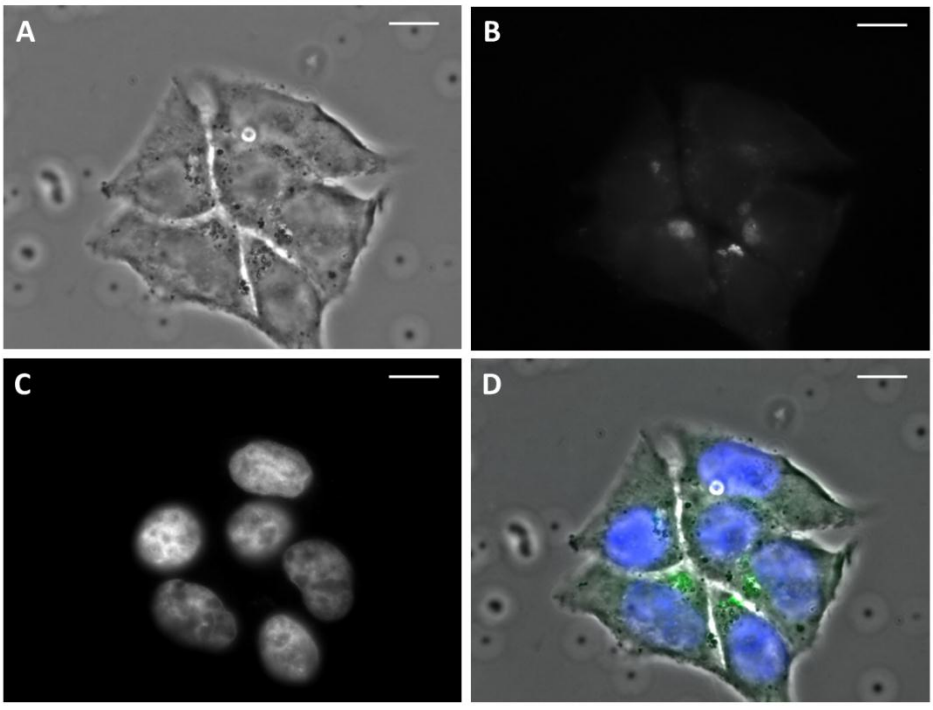

Figure 3.11. Localization of MNP-DMSA-GA within HCT116 cells after 48h incubation at IC_{50}. (A) Bright field, (B) GFP labeling of lysosomes, (C) nuclei counterstained with DAPI and (D) merged images. Scale bar: 10 μm.

Nuclear staining with Hoechst 33258 was also used to evaluate the effects of particles in nuclear morphology (Figure 3.12). The majority of non-treated cells (Figure 3.12 A) presented nuclei with homogeneous distribution of fluorescence, indicating the presence of uncondensed chromatin dispersed through the whole nucleus, which is representative of viable interphase cells. Cells treated with particles at the respective IC_{50} values show some evidence of apoptotic nuclei, namely chromatin condensation and nuclear fragmentation, as indicated by the bright non-homogeneous fluorescence (Figures 3.12 B and 3.12 C). Cell division is apparently not compromised, as some mitotic nuclei are also highlighted by Hoechst fluorescence.

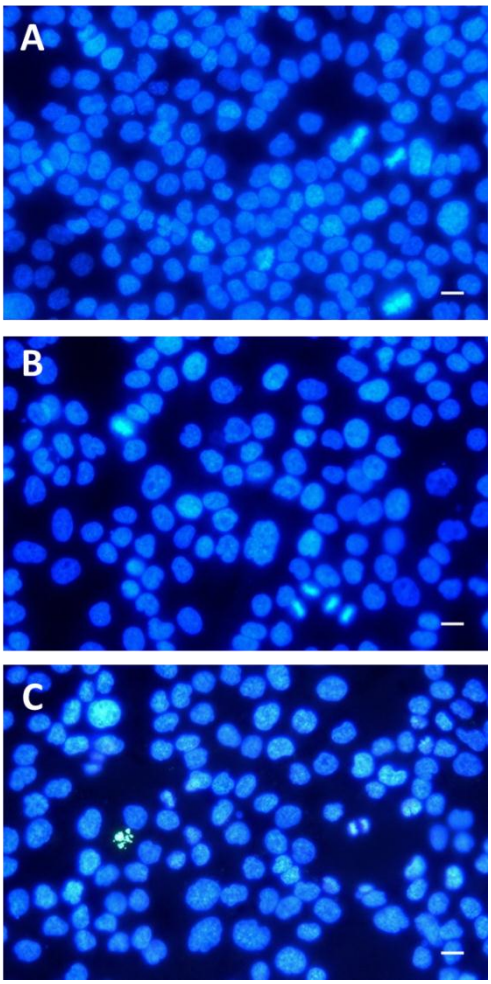

Figure 3.12. Hoechst 33258 fluorescent staining of HCT116 cells nuclei. (A) control cells (no MNPs); (B) cells incubated with MNP-DMSA at its IC_{50} (55 μg/ml) and (C) cells incubated with MNP-DMSA-GA at its IC_{50} (43μg/ml). Scale bar: 10 μm.

To understand whether the decrease of cell viability caused by MNP-DMSA-GA at IC_{50} is related with an increased apoptotic response, a time course real-time PCR analysis of mRNA levels of apoptotic (*p21* and *BAX*) and anti-apoptotic (*BCL-2*) genes was performed (Figure 3.13). The quantification revealed that 3.5h after addition of MNP-DMSA-GA, the pro-apoptosis

genes *p21* and *BAX* were overexpressed compared to untreated control cells while the anti-apoptotic gene *BCL-2* had approximately the same expression as in control cells (Figure 3.13). This behavior suggests an almost immediate trigger of an apoptotic response upon cell-MNP contact (ratio *BAX*/*BCL-2* of 3.6). However, the response is suppressed after 6h and 12h of incubation, as the expression levels of the pro- and anti-apoptotic genes is reversed (ratio *BAX*/*BCL-2* of 0.5) (Figure 3.13). This result suggests that there is an adaptation to the presence of nanoparticles in the culture medium. Nevertheless, at 48h of incubation the ratio *BAX*/*BCL2* slightly increases (1.3) indicating that cells may be triggering an apoptotic response due to prolonged exposition to MNP-DMSA-GA (Figure 3.13). Therefore, the reduction of viability quantified by the MTT assay at 48h incubation with MNP-DMSA-GA (administered at the IC_{50}) may in part be associated with an apoptotic response. Since MTT assay is a metabolic test based on mitochondrial activity, loss of mitochondrial metabolism without loss of cell viability may also contribute to explain the observed MTT results.

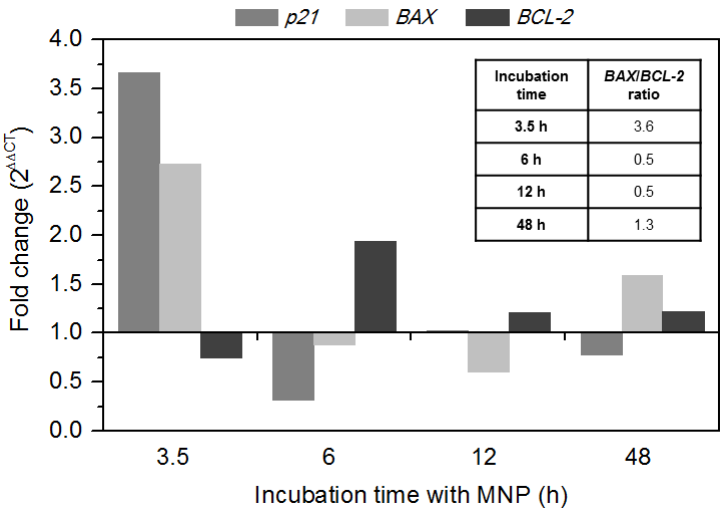

Figure 3.13. Fold changes in pro-apoptotic (*p21* and *BAX*) and anti-apoptotic (*BCL-2*) genes expression at 3.5h, 6h, 12h, and 48h after cell incubation with MNP-DMSA-GA at IC_{50} (43μg/ml).

Given the high relaxivity of MNP-DMSA-GA and enhanced cellular uptake compared to MNP-DMSA, their efficacy for cell labeling by MRI was evaluated (Figure 3.14). Hypointense regions indicating the presence of particles inside (or strongly bound to the surface) of cells are clearly visible in the images of cells incubated with MNP-DMSA-GA in contrast to untreated control cells or cells incubated with MNP-DMSA for all concentrations (Figure 3.14 A). This behavior indicates that GA coating contributes for the efficacy of the particles as MRI contrast agent and is in accordance with other study, where a different cell line was used.[11] In addition, for MNP-DMSA-GA, hypointensity increases (grey density decreases) with increasing concentration of incubated particles, as shown by the histograms of the images (Figure 3.14 B)

and respective grey density quantification (Figure 3.14 C). In other words, for the same number of HCT116 cells, MNP-DMSA-GA give dose-dependent MRI signal, indicating that particle uptake increases with the administered dose.

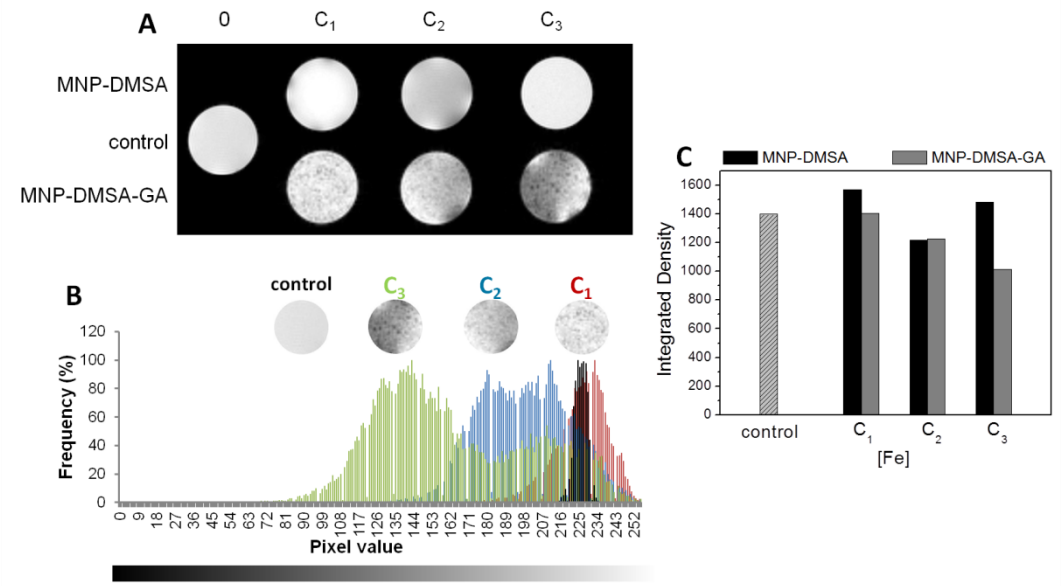

Figure 3.14. Evaluation of *in vitro* MRI cell labeling efficiency with MNP-DMSA and MNP-DMSA-GA. (A) *In vitro* MRI images of HCT116 cells incubated with increasing concentrations of MNP-DMSA and MNP-DMSA-GA, from C_1 to C_3, compared with untreated control cells;(B) histograms of *in vitro* MRI images of cells incubated with MNP-DMSA-GA and (C) quantification of grey density of images in (A). $C_1 = IC_{50}$-$0.25 \times IC_{50}$; $C_2 = IC_{50}$; $C3 = IC_{50}+0.25 \times IC_{50}$.

3.4. Conclusions

We have obtained very stable dispersions of monodisperse superparamagnetic particles (PdI = 0.2) composed by several magnetic cores entrapped in a shell of GA, with hydrodynamic diameter of 344 ± 87 nm. GA was shown to contribute to high transverse and low longitudinal MR relaxivity values (r_2/r_1 ratio of 350), resulting in good MRI contrast enhancement properties, observed both in phantom images of water dispersion of MNP-DMS-GA and in *in vitro* MRI images of HCT116 cells incubated with different concentrations of particles. By quantification of the cellular iron after incubation for 48h with particles, we showed that GA coating on MNP-DMSA enhances MNP cellular uptake by 19 times compared to MNP-DMSA alone. Incubation for different periods revealed that the iron uptake kinetics for MNP-DMSA-GA is fast (less than 12h) and cellular uptake is always enhanced compared to uncoated nanoparticles. After 48h of incubation, MNP-DMSA-GA localize in the lysosomes, which suggests uptake by endocytosis but the evaluation of the presence of asialoglycoprotein receptors in the HCT116 cell line could give new insights on MNP-DMSA-GA cellular uptake mechanism. We also found out that HCT116 cell line is very sensitive to MNPs, given the

observed dose-dependent cell viability decrease in MTT assay at the tested iron concentrations (IC_{50} values of 55 μg/ml for MNP-DMSA and 43 μg/ml for MNP-DMSA-GA). Apoptotic response was detected by up-regulation of pro-apoptotic genes *p21* and *BAX* and down-regulation of anti-apoptotic gene *BCL-2* after 3.5h and also at 48h of incubation with the MNP-DMSA-GA nanoparticles (but to a lesser extend in this last time point). Nonetheless, given the large hydrodynamic diameter and the good MRI contrast enhancement properties, MNP-DMSA-GA present potential for *in vitro* MRI cell labeling applications. Further modification of GA (for example with a fluorophore or radionuclide) would contribute for a multimodal contrast agent, allowing to follow the labeled cells by MRI and other imaging technique(s).

3.5. References

(1) Reddy, L. H.; Arias, J. L.; Nicolas, J.; Couvreur, P. Magnetic Nanoparticles: Design and Characterization, Toxicity and Biocompatibility, Pharmaceutical and Biomedical Applications. *Chem. Rev.* **2012**, *112*, 5818–5878, DOI:10.1021/cr300068p.

(2) Boyer, C.; Whittaker, M. R.; Bulmus, V.; Liu, J.; Davis, T. P. The Design and Utility of Polymer-Stabilized Iron-Oxide Nanoparticles for Nanomedicine Applications. *NPG Asia Mater.* **2010**, *2*, 23–30, DOI:10.1038/asiamat.2010.6.

(3) Dias, A. M. G. C.; Hussain, A.; Marcos, A. S.; Roque, A. C. A. A Biotechnological Perspective on the Application of Iron Oxide Magnetic Colloids Modified with Polysaccharides. *Biotechnol. Adv.* **2011**, *29*, 142–155, DOI:10.1016/j.biotechadv.2010.10.003.

(4) Ali, B. H.; Ziada, A.; Blunden, G. Biological Effects of Gum Arabic: A Review of Some Recent Research. *Food Chem. Toxicol.* **2009**, *47*, 1–8, DOI:10.1016/j.fct.2008.07.001.

(5) Williams, P. A. Structural Characteristics and Functional Properties of Gum Arabic. In *Gum Arabic*; F. Kennedy, J.; O. Philips, G.; A. Williams, P., Eds.; Royal Society of Chemistry, 2011; p. 347.

(6) Roque, A. C. A.; Bicho, A.; Batalha, I. L.; Cardoso, A. S.; Hussain, A. Biocompatible and Bioactive Gum Arabic Coated Iron Oxide Magnetic Nanoparticles. *J. Biotechnol.* **2009**, *144*, 313–320, DOI:10.1016/j.jbiotec.2009.08.020.

(7) Arndt, D.; Gesing, T. M.; Bäumer, M. Surface Functionalization of Iron Oxide Nanoparticles and Their Stability in Different Media. *Chempluschem* **2012**, *77*, 576–583, DOI:10.1002/cplu.201200065.

(8) Banerjee, S. S.; Chen, D.-H. Magnetic Nanoparticles Grafted with Cyclodextrin for Hydrophobic Drug Delivery. *Chem. Mater.* **2007**, *19*, 6345–6349, DOI:10.1021/cm702278u.

(9) Banerjee, S. S.; Chen, D.-H. Grafting of 2-Hydroxypropyl-Beta-Cyclodextrin on Gum Arabic-Modified Iron Oxide Nanoparticles as a Magnetic Carrier for Targeted Delivery of Hydrophobic Anticancer Drug. *Int. J. Appl. Ceram. Technol.* **2010**, *7*, 111–118, DOI:10.1111/j.1744-7402.2008.02332.x.

(10) Banerjee, S. S.; Chen, D.-H. Multifunctional pH-Sensitive Magnetic Nanoparticles for Simultaneous Imaging, Sensing and Targeted Intracellular Anticancer Drug Delivery. *Nanotechnology* **2008**, *19*, 505104, DOI:10.1088/0957-4484/19/50/505104.

(11) Zhang, L.; Yu, F.; Cole, A. J.; Chertok, B.; David, A. E.; Wang, J.; Yang, V. C. Gum Arabic-Coated Magnetic Nanoparticles for Potential Application in Simultaneous Magnetic Targeting and Tumor Imaging. *AAPS J.* **2009**, *11*, 693–699, DOI:10.1208/s12248-009-9151-y.

(12) Bicho, A.; Roque, A. C. A.; Cardoso, A. S.; Domingos, P.; Batalha, Í. L. *In Vitro* Studies with Mammalian Cell Lines and Gum Arabic-coated Magnetic Nanoparticles. *J. Mol. Recognit.* **2010**, *23*, 536–542, DOI:10.1002/jmr.1066.

(13) Ruiz, A.; Salas, G.; Calero, M.; Hernández, Y.; Villanueva, A.; Herranz, F.; Veintemillas-Verdaguer, S.; Martínez, E.; Barber, D. F.; Morales, M. P. Short-Chain PEG Molecules Strongly Bound to Magnetic Nanoparticle for MRI Long Circulating Agents. *Acta Biomater.* **2013**, *9*, 6421–6430, DOI:10.1016/j.actbio.2012.12.032.

(14) Krishnan, K. M. Biomedical Nanomagnetics: A Spin Through Possibilities in Imaging, Diagnostics, and Therapy. *IEEE Trans. Magn.* **2010**, *46*, 2523–2558, DOI:10.1109/TMAG.2010.2046907.

(15) Colombo, M.; Carregal-Romero, S.; Casula, M. F.; Gutiérrez, L.; Morales, M. P.; Böhm, I. B.; Heverhagen, J. T.; Prosperi, D.; Parak, W. J. Biological Applications of Magnetic Nanoparticles. *Chem. Soc. Rev.* **2012**, *41*, 4306–4334, DOI:10.1039/c2cs15337h.

(16) Sun, S.; Zeng, H.; Robinson, D. B.; Raoux, S.; Rice, P. M.; Wang, S. X.; Li, G. Monodisperse MFe2O4 (M = Fe, Co, Mn) Nanoparticles. *J. Am. Chem. Soc.* **2004**, *126*, 273–279, DOI:10.1021/ja0380852.

(17) Conde, J.; Larguinho, M.; Cordeiro, A.; Raposo, L. R.; Costa, P. M.; Santos, S.; Diniz, M. S.; Fernandes, A. R.; Baptista, P. V. Gold-Nanobeacons for Gene Therapy: Evaluation of Genotoxicity, Cell Toxicity and Proteome Profiling Analysis. *Nanotoxicology* **2014**, *8*, 521–532, DOI:10.3109/17435390.2013.802821.

(18) Silva, A.; Luís, D.; Santos, S.; Silva, J.; Mendo, A. S.; Coito, L.; Silva, T. F. S.; da Silva, M. F. C. G.; Martins, L. M. D. R. S.; Pombeiro, A. J. L.; *et al.* Biological Characterization of the Antiproliferative Potential of Co(II) and Sn(IV) Coordination Compounds in Human Cancer Cell Lines: A Comparative Proteomic Approach. *Drug Metabol. Drug Interact.* **2013**, *28*, 167–176, DOI:10.1515/dmdi-2013-0015.

(19) Livak, K. J.; Schmittgen, T. D. Analysis of Relative Gene Expression Data Using Real-Time Quantitative PCR and the 2(-Delta Delta C(T)) Method. *Methods* **2001**, *25*, 402–408, DOI:10.1006/meth.2001.1262.

(20) Schmittgen, T. D.; Livak, K. J. Analyzing Real-Time PCR Data by the Comparative CT Method. *Nat. Protoc.* **2008**, *3*, 1101–1108, DOI:10.1038/nprot.2008.73.

(21) Jasmin; Torres, A. L. M.; Jelicks, L.; de Carvalho, A. C. C.; Spray, D. C.; Mendez-Otero, R. Labeling Stem Cells with Superparamagnetic Iron Oxide Nanoparticles: Analysis of the Labeling Efficacy by Microscopy and Magnetic Resonance Imaging. *Methods Mol. Biol.* **2012**, *906*, 239–252, DOI:10.1007/978-1-61779-953-2_18.

(22) Banerjee, S. S.; Chen, D.-H. Fast Removal of Copper Ions by Gum Arabic Modified Magnetic Nano-Adsorbent. *J. Hazard. Mater.* **2007**, *147*, 792–799, DOI:10.1016/j.jhazmat.2007.01.079.

(23) Chabot, V.; Kim, B.; Sloper, B.; Tzoganakis, C.; Yu, A. High Yield Production and Purification of Few Layer Graphene by Gum Arabic Assisted Physical Sonication. *Sci. Rep.* **2013**, *3*, DOI:10.1038/srep01378.

(24) Batalha, I. L.; Hussain, A.; Roque, A. C. A. Gum Arabic Coated Magnetic Nanoparticles with Affinity Ligands Specific for Antibodies. *J. Mol. Recognit.* **2010**, *23*, 462–471, DOI:10.1002/jmr.1013.

(25) Guardia, P.; Labarta, A.; Batlle, X. Tuning the Size, the Shape, and the Magnetic Properties of Iron Oxide Nanoparticles. *J. Phys. Chem. C* **2011**, *115*, 390–396, DOI:10.1021/jp1084982.

(26) Granitzer, P.; Rumpf, K.; Venkatesan, M.; Roca, A. G.; Cabrera, L.; Morales, M. P.; Poelt, P.; Albu, M. Magnetic Study of Fe3O4 Nanoparticles Incorporated within Mesoporous Silicon. *J. Electrochem. Soc.* **2010**, *157*, K145, DOI:10.1149/1.3425605.

(27) Laurent, S.; Elst, L. Vander; Muller, R. N. Superparamegnetic Iron Oxide Nanoparticles for MRI. In *The Chemistry of Contrast Agents in Medical Magnetic Resonance Imaging*; Merbach, A. S.; Helm, L.; Tóth, É., Eds.; Wiley & Sons. Ltd.: Sussex, 2013; pp. 427–446.

(28) De Haan, H. W.; Paquet, C. Enhancement and Degradation of the R2* Relaxation Rate Resulting from the Encapsulation of Magnetic Particles with Hydrophilic Coatings. *Magn. Reson. Med.* **2011**, *66*, 1759–1766, DOI:10.1002/mrm.22944.

(29) Basly, B.; Felder-Flesch, D.; Perriat, P.; Billotey, C.; Taleb, J.; Pourroy, G.; Begin-Colin, S. Dendronized Iron Oxide Nanoparticles as Contrast Agents for MRI. *Chem. Commun.* **2010**, *46*, 985–987, DOI:10.1039/b920348f.

(30) HCT 116 ATCC ® CCL-247™ Homo sapiens colon colorectal carcinoma http://www.lgcstandards-atcc.org/products/all/CCL-247.aspx?geo_country=pt#generalinformation (accessed May 28, 2014).

(31) Mirshafiee, V.; Mahmoudi, M.; Lou, K.; Cheng, J.; Kraft, M. L. Protein Corona Significantly Reduces Active Targeting Yield. *Chem. Commun. (Camb).* **2013**, *49*, 2557–2559, DOI:10.1039/c3cc37307j.

(32) Mahmoudi, M.; Lynch, I.; Ejtehadi, M. R.; Monopoli, M. P.; Bombelli, F. B.; Laurent, S. Protein-Nanoparticle Interactions: Opportunities and Challenges. *Chem. Rev.* **2011**, *111*, 5610–5637, DOI:10.1021/cr100440g.

(33) Ge, Y.; Zhang, Y.; Xia, J.; Ma, M.; He, S.; Nie, F.; Gu, N. Effect of Surface Charge and Agglomerate Degree of Magnetic Iron Oxide Nanoparticles on KB Cellular Uptake *in Vitro*. *Colloids Surf. B. Biointerfaces* **2009**, *73*, 294–301, DOI:10.1016/j.colsurfb.2009.05.031.

(34) Mu, J. Z.; Gordon, M.; Shao, J. S.; Alpers, D. H. Apical Expression of Functional Asialoglycoprotein Receptor in the Human Intestinal Cell Line HT-29. *Gastroenterology* **1997**, *113*, 1501–1509, DOI:10.1053/gast.1997.v113.pm9352852.

(35) Mu, J. Z.; Fallon, R. J.; Swanson, P. E.; Carroll, S. B.; Danaher, M.; Alpers, D. H. Expression of an Endogenous Asialoglycoprotein Receptor in a Human Intestinal Epithelial Cell Line, Caco-2. *Biochim. Biophys. Acta* **1994**, *1222*, 483–491.

Chapter 4

A value-added exopolysaccharide as a coating agent for MRI nanoprobes

Fucopol, a fucose-containing exopolysaccharide (EPS) produced by the bacterium Enterobacter A47 DSM 23139 using glycerol as a carbon source, was employed as a new coating material for iron oxide magnetic nanoparticles (MNP). The coated particles were assessed as nanoprobes for cell labeling by Magnetic Resonance Imaging (MRI). The MNP were synthesized by a thermal decomposition method and transferred to aqueous medium by ligand-exchange reaction with *meso*-2,3-dimercaptosuccinic acid (DMSA). Covalent binding of EPS to DMSA-stabilized nanoparticles (MNP-DMSA) resulted in a hybrid magnetic-biopolymeric nanosystem (MNP-DMSA-EPS) with a hydrodynamic size of 170 nm, negative surface charge at physiological conditions and transverse to longitudinal relaxivities ratio, r_2/r_1, of 148. *In vitro* studies with two human cell lines (colorectal carcinoma - HCT116 - and neural stem/progenitor cells - ReNcell VM) showed that EPS promotes internalization of nanoparticles in both cell lines. *In vitro* MRI cell phantoms also showed superior performance of MNP-DMSA-EPS in ReNcell VM, for which iron dose-dependent MRI signal drop was obtained at relatively low iron concentrations (12 - 20 μg Fe/ml) and short incubation time. Furthermore, ReNcell VM multipotency was not affected by culture in the presence of MNP-DMSA or MNP-DMSA-EPS for 14 days. Our study suggests that Fucopol-coated MNP represent useful cell labeling nanoprobes for MRI.

Publications

Palma, S.I.C.J.; Rodrigues, C.A.V.; Carvalho, A.; Morales, M. P.; Freitas, F.; Fernandes, A. R.; Cabral, J. M.S.; Roque, A. C. A., *Nanoscale* **2015**, *7*, 14272–14283, DOI:10.1039/C5NR01979F.

Communications in conferences

Posters

Palma S.I.C.J., Marciello M., Carvalho A., Fernandes A.R., Freitas F., Morales M.P., Roque, A.C.A., A new fucose rich bacterial exopolysaccharide for SPION stabilization, 10th International Conference on the Scientific and Clinical Applications of Magnetic Carriers, Dresden, Germany (2014)

Oral Communications

S. Palma, M. Marciello, A. Carvalho, F. Freitas, J. Silva, P. Martins, C. A. V. Rodrigues, A. Fernandes, M. Puerto Morales, J. M. S. Cabral, A. C. A. Roque, Nanosystems for MRI cell labeling using magnetism, biopolymers and pH sensitive bio-coatings, 6th European Conference on Chemistry in Life Sciences, Lisboa, Portugal (2015)

4.1. Introduction

Iron oxide magnetic nanoparticles (MNP) represent an interesting platform with application in several areas, particularly in the biotechnological and biomedical fields, due to their biocompatibility and superparamagnetic properties. In the last two decades, a large number of research studies evaluated the use of MNPs in magnetic resonance imaging (MRI), in hyperthermia, as multimodal imaging agents, as nanovectors for drug and gene delivery, or in a combination of these imaging and therapeutic functions to build theranostic nanosystems.[1–3] Interactions between biological environment and MNPs are mediated by the coating material and functionalization, which allow to tailor the MNPs in terms of specific cell-type targeting, drug release, cellular uptake, multifunctionality or *in vivo* stealth properties. Hydrophilic coatings, usually composed of small molecules (e.g. *meso*-2,3-dimercaptosuccinic acid (DMSA)) or polymers, either synthetic (e.g. polyethyleneglycol (PEG)) or natural (e.g. dextran), are preferred due the compatibility with biological media and the ability to provide colloidal stabilization to the nanosystem.

Clinical application of MNPs is subjected to approval by health regulatory agencies (eg. Food and Drug Administration - FDA), which require the particles to be biodegradable following their administration.[4] Since inert synthetic coatings or encapsulation matrices are mostly not biodegradable, polysaccharides are appealing alternative materials. They are abundant in nature, hydrophilic, biodegradable and generally accepted as biocompatible. In addition, availability of functional groups for chemical modification[5] make polysaccharide-coated MNPs versatile nanoplatforms. Indeed, iron oxide based commercial MRI contrast agents are typically coated with dextran or chemically modified versions of this bacterial polysaccharide (e.g. Ferumoxides (Feridex/Endorem) from Advanced Magnetics (USA) and Ferucarbotran (Resovist), from Bayer Shering Pharma AG (Germany)).[6] Exopolysaccharides (EPSs) are polysaccharides secreted to the extracellular environment by many microorganisms. The extracellular nature of EPS simplifies their extraction process. EPS are mostly composed of neutral monosaccharides but in some cases amino-sugars and/or acidic sugars are also part of the composition. Some non-carbohydrate substituents (such as acetate, pyruvate, succinate, and phosphate) are also found in many microbial EPS.[7] Although dextran is still the most used microbial polysaccharide to coat MNPs for imaging, diagnosis and treatment,[8] other EPSs have been studied and reviewed in the literature.[5] For example, multifunctional MNP bearing a targeting moiety and an anticancer drug were developed based on EPS (mauran and gellan) coatings and showed potential for imaging and magnetic hyperthermia.[9] Similarly, pullulan derived coatings originated MNPs with potential for magnetic hyperthermia in human nasopharyngeal epidermal carcinoma cell line[10] and MRI labeling of rat mesenchymal stem cells.[11]

Fucopol is an EPS produced by *Enterobacter* A47 DSM 23139 using glycerol as the sole carbon source.[7] It is composed of fucose, galactose, glucose, pyruvate, succinate and acetate in the molar ratios 1.6:1.3:1.1:1.2:0.7:1.5. The polymer possesses a residual protein fraction of 5 wt.%.[7] This environmentally-friendly, sustainable EPS is considered a high added value product because, in addition to good flocculating and emulsion stabilizing properties, it is rich in fucose, which is one of the rare sugars, difficult to obtain but with many applications, from pharmaceutical to cosmetics.[7] Preparations containing fucose, fucose-containing oligomers or polymers were shown to have biological properties such as anti-carcinogenic, anti-inflammatory and induction of neuronal growth.[7,12] Our research group has previously shown the good performance of Fucopol as a coating material of magnetic particles employed in human antibody purification.[13] Due to the biological importance of fucose and the properties of the EPS, it was explored as a coating material for magnetic nanoparticles intended for biomedical applications, in particular, as MRI contrast agents.

Fucopol was covalently bound to *meso*-2,3-dimercaptosuccinic acid-functionalized MNP and the resulting nanosystem (MNP-DMSA-EPS) was characterized regarding its composition, size, magnetic and relaxometric properties. After evaluation of MNP-DMSA-EPS *in vitro* cytotoxic potential, the respective cell labeling efficacy was studied in two human cell lines (a colorectal cell line and a neural stem/progenitor cell line). Prussian blue staining, fluorescence microscopy, chemical quantification of iron internalization and *in vitro* MRI of cell phantoms were employed to assess the efficacy of the nanoprobes.

4.2. Experimental Section

4.2.1. Materials

Fucopol exopolysaccharide (EPS)[7] was produced by cultivation of the bacterium *Enterobacter* A47 DSM 23139, using glycerol as the sole carbon source, under controlled bioreactor conditions, as previously described.[11] The polymer was recovered from the culture broth by dialysis of the cell-free supernatant and freeze-dried.

4.2.2. Synthesis and phase transfer of iron oxide magnetic nanoparticles (MNP-DMSA)

Hydrophobic iron oxide magnetic nanoparticles were synthesized by the thermal decomposition of iron tri(acetylacetonate) in benzyl ether using 1,2-tetradecanediol as reducing agent, and oleic acid and oleylamine as surfactants.[14] To render these MNP hydrophilic a ligand-exchange reaction with DMSA was employed.[15] Briefly, a toluene dispersion of hydrophobic MNP was mixed with a solution of DMSA in dimethylsulfoxide (DMSO). After 48 h

incubation at room temperature, the solvent containing the oleic acid and oleylamine was discarded and the black hydrophilic nanoparticles were re-dispersed in ethanol. After several washes by centrifugation the nanoparticles were re-dispersed in milliQ water, basified to pH 10 and dialyzed against milliQ to provide the final DMSA coated MNP (MNP-DMSA).

4.2.3. Preparation of EPS-coated magnetic nanoparticles (MNP-DMSA-EPS)

Fucopol was covalently coupled onto the hydrophilic MNP-DMSA using carbodiimide chemistry. A Fucopol solution (5 mg/ml, in phosphate buffer, 0.1 M, pH 7.6) was prepared and centrifuged to remove any unsolubilized polymer fraction. Only the supernatant (3.7 ± 0.7 mg Fucopol/ml, quantified through the anthrone test[16]) was used for the coating reaction. To activate the carboxylic acid groups of DMSA, N-(3-Dimethylaminopropyl)-N′-ethylcarbodiimide (EDC) and N-Hydroxysuccinimide (NHS) were added to 2 ml of MNP-DMSA (2 mg/ml, in MES buffer, 0.1 M, pH 6) at the concentration of 2 mM and 50 mM, respectively, followed by 15 min of incubation in a rotating agitator (Stuart, SB3) (20 rpm) at room temperature. Then, the pH was adjusted to 7.6 and the activated MNP-DMSA were added dropwise to the polymer solution under vigorous (700 – 1000 rpm) magnetic agitation. The reaction continued in a rotating agitator (20 rpm) overnight at room temperature. MNP-DMSA-EPS were recovered by several cycles of centrifugation (9000 rcf, 15 min) and replacement of the supernatant by milliQ water. The larger aggregates were magnetically removed using a magnetic separator for microcentrifuge tubes (Bilatest M12+12, Sigma Aldrich).

4.2.4. Characterization of magnetic nanoparticles

Particle size and shape were characterized by Transmission Electron Microscopy (TEM) using a 100-kV JEOL JEM1010 microscope equipped with a Gatan Orius 200 SC digital camera. Hydrodynamic size (d_h) and zeta potential of the particles were determined using a Nanosizer ZS (Malvern). The mean value of the intensity-weighted size distribution, measured at pH 7, was used as d_h. Zeta potential variation with pH was measured in a 0.01 M KNO_3 solution (HNO_3 or KOH solutions were used for pH adjustment). To evaluate the particles' hydrodynamic diameter stability in physiological conditions, we have analyzed the Z-Average value of samples dispersed in both Phosphate Buffered Saline (0.01 M; with 0.15 M NaCl, pH 7.4) (PBS) and Dulbecco's Modified Eagle's culture medium supplemented with bovine serum. Two time points were studied: t = 0 h (at the moment of the nanoparticles dispersion) and t = 2 h (2 h after the preparation of the nanoparticles dispersion. Inductively coupled plasma - atomic emission spectroscopy (ICP-AES) (Horiba Jobin-Yvon, Ultima) was used to determine the iron content of the MNP samples. Fourier transform infrared (FTIR) spectra were acquired using a

Nicolet 20 SXC FTIR. Thermogravimetric analysis (TGA) of MNP-DMSA and MNP-DMSA-EPS powder was carried out in a Seiko TG/DTA 320 U, SSC 5200 thermobalance.

Magnetization measurements were performed using a vibrating sample magnetometer (VSM) (MagLab VSM, Oxford Instruments). Magnetization loops were measured at 250 K, corrected by subtracting the diamagnetic contribution of the dispersants (50 μl) and the sample holder, and normalized to the saturation magnetization value (m_{max}) of each sample.

Temperature dependent zero-field cooling (ZFC) and field cooling (FC) magnetization measurements were performed by cooling the samples to 5 K under a zero or a 0.01 T magnetic field, respectively. Then, the magnetization was measured while the samples were heated (3 K/min) to 250 K under a 0.01 T field.

The relaxometric properties of MNP-DMSA-EPS were evaluated in a 7 T NMR Brucker Avance III Spectrometer at 25ºC. Water suspensions of MNP-DMSA-EPS at different iron concentrations were prepared. Longitudinal relaxation time T_1 was measured using an inversion recovery pulse sequence with TR between 3 and 10 s. Transverse relaxation time T_2 was measured using a Call-Purcell-Meiboom-Gill pulse sequence with TE of 1 ms and the number of echoes needed to cover a time interval of about 10 times T_2. Longitudinal ($R_1 = 1/T_1$) and transversal ($R_2 = 1/T_2$) relaxation rates were plotted against iron concentration and a linear behavior was found. The lines slopes are the longitudinal (r_1) and transverse (r_2) relaxivities, that measure the efficiency of the nanoparticles as MRI contrast agents. T_2-weighted MRI phantom images of MNP-DMSA-EPS water suspensions at 0.1, 0.4, 0.8 and 1 mM (Fe) were obtained with a multi-echo image sequence (TR = 5 s; T_t = 8 ms).

4.2.5. Cell culture and labeling

Two adherent human cell lines were used in this work: a colorectal carcinoma cell line (HCT116) and a neural stem/progenitor cell line (ReNcell VM). HCT116 cells were cultured in Dulbecco's modified Eagle's medium (DMEM, Life Technologies) supplemented with 10% (v/v) fetal bovine serum (Life Technologies) and 1% (v/v) of penicillin-streptomycin (Life Technologies) at 37 ºC with 99% relative humidity and 5% CO_2. ReNcell VM cells were seeded in tissue culture plates or glass coverslips sequentially coated with poly-L-ornithine (Sigma-Aldrich, 15 μg/ml, 30 min at 37°C) and laminin (Sigma-Aldrich, 10 μg/ml, 3 h at 37°C), and cultured in DMEM/F12 medium supplemented with 20 ng/ml EGF (Prepotech), 20 ng/mlL FGF-2 (Peprotech), 1% N2 supplement (Life Technologies), 20 μl/ml B27 supplement (Life Technologies), 20 μg/ml additional insulin (Sigma-Aldrich), 1.6 g/l additional glucose (Sigma-Aldrich) and 1% penicillin/streptomycin at 37ºC and 5% CO_2 humidified environment.

Cells were incubated under the standard conditions referred above until 70-80% confluence was reached. Cells were then labeled by incubating with the corresponding culture

medium with different concentrations of MNPs for 48h (in the case of HCT116)[17] or for 4h followed by 24h recovery in fresh culture medium (in the case of ReNcell VM).[18,19] Nanoparticles were sterilized by filtration with a sterile membrane filter of 0.20 μm pore diameter (MNP-DMSA) or by autoclaving 20 min at 120ºC (MNP-DMSA-EPS).

4.2.6. Multi-lineage differentiation of ReNcell VM

ReNcell VM differentiation into neuronal and glial lineages was induced by changing the culture medium and withdrawing EGF and FGF-2. Cells were cultured using a 1:1 mixture of DMEM/F12 supplemented with N2 (1x) and Neurobasal medium (Life Technologies) supplemented with B27 (1×). Medium was changed every 2-3 days. The differentiation process was carried out for 14 days.

Differentiation was evaluated by immunostaining for the neuronal marker β-III Tubulin (Tuj1, Covance) and for astrocyte marker glial fibrillary acidic protein (GFAP, Millipore). Cells were fixed with paraformaldehyde (PFA, 4%, Sigma) for 30 min at room temperature, and then washed twice with phosphate buffered saline (PBS, Life Technologies). Cells were incubated for 45 min at room temperature with blocking solution (PBS with 0,1% Triton X-100 and 10% normal goat serum (NGS)). Afterwards, cells were incubated at 4°C overnight with the primary antibodies diluted (Tuj1 1:2000, GFAP 1:100) in staining solution (PBS with 0,1% Triton X-100 and 5% NGS). Cells were then washed once with PBS and incubated with the appropriate secondary antibody (Life Technologies, dilution 1:500) for 1 h at room temperature in a dark container. Finally, cells were washed once with PBS, incubated with DAPI (1.5 μg/ml in PBS, Sigma) for 2 min at room temperature and washed twice with PBS. The stained cells were visualized under a fluorescence microscope (Leica DMI 3000B).

4.2.7. Cytotoxicity evaluation

The impact of nanoparticles and Fucopol on the viability of HCT116 and ReNcell VM cultures was evaluated using a standard 3-(4,5-dimethylthiazol-2-yl)-2,5-diphenyl tetrazolium bromide (MTT) colorimetric assay as described previously.[20] Briefly, cells were seeded in 96 well plates at 7.5 $\times 10^3$ cells/well and labeled with MNP-DMSA and MNP-DMSA-EPS at different iron concentrations. Cells were also incubated with EPS at concentrations corresponding to the EPS content in MNP-DMSA-EPS at the chosen iron concentrations (calculated from TGA data).

After labeling, the culture medium was removed and replaced by fresh medium containing MTT (0.45 mg/ml). After 3 h of incubation in standard culture conditions, the medium was replaced by dimethyl sulfoxide (DMSO, Sigma-Aldrich) to dissolve the formazan crystals obtained as a result of MTT metabolization. The absorbance of the wells at 540 nm

(abs@450nm) and 630 nm (abs@630nm) was measured in a microplate reader (Microplate Titre Infinite F200, TECAN Spectra). Cell viability was calculated using the equation:

$$cell\ viability\ (\%) = \frac{(abs@540nm - abs@630nm)_{sample}}{(abs@540nm - abs@630nm)_{control}} \times 100 \quad (4.1)$$

where *sample* refers to cells incubated with nanoparticles or EPS, and *control* refers to cells without nanoparticles or EPS.

Determination of the half maximal inhibitory concentration (IC_{50}) for each nanoparticle type and EPS was performed by fitting the viability data to a dose-response sigmoidal curve.[20]

4.2.8. Identification of cellular iron by Prussian blue staining

For bright field microscopy observation, cells were seeded in coverslips on the bottom of the wells of 24-well plates at 1×10^5 cells/well, incubated in standard conditions and labeled with MNP-DMSA (55 µg Fe/ml for HCT116 and 50 µg Fe/ml for ReNcell VM) or MNP-DMSA-EPS (82 µg Fe/ml for HCT116, and 16 µg Fe/ml for ReNcell VM). After labeling, cells were stained with Prussian blue for iron identification and counterstained with neutral red as described previously[20] and visualized by bright field microscopy. Slides were observed using an Olympus CX41 microscope equipped with an Olympus SC30 camera.

4.2.9. Intracellular localization of magnetic nanoparticles

To determine the intracellular location of MNP-DMSA-EPS, fluorescent labeling of lysosomes with GFP was performed and preparations were observed under fluorescence and bright field microscopy to look for co-localization of nanoparticles and lysosomes. HCT116 and ReNcell VM cells were seeded in coverslips at the bottom of 35 mm petri dishes or wells of 24-well plate, at 1×10^4 cells/cm^2, cultured in standard conditions and labeled with MNP-DMSA-EPS at 82 µg Fe/ml and 16 µg Fe/ml, respectively. 20 h before the end of the incubation time, Cell-Light Lysosomes-GFP, BacMam 2.0 reagent (Life Technologies, USA) was added directly to the cells (25 particles per cell) and left incubating overnight. Cells were, then, washed with PBS and fixed with ice-cold paraformaldehyde (4% v/v in PBS). The preparation was air dried and mounted in the microscope slide using 5 µl of DAPI solution. Slides were observed using an Olympus BX51 microscope equipped with an Olympus DP50 camera and the Cell F View Image System Software.

4.2.10. Iron quantification

Cells were plated at 1×10^5 cells/well in 24-well plate wells, cultured in standard conditions and labeled with MNP-DMSA (54 µg Fe/ml for HCT116, and 46 µg Fe/ml for ReNcell VM) or MNP-DMSA-EPS (57 µg Fe/ml for HCT116, and 16 µg Fe/ml for ReNcell VM), as quantified by ICP in the culture media. After labeling, the supernatant was collected from each well and cells were detached from the wells, re-suspended in culture medium, counted using a hemocytometer and centrifuged for 10 min at 5000 rpm. Cell pellet (fraction 1), cell supernatant (fraction 2) and well supernatant (fraction 3) were separately digested with 100 µl of *aqua regia* for 30 min at 90ºC, diluted to 1 ml with milliQ water and analyzed separately for iron by ICP-AES. The iron in the cellular fraction (sum of fraction 1 and fraction 2) was normalized to the number of cells and to the total mass of iron (sum of the three fractions).

4.2.11. *In vitro* MRI of cell phantoms

Cells were plated in 24-well plates at 1×10^5 cell/well, cultured in standard conditions and labeled with MNP-DMSA-EPS at three increasing iron concentrations (61.5, 82 and 102.5 µg Fe/ml for HCT116 cells and 12, 16 and 20 µg Fe/ml for ReNcell VM cells). After labeling, cells were prepared for MR imaging as described previously.[20] Briefly, cells were washed, collected by centrifugation, fixed with cold paraformaldehyde, re-dispersed in PBS and counted using a hemocytometer. 3×10^5 HCT116 cells and 5.7×10^5 ReNcell VM cells were dispersed in 0.1 ml of PBS, mixed with 0.2 ml aliquots of fresh 0.75% (m/v) agarose and transferred to 5 mm diameter NMR tubes for imaging after solidifying. T_2-weighted MR images were obtained in a magnetic field of 7 T, at 25 ºC, using a Bruker Avance III Spectrometer (160 G/cm imaging gradient) and a Flash imaging sequence (TR = 110 ms, TE = 1.7 ms, with a 20º excitation angle and NEX of 32). MRI signal was quantified using ImageJ software (National Institutes of Health) to calculate the histogram, the average pixel value and the integrated density (sum of all pixel values divided by the average pixel value) over a 6 mm^2 circular region of interest placed in the center of each cell phantom image.

4.3 Results and Discussion

4.3.1. Particle size, composition and surface chemistry

Iron oxide magnetic nanoparticles were synthesized by thermal decomposition of iron(III) acetylacetonate in benzyl ether in the presence of tetradecanediol, oleic acid and oleylamine. The resulting particles are monodisperse but hydrophobic. To render them

hydrophilic, the oleic moieties originally at the surface of the particles were replaced by DMSA through a ligand-exchange reaction,[15] leaving carboxylic acid groups at the surface of the particles. The carboxylate functionalities were then used as chemical anchors to couple Fucopol exopolysaccharide (EPS) through the amine groups of the associated protein. EDC/NHS chemistry was chosen to promote the covalent conjugation of the carboxylic and amine groups. During the coating reaction, and due to its high molecular weight (5.8×10^6 g/mol),[7] Fucopol forms a network that entraps multiple cores of MNP-DMSA (which alone present d_h = 15±2 nm; d_{core}= 7±1 nm), forming aggregates with hydrodynamic diameter of 168 ± 40 nm (Figure 4.1 A and B) and polydispersity index of 0.25. Each aggregate (particle) is thus estimated to contain 14000 iron oxide magnetic cores.

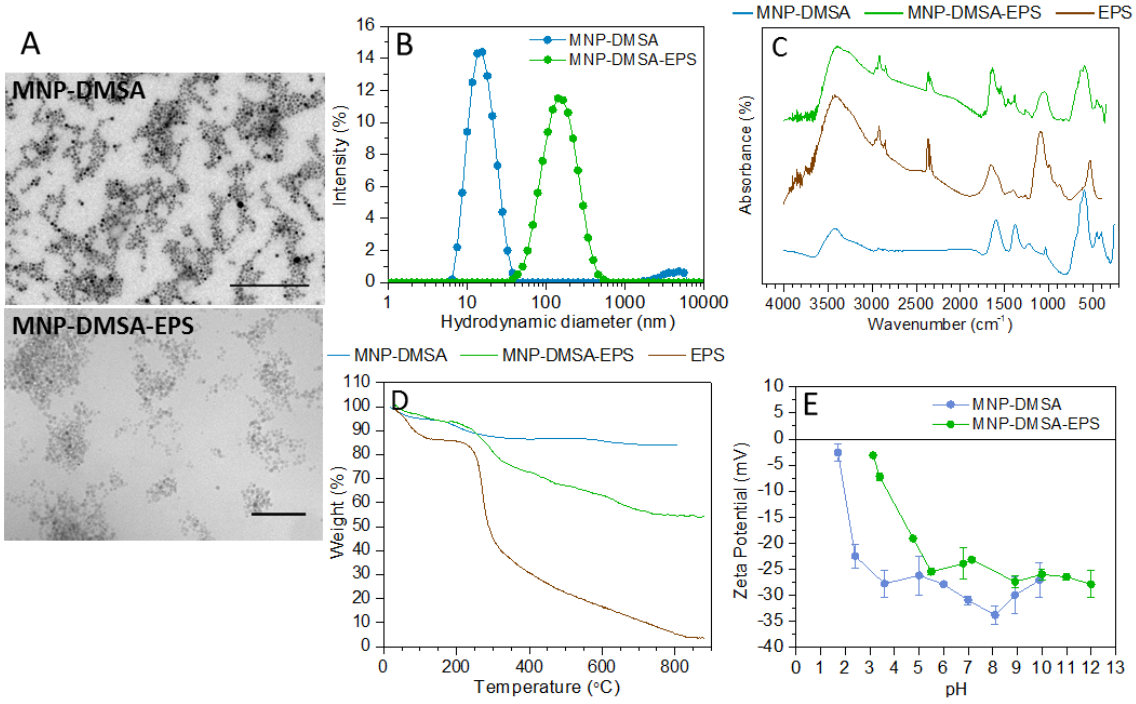

Figure 4.1 Characterization of size and composition of the nanoparticles before and after EPS coating. (A) Morphology of MNP-DMSA and MNP-DMSA-EPS by TEM (scale bars: 100 nm); (B) hydrodynamic diameters; (C) FTIR spectra of particles and EPS; (D) thermogravimetric analysis of particles and EPS; (E) evolution of zeta potential with pH.

Despite being pointed out as a drawback of polysaccharides, the natural batch-to-batch variability of Fucopol was not a problem in this work. Namely, no influence on MNP-DMSA-EPS size, morphology and colloidal stability was observed when different batches of polymer were employed.

Dispersion of the nanoparticles in physiological media like PBS or cell culture medium supplemented with fetal bovine serum (FBS) resulted in aggregation and increase of polydispersity (Figure 4.2 A and B, respectively). Interestingly, while MNP-DMSA maintain the

Z-Average in PBS and culture medium, MNP-DMSA-EPS show stronger aggregation in PBS than in culture medium and, after 2 h of incubation in the later conditions, tend to their native Z-Average (139 ± 35 nm, measured in water at pH 7). This behavior thus shows that interaction with the dispersant is a dynamic process.

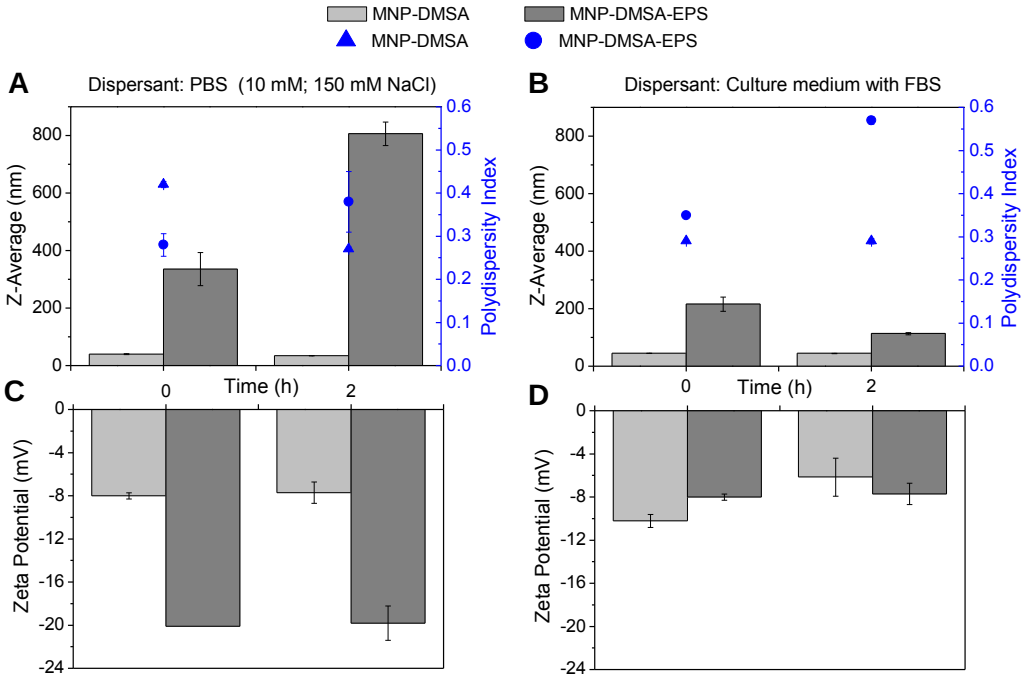

Figure 4.2. Variation of hydrodynamic diameter, polydispersity index and zeta potential of MNP-DMSA and MNP-DMSA-EPS dispersed in different conditions. (A and C) MNPs dispersed in phosphate buffered saline (PBS); (B and D) MNPs dispersed in DMEM culture medium with fetal bovine serum (FBS). Measurements were taken immediately after adding the particles to the dispersants and after 2 h of incubation in those dispersants.

FTIR spectrum of MNP-DMSA-EPS (Figure 4.1 C) presents, in the regions of 600 cm^{-1} and 400 cm^{-1}, the typical bands from Fe-O bonds vibrations in the spinel structure of magnetite.[21] Compared to MNP-DMSA, extra bands of weak intensity attributed to the oxidation of magnetite to maghemite appear together with these two main bands, in particular in the 600 cm^{-1} region, for MNP-DMSA-EPS.[21] The coating reaction thus has an effect on the iron oxide crystalline structure at the surface of the particles. FTIR was also used to confirm the presence of the EPS shell on the nanoparticles. Indeed, the Fucopol fingerprint band (the envelope between approximately 1200 and 900 cm^{-1})[7] is also present in MNP-DMSA-EPS spectrum and not in that of MNP-DMSA. This band corresponds to skeletal C-O and C-C vibrations bands of glycosidic bonds and pyranoid rings.[22] Also, the less intense band at 1265 cm^{-1}, present in both EPS and MNP-DMSA-EPS spectra, can be associated with the vibration of C-O-C of acyl groups.[22] The band present at ~1650 cm^{-1} in MNP-DMSA-EPS may be attributed to contributions from C=O stretching vibrations from the peptide bond (amide I band)[23] formed

through the covalent conjugation of EPS amine and DMSA carboxyl groups. It may also be associated with the vibrations of C=O from carboxylates present in EPS. The appearance of a band at around 1540 cm^{-1} in the spectrum of MNP-DMSA-EPS that resembles the amide II band (associated with N-H bending and C-N stretching vibrations in amide bonds),[23] confirms the effectiveness of the covalent conjugation of EPS onto the nanoparticles.

The TGA curves (Figure 4.1 D) also support the presence of EPS on MNP-DMSA-EPS due to the similar weight loss profiles of this sample and free EPS between 200ºC and 800ºC (a first accentuated step at 275ºC followed by a less pronounced and longer step). The curves of MNP-DMSA and MNP-DMSA-EPS present an initial weight loss of 5% due to water removal, followed by loss of DMSA or DMSA and EPS. MNP-DMSA curve reveals that DMSA is lost at around 200ºC and corresponds to approximately 11% of MNP-DMSA total weight. After coating with EPS, 40% of the nanoparticles weight is lost (Figure 4.1 D), which means that EPS constitutes 29% of the nanoparticles total weight. Taking in consideration the EPS molecular weight, the density of Fe_2O_3 (5.24 g/cm^3) and the number of cores per aggregate calculated above, one can estimate 725 EPS molecules per aggregate, that corresponds to 0.05 EPS molecules per core.

Due to the presence of succinate, pyruvate and glucuronic acid in the composition of EPS,[7] EPS-coated nanoparticles maintain negative zeta potential for pH values higher than 3 (Figure 4.1 E). However, the presence of salt in solution affects the zeta potential. We observe a value of -32 ± 4 mV in milliQ water, at pH 7, which increases to -23.2 ± 0.2 mV when the dispersion contains 0.01 M of KNO_3. This shows that colloidal stability does not depend only on steric interactions between the polymer chains but also on electrostatic interactions. It is known that interaction of nanoparticles with complex biological fluids leads to the formation of a protein corona that changes the particles' surface properties and may influence their stability and interaction with cells.[24–26] In this work, besides causing an initial aggregation of MNP-DMSA and MNP-DMSA-EPS, the interaction of particles with cell culture medium supplemented with FBS increased their surface charge to values near neutral (Figure 4.2. D), probably due to adsorption of proteins and other biomolecules that compose the culture medium onto the surface of the MNPs.

4.3.2 Magnetic properties and relaxivities measurements

The magnetization measurements at room temperature (Figure 4.3 A) revealed that MNP-DMSA and MNP-DMSA-EPS present superparamagnetic behavior. Wasp-waist loops are observed for both samples (Figure 4.3 A and Figure 4.4 A), but in larger extent for MNP-DMSA-EPS. This indicates that the iron cores are composed of two distinct magnetic phases[27,28] and that the EPS coating reaction magnified the differences in magnetic anisotropy of those two

phases. This is consistent with a core-shell structure for the magnetic cores in MNP-DMSA-EPS, composed of a well crystalline magnetite core and a more oxidized surface layer, as suggested by the FTIR spectra (Figure 4.1 C), and further distorted by the polymer coupling as suggested by the saturation at larger fields (Figure 4.3 A). When the exchange between a soft magnetic material and a hard material is positive, the loop is conventional. However, for negative (antiferromagnetic) exchange, the wasp-waist loop is obtained.[28]

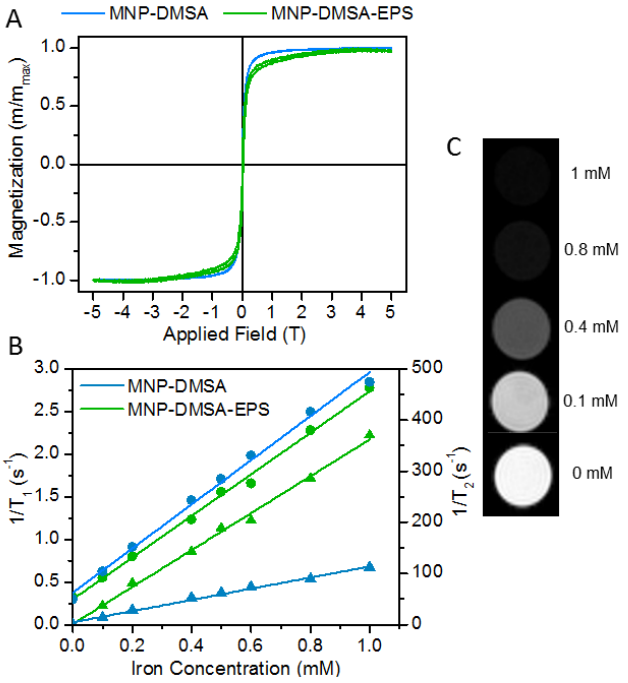

Figure 4.3. Evaluation of magnetic and relaxometric properties of MNP-DMSA and MNP-DMSA-EPS. (A) Magnetization loops of the nanoparticles before and after coating with EPS, measured at 250 K; (B) Determination of longitudinal (r_1) and transversal (r_2) relaxivity values before and after coating with EPS (circles: $1/R_1$; triangles: $1/R_2$); (C) In vitro T_2-weighted MRI phantoms of water dispersions of MNP-DMSA-EPS at different iron concentrations.

To evaluate the potential of the EPS-coated nanoparticles as MRI contrast agent we have evaluated their ability to change the proton longitudinal (T_1) and transverse (T_2) relaxation times at room temperature. Figure 4.3 B shows the linear dependence found between the longitudinal ($R_1=1/T_1$) and transverse ($R_2=1/T_2$) proton relaxation rates and iron concentration for MNP-DMSA and MNP-DMSA-EPS in water suspensions. From the slope of these linear relations, we conclude that MNP-DMSA-EPS presents low longitudinal relaxivity, r_1, (2.4 $mM^{-1}s^{-1}$) and high transverse relaxivity, r_2, (361 $mM^{-1}s^{-1}$) as it is typical of superparamagnetic nanoparticles, which can act as negative MRI contrast agents (decrease in MRI signal, i.e., a darkening effect). Compared to MNP-DMSA (r_1 = 2.6 $mM^{-1}s^{-1}$ and r_2 = 110 $mM^{-1}s^{-1}$), MNP-DMSA-EPS maintain the longitudinal value but increase the transversal relaxivity (Figure 4.3 B). The larger transverse relaxivity could be

associated with the clustered nature of MNP-DMSA-EPS because the aggregation of several small nanoparticles increases the effective magnetic size of the system.[29,30] However, the peak for the blocking temperature in the zero field cooling curve (ZFC) of MNP-DMSA-EPS (Figure 4.4 B) is not significantly shifted to the right in comparison to the uncoated nanoparticles, suggesting that the aggregation alone does not justify the increase in r_2. On the other hand, significant dipolar interactions do take place within MNP-DMSA-EPS as ZFC curve keeps increasing after the blocking temperature, which also has the effect of increasing the effective magnetization of the nanoparticles and, consequently, can lead to the increase of the transverse relaxivity value.

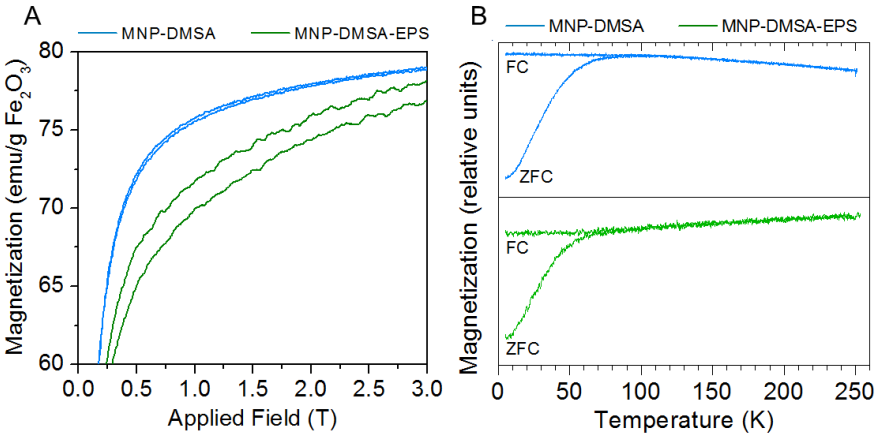

Figure 4.4. Details regarding magnetic properties of MNP-DMSA and MNP-DMSA-EPS. (A) Detail of MNP-DMSA and MNP-DMSA-EPS magnetization loops. (B) Zero-field cooling (ZFC) and field cooling (FC) curves.

Comparison of MNP-DMSA-EPS with similar hydrodynamic size commercial MRI agent Endorem/Feridex (d_h between 120 nm and 180 nm) reveals that our nanoparticles present a much higher r_2 value and similar r_1 (r_1 = 2.2 $mM^{-1}s^{-1}$ and r_2 = 182 $mM^{-1}s^{-1}$ for Endorem/Feridex) at the same magnetic field[31], what makes the ratio r_2/r_1 1.8 times larger for our particles (148 vs. 83). This ratio is used to quantify and compare the efficacy of a negative contrast agent for MRI. For negative contrast agents, larger r_2/r_1 ratios indicate more sensitive systems, as lower nanoparticle concentration is sufficient to darken MRI signal. Therefore, we anticipate that our EPS-coated MNP could increase the efficacy of MRI contrast compared to Endorem/Feridex, which has also a bacterial exopolysaccharide coating and similar clustering degree, given the respective hydrodynamic diameter. In the T_2-weighted MRI phantom images obtained for aqueous suspensions of MNP-DMSA-EPS (Figure 4.3 C), it is visible that signal intensity decreases (darkening) with the increase of nanoparticle concentration, similar to what happens with dispersions of commercial superparamagnetic contrast agents.[32] Even for

the lower iron concentration (0.1 mM = 5.6 µg/ml) there is a noticeable signal difference between water and the nanoparticles dispersion.

4.3.3 Cell-nanoparticle interactions

Given the promising performance of MNP-DMSA-EPS, revealed by their relaxivities values, we further tested their efficacy as MRI negative contrast agent to label *in vitro* cultured cells. We have used HCT116 and ReNcell VM human cell lines as model systems to study interactions between MNPs and cells, namely, the impact on cell viability, iron uptake, intracellular localization of internalized nanoparticles and effect on MRI cell phantoms.

We aimed to assess the impact of Fucopol (EPS) coating on nanoparticle cytotoxicity. Therefore, for comparison purposes, we have evaluated MNP-DMSA-EPS, MNP-DMSA and EPS cytotoxicity profiles in parallel, using the MTT assay (colorimetric test based on cellular metabolic activity) for this purpose.

In the concentrations range tested, the two cell lines present distinct viability profiles after incubation with MNPs or EPS alone (Figure 4.5, Figure 4.6). After 48h of incubation with cells, MNP-DMSA, MNP-DMSA-EPS and EPS have an effect on the viability of HCT116 cells (Figure 4.5 A), with relative half maximal inhibitory concentrations (IC_{50}) of approximately 55 µg Fe/ml for MNP-DMSA, 82 µg Fe/ml for MNP-DMSA-EPS and 96 µg Fe/ml for free EPS dissolved in the culture medium. Interestingly, HCT116 cell viability in presence of MNP-DMSA-EPS is lower than in the presence of MNP-DMSA or EPS alone. Stronger stress reaction of colon epithelial cancer cells to stabilized MNP compared to bare MNP or free stabilizer molecules were reported previously and justified by increased contact area between cells and stabilizer molecules upon contact with coated MNPs.[33] The different reactions to the same particle types are probably related with distinct sensitivity of the cell types to the tested materials and with nanoparticles exposure times. As Laurent *et al*. have previously demonstrated[34], cytotoxicity profile resulting from the same nanoparticles, iron concentrations and incubation times is strongly dependent on cell type. On the other hand, exposition time is also an important factor that influences the response of a certain cell line to the presence nanoparticles. In some cases, longer incubation times promote the recovery of viability,[17] but in others it enhances the particles cytotoxic effect.[17,35] In our study, 4h exposition of ReNcell VM cells to nanoparticles or EPS followed by 24h of recovery did not cause a pronounced decrease in the cell viability profile (Figure 4.5 B, Figure 4.6), which is similar to the results found by other authors for primary human fetal neural precursor cells[19] and adipose-tissue derived stem cells.[35] In the iron concentration range and exposition time used in our work, ReNcell VM cells viability is maintained above 80% and no IC_{50} value is reached for the three materials.

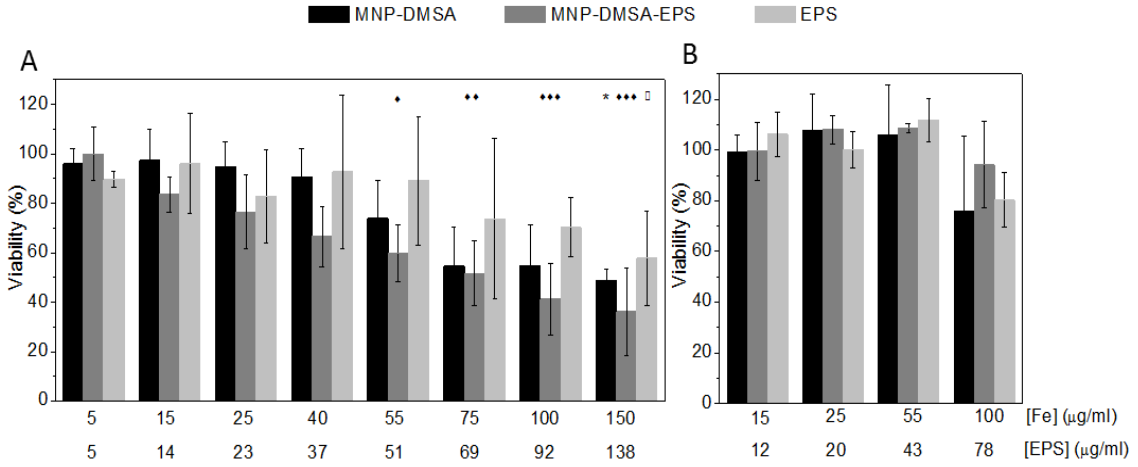

Figure 4.5. Cell cytotoxicity assay results for HCT116 and ReNcell VM cells incubated with MNPs and EPS. (A) HCT116 cell line, after 48h exposition to nanoparticles and EPS; (B) ReNcell VM cell line, after 4h exposition to nanoparticles and EPS plus 24h of recovery in fresh medium. Data is expressed as mean ± standard deviation of at least two independent experiments. Different symbols indicate statistical difference of cells incubated with MNP-DMSA (*), MNP-DMSA-EPS (♦) or EPS (□) compared to untreated control cells. Regular two-way ANOVA, followed by post-hoc pairwise comparison with Tukey's test was performed for statistical analysis using GraphPad Prism 6.0 software (USA); 1 symbol ($p<0.05$), 2 symbols ($p<0.005$), 3 symbols ($p<0.001$).

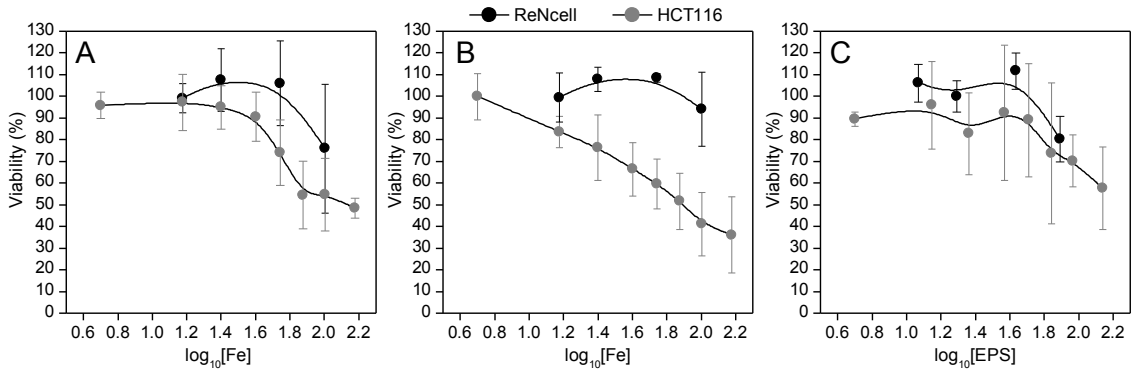

Figure 4.6. Representation of cell cytotoxicity assay results in logarithmic form ($\log_{10}$ [Fe] (or $\log_{10}$ [EPS])). Effect of (A) MNP-DMSA, (B) MNP-DMSA-EPS and (C) EPS on cell viability for HCT116 (grey symbols) after 48h of incubation and ReNcell VM (black symbols) after 4h of incubation plus 24h of recovery in fresh medium. Points are connected by a B-spline to guide the eye.

Microscopic observation of Prussian blue stained preparations (Figure 4.7 A) allowed a preliminary evaluation of the particles labeling efficacy. No significant alteration of cell morphology was detected in MNP treated cells compared to untreated cells and no iron was detected inside the nucleus. MNP-DMSA-EPS are visible in both cell types as blue spots and aggregates distributed in the cytoplasm or attached to the cell surface. In ReNcell VM cells the blue spots are larger and more intense. This may be related with a stronger uptake of MNP-DMSA-EPS in ReNcell VM than in HCT116 cells or simply reflects the different incubation conditions used for the two cell types. Much less cellular uptake was observed when MNP-

DMSA were used. Both particle types possess negative zeta potential (that comes close to neutral after contact with culture medium), however MNP-DMSA-EPS present higher internalization in the two cell lines used in this work. Interactions between the cell membranes and nanoparticles' surfaces probably explain the first contact between MNPs and cell membrane, but given the size of the aggregates formed by MNP-DMSA-EPS, cell membrane-nanoparticle interactions may be facilitated. Moreover, the presence of fucose residues (which are known to be involved in cell-cell adhesion, cell-matrix adhesion, and cell-cell signaling processes[36]) may also contribute to enhanced uptake of MNP-DMSA-EPS compared to MNP-DMSA through interaction with cell surface receptors.

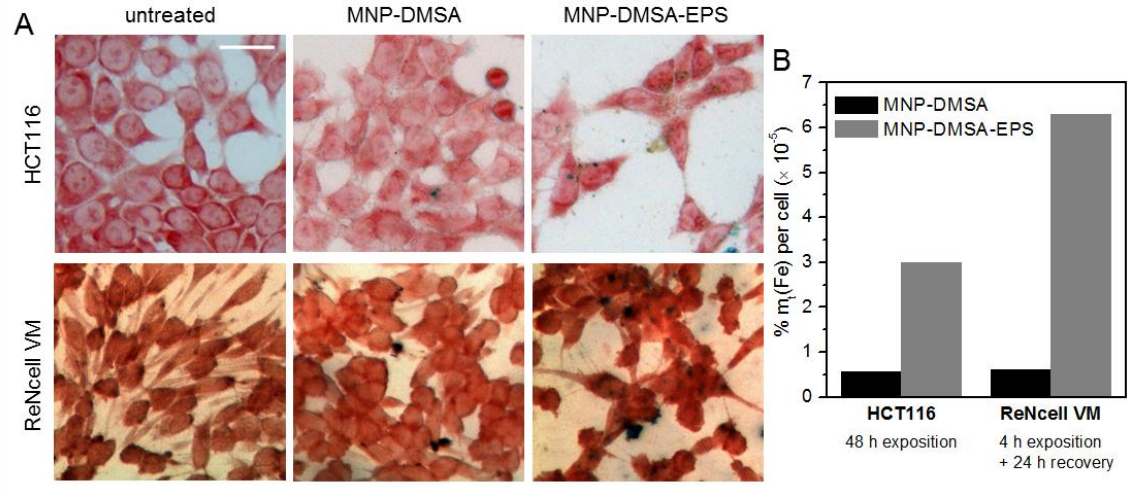

Figure 4.7. Observation and quantification of iron in cell cultures incubated with MNP-DMSA and MNP-DMSA-EPS. HCT116 cells were exposed to the nanoparticles for 48h. ReNcell VM cells were exposed to the nanoparticles for 4h, followed by a recovery period of 24h. (A) Bright field microscopy images of Prussian blue stained cells (scale bar: 10µm); (B) Proportion of total iron per cell, quantified by ICP.

Table 4.1. Uptake of iron by HCT116 and ReNcell VM after incubation with MNP-DMSA and MNP-DMSA-EPS.

Cell line	***Incubation time with MNPs***	***MNP in the culture medium (µg Fe/ml)***		***Relative Fe uptake % mt(Fe)/cell (×10^{-5})***		***Absolute Fe uptake (pg Fe/cell)***	
		MNP-DMSA	MNP-DMSA-EPS	MNP-DMSA	MNP-DMSA-EPS	MNP-DMSA	MNP-DMSA-EPS
HCT116	48 h	54	46	0.57	3.00	1.22	8.35
ReNcell VM	4h + 24 h recovery	57	16	0.62	6.30	1.11	4.76

Quantification of iron in cell fractions by ICP-AES after labeling (Figure 4.7 B and Table 4.1) confirmed the Prussian blue observations. Since we have incubated HCT116 and ReNcell VM cells with different iron concentrations for each particle type, it was important to normalize the mass of cellular iron to the total mass of iron from MNPs in cell culture and to the number of cells. The normalized values show the same percentage of iron uptake by both cell lines when

incubated with MNP-DMSA However, after EPS conjugation to MNP-DMSA, a 5-fold and a 10-fold increase of cellular iron percent was observed for HCT116 and ReNcell VM cells, respectively (Figure 4.7 B and Table 4.1). In this case, cellular iron is mainly due to internalized nanoparticles with a small contribution of nanoparticles adsorbed to the cell surface. On the other hand, for MNP-DMSA, internalized and adsorbed nanoparticles contribute in equal proportions for the total iron found per cell (Figure 4.8 and Table 4.2). In ReNcell VM, although particle concentration and exposition time were lower, the double percentage of iron was found in the cellular fraction when compared with HCT116 cells (Table 4.1). According to the literature, fucose-galactose compounds mediate a pathway for the modulation of neuronal growth and morphology[37] and can be used in culture of neurons *in vitro* to induce neuronal growth and neurite elongation.[38] Fucose and galactose are the main components of Fucopol and thus this EPS may contribute to the enhanced MNP-DMSA-EPS uptake by neural stem/progenitor cells in relation to HCT116 cells.

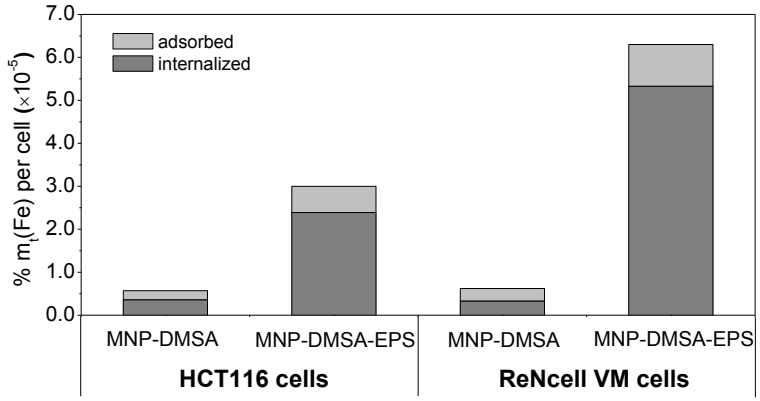

Figure 4.8. Contribution of internalized and adsorbed nanoparticles for the cellular iron found in cells after labeling with MNP-DMSA or MNP-DMSA-EPS. (A) HCT116 cells (B) ReNcell VM cells.

Table 4.2. Distribution of cellular iron between internalized and adsorbed fractions

	Cell line			
	HCT166		***ReNcell VM***	
	% internalization	% adsorption	% internalization	% adsorption
MNP-DMSA	63	37	53	47
MNP-DMSA-EPS	80	20	85	15

Comparison of our results with other studies is complex because several factors can influence labeling efficiency. These include, for example, cell type, concentration of iron, incubation time, presence/absence of transfection agents, nanoparticle coating material or even the experimental protocol used for labeling efficiency evaluation. Previous reports dealing with human colon cancer and neural stem cells treated with iron oxide nanoparticles coated with other polysaccharides observed iron internalization at different experimental conditions.

Compared to our results, LS174T colon cancer cell line presented lower iron uptake upon incubation with dextran-coated MNP (0.006 pg Fe/cell, after incubation for 1h at 100 µg/ml) but enough to obtain MRI contrast *in vitro*.[39] More recently, oleic acid coated MNP encapsulated in the polysaccharide hyaluronan (HA) were shown to have an inhibitory effect towards several human cancer cell lines (including HCT116) and visible by MRI after injection in a murine intramuscular glioblastoma tumor model. While nanoparticles studied in our work were non-toxic at low iron concentrations, and do not inhibit growth, HA-MNPs originated negative viabilities at 10 – 500 µg Fe/ml for 24, 48 and 72 h.[40] Regarding stem cells, the standard MRI labeling protocols are based in the utilization of a transfection agent (TA) together with commercially available iron oxide magnetic nanoparticles to promote internalization.[6,18,41] However, TAs are usually complex to use and cytotoxic.[6,42] Therefore, incubation of cells with the nanoparticles alone would be preferred. Some work has been done on modification of polysaccharide coatings, namely with positively charged chemical groups, to produce magnetic nanomaterials that provide enough labeling efficacy *per se*[11,35] but in this work we have evaluated the performance of MNP coated with the EPS Fucopol without any modification. We have seen that 4h of incubation with MNP-DMSA-EPS at 16 µg Fe/ml allowed a labeling efficiency of 5 pg Fe/cell in ReNcell VM (Table 1), similar to what was reported previously for Feridex to label neural progenitor cells (75 µg Fe/ml, 48 h, uptake of 5.1 pg Fe/cell)[43] and mesenchymal stem cells derived from the iliac crest bone marrow (25 µg Fe/ml, 24h, uptake of 4.9 pg Fe/cell).[44] Adipose tissue-derived stem cells labeled with the experimental TMAD-03 (trimethylamine dextran-coated) MNPs (10 µg Fe/ml, 1h) internalized slightly higher amounts of iron (~8 pg Fe/cell).[35] Our results thus show that, in particular for neural stem/progenitor cells, MNP-DMSA-EPS allow iron internalization efficiencies identical to those reported with commercial contrast agents, using lower iron concentrations, short incubation times and without using TA.

MNP-DMSA-EPS present hydrodynamic diameter in the range of 170 nm, therefore internalization by passive diffusion across the cell membrane would not be possible. The anticipated cell uptake mechanism is endocytosis, which is described for experimental and commercial MNPs in this size range.[45,46]

In order to confirm this assumption, a co-localization study of MNP-DMSA-EPS and lysosomes was performed, since these structures are the end-destination of materials internalized by endocytosis. Figure 4.9 shows bright field and fluorescence microscopy images of cells with GFP-labeled lysosomes after incubation with MNP-DMSA-EPS. It is clear that, in fact, nanoparticles (represented by black dots in bright field images) co-localize with lysosomes (visible as bright dots under fluorescence images) in the merged images (Figure 4.9 A-a'' and Figure 4.9 B-b''). Large MNP-DMSA-EPS aggregates that were not internalized are also visible

in the bright field images as white-shining structures at the cell surface (Figure 5A-a) and in the extracellular space (Figure 4.9 B-b).

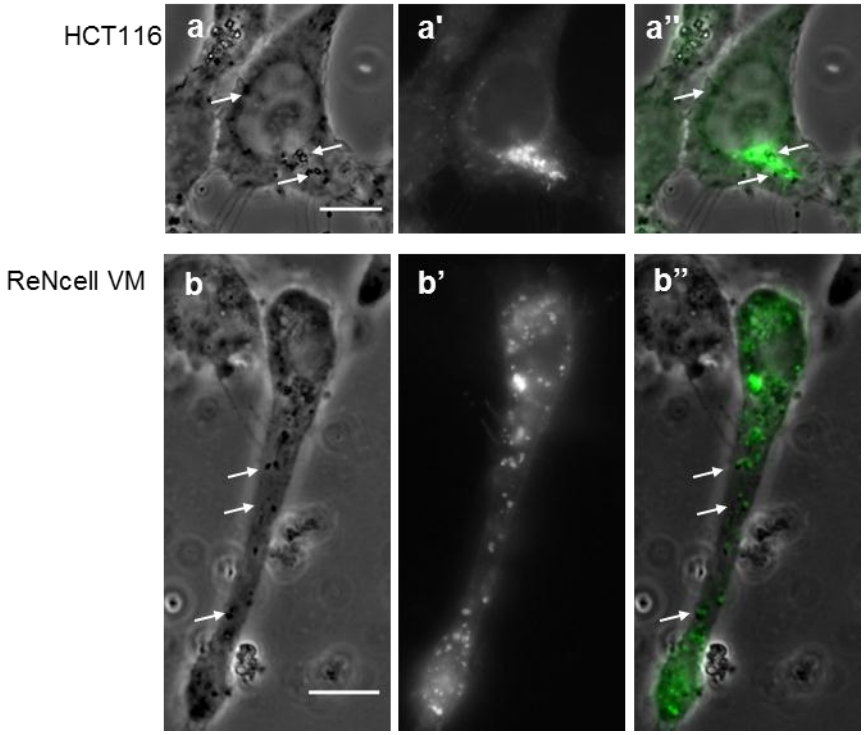

Figure 4.9. Tracking the localization of MNP-DMSA-EPS within (A) HCT116 cells and (B) ReNcell VM cells by microscopy. (a and b) bright field; (a' and b') GFP labeling of lysosomes and (a'' and b'') merged images. (Scale bar: 10 µm).

4.3.4 Differentiation of MNP labeled neural stem/progenitor cells

Since ReNcell VM is a human neural stem/progenitor cell line, it is important to ensure that multipotency is maintained in the presence of the nanoparticles. After labeling with MNP-DMSA and MNP-DMSA-EPS, the cells were induced to differentiate for 14 days and the ability to generate neurons and glial cells was inspected by immunohistochemistry against neuronal (β-III Tubulin) and glial cell (GAFP) markers. As shown in Figure 4.10, no significant differences in expression of these markers in labeled cells (Figure 4.10 d-f and Figure 4.10 g-i) are observed when compared against unlabeled control cells (Figure 4.10 a-c), indicating that the presence of MNPs does not have an impact on multipotency. Our results are in accordance with previous studies, where under similar culture conditions, but using MNPs with a different coating polymer, human neural precursor stem cells were shown to be able to retain the multilineage differentiation capability.[19]

After the 14 days culture period, aggregates of MNP-DMSA-EPS are still visible in the culture (extracellular space and near the cell outer membranes), similar to what was observed in

Prussian blue images (Figure 4.7 A) suggesting long term retention of MNP, which is needed for *in vivo* cell tracking in cell-replacement therapies.

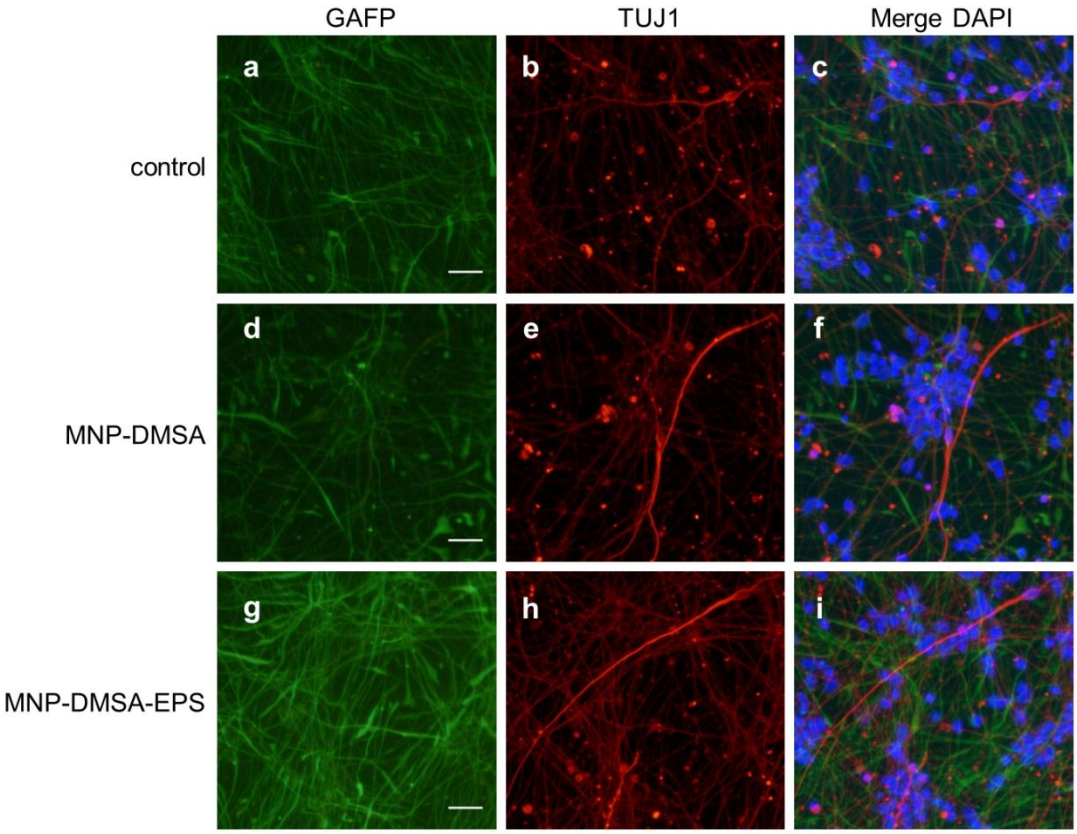

Figure 4.10. Immunohistochemistry of post-labeled ReNcell VM cells at day 14 of culture. Scale bar: 20 µm.

4.3.5 In vitro MRI of MNP-DMSA-EPS labeled cells

As concluded from the obtained relaxivities, MNP-DMSA-EPS are potentially efficient to produce contrast enhancement in MRI. In addition, ICP-AES analysis showed that these nanoparticles are internalized by both cell lines. Therefore, to evaluate MNP-DMSA-EPS efficacy to provide contrast enhancement after being internalized by the cells, agarose dispersions of labeled cells were studied by MRI. Hypointense regions are visible in T_2-weighted MR images of MNP-DMSA-EPS labeled cells in contrast to unlabeled (control) cells (Figure 4.11), which confirms internalization (or surface adherence) of particles. However, in contrast to what is observed for HCT116 cells, labeling ReNcell VM cells with increasing particle concentrations originated increasingly darker images, as is evident in C_1, C_2, and C_3 phantoms and respective histograms in Figure 4.11 A and Figure 4.11 B. Figure 4.11 C shows the quantification of the phantoms grey densities and confirms that for neural progenitor/stem cells,

hypointensity increases with the concentration of nanoparticles used for labeling. Although for C_1 grey density is identical to that of unlabeled cells, for C_2 and C_3 signal losses of 20% and 43% were obtained, respectively. A linear relation was found for the variation of the integrated density of ReNcell VM MRI phantom images as a function of the iron concentration used for labeling ($r^2 = 0.997$) (Figure 4.11 D).

MRI labeling efficacy depends on the cell line and on the labeling conditions. Our results indicate that the conditions used in this work are adequate to label and detect ReNcell VM cells by *in vitro* MRI, but to label HCT116 cells further optimization may be required. In a previous work, we have shown MNP dose dependent contrast enhancement using the same colorectal cancer cell line and incubation period, with gum Arabic-coated MNP-DMSA at lower iron concentrations than in the present study.[20] Besides the distinct iron loads, differences in composition of the polysaccharide coatings could cause distinct interactions between cell membranes and particles, which justify the differences in detectability by MRI.

The use of SPIONs to track and monitor stem cells after transplantation is important to help understanding the dynamics of cells proliferation, differentiation and migration. Therefore several approaches have been reported to develop effective MRI nanoprobes to label stem cells.[6] When compared to our results for neural stem cells, Yukawa *et al.*[35] obtained only subtle signal decrease in T_2-weighted MRI phantom images of mesenchymal stem cells incubated with TMAD-03 at increasing iron concentrations (20, 30 and 50 µg Fe/ml). On the other hand, Andreas *et al.*[44] reported MRI signal losses of approximately 20% and 50% for mesenchymal stem cells incubated for 24h with Resovist at 50 and 100 µg Fe/ml, respectively. Interestingly, MNP-DMSA-EPS gave rise to similar signal losses at lower iron doses (Figure 4.7C). Eamegdool *et al*.[19] found out that the minimum iron uptake necessary for full identification of neural precursor stem cells neurospheres by *in vitro* MRI was between 5 and 10 µg Fe/ml. We thus hypothesize the feasibility of neurosphere labeling with MNP-DMSA-EPS given the good labeling efficacy and MRI signal obtained in the referred range of iron concentrations, in our work.

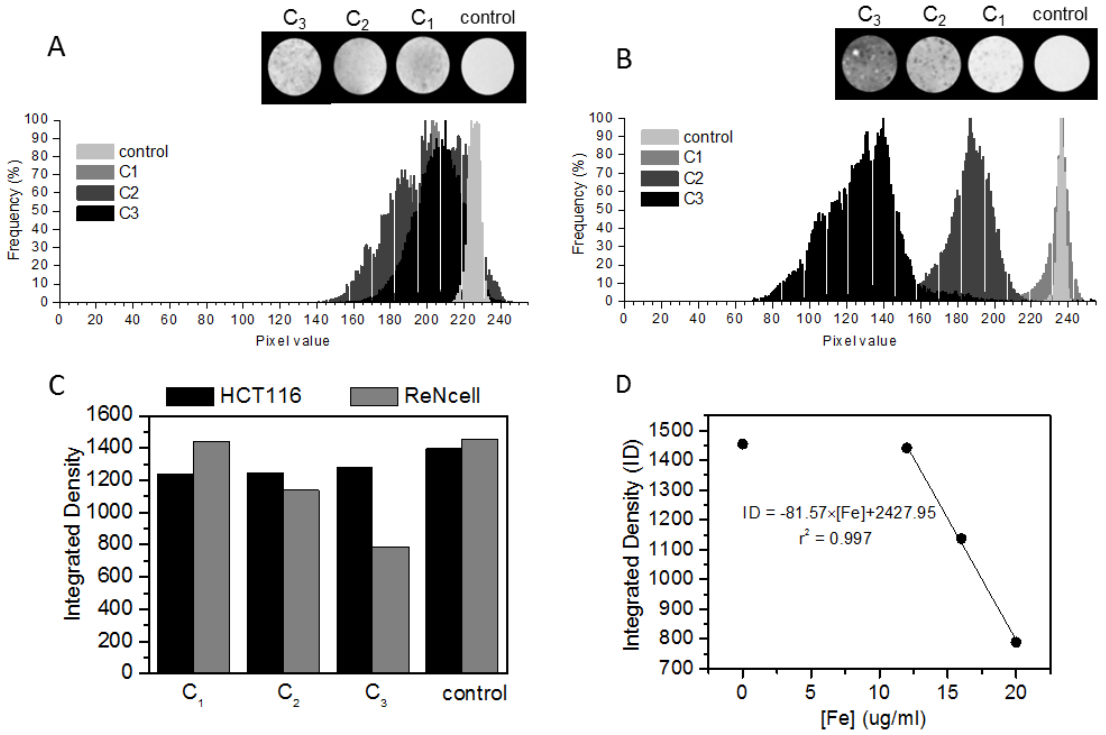

Figure 4.11. Efficacy of MNP-DMSA-EPS for *in vitro* MRI cell labeling. *In vitro* MRI images and corresponding histograms of (A) HCT116 and (B) ReNcell VM cells labeled with increasing concentrations of MNP-DMSA-EPS, from C_1 to C_3, compared with unlabeled control cells. (C) Grey density quantification of images in (A) and (B). For HCT116 cells, C_1= 61.5 µg Fe/ml, C_2 = 82 µg Fe/ml, C_3 = 102.5 µg Fe/ml. For ReNcell VM cells, C_1= 12 µg Fe/ml, C_2 = 16 µg Fe/ml, C_3 = 20 µg Fe/ml. (D) Linear adjustment of signal intensity (integrated density) of ReNcell VM MRI phantom images as a function of iron concentration in MNP-DMSA-EPS added to the culture medium. The first data point (signal intensity of unlabeled cells in agarose) was not accounted for the fitting.

4.4 Conclusion

We have demonstrated the feasibility of a new biopolymer, the EPS Fucopol, as a coating material for iron oxide magnetic nanoparticles, and the suitability of the hybrid biopolymeric-magnetic particles for *in vitro* cell labeling by MRI. Fucopol is a biodegradable exopolysaccharide produced by *Enterobacter* A47 DSM 23139 when this bacterium is grown in a bioreactor using glycerol as a carbon source. The nanosystem preparation method was reproducible even when using different batches of EPS. Covalent coupling of the biopolymer onto DMSA-functionalized MNP was effective and produced aggregates with hydrodynamic size in the range of 170 nm and stable negative zeta potential. The relaxivities ratio r_2/r_1 is higher than the one reported for the commercial MRI contrast agent Feridex, with similar size and coated with the bacterial polysaccharide dextran. The *in vitro* cell culture assays showed that EPS-coated nanoparticles were internalized via endocytosis by the human cell lines HCT116 and ReNcell VM. Under the tested conditions, MNP-DMSA-EPS did not show cytotoxic effect in

the neural stem/progenitor cell line nor affected their multipotency after 14 days of culture. In contrast to what was observed for HCT116, MNP-DMSA-EPS provided iron dose dependent MRI contrast enhancement in agarose dispersions of cells. The amount of cell-associated iron after ReNcell VM incubation with EPS-coated nanoparticles at the tested conditions is similar to the values reported for other stem cell lines labeled with Feridex for longer incubation periods and higher iron concentrations, suggesting potential applicability of our nanoparticles for stem cell labeling. Given the availability of carboxylic and hydroxyl groups in EPS, reporter and/or targeting molecules could be further conjugated to produce multimodal imaging agents with increased affinity for desired cell types. We conclude that EPS Fucopol-coated MNP are viable alternative tools to develop contrast agents for MRI techniques, being able to efficiently label cells through incubation without the need of additional transfection agents.

4.5 References

(1) Cohen, Y.; Shoushan, S. Y. Magnetic Nanoparticles-Based Diagnostics and Theranostics. Curr. Opin. Biotechnol. 2013, 24, 672–681, DOI:10.1016/j.copbio.2013.01.006.

(2) Krishnan, K. M. Biomedical Nanomagnetics: A Spin Through Possibilities in Imaging, Diagnostics, and Therapy. IEEE Trans. Magn. 2010, 46, 2523–2558, DOI:10.1109/TMAG.2010.2046907.

(3) Shin, T.-H.; Choi, Y.; Kim, S.; Cheon, J. Recent Advances in Magnetic Nanoparticle-Based Multi-Modal Imaging. Chem. Soc. Rev. 2015, 44, 4501–4516, DOI:10.1039/c4cs00345d.

(4) Modo, M.; Kolosnjaj-Tabi, J.; Nicholls, F.; Ling, W.; Wilhelm, C.; Debarge, O.; Gazeau, F.; Clement, O. Considerations for the Clinical Use of Contrast Agents for Cellular MRI in Regenerative Medicine. Contrast Media Mol. Imaging 2013, 8, 439–455, DOI:10.1002/cmmi.1547.

(5) Uthaman, S.; Lee, S. J.; Cherukula, K.; Cho, C.-S.; Park, I.-K. Polysaccharide-Coated Magnetic Nanoparticles for Imaging and Gene Therapy. Biomed Res. Int. 2014, Article ID 959175.

(6) Li, L.; Jiang, W.; Luo, K.; Song, H.; Lan, F.; Wu, Y.; Gu, Z. Superparamagnetic Iron Oxide Nanoparticles as MRI Contrast Agents for Non-Invasive Stem Cell Labeling and Tracking. Theranostics 2013, 3, 595–615, DOI:10.7150/thno.5366.

(7) Freitas, F.; Alves, V. D.; Torres, C. a. V.; Cruz, M.; Sousa, I.; Melo, M. J.; Ramos, A. M.; Reis, M. A. M. Fucose-Containing Exopolysaccharide Produced by the Newly Isolated Enterobacter Strain A47 DSM 23139. Carbohydr. Polym. 2011, 83, 159–165, DOI:10.1016/j.carbpol.2010.07.034.

(8) Tassa, C.; Shaw, S. Y.; Weissleder, R. Dextran-Coated Iron Oxide Nanoparticles: A Versatile Platform for Targeted Molecular Imaging, Molecular Diagnostics, and Therapy. Acc. Chem. Res. 2011, 44, 842–852, DOI:10.1021/ar200084x.

(9) Sivakumar, B.; Aswathy, R. G.; Sreejith, R.; Nagaoka, Y.; Iwai, S.; Suzuki, M.; Fukuda, T.; Hasumura, T.; Yoshida, Y.; Maekawa, T.; *et al.* Bacterial Exopolysaccharide Based Magnetic Nanoparticles: A Versatile Nanotool for Cancer Cell Imaging, Targeted Drug Delivery and Synergistic Effect of Drug and Hyperthermia Mediated Cancer Therapy. J. Biomed. Nanotechnol. 2014, 10, 885–899.

(10) Gao, F.; Cai, Y.; Zhou, J.; Xie, X.; Ouyang, W.; Zhang, Y.; Wang, X.; Zhang, X.; Wang, X.; Zhao, L.; *et al.* Pullulan Acetate Coated Magnetite Nanoparticles for Hyper-Thermia: Preparation, Characterization and *in Vitro* Experiments. Nano Res. 2010, 3, 23–31, DOI:10.1007/s12274-010-1004-6.

(11) Jo, J.; Aoki, I.; Tabata, Y. Design of Iron Oxide Nanoparticles with Different Sizes and Surface Charges for Simple and Efficient Labeling of Mesenchymal Stem Cells. J. Control. Release 2010, 142, 465–473, DOI:10.1016/j.jconrel.2009.11.014.

(12) Kalovidouris, S. A.; Gama, C. I.; Lee, L. W.; Hsieh-Wilson, L. C. A Role for Fucose alpha(1-2) Galactose Carbohydrates in Neuronal Growth. J. Am. Chem. Soc. 2005, 127, 1340–1341, DOI:10.1021/ja044631v.

(13) Dhadge, V. L.; Morgado, P. I.; Freitas, F.; Reis, M. A.; Azevedo, A.; Aires-Barros, R.; Roque, A. C. A. An Extracellular Polymer at the Interface of Magnetic Bioseparations. J. R. Soc. Interface 2014, 11, 20140743, DOI:10.1098/rsif.2014.0743.

(14) Sun, S.; Zeng, H.; Robinson, D. B.; Raoux, S.; Rice, P. M.; Wang, S. X.; Li, G. Monodisperse MFe 2 O 4 (M) Fe , Co , Mn) Nanoparticles. 2004, 4, 126–132.

(15) Palma, S. I. C. J.; Marciello, M.; Carvalho, A.; Veintemillas-Verdaguer, S.; Morales, M. D. P.; Roque, A. C. A. Effects of Phase Transfer Ligands on Monodisperse Iron Oxide Magnetic Nanoparticles. J. Colloid Interface Sci. 2015, 437, 147–155, DOI:10.1016/j.jcis.2014.09.019.

(16) Morris, D. L. Quantitative Determination of Carbohydrates With Dreywood's Anthrone Reagent. Science 1948, 107, 254–255, DOI:10.1126/science.107.2775.254.

(17) Da Paz, M. C.; Santos, M. de F. M. A.; Santos, C. M. B.; da Silva, S. W.; de Souza, L. B.; Lima, E. C. D.; Silva, R. C.; Lucci, C. M.; Morais, P. C.; Azevedo, R. B.; *et al.* Anti-CEA Loaded Maghemite Nanoparticles as a Theragnostic Device for Colorectal Cancer. Int. J. Nanomedicine 2012, 7, 5271–5282, DOI:10.2147/IJN.S32139.

(18) Jasmin; Torres, A. L. M.; Jelicks, L.; de Carvalho, A. C. C.; Spray, D. C.; Mendez-Otero, R. Labeling Stem Cells with Superparamagnetic Iron Oxide Nanoparticles: Analysis of the Labeling Efficacy by Microscopy and Magnetic Resonance Imaging. Methods Mol. Biol. 2012, 906, 239–252, DOI:10.1007/978-1-61779-953-2_18.

(19) Eamegdool, S. S.; Weible, M. W.; Pham, B. T. T.; Hawkett, B. S.; Grieve, S. M.; Chan-ling, T. Ultrasmall Superparamagnetic Iron Oxide Nanoparticle Prelabelling of Human Neural Precursor Cells. Biomaterials 2014, 35, 5549–5564, DOI:10.1016/j.biomaterials.2014.03.061.

(20) Palma, S. I. C. J.; Carvalho, A.; Silva, J.; Martins, P.; Marciello, M.; Fernandes, A. R.; Del Puerto Morales, M.; Roque, A. C. A. Covalent Coupling of Gum Arabic onto Superparamagnetic Iron Oxide Nanoparticles for MRI Cell Labeling: Physicochemical and *in Vitro* Characterization. Contrast Media Mol. Imaging 2015, 10, 320–328, DOI:10.1002/cmmi.1635.

(21) Cornell, R. M.; Schwertmann, U. The Iron Oxides: Structure, Properties, Reactions, Occurrences and Uses; 2nd ed.; Wiley-VCH GmbH & Co. KGaA: Weinheim, 2003.

(22) Synytsya, A. Fourier Transform Raman and Infrared Spectroscopy of Pectins. Carbohydr. Polym. 2003, 54, 97–106, DOI:10.1016/S0144-8617(03)00158-9.

(23) Barth, A. Infrared Spectroscopy of Proteins. Biochim. Biophys. Acta 2007, 1767, 1073–1101, DOI:10.1016/j.bbabio.2007.06.004.

(24) Yallapu, M. M.; Chauhan, N.; Othman, S. F.; Khalilzad-Sharghi, V.; Ebeling, M. C.; Khan, S.; Jaggi, M.; Chauhan, S. C. Implications of Protein Corona on Physico-Chemical and Biological Properties of Magnetic Nanoparticles. Biomaterials 2015, 46, 1–12, DOI:10.1016/j.biomaterials.2014.12.045.

(25) Salvati, A.; Pitek, A. S.; Monopoli, M. P.; Prapainop, K.; Bombelli, F. B.; Hristov, D. R.; Kelly, P. M.; Åberg, C.; Mahon, E.; Dawson, K. A. Transferrin-Functionalized Nanoparticles Lose Their Targeting Capabilities When a Biomolecule Corona Adsorbs on the Surface. Nat. Nanotechnol. 2013, 8, 137–143, DOI:10.1038/nnano.2012.237.

(26) Mahmoudi, M.; Lynch, I.; Ejtehadi, M. R.; Monopoli, M. P.; Bombelli, F. B.; Laurent, S. Protein-Nanoparticle Interactions: Opportunities and Challenges. Chem. Rev. 2011, 111, 5610–5637, DOI:10.1021/cr100440g.

(27) Roberts, A. P.; Cui, Y.; Verosub, K. L. Wasp-Waisted Hysteresis Loops: Mineral Magnetic Characteristics and Discrimination of Components in Mixed Magnetic Systems. J. Geophys. Res. 1995, 100, 17909, DOI:10.1029/95JB00672.

(28) Bennett, L. H.; Della Torre, E. Analysis of Wasp-Waist Hysteresis Loops. J. Appl. Phys. 2005, 97, 10E502, DOI:10.1063/1.1846171.

(29) Chen, H.; Yeh, J.; Wang, L.; Khurshid, H.; Peng, N.; Wang, A. Y.; Mao, H. Preparation and Control of the Formation of Single Core and Clustered Nanoparticles for Biomedical Applications Using a Versatile Amphiphilic Diblock Copolymer. Nano Res. 2010, 3, 852–862, DOI:10.1007/s12274-010-0056-y.

(30) Berret, J.-F.; Schonbeck, N.; Gazeau, F.; El Kharrat, D.; Sandre, O.; Vacher, A.; Airiau, M. Controlled Clustering of Superparamagnetic Nanoparticles Using Block Copolymers: Design of New Contrast Agents for Magnetic Resonance Imaging. J. Am. Chem. Soc. 2006, 128, 1755–1761, DOI:10.1021/ja0562999.

(31) Basly, B.; Felder-Flesch, D.; Perriat, P.; Billotey, C.; Taleb, J.; Pourroy, G.; Begin-Colin, S. Dendronized Iron Oxide Nanoparticles as Contrast Agents for MRI. Chem. Commun. 2010, 46, 985–987, DOI:10.1039/b920348f.

(32) Huang, J.; Bu, L.; Xie, J.; Chen, K.; Cheng, Z.; Li, X.; Chen, X. Effects of Nanoparticle Size on Cellular Uptake and Liver MRI with Polyvinylpyrrolidone-Coated Iron Oxide Nanoparticles. ACS Nano 2010, 4, 7151–7160, DOI:10.1021/nn101643u.

(33) Schütz, C. A.; Staedler, D.; Crosbie-Staunton, K.; Movia, D.; Chapuis Bernasconi, C.; Kenzaoui, B. H.; Prina-Mello, A.; Juillerat-Jeanneret, L. Differential Stress Reaction of Human Colon Cells to Oleic-Acid-Stabilized and Unstabilized Ultrasmall Iron Oxide Nanoparticles. Int. J. Nanomedicine 2014, 9, 3481–3498, DOI:10.2147/IJN.S65082.

(34) Laurent, S.; Burtea, C.; Thirifays, C.; Häfeli, U. O.; Mahmoudi, M. Crucial Ignored Parameters on Nanotoxicology: The Importance of Toxicity Assay Modifications and “Cell Vision”. PLoS One 2012, 7, e29997, DOI:10.1371/journal.pone.0029997.

(35) Yukawa, H.; Nakagawa, S.; Yoshizumi, Y.; Watanabe, M.; Saito, H.; Miyamoto, Y.; Noguchi, H.; Oishi, K.; Ono, K.; Sawada, M.; *et al.* Novel Positively Charged Nanoparticle Labeling for *in Vivo* Imaging of Adipose Tissue-Derived Stem Cells. PLoS One 2014, 9, e110142, DOI:10.1371/journal.pone.0110142.

(36) Gene, P. S. Alfa-L-Fucose in Histology: A Part of the Cancer Glycome Hiding in Plain Sight. J. Cytol. Histol. 2012, 3, 1000e102, DOI:10.4172/2157-7099.1000e102.

(37) Kalovidouris, S. A.; Gama, C. I.; Lee, L. W.; Hsieh-Wilson, L. C. A Role for Fucose alpha(1-2) Galactose Carbohydrates in Neuronal Growth. J. Am. Chem. Soc. 2005, 127, 1340–1341, DOI:10.1021/ja044631v.

(38) Kalovidouris, S.; Gama, C. I.; Hsieh-wilson, L. C. Methods of Inducing Neuronal Growth by a Fucose-α(1-2) Galactose (fuc-α(1-2) Gal) Moiety and a Lectin. US 7858578 B2, December 7, 2005.

(39) Moore, A.; Marecos, E.; Bogdanov, A.; Weissleder, R. Tumoral Distribution of Long-Circulating Dextran-Coated Iron Oxide Nanoparticles in a Rodent Model. Radiology 2000, 214, 568–574, DOI:10.1148/radiology.214.2.r00fe19568.

(40) Smejkalová, D.; Nešporová, K.; Huerta-Angeles, G.; Syrovátka, J.; Jirák, D.; Gálisová, A.; Velebný, V. Selective *in Vitro* Anticancer Effect of Superparamagnetic Iron Oxide Nanoparticles Loaded in Hyaluronan Polymeric Micelles. Biomacromolecules 2014, 15, 4012–4020, DOI:10.1021/bm501065q.

(41) Frank, J. A.; Miller, B. R.; Arbab, A. S.; Zywicke, H. A.; Jordan, E. K.; Lewis, B. K.; Bryant, L. H.; Bulte, J. W. M. Clinically Applicable Labeling of Mammalian and Stem Cells by Combining Superparamagnetic Iron Oxides and Transfection Agents. Radiology 2003, 228, 480–487, DOI:10.1148/radiol.2281020638.

(42) Singh, N.; Jenkins, G. J. S.; Asadi, R.; Doak, S. H. Potential Toxicity of Superparamagnetic Iron Oxide Nanoparticles (SPION). Nano Rev. 2010, 1, 1–15, DOI:10.3402/nano.v1i0.5358.

(43) Chen, C.-C. V; Ku, M.-C.; D M, J.; Lai, J.-S.; Hueng, D.-Y.; Chang, C. Simple SPION Incubation as an Efficient Intracellular Labeling Method for Tracking Neural Progenitor Cells Using MRI. PLoS One 2013, 8, e56125, DOI:10.1371/journal.pone.0056125.

(44) Andreas, K.; Georgieva, R.; Ladwig, M.; Mueller, S.; Notter, M.; Sittinger, M.; Ringe, J. Highly Efficient Magnetic Stem Cell Labeling with Citrate-Coated Superparamagnetic Iron Oxide Nanoparticles for MRI Tracking. Biomaterials 2012, 33, 4515–4525, DOI:10.1016/j.biomaterials.2012.02.064.

(45) Pinkernelle, J.; Calatayud, P.; Goya, G. F.; Fansa, H.; Keilhoff, G. Magnetic Nanoparticles in Primary Neural Cell Cultures Are Mainly Taken up by Microglia. BMC Neurosci. 2012, 13, 32, DOI:10.1186/1471-2202-13-32.

(46) Matuszewski, L.; Persigehl, T.; Wall, A.; Schwindt, W.; Tombach, B.; Fobker, M.; Poremba, C.; Ebert, W.; Heindel, W.; Bremer, C. Cell Tagging with Clinically Approved Iron Oxides: Feasibility and Effect of Lipofection, Particle Size, and Surface Coating on Labeling Efficiency. Radiology 2005, 235, 155–161, DOI:10.1148/radiol.2351040094.

Chapter 5

An affinity triggered MRI nanoprobe for pH-dependent cell labeling

Iron oxide magnetic nanoparticles (MNP) are negative contrast agents for Magnetic Resonance Imaging (MRI), with a particular focus in oncology as nanoprobes for tumor-specific imaging. Acidity is ubiquitous in malignant tumors microenvironment and can be explored for cancer cell labeling. This work presents a proof-of-concept of a multilayer iron oxide nanoprobe for MRI targeting tumoral pH. The biologically derived and pH-sensitive affinity pair iminobiotin/neutravidin was used as a linker between a poly-l-lysine (PLL) inner layer and a biotinylated poly(ethyleneglycol) (bPEG) outer layer on the MNPs. The nanoparticles' uptake by HCT116 cells *in vitro* is activated by tumor acidic pH as a 2-fold increase in iron uptake per cell was observed at acidic pH compared to physiological pH. This difference was particularly clear by visualizing T_2-weighted MR images of cells incubated with the nanoparticles at both pH conditions. Increased cellular uptake of the nanoprobe in acidic pH resulted in enhanced contrast in MR images, which allowed cells cultured in physiological medium to be distinguished from others cultured in acidified medium. This targeting strategy is potentially applicable to the generality of tumors since the typical hypoxic conditions and high glycolysis rate in cancer cells create an acidic environment common to all cancer types.

.

Communications in conferences

Oral Communication

S. Palma, M. Marciello, A. Carvalho, J. Silva, P. Martins, C. A. V. Rodrigues, M. Puerto Morales, F. Freitas, A. Fernandes, J. M. S. Cabral, A. C. A. Roque, Nanosystems for MRI cell labeling using magnetism, biopolymers and pH sensitive bio-coatings, NANOBIOAPP 2015 - Latest Advances on Nanomaterials for Biomedical Applications. Barcelona, Spain (2015)

5.1. Introduction

Nanotechnology research has triggered the development of colloidal iron oxide magnetic nanoparticles (MNP) for molecular magnetic resonance imaging (MRI), delivery of therapeutics, hyperthermia or theranostics of several diseases.[1–4] Cancer, in particular, has been widely studied due to the need to accurately detect it at an early stage and to deliver treatment specifically to the affected tissues. Tumor targeted MNP-based systems are valuable approaches for that purpose as they combine the inherent MRI contrast enhancement properties of superparamagnetic iron oxide nanoparticles (for diagnosis) with the versatility for surface functionalization with biologically or chemically active moieties (for targeting and therapy).

A possible tumor-targeting strategy consists in creating nanoparticles activated by tumor physiochemical characteristics.[5] In this context, pH difference between the extracellular medium of tumors and healthy tissues can be used to engineer tumor-targeted nanoparticles.[6,7] Acidic extracellular tumor pH mainly results from the high rate glycolytic metabolism and poor perfusion typically found in tumors, as 90% of the pyruvate generated by glycolysis is converted to lactic acid, and co-transported outside the cell with H^+ ions. This process, associated with decreased blood flow rate and poor lymphatic drainage in the tumor, leads to the accumulation of H^+ ions in the extracellular medium thereby causing acidity (pH ranging approximately between 6.5 and 7.0) compared with healthy tissues and blood (pH around 7.4).[5,8,9]

One of the strategies for pH-activation of nanoparticles relies on the hypothesis that the nanoparticles maintain stealth during blood circulation and passively accumulate at tumor sites where, activated by the acidic environment, transform into a more cell-interactive form for enhanced tumor cell internalization, cytotoxicity or release of encapsulated cargo. For example, MNP with a glycol-chitosan (GC) coating generated a T_2*-weighted MR contrast agent with enhanced cellular interactions and MRI contrast at tumor pH both *in vitro* and *in vivo* due to the pH-titrable charge of GC, which becomes positive under acidic conditions.[10] Mok *et al.*[11] reported a dual therapeutic and MR imaging MNP nanosystem for chlorotoxin-mediated tumor-targeted delivery of siRNA. This system makes use of the acid-hydrolyzable linkage between citraconic anhydride and primary amines to block the cytotoxic effect of polyethylenimine (PEI) and reduce cellular interactions at physiological pH. At acidic conditions, due to citraconic anhydride removal, the positive charges of PEI are unblocked and promote cytotoxicity, chlorotoxin is exposed (for receptor-mediated tumor cellular uptake) and siRNA delivered to the intracellular medium. Saha *et al*.[12] developed a pH-sensitive MR contrast agent using melamine-dendron functionalized MNP. In this system, large R_2 values are provided at low pH in physiological salt conditions and decrease for higher pH, with a sharp inflection at pH value just below the pKa of melamine monomer (~5) due to the pH-dependent transient and reversible

clustering of magnetic cores modulated by the interplay between surface charge at different pHs and ionic strength. A more complex nanosystem was recently reported by Ling *et al.,*[13] who developed a multifunctional pH-sensitive nanosystem composed of self-assembled ultrasmall MNP, a fluorescent tag, a photodynamic therapeutic moiety and pH-sensitive ligands. The authors engineered polymeric pH-sensitive ligands based on a protonable imidazole group and used them to fabricate magnetic nanogrenades that upon exposure to acidic extratumoral pH switch charge from negative to positive and swell, promoting cellular uptake. Once inside the cell, the system disassembles and activates T_1-weighted MRI contrast and photoactivity for therapeutic effect.

As an alternative to chemically engineered pH-dependent materials, specific bio-recognition interactions can be explored to derive pH-sensitivity. The complex formed by biotin and avidin (or its analogues) is the strongest known non-covalent interaction (K_d=10^{-15} M)[14] between a protein and ligand, and once formed is not affected by extreme conditions such as pH variations. However, the guanido-version of biotin (iminobiotin) binds to avidin and its derivatives in a pH-dependent fashion. At pH 9.5-11.0, the avidin-iminobiotin complex binds tightly (K_d = 3.4×10^{-10} M) but the bond strength decreases with pH until complete dissociation at pH 4 (K_d = 10^{-3} M).[15] Due to the reversible binding property, this affinity pair has been utilized in bioseparation applications,[16–18] in the production of thin films decomposable by pH[19] and in the development of layer-by-layer acidity-triggered quantum-dot nanoprobes for *in-vivo* tumor imaging by fluorescence.[20]

In this work, we explore for the first time the neutravidin-iminobiotin pH-dependent affinity interaction to develop an affinity-triggered MNP-based MRI nanoprobe for preferential labeling of tumor cells. The system consists of a multilayer-coated magnetic nanoprobe with a pH-removable PEG layer. Increased cellular uptake is triggered by the acidic tumor microenvironment, thereby rendering the cancer cells visible by MRI (Figure 5.1). The multilayer system was deposited onto *meso*-2,3-dimercaptosuccinic acid-functionalized MNP and characterized regarding its size and surface charge after adding each material. The pH responsivity of the final particles was evaluated first in buffer solutions at different pHs and then in *in vitro* cultures of colorectal carcionoma cells (HCT116 cell line) at acidic and physiological pH. Cell phantoms were imaged by MRI to evaluate their efficacy to provide differential contrast depending on the pH of the cultures.

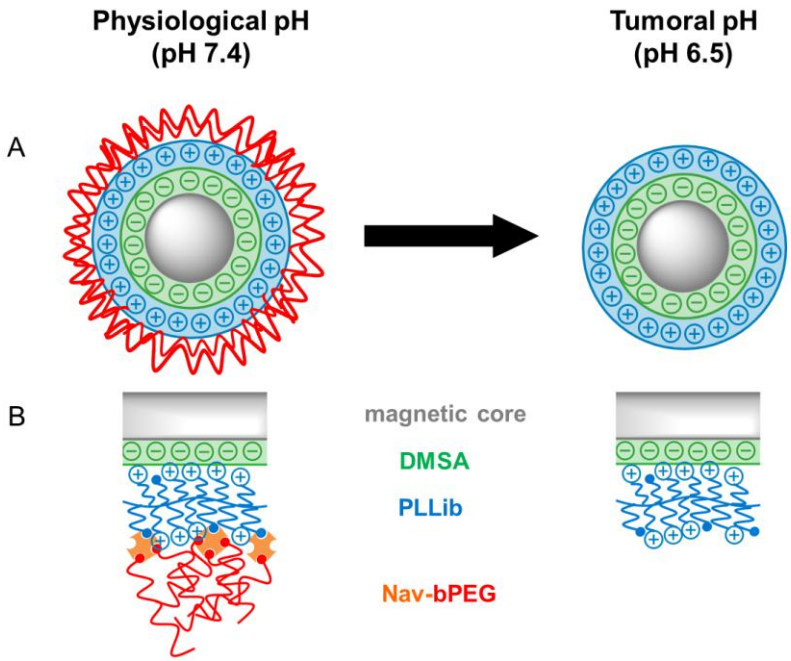

Figure 5.1. Schematic representation of the multilayer pH-sensitive MNPs and concept for achieving preferential interactions with tumoral cells. (A) Overall effect of pH on the MNPs; (B) detail of the multilayer pH-sensitive system built on top of DMSA stabilized MNP. The inner cationic layer of poly-l-lysine (PLL) is employed to promote cell adhesion and consequent cellular uptake. The outer layer of poly(ethyleneglycol) (PEG) works as antifouling, stealth material to prevent non-specific cell uptake. PLL is partially modified with iminobiotin (ib), and PEG bears a biotin (b) moiety. Neutravidin (Nav) interconnects these two materials. In physiological pH, PEG chains cover the cationic PLL layer to minimize cell interactions, whereas in acidic pH, due to the loss of affinity between Nav and ib, Nav-bPEG complex is released and unshields the positive charges from PLLib.

5.2. Experimental Section

5.2.1. Materials

All materials were purchased from Sigma Aldrich unless otherwise specified.

5.2.2. Production of multi-layer functionalized magnetic nanoparticles

5.2.2.1. Synthesis and phase transfer of iron oxide magnetic nanoparticles (MNP-DMSA)

Hydrophobic iron oxide magnetic nanoparticles were synthesized using a variation of Sun's thermal decomposition method,[21,22] as described previously.[23] Briefly, iron tri(acetylacetonate) is decomposed at high temperatures (300 ºC) in benzyl ether, 1,2-

tetradecanediol is used as reducing agent, and oleic acid and oleylamine are used as surfactants for the formation of hydrophobic and monodisperse magnetite nanoparticles (MNP). To render these MNP hydrophilic, a ligand-exchange reaction with DMSA was employed.[23] Briefly, a dispersion of hydrophobic MNP in toluene was mixed with a solution of DMSA in dimethylsulfoxide (DMSO). After 48 h incubation at room temperature, the solvent containing the oleic acid and oleylamine was discarded and the black hydrophilic nanoparticles were re-dispersed in ethanol. After several washes by centrifugation the nanoparticles were re-dispersed in milliQ water, basified to pH 10 and dialyzed against milliQ water (four complete water changes) to provide the final DMSA coated MNP (MNP-DMSA). MNP-DMSA pH was re-adjusted to 7 and particles were filtered through a syringe filter with 0.2 μm diameter pore prior to further use.

5.2.2.2. Coating MNP-DMSA with iminobiotin-modified poly-L-lysine (PLLib) (MNP-DMSA-PLLib)

Poly-L-lysine (MW 15000 – 30000 Da) was functionalized with NHS-activated iminobiotin (Thermo Scientific) on approximately 30% of its primary amines by incubation in aqueous conditions (borate buffer 50 mM, pH 8) for 2 h at 4ºC. Prior to use, the modified PLL was dialyzed against water in a MWCO 10 kDa dialysis membrane, with four complete water changes, to remove unreacted iminobiotin and reaction leftovers. The biotinylation yield is the ratio between the number of primary amines in PLLib after the reaction with NHS-iminobiotin and the number of primary amines in native PLL. The Kaiser test was used to estimate the amount of primary amines, as described previously.[24]

For the deposition of PLLib layer, MNP-DMSA (at 0.7 mg/ml) were added dropwise to an equal volume of PLLib solution (at 1.25 mg/ml) under magnetic agitation (600 rpm) and left incubating under gentle magnetic agitation (200 rpm) for 2 h at room temperature. Dialysis in a MWCO 50 kDa membrane against milliQ water (four complete water changes) was used to wash the particles prior to further use. Filtration near the flame through a syringe filter with 0.2 μm diameter pore was performed to ensure sterility of the particles for the following steps and *in-vitro* testing.

5.2.2.3. Coating MNP-DMSA-PLLib with Nav-bPEG conjugates (MNP-DMSA-PLLib-Nav-bPEG)

Biotin-modified PEG (20 kDa, Lyasan Bio) (bPEG) was incubated with neutravidin (Thermo Scientific) (Nav) to produce Nav-bPEG conjugates. Nav was reconstituted in water milliQ to (A) 5 mg/ml or (B) 0.5 mg/ml and dissolved with Phosphate Buffered Saline (10 mM,

150 mM NaCl) (PBS) at pH 7.4 to (A) 2.3 mg/ml or (B) 0.23 mg/ml. Then, bPEG (8.4 mg/ml in PBS, pH 7.4) was added to Nav (A) solution in the proportion of 2 mol (bPEG) / mol (Nav), and to Nav solution (B) in the proportion of 20 mol (bPEG) / mol (Nav). After 2 h of incubation at room temperature under magnetic stirring (450 rpm), 1 ml of MNP-DMSA-PLLib at 0.3 mg/ml was added dropwise to 3.16 ml of Nav-bPEG solution (A) and (B) under stronger magnetic stirring (600 rpm) and left incubating under gentle magnetic agitation (200 rpm) for 2 h at room temperature.

All the materials, including buffers and water, were autoclaved prior to use and the reactions were performed near the flame to maximize the sterility condition of the produced particles.

5.2.2.4 Characterization of magnetic nanoparticles

Nanoparticle hydrodynamic diameter (d_h) and zeta potential were characterized using a Zetasizer Nano ZS (Malvern). The mean value of the intensity-weighted size distribution measured at pH 7 in low salt conditions (water for MNP-DMSA and MNP-DMSA-PLLib or 1 mM phosphate buffer for MNP-DMSA-PLLib-Nav-bPEG) was considered as the d_h of the pristine nanoparticles. The Z-average was considered instead when characterizing the size of the particles after dialysis to PBS with 150 mM NaCl at different pH values. Zeta potential of the pristine nanoparticles was measured in low salt conditions. Variation of zeta potential of MNP-DMSA and MNP-DMSA-PLLib with pH was measured in a 10 mM KNO_3 solution (HNO_3 or KOH solutions were used for pH adjustment). The primary amine groups on MNP-DMSA-PLLib were quantified through the Kaiser test[24] and from this characterization, the amount of PLL and ib on the particles was estimated. MNP-DMSA concentration was determined by drying and weighting a known volume of particles. The concentration of particles subsequently modified with PLLib and Nav-bPEG was estimated by correction of MNP-DMSA concentration value with the respective dilution factor (resulting from the coating reactions and dialyses). The iron content in MNP samples was determined by Inductively Coupled Plasma - Atomic Emission Spectroscopy (ICP-AES) (Horiba Jobin-Yvon, Ultima).

5.2.2.5. Examination of pH dependent Nav-bPEG release

The pH dependence of Nav-bPEG release was investigated by dialyzing MNP-DMSA-PLLib-Nav-bPEG inside 300 kDa Float-a-Lyzers (Spectrum Laboratories) to PBS at pH 5, pH 6.5, pH 7.4 or pH 8.5. After 20 h of dialysis, the total protein content of the dialysates was quantified using the bicinchoninic acid test[25] (QuantiPro BCA assay kit) and normalized to the mass of MNP and to the mass of Nav-bPEG used for the coating reaction (mass$(Nav\text{-}bPEG)_{in}$),

quantified in the same assay. To correct the total protein concentration values regarding PLLib that is also released during dialysis, control dialyses of MNP-DMSA-PLLib were performed and PLLib released to the dialysates was quantified using the same test. PLLib released per mg of MNP at each pH was then subtracted from the total protein released per mg of MNP to obtain the mass of Nav-bPEG released per mg of MNP at each pH condition. Normalization to mass(Nav-bPEG)$_{in}$ gives the percentage of Nav-bPEG released per mg of MNP (% Nav-bPEG$_{in}$/mg MNP)

Briefly, for the bicinchoninic acid test, samples of the dialysates were individually added to wells of a 96 well plate (150 μl/well) to which the QuantiPro reagent (150 μl of a freshly prepared mixture composed by 25 parts of reagent QA, 25 parts of reagent QB and 1 part of reagent QC) was added. After 1 h of incubation at 60°C in the dark, absorbance at 560 nm was read in a microplate reader (Infinite M200, Tecan). For each assay, a calibration line using a protein standard (0 – 30 μg/ml bovine serum albumin, BSA) was performed and used to determine the protein concentration of the tested samples.

5.2.3. Characterization of *in vitro* cell-MNP interactions

5.2.3.1. Cell culture and labeling

Human colorectal carcinoma cells (HCT116 cell line) were cultured in Dulbecco's modified Eagle's medium (DMEM, Life Technologies, USA) supplemented with 10% (v/v) fetal bovine serum (Life Technologies, USA) and 1% (v/v) of penicillin-streptomycin (Life Technologies, USA) at 37 ºC with 99% relative humidity and 5% CO_2.

For magnetic cell labeling, cells were seeded in 24-well plates (at 1×10^5 cells/well) with either regular or acidic culture medium (0.4 ml) and incubated for approximately 24 h to allow cell adhesion. Then, the culture medium was replaced by fresh medium (either regular or acidic) containing the magnetic nanoparticles (MNP-DMSA-PLLib, MNP-DMSA-PLLib-Nav-bPEG (A) and MNP-DMSA-PLLib-Nav-bPEG (B)) at 10 μg Fe/ml. After 5 h of incubation, the cell-MNP interaction assays detailed hereafter were carried out. DMEM medium was acidified to pH 6.5 by adding some drops of HCl (0.1 M – 5 M) prior to cell seeding and filtered under sterile conditions with a 0.2 μm syringe filter. MNP-DMSA-PLLib-Nav-bPEG (A) and (B) were subjected to pretreatments at pH 7.4 and pH 6.5 for 20 h before being dispersed in culture medium and added to the cells.

5.2.3.2. Identification of cellular iron by Prussian blue staining

Cells were seeded in coverslips on the bottom of the wells and incubated with nanoparticles, after which cells were stained with Prussian blue for iron identification and counterstained with neutral red as described previously.[26] Preparations were mounted on microscope slides using 1 drop of glycerol 1:3 (v/v in PBS) or 1 drop of ProLong Gold Antifade Mountant with DAPI (Life Technologies) for fluorescent staining of cell nuclei. The slides were observed under bright-field and fluorescent illumination using an Olympus BX51 microscope equipped with an Olympus DP50 camera and the AnalySIS Soft Imaging software.

5.2.3.3. Intracellular localization of magnetic nanoparticles

Cells were dispersed in culture medium supplemented with Cell-Light Lysosomes-GFP, BacMam 2.0 reagent (Life Technologies, USA) (22 particles per cell), seeded in coverslips on the bottom of the wells and incubated for 24h according to the supplier's instructions. Then, cells were labeled with the MNP and, after the 5 h incubation period, washed with PBS and fixed with ice-cold paraformaldehyde (4% v/v in PBS) for 15 min in the dark. After removing the paraformaldehyde and washing with PBS, the preparation was air dried and mounted in the microscope slide using a drop of ProLong Gold Antifade Mountant with DAPI (Life Technologies). Slides were observed using an Olympus BX51 microscope equipped with an Olympus DP50 camera and the Cell F View Image System Software.

5.2.3.4. Iron uptake quantification

After labeling, well supernatants were collected (separately); cells were detached from the wells using trypsin, re-suspended in culture medium, counted using a hemocytometer and centrifuged for 10 min at 5000 rpm. Cell pellet (fraction 1), cell supernatant (fraction 2) and well supernatant (fraction 3) were separately digested with 100 µl of *aqua regia* (concentrated HCl/HNO_3, 3:1 (v/v)) for 30 min at 90ºC, diluted to 1 ml with milliQ water and analyzed separately for iron by ICP-AES. The iron in the cellular fraction (sum of fraction 1 and fraction 2) was normalized to the number of cells and to the total mass of iron (sum of the three fractions). A control sample containing only cells was also quantified to provide a calibration for the native iron content of cells.

5.2.3.5. Determination of cell viability

After cell incubation with nanoparticles, the culture medium was removed and cells were detached from the wells using trypsin. Trypsin action was neutralized by adding an equal

volume of culture medium to the wells and mixing. Trypan blue was added in equal volume to 10 μl of these cell suspensions. The viable cells per well were counted using a hemocytometer. The percentage of cell viability in respect to the control (untreated cells) was determined assuming that the number of cells in the control well corresponded to 100% viability.[27]

5.2.3.6. *In vitro* MRI of cell phantoms

For *in vitro* MRI, cells were seeded at 1.25×10^5 cells/well with 0.5 ml of culture medium and two wells per condition were prepared in order to provide sufficient cells for imaging. After labeling with MNP-DMSA-PLLib-Nav-bPEG (A) and MNP-DMSA-PLLib-Nav-bPEG (B), cells were prepared for MR imaging as described previously.[26] Briefly, cells were washed with PBS, detached with trypsin and centrifuged. The pellet was collected and re-suspended in ice-cold paraformaldehyde to fix the cells. To remove the paraformaldehyde, cells were centrifuged and the pellet was re-dispersed in PBS and counted using a hemocytometer. Cell dispersions of 9×10^4 cells in 0.2 ml of PBS were prepared for each condition and mixed with 0.1 ml aliquots of fresh 2 % (w/v) agarose. The samples were then transferred to 5 mm diameter NMR tubes for imaging after solidifying. The final concentration of agarose was 0.5% (w/v) and the final concentration of cells was 3×10^5 cells/ml.

T_2-weighted magnetic resonance (MR) images were obtained in a magnetic field of 7 T, at 25ºC, using a Bruker Avance III Spectrometer (160 G/cm imaging gradient) and a Fast Low Angle Shot gradient (FLASH) imaging sequence with repetition time (TR) = 110 ms, echo time (TE) = 1.7 ms, excitation angle of 20º and number of excitations (NEX) = 32.

For the samples of cells incubated with MNP-DMSA-PLLib-Nav-bPEG (B) in regular and in acidic culture medium, T_2 relaxation times were also determined. Briefly, the average signal was measured as the MR image intensity in a circular region of interest (1.2×10^6 μm^2) placed in the center of each cell phantom, for different echo times. The signal intensities were then plotted against echo times and the signal intensity (SI) function was fitted to the data according to the exponential decay equation $SI = A + C\, e^{(-t/T2)}$, where *SI* is the signal intensity, *t* is the echo time, A is an off-set constant and C is a pre-factor constant. Resulting from these fittings, the transverse relaxation time T_2 was obtained.

5.2.4. Statistical Analysis

All data in figures and text is given as mean ± standard deviation. Statistical analysis was performed by GraphPad Prism 6.0 software. One-way or two-way ANOVA complemented with Tukey's test or Bonferroni's test for multiple comparisons were used when applicable.

The threshold for significance was P = 0.1 and P-values < 0.1 (*), <0.05 (**), <0.005 (***) and <0.0001 (****) were considered significant.

5.3. Results and discussion

5.3.1. Multi-layer MNP assembly

Hydrophobic iron oxide magnetic nanoparticles coated with oleylamine and oleic acid (MNP-OA) were synthesized by the thermal decomposition method and transferred to aqueous phase by replacement of the oleic acid and oleylamine moieties at their surface by DMSA molecules.[23] This process provided the negatively charged template nanoparticles (MNP-DMSA) for further functionalization with the pH-responsive layer system through sequential deposition of coating materials. The assembly of the multi-layered magnetic nanoprobes was followed by assessing, at each layering step, particles size and surface charge (Figure 5.2 and Table 5.1).

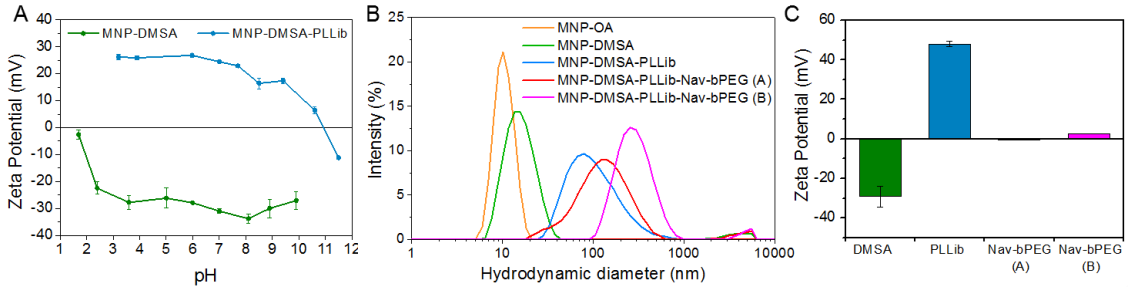

Figure 5.2. Multi-layer MNP assembly. (A) Variation of zeta potential with pH for MNP-DMSA and MNP-DMSA-PLLib; (B) variation of size distribution after sequential deposition of layers onto MNP, measured in low salt conditions; and (C) zeta potential of the particles after addition of each layer, measured in low salt conditions.

The first layer to be added onto of MNP-DMSA was PLL. In order to provide PLL with pH-sensitive anchoring points for the linker neutravidin (Nav) and still maintain its cationic character, partial functionalization of PLL's free amino groups with iminobiotin was carried out. About 28% of the PLL's free amino groups were covalently bound to iminobiotin (36 mol (ib) / mol (PLL)).

Iminobiotin-modified PLL (PLLib) was then deposited onto MNP-DMSA by electrostatic adsorption to produce positively charged nanoprobes with anchoring points for Nav (1.6 μmol (ib) / mg (MNP)). As can be seen in Figure 5.2 A, there was a complete reversal of the particles surface charge due to the presence of amino groups from PLLib. The isoelectric point of the particles shifted from pH 1.5 to pH 11 and therefore, the negative zeta potential observed for MNP-DMSA became positive for MNP-DMSA-PLLib over a wide range of pH values. The

observed increase of hydrodynamic diameter from 16 nm to 139 nm also supports the presence of an extra coating on top of MNP-DMSA. The colloidal suspensions of MNP-DMSA-PLLib were very stable at pH 7.4 and low salt concentrations (1 mM PBS), with a clean size distribution and relatively low PdI (Figure 5.2 B and Table 5.1), but physiological salt conditions (10 mM PBS, 150 mM NaCl) caused flocculation (after ~20 h). This phenomenon was not observed upon addition of the PEG shell, which helped to stabilize the multilayer nanoparticles through inter-particle steric interactions provided by the neutral hydrophilic chains of the polymer.

Table 5.1. Average hydrodynamic diameter and zeta potential of multi-layer nanoparticles at each assembly step.

Nanoparticles	***d_h (nm)***	***pdI***	***Z-Ave (nm)***	***Zeta potential (mV)***
MNP-OA	10 ± 0.3	0.14 ± 0.06	12 ± 3.2	n. a.
MNP-DMSA	16 ± 0.1	0.19 ± 0.01	15 ± 0.1	-29.1 ± 5.2
MNP-DMSA-PLLib	139 ± 10.1	0.22 ± 0.01	97 ± 0.8	48.1 ± 1.4
MNP-DMSA-PLLib-Nav-bPEG (A)	146 ± 7.5	0.31 ± 0.05	109 ± 1.6	-0.4 ± 0.3
MNP-DMSA-PLLib-Nav-bPEG (B)	302 ± 15.6	0.25 ± 0.013	261 ± 7.9	2.6 ± 0.1

The PEG shell is actually a neutravidin-PEG conjugate (Nav-bPEG) in which PEG is functionalized with biotin (bPEG) in one of the chain terminus for strong binding ($K_d = 10^{-15}$ M) to neutravidin. Neutravidin then forms a pH-sensitive bond with iminobiotin from MNP-DMSA-PLLib (Figure 5.1) because Nav-ib affinity is pH-dependent. Two types of multilayer nanoparticles were produced (A and B) by using as a final layer Nav-bPEG conjugates with different proportions of Nav to bPEG (Table 5.2).

The deposition of the Nav-bPEG layer resulted in the neutralization of the particles surface charge at pH 7.4, for both (A) and (B) particles (Figure 5.2 C and Table 5.1), which shows that the inner cationic PLLib layer was effectively shielded by the neutral PEG chains bound to the particles. PEG also contributed for particles stabilization under physiological salt conditions, since flocculation was not observed, unlike MNP-DMSA-PLLib. Neutralization of surface charge with PEG is important from a biological point of view because PEG is known to provide stealth properties to nanoparticles, due to its hydrophilicity, flexibility, and neutral charge in biological fluids. PEG-coated nanomaterials usually have longer circulation times in the blood stream and escape more effectively to the monophagocytic system.[28–30] Hydrodynamic diameter increased in both particle types, supporting the presence of an additional coating on top of MNP-DMSA-PLLib, but the increase was much larger for (B) particles. Due to the larger proportion of bPEG to Nav in Nav-bPEG(B)-coated particles (Table 5.2), there is a tendency for the formation of larger aggregates that deposit by gravity when the particles are left standing in rest but simple agitation provides re-dispersion. Nav-bPEG(A)-coated particles, on the other

hand, were stable, without visible deposition. In this case, the proportion of PEG to Nav and MNP is sufficient to provide particle stabilization trough steric interactions and avoid deposition by gravity.

5.3.2. pH-dependent MNP response

To evaluate pH sensitivity, the multilayer nanoparticles were exposed to different pH conditions by means of dialysis to PBS at pH 5, 6.5, 7.4 and 8.5. Quantification of Nav-bPEG in the buffers after 20 h revealed that the release of Nav-bPEG shell from the nanoparticles differs with pH, as expected, (Figure 5.3) and analysis of samples by DLS showed the consequences on the surface charge, size and polydispersity of the samples (Figure 5.4).

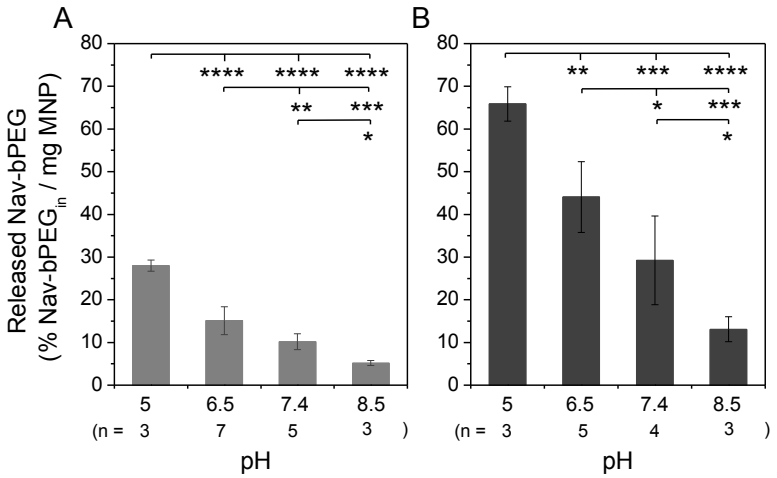

Figure 5.3. pH-dependent dissociation of Nav-bPEG layer from multilayer nanoparticles as a result of 20 h exposition to different pH buffers. (A) MNP-DMSA-PLLib-Nav-bPEG(A) and (B) MNP-DMSA-PLLib-Nav-bPEG(B). (n for each condition is represented between brackets below the graphs). One-Way ANOVA complemented with Tukey's test for multiple comparisons was used to determine P-values.

Table 5.2. Characterization of Nav-bPEG layer. Nav-bPEG conjugation proportion, Nav-bPEG layering conditions and quantification after exposing the multilayer MNPs to different pH conditions.

MNP-DMSA-PLLib-Nav-bPEG	Nav-bPEG conjugation	Nav-bPEG layering	Nav-bPEG layer on the nanoparticles mg $_{Nav\text{-}bPEG}$ / mg $_{MNP}$			
	mol $_{bPEG}$ / mol $_{Nav}$	mg $_{(Nav\text{-}bPEG)in}$ / mg $_{MNP}$	pH 5	pH 6.5	pH 7.4	pH 8.5
(A)	2	26.4 ± 2	19.2 ± 0.3	22.5 ± 0.9	23.8 ± 2.01	25.1 ± 0.2
(B)	20	3.2 ± 0.6	1.0 ± 0.1	1.8 ± 0.2	2.2 ± 0.4	2.7 ± 0.1

The strength of Nav-ib binding its maximal between pH 9.5 and pH 11 ($K_d = 10^{-10}$) and lowers with the pH until complete dissociation of ib from Nav is achieved at pH 4 ($K_d = 10^{-3}$).[15] In accordance with this pH-dependent affinity, Figure 5.3 shows that there was a significant decrease in the amount of Nav-bPEG released from the particles when subjected to increasing

pH conditions. In basic environment (pH 8.5), due to the strong affinity interaction between the ib on the particles and the Nav from Nav-bPEG, most Nav-bPEG is kept bound to the particles. On the other hand, in acidic environment (pH 5), close to the lower limit of affinity, maximal dissociation of Nav-bPEG from the ib anchors on the particles is triggered. The release of Nav-bPEG was incomplete in all of the tested conditions and was lower for MNP-DMSA-PLLib-Nav-bPEG(A). Probably, due to the higher proportion of Nav-bPEG to MNP used to functionalize MNP-DMSA-PLLib-Nav-bPEG(A) (Table 5.2), these particles form more compact aggregates than MNP-DMSA-PLLib-Nav-bPEG(B). The entrapment of Nav-bPEG within the aggregates could hamper the respective release to the dialysates despite the pH-triggered dissociation from ib anchors on the particles.

In Figure 5.4 A, we see that the level of Nav-bPEG shell dissociation in type (A) particles did not expose sufficient PLLib positively charged groups to change the particles zeta potential to positive in the tested conditions. Indeed, neutral zeta potential is observed at all pH conditions, suggesting that there is still PEG covering the PLLib layer. On the other hand, type (B) particles suffered charge reversal to positive from pH 7.4 to pH 6.5 and at pH 5 had a zeta potential of +10 mV, but yet, did not equal the zeta potential of MNP-DMSA-PLLib (subjected to the same pH treatments), which is in accordance with a partial dissociation of the Nav-bPEG from the particles.

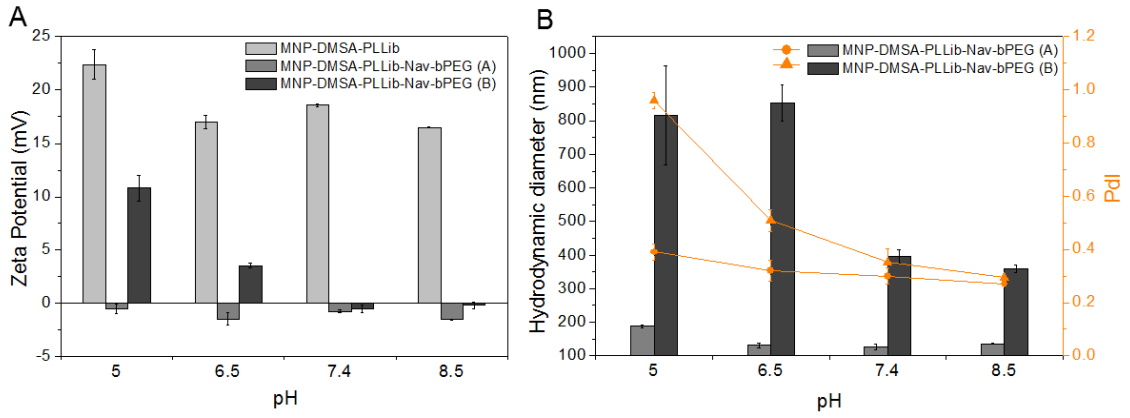

Figure 5.4. Effect of pH treatment on multilayer nanoparticles surface charge and size. (A) Zeta potential compared to MNP-DMSA-PLLib subjected to the same treatment. (B) Hydrodynamic diameter and polydispersity index (MNP-DMSA-PLLib were impossible to measure due to the high polydispersity of the samples).

In the case of MNP-DMSA-PLLib-Nav-bPEG(A), despite the significant differences between the percent of Nav-bPEG release at all tested pHs, particles' hydrodynamic size was kept approximately constant, around 130 nm (the exception is for pH 5, with d_h=190 nm) with only a slight increase of the polydispersity under acidic pH conditions (Figure 5.4 B). We might conclude that the amount of Nav-bPEG shell released was not sufficient to cause important

structural disorganization of nanoparticles. In fact, size distribution profiles at the different pH are kept very similar; only at pH 5 is noticeable the presence of an extra size peak around 30 nm, suggesting some degree of particle dissociation (Figure 5.5 A).

In the case of MNP-DMSA-PLLib-Nav-bPEG(B), although the amount of Nav-bPEG per mass of MNP is approximately 10 times lower than in MNP-DMSA-PLLib-Nav-bPEG(A), the proportion of bPEG to Nav is 10 times higher (Table 5.2). Therefore, and because Nav binds a maximum of four ligands per molecule, part of the bPEG is certainly adsorbed non-specifically onto the particles and contributes to the formation of larger nanoparticle aggregates than for MNP-DMSA-PLLib-Nav-bPEG(A), even at physiological and basic pH (Figure 5.4 B). At acidic pH, triggered by the lower affinity of the pair ib-Nav, Nav-bPEG dissociates from the particles and might take with it some adsorbed Nav-bPEG and bPEG. Under these conditions, positive charges from PLLib which were hidden at higher pHs, become exposed and the particles become polydisperse due to the interaction with buffer salt and start flocculating, similar to MNP-DMSA-PLLib under the same conditions. Size distributions are presented in Figure 5.5 B.

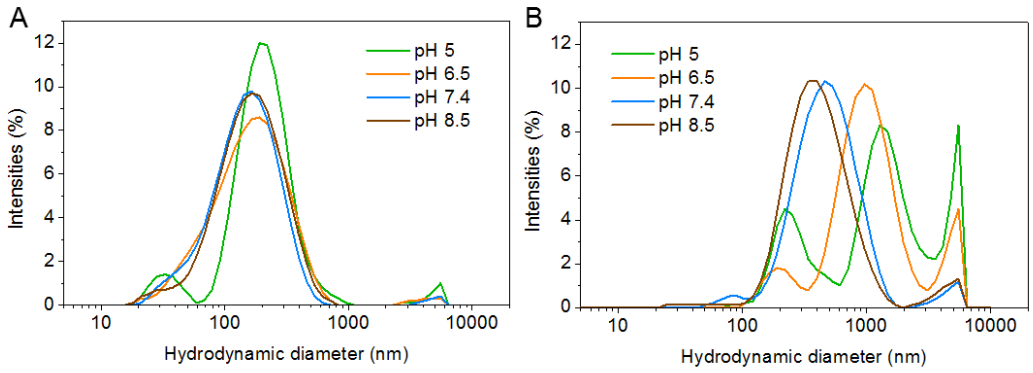

Figure 5.5. Variation of multilayer nanoparticles size distributions after being exposed to PBS at different pHs. (A) MNP-DMSA-PLLib-Nav-bPEG(A) and (B) MNP-DMSA-PLLib-Nav-bPEG(B).

5.3.3. pH-dependent MNP cellular uptake and MR imaging

After observing the pH-dependent erosion of Nav-bPEG shell in saline buffers and the resultant alterations in particles charge and sizes, particles interactions with cells were evaluated. To mimic the tumoral environment and compare the results with physiological conditions, assays with the human colorectal carcinoma HCT116 cell line were performed in acidified culture medium and in standard, non-modified culture medium.

Bright field microscopy of cell preparations stained with Prussian blue after 5 h of incubation with MNP-DMSA-PLLib, MNP-DMSA-PLLib-Nav-bPEG(A) and MNP-DMSA-PLLib-Nav-bPEG(B) in physiological (Figure 5.6 A-D) and acidic conditions (Figure 5.6 a-d) were employed to qualitatively evaluate iron uptake. The Prussian blue images show efficient uptake

of the MNP-DMSA-PLLib, MNP-DMSA-PLLib-Nav-bPEG(A) and MNP-DMSA-PLLib-Nav-bPEG(B), as can be seen by the blue shades inside the cells and attached to the cell membranes, and no clear distinction could be made regarding differences in uptake level between physiological (Figure 5.6 A-D) and acidic cultures (Figure 5.6 a-d). The cellular distribution of iron from MNP-DMSA-PLLib-Nav-bPEG(A) (Figure 5.6 C and 5.6 c) in the cells is similar to the one of MNP-DMSA-PLLib, mainly intracellular (Figure 5.6 B and 5.6 b). However in cells treated with MNP-DMSA-PLLib-Nav-bPEG(B), besides the internalized iron, larger amounts of iron are observed surrounding the cells, attached to the cell membrane. This difference is explained by the higher hydrodynamic diameter of Nav-bPEG(B) multilayer MNP (Figure 5.4), but also reflects the differences between the two Nav-bPEG coatings in terms of MNP's surface chemistry.

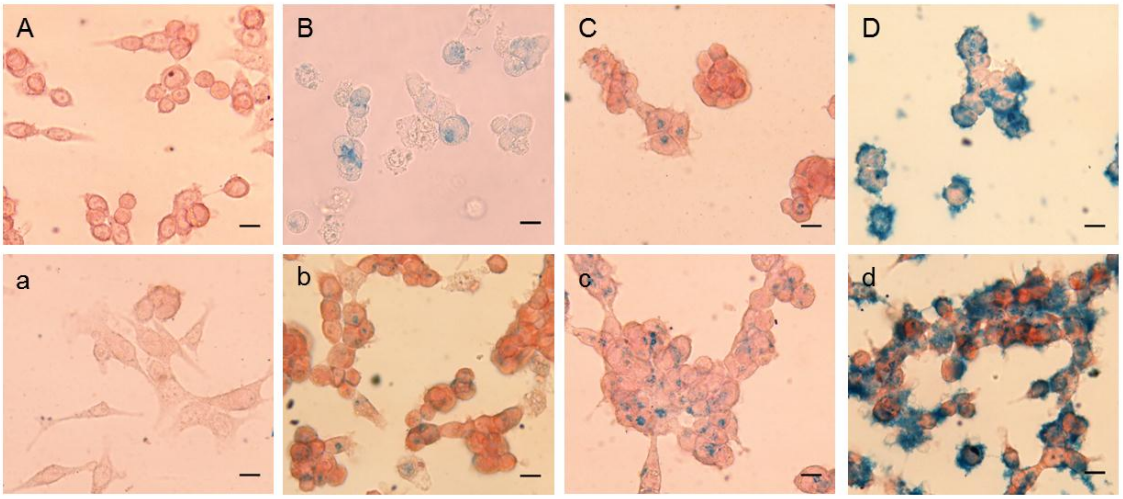

Figure 5.6. Bright field microscopy images of preparations stained with Prussian blue for iron identification, obtained after exposing HCT116 cells to multilayer nanoparticles at 10 μg Fe/ml for 5 h. (A-D) cells incubated in physiological culture medium. (a-d) cells incubated in acidic culture medium. (A and a) untreated cells; (B and b) MNP-DMSA-PLLib; (C and c) MNP-DMSA-PLLib-Nav-bPEG(A); (D and d) MNP-DMSA-PLLib-Nav-bPEG(B)). Scale bar: 10 μm.

When a nanomaterial is put in contact with biological environment, a protein layer (protein corona) rapidly forms around the nanoparticle that overall will affect the interaction of the material with the tissues or cells.[31,32] Generally, neutral and anionic nanoparticles show lower interactions with medium proteins than cationic ones, that interact strongly with proteins and undergo nonspecific binding and, in some cases, can cause cell lysis.[33–35] Since we have used culture medium supplemented with fetal bovine serum (FBS), it is likely that our MNPs may interact first with the culture medium components and afterwards with the cells. Under this hypothesis we can assume that, in the case of MNP-DMSA-PLLib-Nav-bPEG(B), nonspecific adsorption of culture medium proteins enhanced the particles interactions with cells comparatively to the other particle types. Since MNP-DMSA-PLLib-Nav-bPEG(B) have a more

positive zeta potential at tumor pH and broader distribution of sizes than MNP-DMSA-PLLib-Nav-bPEG(A) (Figure 5.4), interactions with medium proteins are favored and probably only the small particles could enter the cells whereas the large ones stayed attached to the membranes by electrostatic interactions with negatively charged cell membrane or through interactions mediated by the medium proteins associated with the particles.

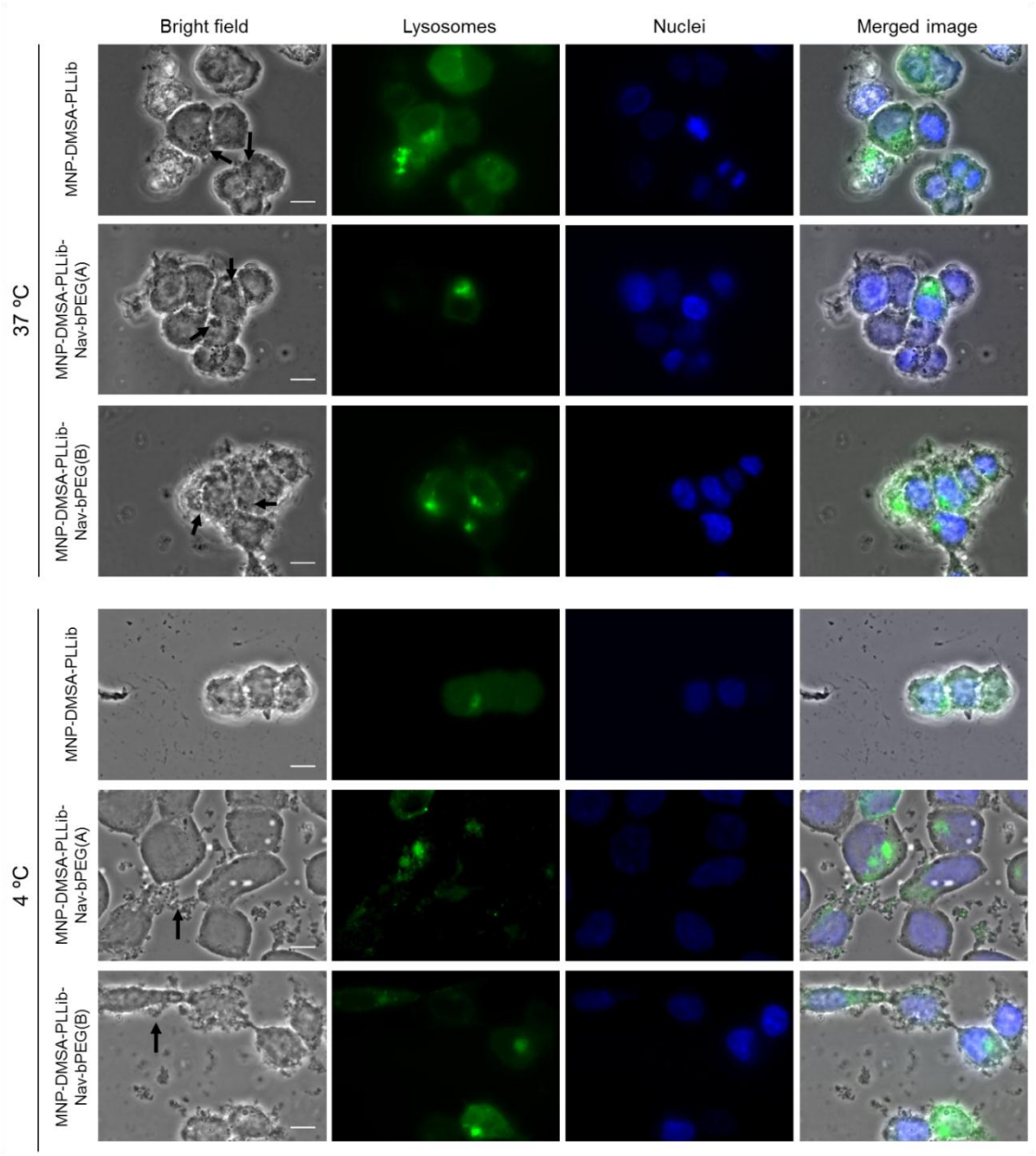

Figure 5.7. Tracking nanoparticles localization after incubation of HCT116 clels for 5 h in acidic culture medium at 37°C and 4°C with MNP-DMSA-PLLib, MNP-DMSA-PLLib-Nav-bPEG(A) and MNP-DMSA-PLLib-Nav-bPEG(B) at 10 μg Fe/ml. Scale bar: 20 μm.

Further inspection of nanoparticle internalization was carried out by observing co-localization of nanoparticles and GFP-labeled lysosomes after 5 h of incubation. Figure 5.7 shows the results for cells incubated with MNPs in acidic conditions, but the same observations were made when physiological culture media was used. At 37 ºC, in the bright field microscopy images, MNPs are identified as black spots and aggregates of black spots in regions of the cytoplasm surrounding the nucleus, which co-localize with green-labeled lysosomes, visible by fluorescent microscopy. When incubation was carried out in the same conditions but at low temperature (4 ºC), MNPs were detected mainly in the extracellular medium and attached to the cell membrane (in particular for MNP-DMSA-PLLib-Nav-bPEG(B)), but not in the lysosome regions. These results indicate that the three types of nanoparticles are internalized via an endocytosis pathway, since at low temperature, energy-dependent processes in the cell (like endocytosis) are blocked and the end-destination of material internalized by endocytosis is the lysosomes. This result is in accordance with other works where PLL-coated iron oxide nanoparticles and multilayer nanoparticles with PEG shell were employed.[20,36] Also, given the multilayer and PLLib coated nanoparticles sizes (>100 nm), other mechanisms would not be expected.

In order to evaluate the effect of the Nav-bPEG coating layer on particles cytotoxicity, cell viability was evaluated after 5 h of incubation with the PLLib-coated nanoprobes and with both multilayer nanoprobes at 10 µg Fe/ml. Figure 5.8 A shows that both type (A) and type (B) Nav-bPEG shells tend to reduce the cytotoxic effect of the nanoparticles because cells treated with MNP-DMSA-PLLib presented much lower viability than cells treated with MNP-DMSA-PLLib-Nav-bPEG. Indeed PEG coatings are commonly used to coat magnetic nanoparticles for biocompatibility purposes due to its hydrophilicity, low immunogenicity and low toxicity.[30,37,38] Compared to MNP-DMSA-PLLib, which are cytotoxic in both physiological ($P < 0.1$) and acidic environments, MNP-DMSA-PLLib-Nav-bPEG(A) and MNP-DMSA-PLLib-Nav-bPEG(B) maintain cell viability levels similar to the one of untreated cells. Interestingly, at pH 7.4, there is a significant difference ($P<0.05$) between viability of cells incubated with PLLib-coated nanoparticles and cells incubated with multilayer nanoparticles with Nav-bPEG(B) shell. This difference is not observed for the multilayer nanoparticles with Nav-bPEG(A) shell, though. Therefore, under physiological conditions, Nav-bPEG(B) layer promotes an effective shield for the positive charges in PLLib layer that (if too exposed) would cause a cytotoxic effect on cells. These results are in accordance with the microscopic observations of cells treated with MNP-DMSA-PLLib and MNP-DMSA-PLLib-Nav-bPEG (Figure 5.6). The protective effect of Nav-bPEG(B) shell tends to be slightly less efficient at acidic pH, probably due to its partial dissociation from the nanoparticles (Figure 5.3 B), in accordance with the increase of zeta potential in PBS at pH 6.5 (Figure 5.4 A).

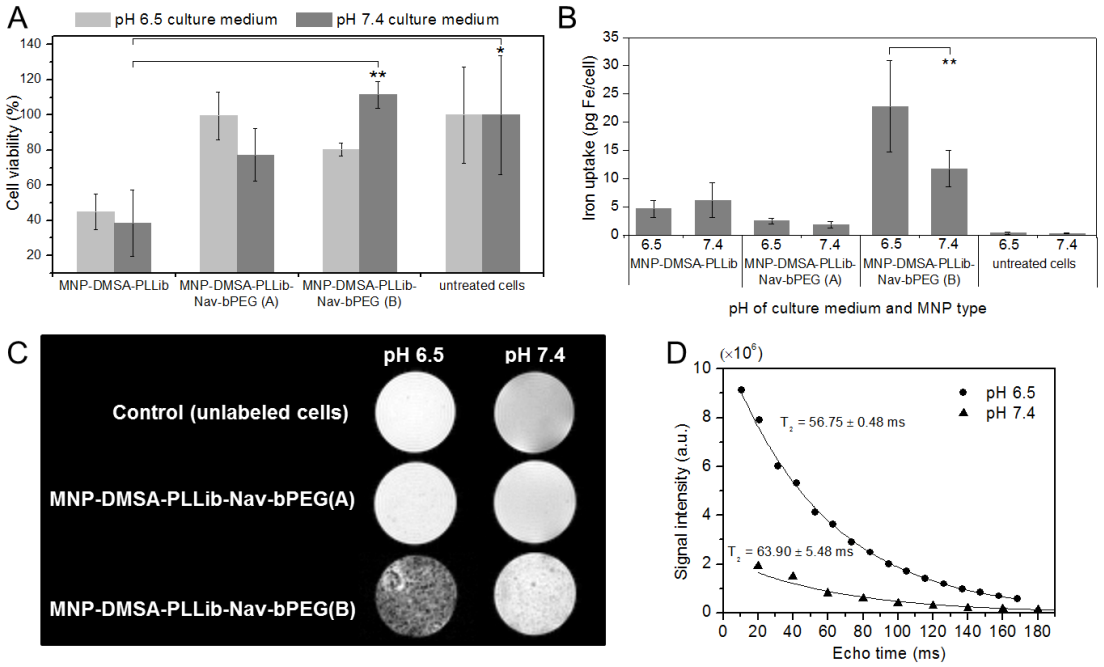

Figure 5.8. pH-dependent cell-nanoparticle interactions after 5 h of incubation with the nanoprobes at 10 μg Fe/ml in acidic (pH 6.5) and physiological (pH 7.4) culture medium. (A) Cell viability by Trypan blue cell counting (n=2); (B) Cellular iron uptake, quantified by ICP-AES (n=3). (C) *In vitro* MRI of unlabeled cells and cells labeled with MNP-DMSA-PLLib-Nav-bPEG(A) and MNP-DMSA-PLLib-Nav-bPEG(B). (D) Determination of the transversal relaxation time, T_2, for MNP-DMSA-PLLib-Nav-bPEG(B) labeled cell samples. For cell viability, regular two-way ANOVA complemented with Bonferroni´s test was used to compare the effect of MNPs at the same pH and to compare the effect of a given MNP at pH 6.5 *vs.* pH 7.4. For iron uptake, regular two-way ANOVA complemented with Bonferroni's test was compare each condition with untreated control cells and to compare pH effect in treated cells.

To quantify the pH dependency of magnetic cell labeling, ICP-AES characterization of cell-associated iron was performed after incubating cells with the nanoparticles (Figure 5.8 B). As observed in the Prussian blue staining images (Figure 5.6), all nanoparticles were taken up by cells in the tested conditions, but the higher content of cell-bound iron was registered for MNP-DMSA-PLLib-Nav-bPEG(B) ($P<0.0001$, at pH 6.5 and $P<0.005$ at pH 7.4, relative to untreated cells). Cell-associated iron is mainly due to internalized nanoparticles but there is also a proportion of nanoparticles adsorbed onto the cell surface (Figure 5.9).

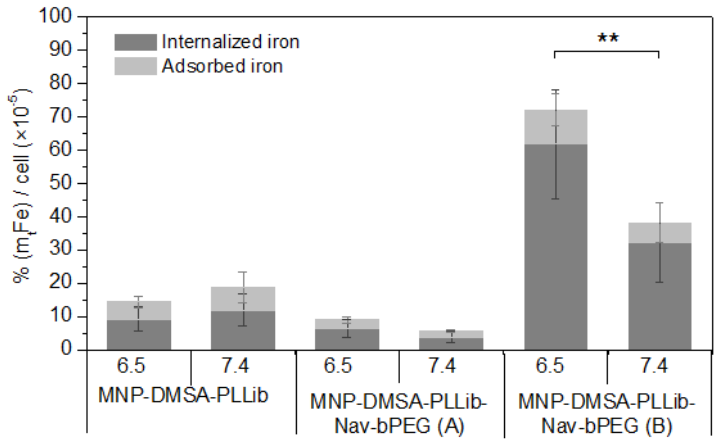

Figure 5.9. Contribution of internalized and adsorbed nanoparticles for the proportion of cellular iron found in cells after labeling.

Both MNP-DMSA-PLLib-Nav-bPEG types showed higher cellular uptake at acidic than at physiological conditions, as evidenced in Figure 5.8 B and Figure 5.9. However, while only a subtle difference was registered for MNP-DMSA-PLLib-Nav-bPEG(A) (2.52 ± 0.5 pg Fe/cell at pH 6.5 and 1.89 ± 0.57 pg Fe/cell at pH 7.4), a significantly higher uptake of MNP-DMSA-PLLib-Nav-bPEG(B) was observed at pH 6.5 (22.82 ± 8.15 pg Fe/cell) than at pH 7.4 (11.79 ± 3.22 pg Fe/cell). Approximately a 2-fold increase in Fe uptake was promoted by MNP-DMSA-PLLib-Nav-bPEG(B) in acidic compared to physiological conditions, which supports our strategy for preferential interaction with cells in the acidic environment characteristic of tumor tissues. The uptake of Fe observed at pH 6.5 in our study (~23 pg Fe/cell after incubation with 10 µg Fe/ml for 5 h) is ~5 times higher than the one reported by other authors for a pH-dependent MNP system that used chlorotoxin (CTX) as active targeting agent for glioma cells (~ 2 pg Fe /cell after incubating with 4 µg Fe/mL for 6 h).[11]

Despite the less cationic character of MNP-DMSA-PLLib-Nav-bPEG(B) compared with MNP-DMSA-PLLib (Figure 5.4 A), the cellular uptake is higher, leading to more effective labelling, as seen in Figures 5.6 D and 5.6 d. In fact, there are several factors that influence the uptake of nanoparticles by cells and surface charge cannot be taken in consideration alone. In particular size and surface chemistry are also important parameters that influence the way nanoparticles interact with cells,[39,40] as discussed previously. Our measurements in 150 mM salt showed that both MMP-DMSA-PLLib and MNP-DMSA-PLLib-Nav-bPEG(B) are polydisperse at pH 6.5 while at pH 7.4 Nav-bPEG(B)-coated nanoparticles form smaller aggregates and are less polydisperse, but have neutral charge (Figure 5.4). Charge reversal due to Nav-bPEG(B) dissociation at pH 6.5, aggregation and advantageous interaction with cell culture components

might be responsible for the differential uptake of MNP-DMSA-PLLib-Nav-bPEG(B) in acidic medium compared to physiological medium.

Superparamagnetic iron oxide nanoparticles with core sizes between 6 and 20 nm are negative MRI contrast agents,[1] i.e., have the ability to shorten the transversal relaxation time (T_2) of water protons in their vicinity, which translates in a darkening effect of MR images in the areas were the nanoprobes are present. The MNP-DMSA that are the basis of this multilayer system were previously shown to possess superparamagnetic and T_2 MRI contrast agent properties.[23,41] To evaluate the multilayer nanoprobes regarding their efficacy as MRI contrast agents and the ability to distinguish the cells according to their culture pH, T_2-weighted MR images of agarose dispersions of 90 000 cells incubated with the multilayer MNPs in acidic and physiological conditions were produced. For cells incubated with MNP-DMSA-PLLib-Nav-bPEG(A), the level of cellular uptake was not sufficient to render the cells visible by MRI compared to unlabeled cells nor to provide differential contrast for the different incubation conditions (Figure 5.8 C). On the other hand, for cells incubated with MNP-DMSA-PLLib-Nav-bPEG(B), the MR images show a clear contrast difference relative to unlabeled cells and, more importantly, show preferential labeling of cells in acidic conditions compared to those in physiological medium (Figure 5.8 C). Labeled cells are detectable as hypointense regions in the images, which are more intense in the acidic than in the physiological sample due to the higher content of MNPs in those cell samples. Correspondingly, T_2 of cells in acidic medium (T_2 = 56.75 ± 0.48 ms) is shorter than in physiological medium (T_2 = 63.90 ± 5.48 ms) (Figure 5.8 D). Similar results were reported by Crayton *et al.*,[10] which showed that cells incubated with glycol-chitosan-coated MNPs exhibited pH-dependence to their T_2 relaxation times and caused increasingly higher signal losses in MR images from pH 7.65 to pH 5.9.

Given the overall results of this study, MNP-DMSA-PLLib-Nav-bPEG(B) multilayer system is a potential effective pH-sensitive nanoprobe for MRI cell labeling. It is interesting to note that the cell phantoms presented in this work contained a relatively small amount of cells compared to other authors' studies[10] and compared to our previous studies (300 000 cells of the same HCT116 cell line).[26,41] Although the coating materials used were different, better contrast was achieved in the present study for cells at acidic conditions, even with a lower administered dose of iron, which also supports the high labelling efficacy of this system.

The multilayer pH-sensitive magnetic nanoprobe MNP-DMSA-PLLib-Nav-bPEG(B) overall presented better performance *in vitro* than MNP-DMSA-PLLib-Nav-bPEG(A), despite its higher polydispersity and size. The observed selectivity for labeling HCT116 cells in acidic compared to physiological medium confirms that the ib-Nav pH-dependent and biologically derived affinity pair is suited to confer pH-sensitivity in the range of values that we tested and that immobilization within the multilayered architecture system does not affect its robustness.

Compared to a similar architecture system,[20] our magnetic nanoprobe presents the advantage of allowing imaging by MRI, which is well established for human-scale diagnosis in the clinic unlike other imaging modalities such as fluorescence. Moreover, it offers the possibility (not explored in this work) of magnetic targeting using an external magnet to direct the nanoprobe to desired areas after systemic injection.

Given the availability of free amine groups in the PLLib layer, a more complex nanoprobe could be engineered using the developed system as template. For example, reporter and/or specific targeting molecules could be attached to create a combined targeting strategy for a pH-sensitive multimodal drug delivery and imaging system.

5.4. Conclusions

In this work, a proof-of-concept of an affinity triggered T_2 MRI contrast agent for cancer cell labeling was presented. The developed nanoprobe is activated by the typically acidic pH found in cancer tissues so that preferential interaction with cells is promoted under those conditions, leading to higher contrast in MRI. While most strategies to produce iron oxide MNP sensitive to pH rely on the use of chemically engineered polymers with pH-sensitive bonds or chemical groups, this work has demonstrated the feasibility of a biologicaly-derived affinity interaction (iminobiotin/neutravidin) to achieve pH activation of such nanoprobes. The MNP-DMSA-PLLib-Nav-bPEG(B) multilayer nanoprobe provideD pH dependent MRI contrast in cell phantoms of HCT116 colorectal carcinoma cells due to its pH-removable PEG shell. Indeed, we have shown that the PEGylated outer layer of MNP-DMSA-PLLib-Nav-bPEG(B) is able to shield the cationic charges of the underlying PLLib layer at physiological pH (pH 7.4) and expose it at acidic pH by means of the neutravidin linker between both layers. The weaker strength of Nav-ib affinity interaction at acidic pH triggers the release of Nav-bPEG from the nanoparticles in acidic environment, which leads to enhanced nanoparticle uptake by HCT116 cells in acidic conditions (22.82 ± 8.15 pg Fe/cell) compared to the observed in physiological pH conditions (11.79 ± 3.22 pg Fe/cell). For cells cultured at pH 7.4, PEG shell also contributes to decrease the cytotoxicity of the nanoprobes. The difference in nanoparticle uptake resulted in clear hypointensity differences between cells cultured in acidic medium (T_2 = 56.75 ± 0.48 ms) and cells cultured in physiological medium (T_2 = 63.90 ± 5.48 ms). As acidity is a characteristic of most of cancer tissues, the presented tumor-targeted nanoprobe architecture allows a general tumor targeting approach and is expected to provide specific MR labeling of tumoral tissues disregarding the type of cancer. We suggest that the iminobiotin/neutravidin based MNP multilayer architecture could contribute to surpass some of the issues associated with ligand/receptor mediated tumor targeting strategies *in vivo*; for example, the heterogeneity among cancer cell populations and

the heterogeneous expression of receptors or antigens on cancer cell membranes,[8] which limit the efficacy of nanoprobes decorated with specific ligands targeting for one biomarker. Also, given the availability of free amine groups in PLLib layer, a more complex nanoprobe could be engineered using the present system as a template. For example, drugs, reporter and/or specific targeting molecules could be attached to produce a pH-sensitive multimodal drug delivery and imaging system.

5.5. References

(1) Colombo, M.; Carregal-Romero, S.; Casula, M. F.; Gutiérrez, L.; Morales, M. P.; Böhm, I. B.; Heverhagen, J. T.; Prosperi, D.; Parak, W. J. Biological Applications of Magnetic Nanoparticles. *Chem. Soc. Rev.* **2012**, *41*, 4306–4334, DOI:10.1039/c2cs15337h.

(2) Sharifi, S.; Seyednejad, H.; Laurent, S.; Atyabi, F.; Saei, A. A.; Mahmoudi, M. Superparamagnetic Iron Oxide Nanoparticles for *in Vivo* Molecular and Cellular Imaging. *Contrast Media Mol. Imaging* **2015**, DOI:10.1002/cmmi.1638.

(3) Shin, T.-H.; Choi, Y.; Kim, S.; Cheon, J. Recent Advances in Magnetic Nanoparticle-Based Multi-Modal Imaging. *Chem. Soc. Rev.* **2015**, *44*, 4501–4516, DOI:10.1039/c4cs00345d.

(4) Baptista, P.; Fernandes, A.; Figueiredo, S.; Vinhas, R.; Cordeiro, M.; Carlos, F.; Mendo, S. Gold Nanoparticle-Based Theranostics: Disease Diagnostics and Treatment Using a Single Nanomaterial. *Nanobiosensors Dis. Diagnosis* **2015**, *Volume 4*, 11, DOI:10.2147/NDD.S60285.

(5) Danhier, F.; Feron, O.; Préat, V. To Exploit the Tumor Microenvironment: Passive and Active Tumor Targeting of Nanocarriers for Anti-Cancer Drug Delivery. *J. Control. Release* **2010**, *148*, 135–146, DOI:10.1016/j.jconrel.2010.08.027.

(6) Du, J.-Z.; Mao, C.-Q.; Yuan, Y.-Y.; Yang, X.-Z.; Wang, J. Tumor Extracellular Acidity-Activated Nanoparticles as Drug Delivery Systems for Enhanced Cancer Therapy. *Biotechnol. Adv.* **2014**, *32*, 789–803, DOI:10.1016/j.biotechadv.2013.08.002.

(7) Medeiros, S. F.; Santos, A. M.; Fessi, H.; Elaissari, A. Stimuli-Responsive Magnetic Particles for Biomedical Applications. *Int. J. Pharm.* **2011**, *403*, 139–161, DOI:10.1016/j.ijpharm.2010.10.011.

(8) Tian, L.; Bae, Y. H. Cancer Nanomedicines Targeting Tumor Extracellular pH. *Colloids Surf. B. Biointerfaces* **2012**, *99*, 116–126, DOI:10.1016/j.colsurfb.2011.10.039.

(9) Estrella, V.; Chen, T.; Lloyd, M.; Wojtkowiak, J.; Cornnell, H. H.; Ibrahim-Hashim, A.; Bailey, K.; Balagurunathan, Y.; Rothberg, J. M.; Sloane, B. F.; *et al.* Acidity Generated by the Tumor Microenvironment Drives Local Invasion. *Cancer Res.* **2013**, *73*, 1524–1535, DOI:10.1158/0008-5472.CAN-12-2796.

(10) Crayton, S. H.; Tsourkas, A. pH-Titratable Superparamagnetic Iron Oxide for Improved Nanoparticle Accumulation in Acidic Tumor Microenvironments. *ACS Nano* **2011**, *5*, 9592–9601, DOI:10.1021/nn202863x.

(11) Mok, H.; Veiseh, O.; Fang, C.; Kievit, F. M.; Wang, F. Y.; Park, J. O.; Zhang, M. pH-Sensitive siRNA Nanovector for Targeted Gene Silencing and Cytotoxic Effect in Cancer Cells. *Mol. Pharm.* **2010**, *7*, 1930–1939, DOI:10.1021/mp100221h.

(12) Saha, I.; Chaffee, K. E.; Duanmu, C.; Woods, B. M.; Stokes, A. M.; Buck, L. E.; Walkup, L. L.; Sattenapally, N.; Huggenvik, J.; Gao, Y.; *et al.* pH-Sensitive MR Responses Induced by Dendron-Functionalized SPIONs. *J. Phys. Chem. C. Nanomater. Interfaces* **2013**, *117*, 1893–1903, DOI:10.1021/jp306128v.

(13) Ling, D.; Park, W.; Park, S.-J.; Lu, Y.; Kim, K. S.; Hackett, M. J.; Kim, B. H.; Yim, H.; Jeon, Y. S.; Na, K.; *et al.* Multifunctional Tumor pH-Sensitive Self-Assembled Nanoparticles for Bimodal Imaging and Treatment of Resistant Heterogeneous Tumors. *J. Am. Chem. Soc.* **2014**, *136*, 5647–5655, DOI:10.1021/ja4108287.

(14) *Avidin-Biotin Technology*; Wilchek, M.; Bayer, E. A., Eds.; Methods in Enzymology; Elsevier, 1990; Vol. 184.

(15) Hofmann, K.; Titus, G.; Montibeller, J. A.; Finn, F. M. Avidin Binding of Carboxyl-Substituted Biotin and Analogs. *Biochemistry* **1982**, *21*, 978–984, DOI:10.1021/bi00534a024.

(16) Orr, G. The Use of the 2-Iminobiotin-Avidin Interaction for the Selective Retrieval of Labeled Plasma Membrane Components. *J. Biol. Chem.* **1981**, *256*, 761–766.

(17) Garret-Flaudy, F.; Freitag, R. Use of the Avidin (imino)biotin System as a General Approach to Affinity Precipitation. *Biotechnol. Bioeng. 71*, 223–234.

(18) Sun, S.; Ma, M.; Qiu, N.; Huang, X.; Cai, Z.; Huang, Q.; Hu, X. Affinity Adsorption and Separation Behaviors of Avidin on Biofunctional Magnetic Nanoparticles Binding to Iminobiotin. *Colloids Surfaces B Biointerfaces* **2011**, *88*, 246–253.

(19) Inoue, H.; Sato, K.; Anzai, J. Disintegration of Layer-by-Layer Assemblies Composed of 2-Iminobiotin-Labeled Poly(ethyleneimine) and Avidin. *Biomacromolecules* **2004**, *6*, 27–29, DOI:10.1021/bm0495856.

(20) Poon, Z.; Chang, D.; Zhao, X.; Hammond, P. T. Layer-by-Layer Nanoparticles with a pH-Sheddable Layer for *in Vivo* Targeting of Tumor Hypoxia. *ACS Nano* **2011**, *5*, 4284–4292, DOI:10.1021/nn200876f.

(21) Sun, S.; Zeng, H.; Robinson, D. B.; Raoux, S.; Rice, P. M.; Wang, S. X.; Li, G. Monodisperse MFe 2 O 4 (M) Fe , Co , Mn) Nanoparticles. **2004**, *4*, 126–132.

(22) Lattuada, M.; Hatton, T. A. Functionalization of Monodisperse Magnetic Nanoparticles. *Langmuir* **2007**, *23*, 2158–2168, DOI:10.1021/la062092x.

(23) Palma, S. I. C. J.; Marciello, M.; Carvalho, A.; Veintemillas-Verdaguer, S.; Morales, M. D. P.; Roque, A. C. A. Effects of Phase Transfer Ligands on Monodisperse Iron Oxide Magnetic Nanoparticles. *J. Colloid Interface Sci.* **2015**, *437*, 147–155, DOI:10.1016/j.jcis.2014.09.019.

(24) Batalha, I. L.; Hussain, A.; Roque, A. C. A. Gum Arabic Coated Magnetic Nanoparticles with Affinity Ligands Specific for Antibodies. *J. Mol. Recognit.* **2010**, *23*, 462–471, DOI:10.1002/jmr.1013.

(25) Wiechelman, K. J.; Braun, R. D.; Fitzpatrick, J. D. Investigation of the Bicinchoninic Acid Protein Assay: Identification of the Groups Responsible for Color Formation. *Anal. Biochem.* **1988**, *175*, 231–237, DOI:10.1016/0003-2697(88)90383-1.

(26) Palma, S. I. C. J.; Carvalho, A.; Silva, J.; Martins, P.; Marciello, M.; Fernandes, A. R.; Del Puerto Morales, M.; Roque, A. C. A. Covalent Coupling of Gum Arabic onto Superparamagnetic Iron Oxide Nanoparticles for MRI Cell Labeling: Physicochemical and *in Vitro* Characterization. *Contrast Media Mol. Imaging* **2015**, *10*, 320–328, DOI:10.1002/cmmi.1635.

(27) Riggio, C.; Calatayud, M. P.; Hoskins, C.; Pinkernelle, J.; Sanz, B.; Torres, T. E.; Ibarra, M. R.; Wang, L.; Keilhoff, G.; Goya, G. F.; *et al.* Poly-L-Lysine-Coated Magnetic Nanoparticles as Intracellular Actuators for Neural Guidance. *Int. J. Nanomedicine* **2012**, *7*, 3155–3166, DOI:10.2147/IJN.S28460.

(28) Yu, M. K.; Park, J.; Jon, S. Targeting Strategies for Multifunctional Nanoparticles in Cancer Imaging and Therapy. *Theranostics* **2012**, *2*, 3–44, DOI:10.7150/thno.3463.

(29) Xie, J.; Xu, C.; Kohler, N.; Hou, Y.; Sun, S. Controlled PEGylation of Monodisperse Fe3O4 Nanoparticles for Reduced Non-Specific Uptake by Macrophage Cells. *Adv. Mater.* **2007**, *19*, 3163–3166, DOI:10.1002/adma.200701975.

(30) Ruiz, A.; Hernández, Y.; Cabal, C.; González, E.; Veintemillas-Verdaguer, S.; Martínez, E.; Morales, M. P. Biodistribution and Pharmacokinetics of Uniform Magnetite Nanoparticles Chemically Modified with Polyethylene Glycol. *Nanoscale* **2013**, *5*, 11400–11408, DOI:10.1039/c3nr01412f.

(31) Yallapu, M. M.; Chauhan, N.; Othman, S. F.; Khalilzad-Sharghi, V.; Ebeling, M. C.; Khan, S.; Jaggi, M.; Chauhan, S. C. Implications of Protein Corona on Physico-Chemical and Biological Properties of Magnetic Nanoparticles. *Biomaterials* **2015**, *46*, 1–12, DOI:10.1016/j.biomaterials.2014.12.045.

(32) Mahmoudi, M.; Lynch, I.; Ejtehadi, M. R.; Monopoli, M. P.; Bombelli, F. B.; Laurent, S. Protein-Nanoparticle Interactions: Opportunities and Challenges. *Chem. Rev.* **2011**, *111*, 5610–5637, DOI:10.1021/cr100440g.

(33) Reddy, L. H.; Arias, J. L.; Nicolas, J.; Couvreur, P. Magnetic Nanoparticles: Design and Characterization, Toxicity and Biocompatibility, Pharmaceutical and Biomedical Applications. *Chem. Rev.* **2012**, *112*, 5818–5878, DOI:10.1021/cr300068p.

(34) Theumer, A.; Gräfe, C.; Bähring, F.; Bergemann, C.; Hochhaus, A.; Clement, J. H. Superparamagnetic Iron Oxide Nanoparticles Exert Different Cytotoxic Effects on Cells Grown in Monolayer Cell Culture versus as Multicellular Spheroids. *J. Magn. Magn. Mater.* **2015**, *380*, 27–33, DOI:10.1016/j.jmmm.2014.10.039.

(35) Chen, J.; Hessler, J. A.; Putchakayala, K.; Panama, B. K.; Khan, D. P.; Hong, S.; Mullen, D. G.; Dimaggio, S. C.; Som, A.; Tew, G. N.; *et al.* Cationic Nanoparticles Induce Nanoscale Disruption in Living Cell Plasma Membranes. *J. Phys. Chem. B* **2009**, *113*, 11179–11185, DOI:10.1021/jp9033936.

(36) Babič, M.; Horák, D.; Trchová, M.; Jendelová, P.; Glogarová, K.; Lesný, P.; Herynek, V.; Hájek, M.; Syková, E. Poly(l-Lysine)-Modified Iron Oxide Nanoparticles for Stem Cell Labeling. *Bioconjug. Chem.* **2008**, *19*, 740–750, DOI:10.1021/bc700410z.

(37) Ruiz, A.; Salas, G.; Calero, M.; Hernández, Y.; Villanueva, A.; Herranz, F.; Veintemillas-Verdaguer, S.; Martínez, E.; Barber, D. F.; Morales, M. P. Short-Chain PEG Molecules Strongly Bound to Magnetic Nanoparticle for MRI Long Circulating Agents. *Acta Biomater.* **2013**, *9*, 6421–6430, DOI:10.1016/j.actbio.2012.12.032.

(38) Mojica Pisciotti, M. L.; Lima, E.; Vasquez Mansilla, M.; Tognoli, V. E.; Troiani, H. E.; Pasa, A. A.; Creczynski-Pasa, T. B.; Silva, A. H.; Gurman, P.; Colombo, L.; *et al. In Vitro* and *in Vivo* Experiments with Iron Oxide Nanoparticles Functionalized with DEXTRAN or Polyethylene Glycol for Medical Applications: Magnetic Targeting. *J. Biomed. Mater. Res. B. Appl. Biomater.* **2014**, *102*, 860–868, DOI:10.1002/jbm.b.33068.

(39) Verma, A.; Stellacci, F. Effect of Surface Properties on Nanoparticle-Cell Interactions. *Small* **2010**, *6*, 12–21, DOI:10.1002/smll.200901158.

(40) Mahmoudi, M.; Meng, J.; Xue, X.; Liang, X. J.; Rahman, M.; Pfeiffer, C.; Hartmann, R.; Gil, P. R.; Pelaz, B.; Parak, W. J.; *et al.* Interaction of Stable Colloidal Nanoparticles with Cellular Membranes. *Biotechnol. Adv.* **2014**, *32*, 679–692, DOI:10.1016/j.biotechadv.2013.11.012.

(41) Palma, S. I.; Rodrigues, C. A.; Carvalho, A.; Morales, M. P.; Freitas, F.; Fernandes, A. R.; Cabral, J. S.; Roque, A. C. A. A Value-Added Exopolysaccharide as a Coating Agent for MRI Nanoprobes. *Nanoscale* **2015**, *7*, 14272–14283, DOI:10.1039/C5NR01979F.

Chapter 6

Concluding Remarks

The project presented in this thesis aimed at designing iron oxide MNP–based T_2 MRI nanoprobes using natural and synthetic polymers as particle coating and functionalization materials. The major contributions of this project were in the development of magnetic nanoprobes bearing a novel biopolymer produced by a biotechnological process, as well as the design of an affinity triggered magnetic nanoprobe for selective targeting of tumor environments using a biologically-derived affinity pair.

The thermal decomposition method was employed to synthesize monodisperse magnetic cores with controlled size and magnetic properties, important for biomedical applications. The hydrophobic MNP that resulted from the synthesis were stabilized in aqueous medium by replacing the hydrophobic ligands by hydrophilic small molecules such as citric acid or *meso*-2,3-dimercaptosuccinic acid (DMSA) through a ligand exchange reaction. After a comprehensive characterization of the physiochemical properties of the hydrophilic MNP, it was concluded that the ligand-exchange protocol with DMSA, besides being more straightforward, provided particles with better magnetization and chemically more versatile for further functionalization.[1] MNP-DMSA with optimal hydrodynamic size distribution and colloidal stability were then used towards the development of MRI nanoprobes with natural/synthetic polymer coatings. A summary of the physiochemical properties and nanoprobe-cell interactions for the developed nanoprobes is found in Table 6.1, Table 6.2 and Figure 6.1.

Most natural polymer-coated MNP described in the literature are produced by adsorption of the polymer onto the MNP surface. However, in order to increase the stability of the coating, permanent conjugation strategies are preferred. Since MNP-DMSA have both thiol and carboxylic acid groups at the surface, the reactivity of these groups was explored to covalently couple the biopolymer gum Arabic (GA), derived from *Acacia senegal* and *Acacia seyal* trees. The use of EDC/NHS chemistry for the establishment of amide bonds between the carboxylic acid groups from MNP-DMSA and the free amine groups in gum Arabic proved to be an efficient strategy to produce a nanoprobe with excellent MRI T_2 contrast enhancement properties (r_2/r_1 = 350) which provided approximately a 20-fold enhancement of relative cellular uptake in human colorectal carcinoma cells (HCT116 cell line) compared to uncoated MNP-

DMSA. Contrast enhancement was clearly visible as dose-dependent hypointensity in *in vitro* MRI phantoms of HCT116 cells incubated with MNP-DMSA-GA.[2] The protocols defined in this work served as the inspiration to explore the feasibility of a new biopolymer, the exopolysaccharide (EPS) Fucopol,[3] as a coating agent for MNP-DMSA to produce cell labelling agents. Since EPS possesses an associated residual protein fraction, the covalent coupling strategy firstly devised to conjugate GA onto MNP-DMSA was optimized and employed to produce MNP-DMSA-EPS with covalently coupled EPS.[4] Like GA, EPS coating led to the formation of aggregates of magnetic cores entrapped in the polymer network which have enhanced relaxometric properties compared to MNP-DMSA (r_2/r_1=148 for MNP-DMSA-EPS *vs*. r_2/r_1=2.3 for MNP-DMSA) (Table 6.1). These nanoprobes were shown to be particularly efficient T_2-contrast agents for *in vitro* cell labeling of human neural progenitor/stem cells (ReNcell VM cell line), promoting a 10-fold increase in the relative uptake of iron per cell compared to MNP-DMSA without affecting the viability and multipotency of the cells. Dose-dependent MRI contrast enhancement was obtained in agarose dispersions of these cells, contrary to *in vitro* MRI of HCT116 cells labeled with the same nanoprobe (Table 6.2 and Figure 6.1).

Table 6.1. Summary of size, colloidal and relaxometric properties of the MNP produced in this thesis.

	MNP-DMSA	***MNP-DMSA-GA***	***MNP-DMSA-EPS***	***MNP-DMSA-PLLib-Nav-bPEG(B)***	***Ferumoxides (Endorem / Feridex)***[5]
d_h (nm)[(a)]	15.0 ± 2.0	290.7 ± 69.2	168.0 ± 40.0	302.0 ± 15.6	120 - 180
PdI	0.31	0.20	0.25	0.25	-
Zeta Potential (mV)	-30.0 ± 6.0	-21.0 ± 6.0	-23.2 ± 0.2	2.6 ± 0.1	< 0
Coating (%)	11.0	21.0	29.0	n.d.	-
r_1 ($mM^{-1}s^{-1}$)	2.6	0.9	2.4	n.d.	2.2
r_2 ($mM^{-1}s^{-1}$)	110.0	314.7	361.0	n.d.	182
r_2/r_1	42.3	349.7	148.0	n.d.	82.7

[(a)]intensities distribution; n.d. = not determined. Zeta potential measured at pH 7 in 10 mM KNO_3.

A combination of synthetic and biological coating layers was also explored in this thesis, showing for the first time, the addition of pH sensitive properties to iron oxide MNPs through the use of a biologically-derived affinity interaction. In order to engineer a dynamic nanoprobe activated by the acidic tumor microenvironment, a pH removable PEG shield was bound to positively charged MNPs. The biologically derived and pH-sensitive affinity pair composed by the protein neutravidin and the ligand iminobiotin was used as a linker between a poly-l-lysine (PLL) inner layer and a biotinylated poly(ethyleneglycol) (bPEG) outer layer on the MNPs. This system was built over the initial MNP-DMSA monodisperse particles taking advantage of the

strong electrostatic interactions between the negatively charged MNP-DMSA surface and the positively charged PLL. Layering conditions were optimized towards differential cellular uptake at tumor and physiological pH. The nanoprobes' uptake by HCT116 cells *in vitro* was shown to be enhanced under acidic pH conditions as a 2-fold increase in iron uptake per cell was observed at acidic pH compared to physiological pH. Increased cellular uptake of the nanoprobes in acidic pH resulted in enhanced contrast in T_2-weighted MR images, which allowed cells cultured in physiological medium to be distinguished from others cultured in acidified medium (Table 6.2 and Figure 6.1).

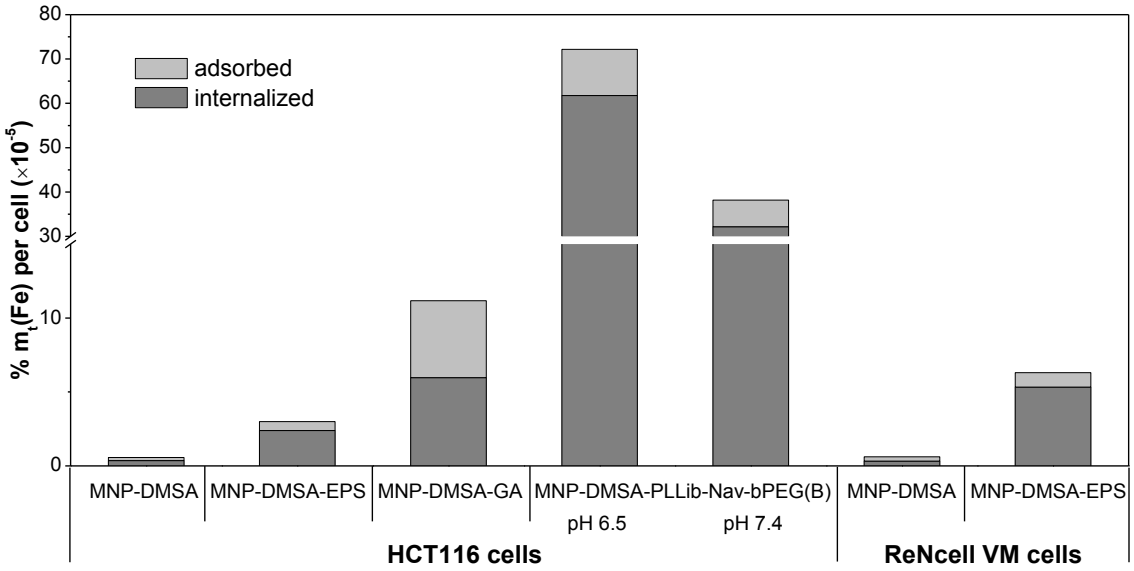

Figure 6.1. Summary of the average relative iron uptake per cell upon incubation with the MNPs developed in the context of this thesis. See incubation conditions in Table 6.2

While biopolymers have intrinsic biocompatibility and biodegradability properties and are greener products, synthetic polymers offer engineering versatility and possibility of being tailor-made with specific properties. The work described in this thesis took advantage of these features to create new polymer-coated MRI nanoprobes with differing architectures and cell interaction abilities. The nature of the polymeric coating, as well as its relative amount in the nanoprobe composition were shown to influence the size, colloidal properties and relaxivities of the nanoprobes, which was particularly observed for biopolymer-coated nanoprobes (Table 6.1). Importantly, the effect of polymers nature and coating architecture was noticeable in the interactions of the nanoprobes with *in vitro* cell cultures (Figure 6.1 and Table 6.2). Independently of the incubation time and cell type, the presence of a polymeric coating on the nanoprobes contributed to an increase in the fraction of cell-associated iron compared to uncoated MNP-DMSA. Then, different cellular uptake levels were observed depending on the nature of the polymers and on the nanoprobe's architecture. For the same coating

polymer, different uptake was observed depending on the cell type (Figure 6.1). Several factors influence interactions of MNP with cells.[6] With this work it can be concluded that a balance between MNPs intrinsic physiochemical characteristics (such as particle size, shape, charge and surface chemistry) and incubation conditions (incubation time, iron concentration administered, constitution of the culture medium) might be optimized towards efficient and safe magnetic labeling of a determined cell type.

GA and EPS-coated MNPs were shown to be biocompatible in the range of concentrations tested and taken up by cells non-specifically without the need for transfection agents. These hybrid magnetic-biopolymeric nanoplatforms are therefore suggested as potential nanoprobes for *in vitro* cell labeling and *in vivo* cell tracking by MRI, for example in the context of cell transplantation applications, such as stem cell therapy. On the other hand, through the combination of the synthetic polymers PLL and PEG with the biologically derived affinity pair neutravidin/iminobiotin, a multilayer pH-dependent cell labeling nanoprobe was engineered. A known affinity pair found in Nature was employed to render pH-responsive properties to the active layers of the nanoprobe. However, other tailor-made affinity pairs can be optimized or developed to specifically target the needs for tumor cell labelling, for instance by presenting a sharper dissociation behavior at tumoral pH conditions. Considering the scenario of *in vivo* nanoprobe administration, different behaviors would be expected as a consequence of the particles differing architectures. While biopolymer-coated MNP would be expected to passively accumulate in tumor tissue via EPR and internalized non-specifically, multilayer MNP internalization after EPR-mediated accumulation would be enhanced in response to tumor acidic environment.

More than static systems, the nanoparticles developed in the scope of this thesis, are versatile nanoplatforms for further functionalization. Given the availability of chemical functional groups on the polymeric coatings (carboxylic acid and hydroxyl groups in GA and EPS, and amine in PLL), more complex nanoprobes could be engineered. Targeting ligands, therapeutic moieties and/or reporter molecules could be conjugated to produce multimodal and theranostic nanodevices with tissue-specific uptake, which ultimately would contribute to the improvement of disease diagnosis accuracy and to the reduction of side effects associated with certain therapies.

Table 6.2. Overall summary of the interactions between the different MNP produced in this thesis and *in vitro* cell cultures.

MNP type	***Cell line***	***Incubation time***	***Relative IC_{50} (µg Fe/ml)***	***MNP in the culture medium (µg Fe/ml)***	***Absolute Fe uptake (pg Fe/cell)***	***In vitro MRI T_2-weighted contrast enhancement***
MNP-DMSA	HCT116	48 h	55	54	1.3	No efficient contrast enhancement
	ReNcell VM	4h + 24 h recovery	n. d.	57	1.1	n.d.
MNP-DMSA-GA	HCT116	48 h	43	31	17.3	Fe dose-dependent hypointensity I.D.=-18.1[Fe]+1994.8 (r^2 = 0.995)
MNP-DMSA-EPS	HCT116	48 h	82	46	8.4	Modest hypointensity compared with untreated cells. No linear variation.
	ReNcell VM	4h + 24 h recovery	n. d.	16	4.8	Fe dose-dependent hypointensity I.D.=-81.6[Fe]+2428 (r^2 = 0.997)
MNP-DMSA-PLLib-Nav-bPEG(B)	HCT116 (acidic medium)	5 h	n. d.	10	22.8	Increased hypointensity in acidic cell samples (T_2=56.8 ms) compared to neutral samples (T_2=63.9 ms)
	HCT116 (neutral medium)				11.8	

Iron concentration in the culture medium as determined by ICP-AES; average values of Fe uptake are presented. I.D.=integrated density; n.d. = not determined.

6.1. References

(1) Palma, S. I. C. J.; Marciello, M.; Carvalho, A.; Veintemillas-Verdaguer, S.; Morales, M. D. P.; Roque, A. C. A. Effects of Phase Transfer Ligands on Monodisperse Iron Oxide Magnetic Nanoparticles. *J. Colloid Interface Sci.* **2015**, *437*, 147–155, DOI:10.1016/j.jcis.2014.09.019.

(2) Palma, S. I. C. J.; Carvalho, A.; Silva, J.; Martins, P.; Marciello, M.; Fernandes, A. R.; Del Puerto Morales, M.; Roque, A. C. A. Covalent Coupling of Gum Arabic onto Superparamagnetic Iron Oxide Nanoparticles for MRI Cell Labeling: Physicochemical and *in Vitro* Characterization. *Contrast Media Mol. Imaging* **2015**, *10*, 320–328, DOI:10.1002/cmmi.1635.

(3) Freitas, F.; Alves, V. D.; Torres, C. a. V.; Cruz, M.; Sousa, I.; Melo, M. J.; Ramos, A. M.; Reis, M. A. M. Fucose-Containing Exopolysaccharide Produced by the Newly Isolated Enterobacter Strain A47 DSM 23139. *Carbohydr. Polym.* **2011**, *83*, 159–165, DOI:10.1016/j.carbpol.2010.07.034.

(4) Palma, S. I.; Rodrigues, C. A.; Carvalho, A.; Morales, M. P.; Freitas, F.; Fernandes, A. R.; Cabral, J. S.; Roque, A. C. A. A Value-Added Exopolysaccharide as a Coating Agent for MRI Nanoprobes. *Nanoscale* **2015**, *7*, 14272–14283, DOI:10.1039/C5NR01979F.

(5) Basly, B.; Felder-Flesch, D.; Perriat, P.; Billotey, C.; Taleb, J.; Pourroy, G.; Begin-Colin, S. Dendronized Iron Oxide Nanoparticles as Contrast Agents for MRI. *Chem. Commun.* **2010**, *46*, 985–987, DOI:10.1039/b920348f.

(6) Murugan, K.; Choonara, Y. E.; Kumar, P.; Bijukumar, D.; du Toit, L. C.; Pillay, V. Parameters and Characteristics Governing Cellular Internalization and Trans-Barrier Trafficking of Nanostructures. *Int. J. Nanomedicine* **2015**, *10*, 2191–2206, DOI:10.2147/IJN.S75615.